Physical-chemical characterization of nanoparticles in relevant biological environments and their interactions with the cell surface

Desirè Di Silvio

PhD

2015

Physical-chemical characterization of nanoparticles in relevant biological environments and their interactions with the cell surface

Desirè Di Silvio, 2015

Abstract

Nanoparticles (NPs) are versatile tools for nanomedicine and tuning features such as material, size and charge, imaging and targeting can be accomplished. However, NPs behaviour *in vivo* is modified upon interaction with the biological matter and formation of a protein corona (PC) coating the NP. The PC determines the NP biological identity and it is the ultimate interface with the surrounding environment. Therefore, a deep characterization of the NPs in biological media is important to predict adverse effects and improve NPs design.

The aim of this thesis was to understand the effect of the PC formation from different biological fluids on NP- membranes interactions. For this purpose, core-shell gold and magnetite NPs coated by poly-maleic anhydride and pegylated were characterized my means of scattering, microscopic and spectroscopic techniques.

Such NPs were characterized in serum and PC complexes were isolated. Sucrose-gradient ultracentrifugation (UC) was used guaranteeing quantitative recovery of homogeneous NP PC populations, simultaneously present *in situ,* and a lower impact on the *in situ* structures compared to conventional centrifugation protocols.

NP interactions with supported lipid bilayers (SLB) were investigated by QCM-D and neutron reflectometry allowing resolving at the sub-nanometer scale any structural reorganization of the SLB upon NP application. Carboxylated NPs generally caused lipid hydration with different mechanisms, while HC NPs compared to *in situ* NPs and pure FBS had a lower impact on the bilayers possibly indicating a major impact of the soft corona.

The last part of the project was focused on the PC evolution during simulated *in vitro* digestion with NPs. UC was suitable to isolate PC complexes from gastric and intestinal phases and SDS-PAGE and LC-MS suggested a PC ability to protect peptides from digestion degradation. The biological impact of the PC complexes was studied by confocal microscopy on Caco-2 cells revealing cells morphological alterations.

Acknowledgments

First, I want to thank my supervisors, Dr Francesca Baldelli Bombelli and Dr Alan Mackie, for their constant help and support during these long and, sometimes, tough years. Thanks to them I had the opportunity to learn a lot and not only scientifically. A big thank to Dr Roger Parker, Dr Andrew Mayes, Dr Balazs Bajka, Dr Neil Rigby and Dr Marco Maccarini because they have always been helpful and nice to me.

I need to thank friends because without them I don't think I would have made it. You, guys, are so many that probably I will forget someone…I apologize in advance!

I start with people that I met at first and have been with me until the end of this journey: Marco, Luca, Laura, Veronica, Sonia, Dani, Victor, Aiste, Jay and Cesar have been the constant of these years since the first day. Laura, Luigi and Bruno, in particular, made me feel the warmth of a family when I needed mine most!

I was so lucky with housemates who now are friends and friends who only after became housemates: Ana, Hanae, Claudia, Francesca and Veronica thanks to you all: home was always a safe and funny place to stay!

There are my "pub friends" who are so much more than that: Friday has always been the best day during the week! I already miss you and our routine at the Gradbar, the Walnut and, only on the best nights, Tapas and Karma. We should organize a reunion in few years' time. Thanks Yohan, Doroty, George, Julien, Tony, Davide and even Paul (!).

Then there are all the people that I met and became import to me: Melania, Teresa, Matteo, Francesco, Leo, Benedetta, Alberto, Simone, Alex.

I would have not made it without Paola, Mariarita and Lidia either. When I was missing home, you were always there to remember me that the distance is relative when you go back and it is like you have never left!

Special thanks are for my family: my parents and my brother, Enza, Antonio and Mirko. Without you, I would have not been here in the first place. You supported me no matter what and you always believed I could do it even when I did not. You have always been proud of me and that gave me the strength to go on, finish and go back to you. Love you!

Per primi, voglio ringraziare i miei supervisor, la Dr Francesca Baldelli Bombelli e il Dr Alan Mackie, per il loro costante aiuto e sostegno nel corso di questi lunghi e, a volte, duri anni. Grazie a loro ho avuto l'opportunità di imparare molto e non solo scientificamente. Un grande ringraziamento al Dr Roger Parker, il Dr Andrew Mayes, il Dr Balazs Bajka, il Dr Neil Rigby e il Dr Marco Maccarini perché sono sempre stati disponibili e gentili con me.

Devo ringraziare gli amici, perché senza di loro non credo che ce l'avrei fatta. Voi ragazzi siete così tanti che probabilmente dimenticherò qualcuno ... Mi scuso in anticipo!

Comincio con le persone che ho incontrato all'inizio e sono stati con me fino alla fine di questo viaggio: Marco, Luca, Laura, Veronica, Sonia, Dani, Victor, Aiste, Jay e Cesar sono stati la costante di questi anni dal primo giorno. Laura, Luigi e Bruno, in particolare, mi ha fatto sentire il calore di una famiglia quando ne avevo più bisogno!

Sono stata così fortunata con le mie coinquiline che ora sono amiche e amiche che solo dopo sono diventate coinquiline: Ana, Hanae, Claudia, Francesca e Veronica grazie a tutte voi: casa è sempre sempre un luogo sicuro e divertente!

Ci sono i miei "amici del pub" che sono molto di più di questo: Venerdì è sempre stato il miglior giorno della settimana! Già mi manca la nostra routine al Gradbar, il Walnut e, solo sulle migliori notti, Tapas e il Karma. Dovremmo organizzare una reunion fra qualche anno. Grazie Yohan, Doroty, George, Julien, Tony, Davide e anche Paul (!).

Poi ci sono tutte le persone che ho incontrato e sono diventate importanti: Melania, Teresa, Matteo, Francesco, Leo, Benedetta, Alberto, Simone, Alex.

Non ce l'avrei nemmeno mai fatta senza Paola, Mariarita e Lidia. Quando mi mancava casa, eravate sempre lì a ricordarmi che la distanza è relativa quando si torna ed è come non si fosse mai partiti!

Un ringraziamento particolare per la mia famiglia: i miei genitori e mio fratello, Enza, Antonio e Mirko. Senza di voi, io non sarei stata qui, in primo luogo. Mi avete sostenuta, nonostante tutto e avete sempre creduto che ce l'avrei fatta anche quando io non lo pensavo. Siete sempre stati orgogliosi di me e che mi avete dato la forza per andare avanti, finire e tornare da voi. Vi voglio bene!

TABLE OF CONTENTS

TABLE OF CONTENTS ..... **i**

LIST OF FIGURES ..... **vi**

LIST OF TABLES ..... **xv**

LIST OF ABBREVIATIONS ..... **xviii**

CHAPTER 1 INTRODUCTION **1**

1.1 NANOTECHNOLOGY AND NANOMEDICINE 1

1.2 NANOCARRIERS FOR DRUG DELIVERY 1

1.3 RATIONALE TO DEVELOP NANOPARTICLES FOR BIOMEDICAL APPLICATIONS 5

1.3.1 Colloidal properties of nanoparticles 5

1.3.2 NP Size effects on the interaction with the biological matter 6

1.3.3 NP Shape effects on the interaction with the biological matter 8

1.3.4 Surface charge and functionalities effects on the interaction with the biological matter 9

1.4 INORGANIC NANOPARTICLES 10

1.4.1 Gold nanoparticles 10

1.4.2 Magnetic nanoparticles 10

1.5 PROTEIN CORONA DEFINES THE NP BIOLOGICAL IDENTITY 11

1.5.1 Protein corona formation 12

1.5.2 Intrinsic and extrinsic parameters affecting biomolecular PC 14

1.5.3 Biomolecular-corona composition 16

1.5.4 Impact of PC on NP properties and biological response 17

1.6 PROJECT OBJECTIVE 19

1.7 BIBLIOGRAPHY 21

CHAPTER 2 MATERIALS AND METHODS **29**

2.1 INTRODUCTION 29

2.2 NANOPARTICLES SYNTHESIS AND FUNCTIONALIZATION 30

2.2.1 Polystyrene and Silica Nanoparticles 30

2.2.2 Magnetite Nanoparticles (Fe_3O_4) 30

2.2.3 Gold Nanoparticles (Au NPs) 31

Table of Contents

2.2.4 Core-shell NPs coated by poly (maleic anhydride-alt-1-octadecene) 32
2.2.5 PEG-functionalization 33
2.2.6 Fluorescent dye labelling 34
2.2.7 Drug loading 35
2.3 CHARACTERIZATION 35
2.3.1 Scattering techniques 35
2.3.1.1 Dynamic Light Scattering (DLS) 35
2.3.1.2 Zeta-potential 38
2.3.1.3 Nanoparticle Tracking Analysis (NTA) 39
2.3.1.4 Neutron Reflectometry (NR) 40
2.3.1.4.1 Neutron Reflectometry geometry 41
2.3.1.4.2 Neutron Reflectometry profile for rough surfaces 43
2.3.2 Spectroscopic techniques 46
2.3.2.1 UV-vis Spectroscopy (UV-vis) 47
2.3.2.2 Fluorescence Spectroscopy 47
2.3.2.3 Inductively coupled plasma atomic emission spectroscopy (ICP-AES) 48
2.3.2.4 Attenuated total reflectance- Fourier transform infrared spectroscopy (ATR-FTIR) 48
2.3.3 Microscopy 49
2.3.3.1 Transmission electron microscopy (TEM) 49
2.3.3.2 Fluorescence microscopy 50
2.3.3.3 Confocal microscopy 50
2.3.4 Separation techniques 51
2.3.4.1 Size exclusion chromatography (SEC) 51
2.3.4.2 Density-gradient ultracentrifugation (UC) 52
2.3.4.3 Electrophoresis: Agarose gel 53
2.3.4.4 Electrophoresis: SDS-PAGE 54
2.3.4.5 Liquid chromatography- mass spectrometry (LC-MS) 54
2.3.5 Quartz Crystal Microbalance with Dissipation Monitoring (QCM-D) 55
2.4 STUDIES WITH CELL LINES 57
2.4.1 Caco-2 57
2.4.2 M2O2 59
2.5 BIBLIOGRAPHY 60

CHAPTER 3 SYNTHESIS AND CHARACTERIZATION OF CORE-SHELL NPS 65

3.1 SHORT OUTLINE OF THE CHAPTER 65
3.2 SYNTHESIS IN ORGANIC SOLVENT 65
3.3 TRANSFER OF NPS IN AQUEOUS ENVIRONMENT 67
3.4 PURIFICATION OF POLYMER COATED NPS 70
3.4.1 Size exclusion chromatography 71
3.4.2 Sucrose gradient ultracentrifugation 72
3.5 SURFACE FUNCTIONALIZATION 75
3.5.1 Pegylation 75
3.5.2 Fluorescent labelling of the NPs 77
3.6 DRUG LOADING 82
3.7 POLYSTYRENE AND SILICA NPS 85
3.8 CONCLUSIONS 89
3.9 BIBLIOGRAPHY 91

CHAPTER 4 ISOLATION OF PROTEIN CORONA COMPLEXES FROM BLOOD SERUM 93

4.1 INTRODUCTION 93
4.2 OVERVIEW OF THE METHODOLOGY 94
4.3 POLYSTYRENE NPS 95
4.3.1 Polystyrene NPs functionalized with carboxylic groups 95
4.3.2 Polystyrene NPs functionalized with pegylated groups 99
4.4 SILICA NPS 102
4.5 POLYMER COATED MAGNETITE NPS 102
4.5.1 Fe_3O_4 102
4.5.2 Fe_3O_4-PEG 104
4.6 EFFECT ON CELL UPTAKE OF THE HC COMPLEXES ISOLATED BY ULTRACENTRIFUGATION AND CENTRIFUGATION 106
4.7 CONCLUSIONS 109
4.8 BIBLIOGRAPHY 110

CHAPTER 5 INTERACTIONS BETWEEN NPS AND LIPIDS MEMBRANE 112

5.1 INTRODUCTION 112
5.2 SUPPORTED LIPID BILAYERS 113
5.3 NP – SLB INTERACTIONS IN PHYSIOLOGICAL BUFFER 115
5.3.1 Size effect 116

5.3.2 Charge and surface coating effect 119
5.4 PROTEINS EFFECT 120
5.4.1 In situ NP – SLB interactions 122
5.4.2 HC NPs 123
5.5 FLUORESCENCE IMAGING OF QCM-D CHIPS 126
5.6 PROBING NPS- SLB INTERACTIONS BY NEUTRON REFLECTOMETRY 128
5.6.1 Insight into internal structure of SLB 128
5.6.2 Effects of pristine NPs on the SLB 130
5.6.2.1 PS-COOH20 133
5.6.2.2 Fe_3O_4 135
5.6.2.3 Fe_3O_4-PEG 138
5.6.2.4 Short summary of pristine NPs impact on SLB 139
5.6.3 Proteins effect on the SLB: In situ PS-COOH20 140
5.6.4 Proteins effect on the SLB: HC PS-COOH20 144
5.7 CONCLUSIONS 145
5.8 BIBLIOGRAPHY 147

CHAPTER 6 ISOLATION OF PROTEIN CORONA NPS FROM DIGESTIVE FLUIDS 151

6.1 INTRODUCTION 151
6.2 INFOGEST PROTOCOL AND STABILITY OF NPS IN DIGESTIVE FLUIDS 153
6.3 SKIMMED MILK POWDER DIGESTION 154
6.3.1 Simulated oral digestion 154
6.3.2 Simulated gastric digestion 156
6.3.3 Simulated duodenal digestion 158
6.4 BREAD SIMULATED DIGESTION 159
6.4.1 Simulated gastric digestion 160
6.4.2 Simulated duodenal digestion 165
6.4.3 Caco-2 transport experiment 169
6.4.3.1 NPs translocation through a Transwell dish without cells 169
6.4.3.2 NPs translocation through a Transwell dish with Caco-2 monolayer 171
6.4.3.3 Confocal imaging of Caco-2 monolayer 172
6.5 CONCLUSIONS 179
6.6 BIBLIOGRAPHY 181

Table of Contents

CHAPTER 7 CONCLUSIONS AND FUTURE WORK.....185

CHAPTER 8 APPENDIX 189

8.1 SUCROSE-GRADIENT ULTRACENTRIFUGATION OPTIMIZATION FOR RECOVERING PC NPS: SILICA NPS 189

8.2 TECHNICAL TIP: HIGH-RESOLUTION ISOLATION OF NANOPARTICLE–PROTEIN CORONA COMPLEXES FROM PHYSIOLOGICAL FLUIDS 192

8.3 EFFECT OF PROTEIN CORONA MAGNETITE NANOPARTICLES DERIVED FROM BREAD IN VITRO DIGESTION ON CACO-2 CELLS MORPHOLOGY AND UPTAKE 211

8.4 NANOSCOPIC AGENTS IN A PHYSIOLOGICAL ENVIRONMENT: THE IMPORTANCE OF UNDERSTANDING THEIR CHARACTERISTICS.....232

8.5 Fe_3O_4-COOH NPS CALIBRATION CURVE 234

8.6 BIBLIOGRAPHY 235

List of Figures

Figure 1.1 Model of a nanocarrier. The core (orange sphere) can be an inorganic particle coated by a hydrophilic layer (blue layer), a nanocapsule, a micelle, a liposome, a polymer self-assembling system or a dendrimer. The coating layer carries hydrophilic ligands as PEG chains (red curves), targeting peptides (grey curves) that can be functionalized by optical and targeting molecules (green semi-circles and yellow arrows respectively). Drugs can be embedded in the hydrophobic region of the NPs (red and yellow crystals) 2

Figure 1.2 Schematic representation of targeting mechanisms involving cancer tissues. A) Passive targeting. Thanks to the leaky vasculature and the poor lymphatic drainage, NPs from the blood stream, diffuse in the tumor. B) Active targeting. NPs are functionalized by ligands that specifically bind receptors overexpressed on cancer cells[1].....3

Figure 1.3 DLVO energy diagram. Van der Waals (dashed line) and electrostatic double layer (dotted line) contribute to total DLVO forces (full curve) represented versus the separation distance between two spheres (d).....6

Figure 1.4 Cellular uptake pathways. Phagocytosis (a), Macropinocytosis (b), Caveolar-mediated endocytosis (c), Clathrin-mediated endocytosis (d) and clathrin-independent and caveolin-independent endocytosis (e). NPs are represented by blue circles (> 1 μm), blue stars (~ 120 nm), red stars (~ 90 nm) and yellow rods (~ 60 nm).[36] 7

Figure 1.5 Schematic drawing of the PC NPs interacting with the cell membrane. The red and the blue circles around the NP delimit the hard corona and soft corona protein layers, respectively. The blue arrows indicate the dynamic nature of the PC where the adsorbed proteins exchange with the free ones. On the right, the PC does not hinder the targeting group (green receptor), PC hampers the binding to the receptor (red receptor)[93] 12

Figure 1.6 Model of PC NP based on the Vroman effect. The PC is made of several proteins layers characterized by their own dissociation constants (K_d) The inner layer is the hard corona (HC), the outer layers is the soft corona (SC).....13

Figure 2.1 Schematic representation of the NP transfer in aqueous solutions. NPs in chloroform were mixed with an excess of PMAO in organic solvent (in the box the monomer structure) and slowly evaporated under controlled pressure. The dry film was dissolved in a basic aqueous solution. 33

Figure 2.2 A) Geometry of a reflectometry experiment. Θ_i and θ_f are the incident and the reflected angles respectively and k_i and k_f the incident and reflected wave vectors. B) Typical profile for a surface in a reflectometry experiment: the solid line represented the best fit for the data collected.....42

Figure 2.3 Scattering lengths densities of some macromolecules in relation to the mixture H_2O/D_2O composition. Intersection points give the percentage of D_2O in the solvent necessary to match contrast the SLDs of components of the system. 44

Figure 2.4 Supported lipid bilayer modelling. A) The SLB is modelled by 5 layers: L1 is the superficial SiO_2; L2 and L3 are the inner head and tail, respectively; L4 and L5 the outer tail and head respectively. A Si subphase and a solvent superphase are present in the model. B)

Description of the lipid geometry: the head and the tail are defined by a thickness ($t_{h,t}$) and a volume ($V_{h,t}$), the area per molecule, A, is common to the two fragments. 46

Figure 2.5 Schematic representation of a confocal microscope. The screen with the pinhole blocks the unfocused light. The rotating mirrors allow to scan the entire sample pixel by pixel.[45] 51

Figure 2.6 Scheme of a QCMD cell.[70] The quartz crystal is placed between two gold electrodes. One electrode surface is exposed to solutions in flow. When AC is applied, the crystal oscillates and an adsorbed mass changes the frequency of oscillation. An exponential decay of frequency will result from the circuit opening 56

Figure 2.7 Example of QCMD experiment output data. Frequency (red line) and Dissipation (blue line) at the third overtone were monitored over time because of the better signal/noise ratio. Before each stage, equilibrium of the system was reached. A vesicles solution in PBS buffer was injected (a). When the bilayer formed, solvation water was expelled from the vesicles core and it caused another significant change in both signals (b). After washings to get rid of the vesicles in excess, NPs solution was sent through (c) and other washings were performed (d). 58

Figure 2.8 Diagram illustrating a Transwell Permeable Support device. Cells are grown in monolayer on a permeable membrane and two chambers, the apical and the basolateral are separated by the membrane and have independent access. 59

Figure 3.1 TEM images and size distributions obtained by TEM images. Images are at a magnitude of 50kx (a, Au NPs) and 40kx (c, Fe_3O_4). Statistics was done on about 500 NPs for each type of NP. 66

Figure 3.2 DLS Intensity-averaged size distributions of the hydrodynamic diameters for Au and Fe_3O_4 NPs. The original samples were diluted in toluene 20 times and the results are the average of three successive measurements 67

Figure 3.3 DLS auto-correlation functions of aqueous dispersions of Au NPs transferred by TMAH and NaOH. DLS curves were fitted by the double exponential equation 2.11.. 69

Figure 3.4 TEM images and histogram distribution of the carboxylated Au NPs and Fe_3O_4 (a and c respectively). Images are at a magnitude of 50kx. 250 particles were measured for each sample by ImageJ and the size distribution represented trough histograms (b and d, Au NPs and Fe_3O_4)... 70

Figure 3.5 Auto-correlation data (a) and intensity-averaged size distributions (b) obtained by DLS of Fe_3O_4 NP aqueous dispersions before (red lines) and after (blue lines) dialysis..…...71

Figure 3.6 Trends for hydrodynamic diameters (dH , full markers, left axis) and polydispersity indexes (PdI, empty markers, right axis) obtained from cumulant analysis of the auto-correlation functions of the fractions collected from Sephacryl S-500 SEC on Au (circles, a) and Fe_3O_4 NPs (triangles, b).... 72

Figure 3.7 TEM images and histogram distribution of the three fractions collected by SEC of Au NP aqueous dispersions. a-b) Fraction 1; c-d) Fraction 2; e-f) Fraction 3 relative to the samples whose parameters are reported in Table 3.5. Images were at a magnification of 50kx (a, c) and 40kx (b)... 73

Figure 3.8 Polymer and NPs detection by 2% agarose gel. A gel was loaded with NPs before dialysis (lane 1, 1*), after dialysis (lane 2, 2*), after SEC (lane 3, 3*) and imaged under visible light (a) and UV filter (b). C) Picture of a tube loaded with Fe_3O_4 after UC. D) Gel loaded with

aliquots collected from the top of the tube. Lanes 1-8 were imaged under UV filter while lanes 10 and 16 were imaged under visible light... 74

Figure 3.9 DLS intensity-averaged size distributions of Fe_3O_4 dispersions purified by UC (dotted line) and SEC (solid line)... 74

Figure 3.10 TEM images and relative histograms for pegylated Au NPs (a-b) and pegylated Fe_3O_4 (c-d). Images were at a magnification of 50kx and 40kx respectively (a-c). Statistics were done on 50 NPs... 76

Figure 3.11 1.5% Agarose gel run at 100V for one hour. a) carboxylated Au NPs; b) pegylated Au NPs; c) carboxylated Fe_3O_4; d) pegylated Fe_3O_4. 77

Figure 3.12 Auto-correlation data obtained by DLS comparing Fe_3O_4 dispersed in water (red circles) and PBS (blue triangle) 77

Figure 3.13 A) FA isomer. B) Emission spectra of FA in THF (dotted line) and PMAO modified with FA in THF (solid line). The concentration of the dye was 0.057 mM. The excitation wavelength was 430 nm 78

Figure 3.14 Analysis of the aliquots collected after UC of Fe_3O_4 coated with FA-PMAO. A) Fluorescence emission intensity (λ_{ecc}= 430 nm; λ_{em}= 513 nm) and UV absorption (λ_{abs}= 231 nm) of the 12 fractions collected from the top of the gradient to the bottom. B) 2% agarose gel of the sample before UC (first lane on the left) and the 12 fractions.....79

Figure 3.15 A) UV-vis spectra in PBS of unlabelled Fe_3O_4 (dotted line) and FA-labelled Fe_3O_4 (solid line). B) Emission spectra (λ_{ecc}= 430 nm) of unlabelled Fe_3O_4 (dotted line) and labelled ones (solid line).....80

Figure 3.16 Chemical structure (a) and absorbance and emission spectra in methanol (b) of BODIPY®FL EDA from LifeTechnologies.com 81

Figure 3.17 A) UV-Vis spectra of BODIPY modified Fe_3O_4, unlabelled Fe_3O_4 and washing solution. B) Fluorescence emission spectrum of the same samples at a λ_{ecc}= 500 nm 81

Figure 3.18 DLS auto-correlation data (a) and intensity-averaged size distributions (b) obtained from DLS of carboxylated unlabelled Fe_3O_4 (dashed line) and labelled carboxylated (black line) and pegylated (red line) Fe_3O_4. 80

Figure 3.19 Hydrodynamic diameters by intensity percentage of Leflunomide loade2 Au NPs with the two approaches. A) Drug in chloroform was added during the coating phase. B) The drug in chloroform was added after transfer of the NPs in water. Dialysis and SEC were performed to purify the final product..... 83

Figure 3.20 TEM images of Au NPs without drug (a) and with the drug (b). Magnification was 40kx and 60kx respectively.. 83

Figure 3.21 A) Uv-vis spectra for Au NPs with and without drug and the drug in chloroform (5 µg/ml). The plasmonic resonance band at 516 nm and a peculiar peak for Leflunomide at 260 nm were marked with dashed black lines. B) ATR-FTIR spectrum of Leflunomide in chloroform. The frequencies of some peaks were highlighted and assignation was represented in Table 3.10.. 84

Figure 3.22 ATR-FTIR spectra of Leflunomide-loaded Au NPs (blue line) and unloaded NPs (red line). Relevant bands were labelled and the increase in intensity and shifts could be due to the additional vibration of drug in the polymeric shell. 85

Figure 3.23 TEM images of PS-COOH20.Image was collected with a magnification of 29kx. Few drops of NPs' dispersions were placed on a copper grid and stained by uranyl acetate (picture taken by C. Webster). 87

Figure 3.24 Emission intensities for PS NPs in PBS. The excitation wavelength was 490 nm. 88

Figure 3.25 Concentration of PS NPs (mg/ml) versus emission intensity. The emission reported was for the maximum emission wavelength of 515 nm. 89

Figure 4.1 Scheme of the methodology to isolate and study HC NPs. NPs were incubated in biological fluid and then subjected to sucrose gradient (UC). In the image of the vial on the far left pink dots are NPs and the yellow background is the biological medium. In the images of the UC tubes (middle images), green dots represent some proteins that form diverse coronas around the NPs and are separated by UC exploiting density differences. 95

Figure 4.2 HC complexes of PS-COOH100. SDS-PAGE gel of the HC complexes of PS-COOH100 NPs in 90% (a) and 55% (b) FBS, isolated by conventional centrifugation methods (hard corona, HC) and sucrose ultracentrifugation (UC) respectively, as indicated by the label below the tracks of the gel. The concentration of the sucrose gradient was 5-30% w/w: at 55% FBS, UC1 and UC2 corresponded to sucrose concentrations of 13% and 21% w/w respectively; at 90% FBS, UC1 and UC2 corresponded to sucrose concentrations of 13% and 21% w/w respectively. 97

Figure 4.3 Fluorescence intensity emissions of the supernatant solutions compared to that of the initial stock solutions when centrifugal washings are performed on in situ samples of PS NPs incubated in 90% FBS. The excitation and emission wavelengths were 490 nm and 515 nm, respectively. 98

Figure 4.4 HC complexes of PS-COOH20. a) Intensity averaged size distribution of 20 nm PS NPs in situ in 90% FBS (black dots), relative HC complexes isolated by centrifugation (HC, red triangles) and ultracentrifugation (UC2, green empty triangles). B-C) SDS-PAGE gel of the complexes in 90% and 55% FBS, respectively, isolated by conventional centrifugation methods (hard corona, HC) and ultracentrifuge (UC1-2-3) as indicated by the label below the tracks of the gel. The concentration of the sucrose gradient was 4-40% w/w: at 55% FBS, UC corresponded to sucrose concentrations of 28% w/w; at 90% FBS, UC1, UC2 and UC3 corresponded to sucrose concentrations of 8%, 20% and 36% w/w respectively.....100

Figure 4.5 HC complexes of PS-PEG. a) Size distribution by intensity percentage of PS-PEG NPs in situ in 90% FBS (black dots), HC complexes isolated by centrifugation (HC, red triangles) and ultracentrifugation (UC, green empty triangles). B-C) SDS-PAGE gel of the HC complexes of PS-PEG NPs in 90% an 55% FBS respectively, isolated by ultracentrifugation (UC) and conventional centrifugation methods (HC), as indicated by the label below the tracks of the gel. The concentration of the sucrose gradient was 3-30% w/w: both at 55% and 90% FBS, UC corresponded to sucrose concentration of 15% w/w. 101

Figure 4.6 Characterization of SiO_2 NPs. In graph a) and b) are reported size distributions by intensity percentage of SiO2 NPs in 10% and 90% FBS respectively, compared to NPs in PBS (dashed line). C) SDS-PAGE gel of the hard corona complexes of SiO2 NPs in 10% and 90% FBS isolated by ultracentrifugation (UC) and conventional centrifugation methods (HC), respectively, as indicated by the labels below the tracks of the gel. The concentration of the sucrose gradient was 3-30% w/w: At 10% FBS UC1 and UC2 corresponded to sucrose concentrations of 15-18% and 21-24% w/w; at 90% FBS one single band at 12% w/w of sucrose concentration was isolated. 103

Figure 4.7 Characterization of Fe_3O_4 NPs. In graph a) are reported size distributions by intensity percentage of the NPs in 55% FBS in situ and HC complexes isolated by centrifugation (HC) and by ultracentrifuge (UC1-2). B) SDS-PAGE gel of the hard corona complexes in 55% and 90% FBS isolated by ultracentrifugation (UC) and conventional centrifugation methods (HC), respectively, as indicated by the labels below the tracks of the gel. The concentration of the sucrose gradient was 7-70% w/w: At 55% FBS UC1, UC2 and UC3 corresponded to sucrose concentrations of 35%, 56% and 63% w/w; at 90% FBS the two enriched bands were localized at 42% and 63% w/w of sucrose concentration. 104

Figure 4.8 Characterization of pegylated Fe_3O_4 NPs. In graph a) are reported size distributions by intensity percentage of the NPs in 55% FBS in situ and HC complexes isolated by centrifugation (HC) and by ultracentrifuge (UC). B) SDS-PAGE gel of the hard corona complexes in 55% isolated by ultracentrifugation (UC) and conventional centrifugation methods (HC), respectively, as indicated by the labels below the tracks of the gel. The concentration of the sucrose gradient was 7-70% w/w: One band enriched in PC complexes was isolated and corresponded to sucrose concentrations of 42% w/w.. 106

Figure 4.9 SDS-PAGE gel of the hard corona complexes in 55% formed by fluorescently labelled Fe_3O_4 NPs NPs isolated by ultracentrifugation (UC) and conventional centrifugation methods (HC), respectively, as indicated by the labels below the tracks of the gel. The concentration of the sucrose gradient was 7-70% w/w: Two bands enriched in PC complexes, UC1 and UC2, were isolated and corresponded to sucrose concentrations of 35% and 56-63% w/w.....107

Figure 4.10 Fe_3O_4 PC uptake. Confocal images of M202 cells after 2 hours of incubation with Fe_3O_4 PC complexes (10^{12} NPs/ml) isolated a)by centrifugation (HC), and (b) and (c) by ultracentrifugation. Actin filaments were stained by Texas Red®-X Phalloidin (red channel), nuclei by Hoechst33342 (blue channel) and NPs by BODIPY FL EDA (green channel)....107

Figure 4.11 Fe_3O_4 PC uptake. Confocal images of M202 cells after 4 hours and 24 hours of incubation with Fe_3O_4 PC complexes (10^{12} NPs/ml) isolated a)by centrifugation (HC), and (b) and (c) by ultracentrifugation. Actin filaments were stained by Texas Red®-X Phalloidin (red channel), nuclei by Hoechst33342 (blue channel) and NPs by BODIPY FL EDA (green channel).....108

Figure 5.1 DLS Intensity-averaged size distributions of the hydrodynamic diameters for DOPC and DOPC:SM 75:25 liposomes. The initial solution (20mg/ml) was diluted 50 times.....114

Figure 5.2 Frequency (a) and dissipation (b) profile obtained from the formation of DOPC (full line) and DOPC:SM (dashed line) SLB. In step 1, vesicles are injected in the chamber; at 2, vesicles start to collapse until a SLB is formed (3). Buffer washings are performed (4) to obtain the final SLB (5). Profile represents frequency and dissipation at the third overtone. 115

Figure 5.3 Frequency and dissipation variations during QCM-D experiments for interactions between DOPC: SM SLB and PS-COOH100, PS-COOH20, Fe_3O_4. A) Frequency shifts during the different steps of the experiments: the SLB after washings (SLB), the two NPs injections (NPs) and the two washings (WASH1-2). B) Dissipations of the SLB before the NPs injections (SLB) and at the end of the experiments. Experiments were done in triplicates. 117

Figure 5.4 Thickness variations during each step of QCM-D experiments on pristine PS-COOH20 at different concentrations. .Experiments were done in triplicates.....118

Figure 5.5 Frequency and dissipation variations during QCM-D experiments for interactions between DOPC: SM SLB and PS and carboxylated Fe_3O_4 and Fe_3O_4-PEG NPs. A) Frequency

shifts during the different steps of the experiments: the SLB after washings (SLB), the two NPs injections (NPs) and the two washings (WASH1-2). B) Dissipations of the SLB before the NPs injections (SLB) and at the end of the experiments. Experiments were done in triplicate 120

Figure 5.6 Frequency and dissipation variations during QCM-D experiments for interactions between DOPC and DOPC:SM SLB and FBS 55% v/v. A) Frequency shifts during each steps of the experiments: the SLB after washings (SLB), the two FBS injections (FBS) and the two washings (WASH1-2). B) Dissipations of the SLB before during all the phases of the experiments. Experiments were in triplicate.....121

Figure 5.7 Frequency shifts associated to each phases of QCM-D experiments in which Fe_3O_4 are injected on SLB covered by FBS proteins (striped bar). In PBS and *in situ* NPs were compared Experiments were done in triplicate.....122

Figure 5.8 Frequency shifts reported to the SLB shift following in situ NPs injections and washings. NPs were added in excess of serum proteins after one hour of incubation at 37°C, left to equilibrate on the SLB and washed by PBS. A) 100 nm diameter PS NPs; b) diameter < 50 nm NPs. Experiments were done in triplicate.....124

Figure 5.9 Frequency shifts reported to the SLB shift following HC NPs injections and washings. NPs were at concentration of 0.1 m^2/ml. PS-COOH100, PS-COOH100NF and PS-PEG were isolated by centrifugation; PS-COOH20, Fe_3O_4 and Fe_3O_4-PEG were isolated by ultracentrifugation, dialysed against PBS and concentrated by Amicon MWCO 50kD. Experiments were done in triplicate.....125

Figure 5.10 Hard corona composition is reported for carboxylated PS NPs. A) PS-COOH100; B) PS-COOH20; C) PS-COOH10NF. Lane are named: HC (stock of HC NPs before QCM-D experiment); F_IS (*in situ* NPs were recovered after they were added on the SLB and HC was obtained by centrifugation or ultracentrifugation); F_HC (the HC NPs were recovered after QCM-D experiment and analysed by SDS-PAGE). 126

Figure 5.11 Fluorescence micrographs of QCM-D chips after experiments. Near blue filter was used to captured images at several magnification and a scale bar is provided. Samples were kept hydrated but a certain amount of dryness and aggregation, induced during the imaging process, cannot be excluded.....127

Figure 5.12 NR profiles for all the DOPC SLBs prepared. Data were collected in D_2O contrast. Raw data are reported as $\log_{10}$ R as function of the momentum transfer **Q**. The NP used during the experiment names each SLB. PS-COOH20, Fe_3O_4 and Fe_3O_4-PEG were used in PBS, while HC PS-COOH20 were HC NPs isolated by UC and IS PS-COOH20 were NPs in 55% FBS. 130

Figure 5.13 A) Neutron reflectometry profiles for DOPC SLB plotted as $\log_{10}$ R as function of the momentum transfer **Q**. Raw data and fits for the three contrasts are reported: circles and green lines for D_2O, triangles and blue lines for SMW, squares and red lines for H_2O. Solid and dashed lines are respectively fits with models without (Rfit) and with constrains (Gfit). B) Correspondent SLD profiles in the three contrasts for the fittings. 130

Figure 5.14 NR curves for pristine NPs: a) PS-COOH20, b) Fe_3O_4-PEG, c) Fe_3O_4. Plots are in R $\mathbf{Q}^4$ vs **Q**. Data refer to SMW contrasts and NR profile of the SLB before (light blue circles) and after (dark blue circles) the injection of NPs are reported.....132

Figure 5.15 Plots of log (R) (reflected intensity divided by incident intensity) vs **Q** for SLB treated with PS-COOH20 NPs. A) SLB raw data with correspondent fittings; SLB after NPs injection fitted with 5-layers model (B) and 6-layers model (C).....134

Figure 5.16 SLD profiles describing the original SLB (a) and the SLB after NPs flowing (b). The profiles are obtained by the raw data fittings displayed in Fig. 5.15a-b. 135

Figure 5.17 NR profiles for DOPC SLB (a) treated by Fe_3O_4 NPs and modelled by 5-layers (b) and 6-layers models (c). Data are presented as R$\mathbf{Q^4}$ vs **Q**.....137

Figure 5.18 NR profiles for DOPC SLB (a) treated by Fe_3O_4 -PEG and modelled by 5-layers (b) and 6-layers models (c). Data are presented as log (**R**) vs **Q**. D-E) SLD profiles for SLB before and after NPs injection obtained from fittings in a-b) respectively 139

Figure 5.19 NR profiles for SLB (SLB), SLB after proteins injection (FBS) and after injection of in situ NPs. Data are presented as R $\mathbf{Q}^4$ vs **Q**. 141

Figure 5.20 SLD profiles derived from fitting the raw data with a 5-layers model without constrains. A)SLB; b) SLB after addition of FBS; c) SLB after addition of *in situ* PS-COOH20. 142

Figure 5.21 NR data describing the SLB after FBS flow (a) and *in situ* PS-COOH20 (b). Markers represent raw data, solid lines their simultaneous fittings by 6-layers model. The proteins layer exposed to the bulk phase was simplified assuming FBS composed by Albumin molecules. 143

Figure 5.22 NR profiles for SLB (SLB) and the SLB after HC PS-COOH20. Data are presented as R $\mathbf{Q^4}$ vs **Q** 144

Figure 5.23 NR profiles for DOPC SLB (a) treated by HC PS-COOH20 and modelled by 5-layers model (b). Data are presented as log (**R**) vs **Q**. C-D) SLD profiles for SLB before and after NPs injection obtained from fittings in a-b) respectively. 145

Figure 6.1 A) Hydrodynamic diameters variation by time for Fe_3O_4 NPs incubated in PBS (triangle), in SSF (circle) and SGF (upside-down triangle) at 37°C. B) PdI variation for the same samples. Hydrodynamic diameters and PdI were obtained by DLS from cumulant analysis of the auto-correlation data. 155

Figure 6.2 Hydrodynamic diameter distributions measured by NTA on NPs incubated in salivary mixture (black line), after UC (green dashed line) and after three centrifugation/washing steps. 156

Figure 6.3 Fe_3O_4 NPs in simulated salivary fluid. a) SDS-PAGE of fractions 1;4 and 5-7 (joined together from UC, HC NPs isolated by centrifugation and 5 fractions from a control UC experiment without NPs (1*-5*). b) Schematic drawing of the sucrose layers arrangement in the UC tube showing where NPs and proteins were located in samples with NPs (NPs) and without NPs (Ctr). 156

Figure 6.4 Fe_3O_4 NPs in simulated gastric fluid. a) Size distributions obtained from NTA for Fe_3O_4 NPs incubated with gastric fluids and relative PC complexes isolated by ultracentrifugation (UC) and centrifugation (HC). b) SDS-PAGE of the samples isolated by ultracentrifugation (UC) and conventional centrifugation (HC) methods, respectively, as indicated by the labels below the tracks of the gel. Red dashed lines on the gel highlighted bands analysed by LC-MS. 157

Figure 6.5 Fe_3O_4 NPs in SIF. Size distributions obtained from NTA analysis for NPs incubated with intestinal fluids for one hour and relative PC complexes isolated by ultracentrifugation (UC) and centrifugation (HC). 158

Figure 6.6 SDS-PAGE of Fe_3O_4 NPs in SIF. A) SDS-PAGE gel containing UC fractions of the sample of NPs incubated in intestinal fluids. Lane 8 contains the PC complexes; lanes labelled HC and SC contained SC and HC complexes, respectively, isolated by conventional

methods. B-C) Control samples without NPs to show no contaminations from free proteins in the lanes with the PC complexes. D) Schematic drawing of the sucrose layers arrangement in the UC tube showing where NPs and proteins were located in samples with NPs (NPs) and without NPs (Ctr). 160

Figure 6.7 A) Schematic drawing of the sucrose layers arrangement in the UC tube showing where NPs and proteins were located. Pink fractions (2-5) contained NPs while blue fractions contained floating starch residues. A control experiment only on digested bread without NPs underwent UC and it was sampled with the same modality. B) SDS-PAGE of PC-NPs obtained pooling together fractions 2-5 (G-NP lane) and some bands from the digestion run without NPs (lanes marked with* symbol). Some bands are framed with dashed lines and numbers and they were characterized by LC-MS. 161

Figure 6.8 A) Schematic drawing of the sucrose layers arrangement in the UC tube showing where NPs and proteins were located. Green fractions contained bile salts and low density peptides. Pink fractions (4-9 and 14-16) contained NPs. A control experiment only on digested bread without NPs was also measured and investigated. B) SDS-PAGE of PC-NPs obtained pooling together fractions 4-9 and 14-16 (D1-NP and D2-NPs lanes respectively). Lanes labelled with* symbol contained aliquots from a control UC run without NPs. Some bands are framed with dashed lines and numbers and they were characterized by LC-MS. 166

Figure 6.9 Fluorescence emission intensities for samples from the basolateral chambers after 1, 2, 3, and 4 hours of incubation (BL 1h, 2h, 3h, 4h) and for the apical chambers at the beginning of the experiment (AP t0) and after 4 hours (AP 4h). Fluorescence emission was measured with a plate reader with excitation wavelength at 492 nm and emission at 520 nm. Data are the average of three different replicates and they are normalized to AP t0. 170

Figure 6.10 Changes of TEER values before and after incubation of NPs for 4 hours..... 171

Figure 6.11 Confocal snapshots of Caco-2 monolayer after four hours of incubation with SFM:PBS 1:1 (PBS), Carboxyfluorescein (CF), bare Fe3O4 (Fe3O4), PC complexes isolated from gastric (G-NPs) and duodenal digestion (D1-NPs and D2-NPs). F-Actin filaments were stained by Phalloidin- Texas Red (591/608 nm) and nuclei by Hoechst 33342 (350/461 nm). Fe3O4 NPs were labelled by BODIPY FL-EDA (500/510 nm). Images were rendered using ImageJ. 173

Figure 6.12 Confocal stacks of pristine NPs incubated monolayer. A) Orthogonal stacks of the cells. B) Zoomed detail highlighted by green arrow. Actin filaments were stained by Phalloidin- Texas Red (591/608 nm) and nuclei by Hoechst 33342 (350/461 nm). Fe_3O_4 NPs were labelled by BODIPY FL-EDA (500/510 nm). Images are rendered by ImageJ. 174

Figure 6.13 Confocal stacks of G-NPs incubated Caco-2 monolayer. A) Orthogonal stacks and some zoomed details (b-c) highlighted by arrows. D) View from the bottom of the monolayer; f) stack in the zeta direction in which is visible the cell skeleton auto- fluorescing in green and porous channels containing green labelled NPs. Actin filaments were stained by Phalloidin- Texas Red (591/608 nm) and nuclei by Hoechst 33342 (350/461 nm). Fe_3O_4 NPs were labelled by BODIPY FL-EDA (500/510 nm). 176

Figure 6.14 Confocal stacks of D1-NPs incubated monolayer. A) Orthogonal stacks of Caco-2 cells and some highlighted details. B) 3D reconstruction of cells skeleton, NPs and support membrane. C) Nuclei and NPs clusters viewed from the top. Arrows show same details in a different prospective. Actin filaments were stained by Phalloidin- Texas Red (591/608 nm) and nuclei by Hoechst 33342 (350/461 nm). Fe_3O_4 NPs were labelled by BODIPY FL-EDA (500/510 nm). Rendering was done by ImageJ 177

Figure 6.15 Confocal stacks of D2-NPs incubated monolayer. A) Orthogonal stacks of Caco-2 cells in the XY, YZ, XZ planes. B-C) view from the bottom and the side of the monolayer showing nuclei and NPs. D-E-F) sequence of layers from 1 to 19 divided in the three channels, red (actin), green (NPs) and blue (nuclei) respectively. Actin filaments were stained by Phalloidin- Texas Red (591/608 nm) and nuclei by Hoechst 33342 (350/461 nm). Fe_3O_4 NPs were labelled by BODIPY FL-EDA (500/510 nm). Rendering was done by ImageJ. 178

Figure 8.1 Hydrodynamic diameter distributions measured by NTA on SiO_2 NPs incubated in 10% FBS. The black dashed line represents the in situ NPs before UC. The aliquots concentration is reported to the most concentrated aliquot to facilitate the comparison among fractions isolated by UC. Curves are the average of three measurements of 60 seconds. 190

Figure 8.2 A) Scheme of the sucrose layers arrangement after UC of SiO_2 NPs incubated in 10% FBS. The yellow area at the top of the gradient represented weakly bound proteins; blue and pink areas represented the two PC complexes. B) Hydrodynamic diameter distributions measured by NTA. The black dashed line represents the in situ NPs before UC. The aliquots concentration is reported to the most concentrated aliquot to facilitate the comparison among fractions isolated by UC. Curves are the average of three measurements of 60 seconds.. ...191

Figure 8.3 Concentration of Fe_3O_4-COOH NPs (NPs/ml) versus emission intensity. The solid line is the best linear fit of the emissions collected. The measurements were done by plate reader with excitation wavelength at 492 nm and emission at 520 nm. NPs were dispersed in serum free media without phenol red.....234

List of Tables

Table 2.1 List of the commercially available NPs employed in the study (nominal diameter and surface groups are reported). 30

Table 2.2 Parameters describing headgroup and tail fragments in DOPC lipid reported in Nagle et al.[40] 46

Table 2.3 Parameters used during ultracentrifugation through sucrose gradient for bare nanoparticles purified from the free polymer and for NPs in situ to isolate the hard corona. 54

Table 3.1 Comparison of the averaged diameters measured by DLS[1] and TEM. 66

Table 3.2 Parameters used to derive the concentration of particles in NPs/ml from the element concentration (mg/ml) in the dispersion derived from ICP- AES. 67

Table 3.3 Polymer coating optimization. 68

Table 3.4 Comparison between hydrodynamic diameters obtained by cumulant analysis and by double-exponential fitting (eq. 2.11) of the auto-correlation functions for TMAH and NaOH stabilised NPs represented in Fig. 3.3. 70

Table 3.5 DLS data[1] of purified Fe_3O_4 and Au NP dispersions obtained through size exclusion chromatography. Fe_3O_4 F1 (fractions 13-25), F2 (fractions 24-37); Au F1 (fractions 10-20), F2 (fractions 21-24), F3 (fractions 30-38).. 72

Table 3.6 DLS data[1] of purified Fe_3O_4 obtained by SEC and UC. SEC sample is F1 (fractions 13-25), UC corresponds to sucrose concentration of 33-50% w/w... 74

Table 3.7 Hydrodynamic diameters, polydispersity indexes, z-potential and dry diameters of pegylated Au NPs and Fe_3O_4. DLS was done on dispersion purified by SEC and UC. TEM images were collected for samples after dialysis Au-PEG NPs and Fe_3O_4-PEG isolated by UC corresponded to sucrose concentrations of 30-45% and 25-35% w/w respectively... 76

Table 3.8 Hydrodynamic diameters, polydispersity indexes and z-potential of pegylated Fe_3O_4 through EDAC coupling. 77

Table 3.9 Hydrodynamic diameters, polydispersity indexes and z-potential measured by DLS[1] of FA-labelled and unlabelled Fe_3O_4. UC F7-11 and UC F12 corresponded to sucrose concentration of 54-66% and 70% w/w respectively. 80

Table 3.10 Vibrational frequencies and relative assignments for ATR-FTIR spectra of Leflunomide in chloroform and after encapsulation in the NPs shell. 86

Table 3.11 Size and z-potential characterization of polymeric NPs in PBS. DLS and NTA data are reported. 87

Table 3.12 Characterization by DLS and NTA of the pegylated PS NPs commercially available. 88

Table 4.1 DLS and NTA characterization of PS-COOH100 NPs in PBS, 55-90% FBS and of HC complexes isolated by centrifugation (HC) and ultracentrifugation (UC 1-2). The concentration of the sucrose gradient was 5-30% w/w: at 55% FBS, UC1 and UC2 corresponded to sucrose concentrations of 13% and 21% w/w respectively; at 90% FBS, UC1 and UC2 corresponded to sucrose concentrations of 13% and 21% w/w respectively. 96

Table 4.2 DLS and NTA characterization of PS-COOH20 NPs in PBS, 55-90% FBS and of HC complexes isolated by centrifugation (HC) and ultracentrifugation (UC 1-2-3). The concentration of the sucrose gradient was 4-40% w/w: at 55% FBS, UC corresponded to sucrose concentrations of 28% w/w; at 90% FBS, UC1, UC2 and UC3 corresponded to sucrose concentrations of 8%, 20% and 36% w/w respectively.).....99

Table 4.3 DLS and NTA characterization of PS-PEG NPs in PBS, 55% and 90% FBS and of HC complexes isolated by centrifugation (HC) and ultracentrifugation (UC). The concentration of the sucrose gradient was 3-30% w/w: both at 55% and 90% FBS, UC corresponded to sucrose concentration of 15% w/w.....101

Table 4.4 DLS and NTA characterization of silica NPs in 10% and 90% FBS. The concentration of the sucrose gradient was 3-30% w/w: at 10% FBS UC1 and UC2 corresponded to sucrose concentrations of 15-18% and 21-24% w/w; at 90% FBS one single band at 12% w/w of sucrose concentration was isolated. 103

Table 4.5 DLS and NTA characterization of Fe_3O_4 NPs in 55% and 90% FBS. The concentration of the sucrose gradient was 7-70% w/w: At 55% FBS UC1, UC2 and UC3 corresponded to sucrose concentrations of 35%, 56% and 63% w/w, UC2 and UC3 were pooled together; at 90% FBS the two enriched bands were localized at 42% and 63% w/w of sucrose concentration.....105

Table 4.6 DLS and NTA characterization of pegylated Fe3O4 NPs in 55% FBS. The concentration of the sucrose gradient was 7-70% w/w: One band enriched in PC complexes was isolated and corresponded to sucrose concentrations of 42% w/w.....105

Table 5.1 *DOPC and DOPC:SM 75:25 liposomes after extrusion.*.....114

Table 5.2 Parameters measured and calculated for vesicles of different composition after collapsing in a lipid bilayer.....115

Table 5.3 NPs employed in QCM-D experiments described by size distributions and Z-potential in PBS.. 116

Table 5.4 NPs employed in QCM-D experiments described by size distributions of in situ NPs after incubation for one hour at 37°C and after injection on the SLB 122

Table 5.5 HC NPs employed in QCM-D experiments described by size distributions. NPs were incubated for one hour at 37°C and subjected to centrifugation or ultracentrifugation as was described in Chapter 4. The HC complexes were analysed before and after transit through QCM-D. 124

Table 5.6 Parameters acquired from the modelling of NR profiles of DOPC SLBs by models with (Gfit) and without constrains (Rfit). Gfit parameters are obtained applying equations in paragraph 2.3.1.4.2. Data are referred to the experiment named HC PS-COOH20 and plots in Fig. 5.13.. 130

Table 5.7 PS-COOH20 induced structural changes on SLB. Model with constrains (Gfit) was applied. The parameters describing the SiO_2 layer and the roughness of the layers were kept constant to evaluate the effects on thicknesses (t) and solvent penetration degrees (φ). Gfit parameters are obtained applying equations in paragraph 2.3.1.4.2.. 135

Table 5.8 Fe_3O_4 induced structural changes on SLB. Model with constrains (Gfit) was applied. The parameters describing the SiO_2 layer and the roughness of the layers were kept constant to evaluate the effects on thicknesses (t) and solvent penetration degrees (φ). Gfit parameters are obtained applying equations in paragraph 2.3.1.4.2.....136

Table 5.9 Fe_3O_4-PEG induced structural changes on SLB. Model with constrains (Gfit) was applied. The parameters describing the SiO_2 layer and the roughness of the layers were kept constant to evaluate the effects on thicknesses (t) and solvent penetration degrees (φ). Gfit parameters are obtained applying equations in paragraph 2.3.1.4.2.. 139

Table 5.10 Proteins induced structural changes on SLB. Model without constrains (Rfit) was applied. The parameters describing the SiO_2 layer and the roughness of the layers were kept constant to evaluate the effects on thicknesses (t) and solvent penetration degrees (φ). 142

Table 5.11 Proteins induced structural changes on SLB. Model without constrains (Rfit) was applied. The parameters describing the SiO_2 layer and the roughness of the layers were kept constant to evaluate the effects on thicknesses (t) and solvent penetration degrees (φ).. 143

Table 5.12 HC PS-COOH20 induced structural changes on SLB. Model with constrains (Gfit) was applied. The parameters describing the SiO_2 layer and the roughness of the layers were kept constant to evaluate the effects on thicknesses (t) and solvent penetration degrees (φ). Gfit parameters are obtained applying equations in paragraph 2.3.1.4.2.. 144

Table 6.1 Electrolytes final concentrations in SSF, SGF, SIF according to INFOGEST recommendations.[19] 153

Table 6.2 Characterization by DLS and NTA of Fe_3O_4 in PBS before undergoing digestion and PC complexes isolated by UC after dialysis (G-NPs). 162

Table 6.3 Identification of protein bands extracted from gel shown in Fig.6.7b 163

Table 6.4 Characterization by DLS and NTA of Fe_3O_4 in PBS before undergoing digestion and PC complexes isolated by UC after dialysis (D1- and D2-NPs). 165

Table 6.5 Identification of protein bands extracted from gel shown in Fig.6.8b. 167

Table 6.6 Vectorial transport ratio obtained from the molar ratio or the number of NPs ratio (Fe_3O_4, G-NPs, D1-NPs, D2-NPs) measured in the apical and basolateral chambers. 171

Table 7.1 Panel of NPs employed throughout the work for which PC NPs where recovered using both sucrose-gradient ultracentrifugation and standard washing/centrifugation cycles as reported in Chapters 2 and 4.. 186

List of Abbreviation

4MW	4 match water
APM	Area per molecule
AR	Aspect ratio
Au	Gold
b	Scattering length
BBB	Blood Brain Barrier
CF	Carboxyfluorescein
D	Diffusion coefficient
D_3	Dissipation factor
D_H	Hydrodynamic diameter
DLS	Dynamic Light Scattering
DLVO	Derjaguin, Landau, Verwey, Overbeak
DOPC	1,2-dioleoyl-sn-glycero-3-phosphocholine
DTT	Dithiothreitol
EDAC	N-(3-Dimethylaminopropyl)-N′-ethylcarbodiimide
EDL	Electrostatic double layer
ENM	Engineered nanomaterial
EPR	Enhanced permeability and retention
f	Frequency
FA	Fluorescein-amine
FA	Fluoresceinamin
FBS	Foetal bovine serum
Fe_3O_4	Magnetite
FR	Folic acid receptor
FTIR-ATR	Fourier Transform Infrared- Attenuated Total Reflectance
g_2	Field time-dependence autocorrelation function
GI	Gastrointestinal
GRP	Gastrin-releasing peptide
GUV	Giant unilamellar vesicles

List of Abbreviations

HC	Hard corona
ICP-AES	Inductively Coupled Plasma Atomic Emission spectroscopy
K_d	Apparent binding constant
LC-MS	Liquid chromatography- mass spectrometry
m	Hydrated Mass
MDR	Multi drug resistance
MQW	Milli-q water
MRI	Magnetic resonance imaging
MWCO	Molecular weight cut-off
NIR	Near infra-red
NP	Nanoparticle
NR	Neutron Reflectometry
NTA	Nanoparticle Tracking Analysis
PBS	Phosphate Buffer Saline
PC	Protein corona
PdI	Polydispersity index
PDT	Photodynamic therapy
PEG	Poly ethylene glycol
PMAO	Poly (maleic anhydride-alt-1-octadecene)
POPC	1-palmitoyl-2-oleoyl-sn-glycero-3-phosphocholine
PS	Polystyrene
PTT	Photothermal therapy
PVA	Polyvinyl alcohol
Q	Momentum transfer
QCM-D	Quartz crystal microbalance with dissipation monitoring
QSAR	Quantitative structure–activity-relationship
R	Reflectivity
RCF	Relative centrifugal force
RES	Reticulo-endothelial system
r_H	Hydrodynamic radius
SC	Soft corona
SEC	Size exclusion chromatography
SFM	Serum free medium
SGF	Simulated gastric fluid

SIF	Simulated intestinal fluid
SiO_2	Silica
SLB	Supported lipid bilayer
SLD	Scattering length density
SM	Sphingomyelin
SMW	Silica match water
SPION	Superparamagnetic iron oxide nanoparticle
SPR	Surface plasmon resonance
SSF	Simulated salivary fluid
t	Thickness
TBE	Tris/Borate/EDTA buffer
TEER	Trans Epithelial Electric Resistance
TEM	Transmission Electron Microscopy
TfR	Transferrin receptor
THF	Tetrahydrofuran
TMAH	Tetramethyl ammonium hydroxide pentahydrate
UC	ultracentrifugation
USPION	Ultrasmall superparamagnetic iron oxide nanoparticle
UV-vis	Ultraviolet-visible spectroscopy
V	Volume
VdW	Van der Waals
Zp	Zeta-potential
σ	Roughness
τ	Correlation delay time
φ	Solvent penetration degree

Chapter 1. Introduction

1.1 Nanotechnology and nanomedicine

Nanotechnology is the branch of science that studies the development and the manipulation of matter at the nanoscale. By definition, engineered nanomaterials (ENMs) have at least one dimension between 1 and 100 nm. They find applications in many aspects of human life and according to the BCC research report "Nanoparticles in biotechnology, drug development and drug delivery" of 2014 (www.bccresearch.com), nanotech market is expected to reach $79.8 billion by 2019. Nanotechnology fields span from health and safety to IT, industry, energy, environment, transports and aerospace.

Nanomedicine, nanotechnology applied to medicine, is gaining more and more interest and it accounts for over the 5% of nanotechnology research reports worldwide. In fact, ENMs present peculiar features with respect to the correspondent bulk materials that can be exploited to improve diagnostics and therapeutics for the treatment of various diseases. While in the last century, progress in medicine was due to the discovery of new drugs, nowadays the tendency is to improve the pharmacokinetic and pharmaco-dynamic properties of existing molecules by combining them with ENMs.[1] Nanotechnology can help to overcome some limits that make drugs unsuitable for the market such as chemical-physical stability, toxicity, dosage, lack of effective targeting and short circulating time in the body.

Cancer treatments, for example, can benefit from the employment of ENMs. In fact, drawbacks of cancer therapy are due to drugs toxicity, non-specificity and development of cellular resistance to several drugs (MDR).[2] The most effective drugs such as doxorubicin, paclitaxel and cisplatin also affect normal cell functions inducing cell death and blocking proliferation. Unfortunately, conventional chemotherapeutics are not able to distinguish between healthy and compromised tissues, especially affecting high proliferative cells including hair and bone marrow.[3] Moreover, in most cases the therapy is effective only if the disease is treated at an early stage, thus the possibility to design ENMs that work both as drug carriers and diagnostic and imaging tools is fundamental.

1.2 Nanocarriers for drug delivery

Theranostic drug delivery systems are nanocarriers that combine diagnostic and therapeutic actions.[4] Nanodevices used in medicine need to meet some requirements: biocompatibility,

physical and chemical stability, long circulation time to reach the target inside the body, higher uptake in the selected site with respect to other cells and tissues. The final goal is the enhancement of the drug pharmacokinetic and absorption profiles. The design of such a device leads toward the development of personalized treatments and prognoses improvement.[5]

Nanoparticles (NPs), nano-capsules, nano-emulsions, micellar systems and dendrimers can be numbered among nanocarriers. In Fig. 1.1 is represented an ideal model of a nanocarrier bearing many different functionalities that can be tuned depending on the desired use. The core, the surface layer and the ligands offer multiple solutions to regulate targeting, drug loading, and imaging properties.

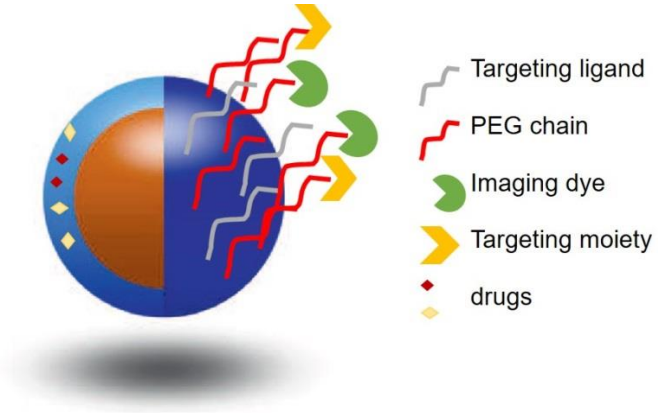

Figure 1.1 Model of a nanocarrier. The core (orange sphere) can be an inorganic particle coated by a hydrophilic layer (blue layer), a nanocapsule, a micelle, a liposome, a polymer self-assembling system or a dendrimer. The coating layer carries hydrophilic ligands as PEG chains (red curves), targeting peptides (grey curves) that can be functionalized by optical and targeting molecules (green semi-circles and yellow arrows respectively). Drugs can be embedded in the hydrophobic region of the NPs (red and yellow crystals).

There are already some nano-formulations on the market and many more in clinical trials.[6] Liposomes and polymeric formulations are available for the treatment of several diseases with embedded drugs, such as doxorubicin and paclitaxel reducing their cytotoxicity and prolonging their blood circulation to increase the drug concentration at the desired site (Doxil® and Abraxane®). These formulations exploit passive targeting to accumulate in the tumoral tissues. The passive targeting is based on the enhanced permeability and retention effect (EPR),[7] a phenomenon due to the physiological conformation of diseased tissues (cancer and inflammation). These tissues exhibit leaky vasculature and a less efficient lymphatic drainage system that allow a preferential accumulation of NPs with a longer permanence than in normal tissues. Active targeting is a complementary way to achieve accumulation of the nanocarrier at the desired site: NPs are coated with a ligand that binds specifically to a receptor particularly abundant on the cells of interest with respect to the others present in tissues or organs.

Targeting agents take advantage of specific interactions between ligand-receptor and antigen-antibody common pairs with high affinity: targeting agents can be proteins, peptides and antibodies (Fig. 1.2).

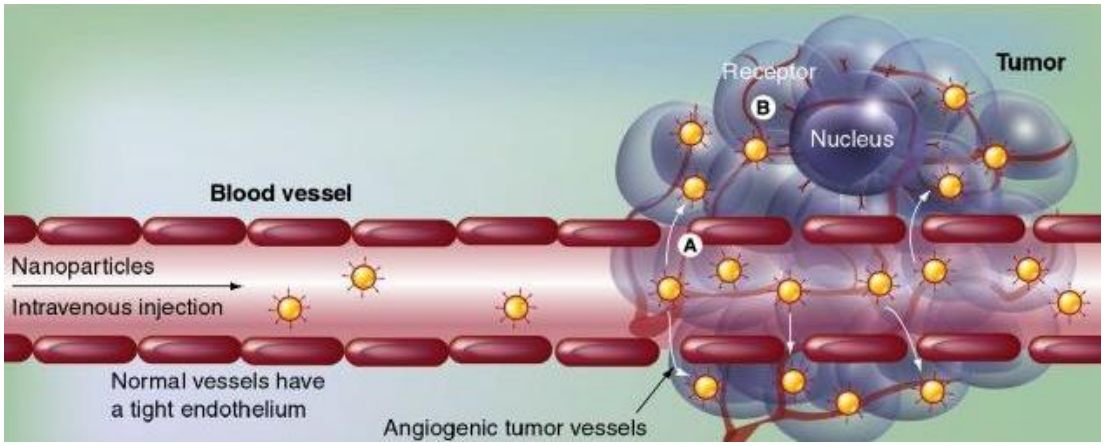

Figure 1.2 Schematic representation of targeting mechanisms involving cancer tissues. A) Passive targeting. Thanks to the leaky vasculature and the poor lymphatic drainage, NPs from the blood stream, diffuse in the tumor. B) Active targeting. NPs are functionalized by ligands that specifically bind receptors overexpressed on cancer cells.[1]

A receptor widely used for cancer cell targeting is the transferrin receptor (TfR): many colloidal formulations are functionalized with transferrin and anti-transferrin receptor antibodies because the receptor is overexpressed on tumour cells and proliferating primary malignant cells. The conjugation with transferrin of several drugs (doxorubicin, chlorambucil, oxaliplatin) showed improved cytotoxicity and less side effects with some of them in clinical trials (MPB-426 and SGT-53).[8] Transferrin was used to modify liposomes carrying two drugs for melanoma treatment and to overcome MDR. The combination with TAT peptide enhanced the targeting efficiency and the therapeutic action *in vivo*.[9] Furthermore, Tf targeting has been shown to increase blood brain barrier (BBB) NP translocation that is a major obstacle for the treatment of brain pathologies. Transferrin modified NPs were shown to be very efficient in targeting glioblastomas: Tf-coated Gadolinium NPs where tested as labelling and imaging agents.[10] Recently Dixit et al. developed transferrin-peptide gold NPs (Au) co-coated with growth epidermal factor for glioblastomas photodynamic therapy.[11] Kim et al. studied anti-TfR antibody coated liposomes to deliver temozolomide chemotherapeutic to glioblastomas.[12] In both cases, *in vivo* tests showed enhanced and faster accumulation of NPs in the tumour with an extension of animal survival period. In the case of Au NPs the accumulation increase was of 5-6 folds with respect to untargeted NPs, while for liposomes, the encapsulated drug

was 4-fold more effective in controlling tumour growth by using a dose 2.7–fold lower than the free drug.

Endocytosis via folic acid receptor (FR) is another well explored route to improve targeting toward epithelial cancer, myeloid leukaemia and activated macrophages during inflammation.[13] The FR binds the folic acid or folate with a very high affinity ($K_D \sim 10^{-9}$).[14] Many nanoformulations based on folate-functionalized NPs are under investigation in clinical trials (Hapten[15], folate-pRNA[16], Docetaxel loaded folic acid-liposome[17]).

Antibodies have been extensively adopted in cancer therapy and there are many antibody based treatments commercially available.[18] Herceptin and Rituxamab have been on the market since 1997. They are employed as ligands in many nanosystems.[19] Herceptin binds the human epidermal growth factor receptor ((HER)-2), overexpressed in breast cancer cells and it has been used in multimodal treatments exploiting the synergy with iron oxide hyperthermia therapy and the chemotherapeutic docetaxel. Herceptin plays the double role of targeting agent and anti-tumour drug.[20]

Peptides of 10-15 aminoacids are a valid alternative to antibodies because they are much simpler to synthesize, cheaper and were shown to be less immunogenic with respect to proteins and antibodies. They can be divided into three main groups: antimicrobial, cell penetrating and targeting peptides.[21] Antimicrobial peptides act forming holes in membranes and are suitable to treat infections such as Pseudomonas in the lungs: they have been associated to polymeric NPs to achieve penetration in bacterial biofilms.[22] Cell penetrating peptides can cross cell membrane without inducing toxicity and when associated with NPs, e.g. liposomes, the uptake efficiency can increase over 1000-fold compared to the free TAT peptide.[23] The RGD motif is a targeting peptide that was widely used to functionalize Au[24,25] and albumin NPs,[26] liposomes[27] and dendrimers.[28] RGD-motif binds to integrin receptors that play an important role in angiogenesis and are overexpressed in endothelial cancer cells but not in normal ones.[29] Another example is the bombesin peptide that binds to gastrin-releasing peptide (GRP) receptors overexpressed in prostate, breast and small-cell lung carcinoma. Chanda et al.[30] studied bombesin-functionalized conjugated Au NPs *in vivo* and they found a selective uptake of the functionalized NPs in prostate cancer cells and a minor accumulation in reticulo-endothelial system (RES) organs. Bombesin-dextran coating was used recently on superparamagnetic iron oxide NPs to image breast cancer cells and the increased contrast of tumour cells was associated to the prolonged circulation time in blood that allowed higher targeting efficiency.[31] The increased expression of fibronectin in micrometastasized cell

membrane was exploited for early imaging of breast cancer metastasis: a pentapeptide was linked to gadolinium NPs and metastasis smaller than 0.5 mm could be imaged.[32]

1.3 Rationale to develop nanoparticles for biomedical applications

Nanocarriers for medical applications need a careful design because biodistribution, cell internalization and toxicity depend primary on their physical-chemical properties such as size, material, shape, charge and surface functionalities. All those properties together with the environmental conditions combine to determine NPs fate *in vivo*. It is difficult to study the effects of these parameters independently, but some general considerations can be done.

1.3.1 Colloidal properties of nanoparticles

Nanoparticles in solution are a dispersion. The nanometer dimensions give features to the particles that distinguish them from bulk material. First, at room temperature NPs have a kinetic translation energy that is sufficient for causing NPs to move randomly in solution, while this energy is negligible for macroscopic objects. The second feature is the absence or almost of inertia. It means that the response to any impulse can be considered immediate for NPs. This property allows, for example, the movement of particles applying an external field (e.g. magnetic or electric). NPs interact with light and, according to their shape, composition and size, they can show interesting optical properties.[33] Among forces acting on NPs, gravitational force is negligible compared to other forces as it decreases with the third power of the mass. Intermolecular forces are long-range forces that act in distances of tens of nanometers. Because of the inter-particles forces, NPs in solution tend to stick together. To benefit from NPs properties and have a uniform response in terms of reactivity, bioavailability and toxicity, it is desirable to prevent NPs aggregation. Aggregation can occur as a consequence of either Brownian motions, if NPs collide and stick together, or gravitational agglomeration that occur when slowly settling NPs are “captured” by bigger particles during sedimentation. One of the most applied theories to explain colloidal stability is the DLVO theory. It was developed by Derjaguin, Landau, Verwey and Overbeak and bases aggregation on attractive and repulsive forces, namely van der Waals (vdW) and electrostatic double layer (EDL) forces. VdW interactions depend on the rotation and oscillation of dipoles of atoms and molecules and generally are attractive forces that act at short range. The surface charge and the surrounding solvent determine electrostatic double layer interactions. The ionic strength of the solution affects the extension of the EDL: while low ionic strengths assure its maximum

extension, high ion concentrations mask charges and the EDL is reduced. In Fig. 1.3 the theory is applied to two spheres. VdW forces determine interactions at the short and long range, while EDL interactions act at medium range distance. Net attraction is represented by two minima: a primary one for which aggregation is irreversible and a shallow one for which aggregation is reversible.

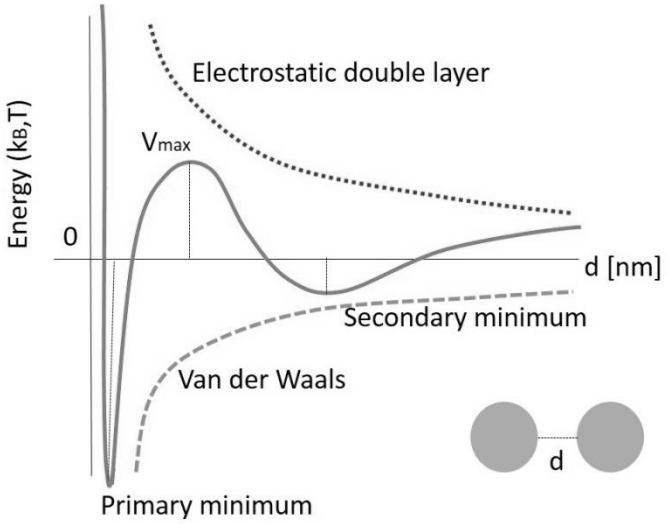

Figure 1.3 DLVO energy diagram. Van der Waals (dashed line) and electrostatic double layer (dotted line) contribute to total DLVO forces (full curve) represented versus the separation distance between two spheres (d).

Low charge and high ionic strength enhance the vdW contribution; high surface charge and low salt concentration enhance EDL forces.

Classical DLVO theory is not always able to explain inter-particles interactions especially for small ones. Forces other than vdW and EDL have been introduced in extended DLVO theories.[34] Hydrophobic, steric and osmotic forces are repulsive, while bridging and magnetic interactions are attractive and often more than one exists to determine NPs colloidal status. They are due to particular materials, coatings or media.

1.3.2 NP Size effects on the interaction with the biological matter

The optimal size of NPs suitable for biomedical applications is considered generally to be between 10 and 150 nm: smaller NPs are removed very quickly by extravasation and renal clearance, while the bigger ones accumulate mainly in the spleen, liver and bone marrow and are more exposed to the action of macrophages. Smaller NPs penetrate better hypovascular and hypopermeable solid tumours (pancreatic tumour for example) showing a more effective EPR effect.[35] NP size is one of the factors that influence the pathway of cellular uptake, the control of NP dimensions guarantees a better prediction for the final fate of the NP inside the

cell (Fig. 1.4).[36] One example in the literature where the authors took advantage of the environmental conditions is the work of Kim et al.[37] in which "smart" ENMs such as poly(ethylene-oxide)-b-poly(methacrylic-acid) (PEO-b-PMA) pH-responsive block-copolymers were developed. In fact, cross-linked PEO-PMA polymers at physiologic pH form micelles whose core is anionic. These micelles were loaded with doxorubicin that is a weak base at pH 7.4 achieving a loading efficiency of 50% w/w. Lysosomes are characterized by an acidic pH (~ 4.5-5.5) and in this environment, carboxylic groups on micelle cores were protonated causing micelle swelling and release of the drug.

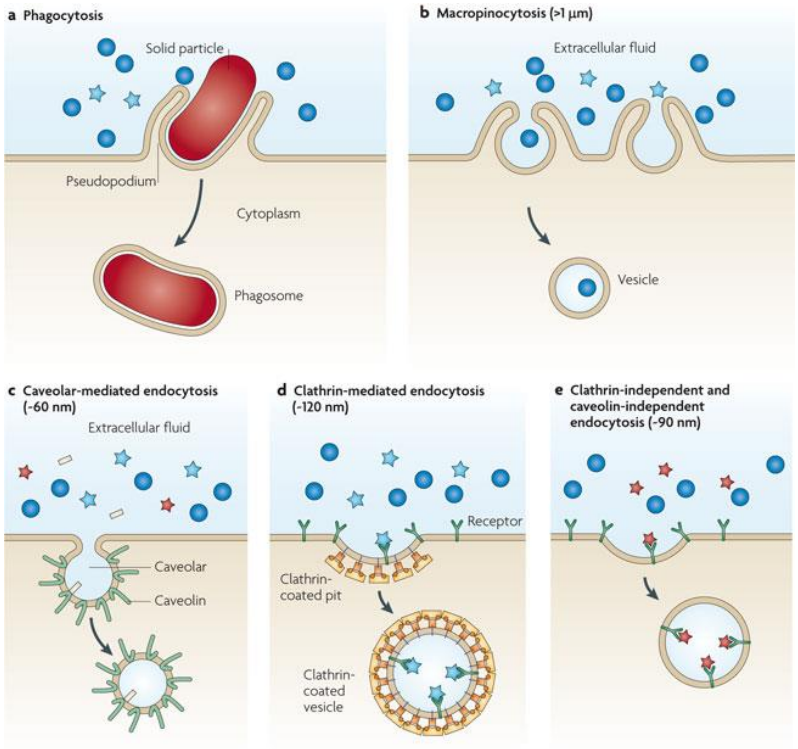

Figure 1.4 Cellular uptake pathways. Phagocytosis (a), Macropinocytosis (b), Caveolar-mediated endocytosis (c), Clathrin-mediated endocytosis (d) and clathrin-independent and caveolin-independent endocytosis (e). NPs are represented by blue circles (> 1 μm), blue stars (~ 120 nm), red stars (~ 90 nm) and yellow rods (~ 60 nm).[36]

Many reports in the literature suggest that particles in the micron range (1-10 μm) enter the cells through phagocytosis, mainly in macrophages and neutrophils. In all the other cells NPs mostly enter by pinocytosis through the formation of invaginations in the membrane and the size of the formed vesicles is the limiting factor for the cargo dimensions.[38] NPs of size around 1 μm will likely be taken up by macropinocytosis; clathrin-mediated endocytosis and the following lysosomal degradation occurs mainly for NPs between 120 and 200 nm. Caveolae-mediated endocytosis involves mainly NPs of about 60-80 nm and the formed vesicles reach the endoplasmic reticulum and the nucleus, while NPs smaller than 50 nm use clathrin- and

caveolein-indipendent pathways avoiding lysosomal degradation. However, many exceptions have been reported mostly due to the combined effects of NP physical-chemical features and experimental conditions.[39] Zhu and co-workers[40] studied the uptake of silica NPs in HeLa cells as a function of their size: largest NPs of about 300 nm followed clathrin- dependent and caveolin- independent pathways; NPs around 150 nm were internalized through clathrin- and caveolin- dependent endocytosis. NPs of 55 nm were subjected of both energy required clathrin- and caveolin- dependent endocytosis and energy- independent pathways. The cellular uptake of carboxylated polystyrene NPs of diameter ranging from 40 nm to 2 μm was studied in different cell lines: it was found size-dependent but the kinetics of uptake varied.[41] Cellular uptake showed to be size-dependent also for silica NPs,[40,42] Au NPs[43,44] and iron oxide NPs.[45] Many studies reported that the maximum internalization involves NPs of 50 nm.[42,44] Mathematical modelling is very useful to study mechanisms of internalization. In fact, by computational analysis, it was proved that NPs smaller or as big as the membrane width can penetrate the hydrophobic core of the lipid bilayer or create pores in the membrane, while NPs that are bigger than the thickness of the cell membrane are internalized by wrapping.[46] Adhesion and elastic forces influence the wrapping phenomenon and they are competitive. Elastic forces depend on the membrane and involve its bending capacity and its tension and they compete against the NPs wrapping. Adhesion forces are favourable forces and can be unspecific or specific. Unspecific adhesion is based on electrostatic and vdW interactions. Specific forces involve receptor-mediated endocytosis.[47] By computational studies[48-50] it was possible to explain the existence of an optimal diameter for internalization when the adhesion forces, and in particular the specific one, are big enough to overcome bending and stretching of the membrane and promote the diffusion of receptors to the binding site. Nevertheless, more factors such as the NPs shape and the presence of proteins in the environment can influence receptors-mediated endocytosis.

1.3.3 NP Shape effects on the interaction with the biological matter

Shape is another important NPs' feature. The effect of the aspect ratio (AR) has been studied for many NPs. Au and silver NPs optical properties change with size and shape.[51,52] The shape affects also the internalization of NPs in cells as different contact area modifies the bending energy and receptors distributions. However, the analysis of the AR by itself is not enough to draw conclusions. For Chithrani and co-workers spherical Au NPs showed a better internalization efficiency than rod-like Au particles with similar volume.[43] Instead, mesoporous silica NPs with larger AR were found to be taken up faster and in larger amount compared to spherical NPs inducing remodelling of cell cytoskeleton and apoptosis in human

melanoma cells.[53] Ammonium-functionalized carbon nanotubes showed to be internalized in mammalian cells through non-endocytic pathways and non-disruptive spontaneous penetration in cell membrane,[54] like nanoneedles.[55] In general filamentous NPs like magnetic nanowires[56] and nanotubes[57] have longer blood circulation times. Geng et al. injected long filomicelles in mice and they related their long blood half-life (one week) to the shear of blood flow.[58] The NPs elongation as consequence of the shear forces made the contact with cells more difficult and hence the internalization less for filomicelles than spherical particles.

1.3.4 Surface charge and functionalities effects on the interaction with the biological matter

NP surface charge and functionalization are key-factors for inter-particle and NP-cell interactions. NP surface charge and ligands contribute to NPs stability and/or solubility. According to the DLVO theory, spherical particles are stable is solution either because of electrostatic repulsions or of a coating that reduces NP surface energy limiting vdW attractions. Hydrophilic coatings assure a physical distance among the NPs promoting interactions with the solvent molecules.

Surface hydrophilic moieties minimize the adsorption of proteins in the biological environment[59,60] and in the blood stream, so that NPs are less exposed to macrophages action prolonging their half-life. Polyethylene glycol chains, albumin and carbohydrates based coatings help in increasing the hydrophilicity of the NPs.[61-63] Furthermore, they help reducing intrinsic cytotoxicity of some nanoagents.[64] Pegylation density and chain length has been shown to affect cell internalization[59,65,66] and *in vivo* biodistribution.[67] Low-density pegylation (below 10%), in which the chains assume a mushroom conformation, is optimal to reduce macrophages action and still get a good accumulation of the NPs in the tumour site. Pegylation was shown to be useful for promoting NP transport in mucus.[68]

Positively charged NPs have higher affinity to cell surfaces that express a slight negative charge and this electrostatic attraction explains the higher uptake and cytotoxicity of cationic NPs compared to negative charged NPs.[69] Negatively charged NPs, like Doxil (PEG surface), mostly penetrate the cell following the caveolae-mediated endocytocis,[70] although different uptake pathways can be involved when dealing with different cell lines.[71]

1.4 Inorganic nanoparticles

Inorganic NPs are interesting in cancer treatments because they can confer to the nanocarrier additive optical or magnetic properties originating from the NP core. In particular, gold (Au) and iron-based NPs also offer biocompatibility and a certain inertness compared to other materials.

1.4.1 Gold nanoparticles

Gold NPs are plasmonic noble metal NPs that have unique optical properties due to surface plasmon resonance (SPR). Upon exposure to light, electrons of the conduction band of Au NPs oscillate in a combined coherent way. The oscillation close to NPs surface causes charge separation with respect to the regular arrangement and dipole oscillation in the light electric field direction. The amplitude of the oscillation is maximum at a particular frequency that is the SPR. The SPR produces a strong absorption of the incident light. It depends on the electron charge density thus size, shape, structure and surrounding medium can affect it. SPR of spherical Au NPs with diameter of 20 nm absorbs light around 520 nm. The SPR decreases considerably for NPs smaller than 10 nm, while an increase in NPs size causes red-shift and higher band intensity; on the other side, NPs bigger than 100 nm show a broader band.[72] When the NPs AR is different form 1 as for nanorods, the SPR band is split into two bands: one weak in the visible region and one stronger in the near infra-red (NIR) which is red-shifted with AR increase.[73] Au nanostars can be characterized by multiple bands, one due to the core in the visible region and others in the NIR due to tip-core interactions, enhanced electromagnetic field at the tip site and less uniform shape.[74] The NIR adsorption is particularly interesting because it can be exploited in Photodynamic and Photothermal Therapies (PDT and PTT respectively). These therapies use photosensitizers to irreversibly damage and kill cells by generation of reactive oxygen species or local heat release following electrons excitation. Au NPs can do both upon irradiation by NIR light[72,75-77] and this is convenient because NIR light is the one that can penetrate deeper in tissues and, being less energetic, is less disruptive for healthy tissues surrounding the tumour site.

1.4.2 Magnetic nanoparticles

Magnetic NPs, as magnetite (Fe_3O_4), can be used to develop theranostic systems as they combine imaging (especially magnetic resonance imaging, MRI), hyperthermal and targeting drug delivery properties. Superparamagnetism is the key property related to small magnetic

particles (< 25 nm): they can be considered like small magnets that in absence of an external magnetic field show an average magnetization of zero as a result of random thermal flipping. When a magnetic field is applied, all NPs orientate and exhibit larger magnetic susceptibility and saturation compared to other paramagnetic materials.[78] Ideally, such NPs could be guided to the desired site by a high gradient magnetic field, but one of the main limitations of the guided targeting is that the gradient strength decreases going deep inside the body.[79] Superparamagnetic iron oxide NPs (SPIONs) are used as contrast agents for MRI. They act shortening the relaxation times of the surrounding water and decreasing the signal intensity to enhance the signal difference between the contrast agent and the surrounding water protons. The size,[80] the colloidal status[81] and the coating density[82] play an important role in determining relaxivity values (1/T) so a careful optimization of the design is always needed.
Another advantage of superparamagnetic NPs is the ability to accumulate energy by application of an external alternating magnetic field and release it as heat in consequence of the relaxation of rotating magnetic moments: magnetic hyperthermia is a therapy for controlled cancer cell death. Recently Kim and coworkers[83] coated Fe_3O_4 NPs with a pegylated polymer and they encapsulated doxorubicin. They combined the chemotherapeutic action of the drug to the hyperthermia effect on cells and on modulation of drug release.

1.5 Protein corona defines the NP biological identity

The large surface-to-volume ratios that characterize NPs are translated in massive surface free energy. The interaction of NPs with the surrounding biological matter (proteins, lipids, natural organic matter) decreases this potential. Result of these interactions is the formation of a "protein corona" (PC) around the NP surface providing the NP with a novel identity.[84,85] The factors influencing the PC formation are related to the NP physical-chemical properties (size, shape, surface charge and coating) and environmental factors such as media composition, temperature and time of exposure.[86]

PC constitutes a complex bio-nano interface that is responsible for NPs biological identity.[87,88] Its characterization is essential to understand the interaction of the NP with the biological matter, as what the cell "sees" is not the pristine NP but the PC interface.[89] Thus, the biological identity of the NP determines the biological response and NP cellular fate giving positive or negative outcomes, e.g. on colloidal stability and cell uptake.[90,91] In Fig. 1.5 PC NPs are illustrated in a schematic drawing where their dynamic interactions with the surrounding free proteins and the receptors in the cell membrane are highlighted. The PC is composed of a

"hard corona" (HC) and a "soft corona" (SC) according to the strength of the proteins binding to the NP surface. The formation of the PC strongly affects the NP interaction with cell membranes. The comprehensive understanding of PC evolution and its features should lead to the development of more efficient and safer nanomaterials prior their application *in vivo*.[92]

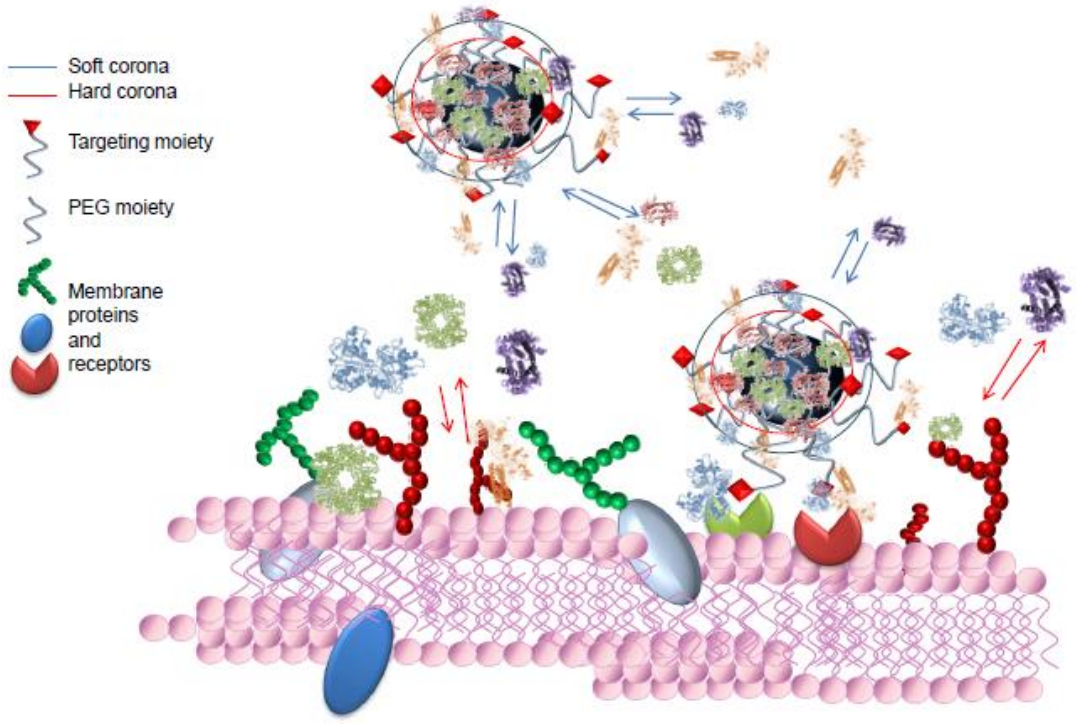

Figure 1.5 Schematic drawing of the PC NPs interacting with the cell membrane. The red and the blue circles around the NP delimit the hard corona and soft corona protein layers, respectively. The blue arrows indicate the dynamic nature of the PC where the adsorbed proteins exchange with the free ones. On the right, the PC does not hinder the targeting group (green receptor), PC hampers the binding to the receptor (red receptor).[93]

1.5.1 Protein corona formation

The formation of the PC is a thermodynamically driven process. The process has been studied extensively, but it is still debated and several models have been elaborated based on experimental evidences (Fig. 1.5).

The first proposed model describes the formation of the PC as driven by proteins adsorption and desorption from NP surface with variable rates that depend on the protein binding affinities and relative concentrations.[94] The coating occurs immediately when NPs enter in the biological medium. According to the model, at first, most abundant proteins bind to the NP surface. Over time, proteins that have higher affinities to the NP surface displace these proteins. This evolution phenomenon is known as "Vroman effect" and it was first observed on flat

surfaces.[95] The apparent binding constant (K_d) under equilibrium conditions determine which protein binds stronger the NP surface.[96] HC and SC are defined according to the binding strength of the proteins. HC is made of proteins that are strongly bound to the surface and exchange very slowly with the surrounding, for that it is quite stable over time and it is able to preserve a "protein fingerprint" of the environment in which the NPs transited. HC generally is shown to be composed of few tens of proteins that are not often among the most abundant in plasma (Fig. 1.6). On the contrary, SC is formed by one or more layers of proteins weakly bounded to NP surface or to HC proteins. For that, their exchange with the neighbouring proteins is fast. This model, although supported by experimental evidence, is not always able to explain some observed behaviours. For example, Jansch et al.[97] did not observe the Vroman effect when they incubated ultrasmall SPIONs (USPION) in plasma proteins and the same was found for nanoemulsions.[98]

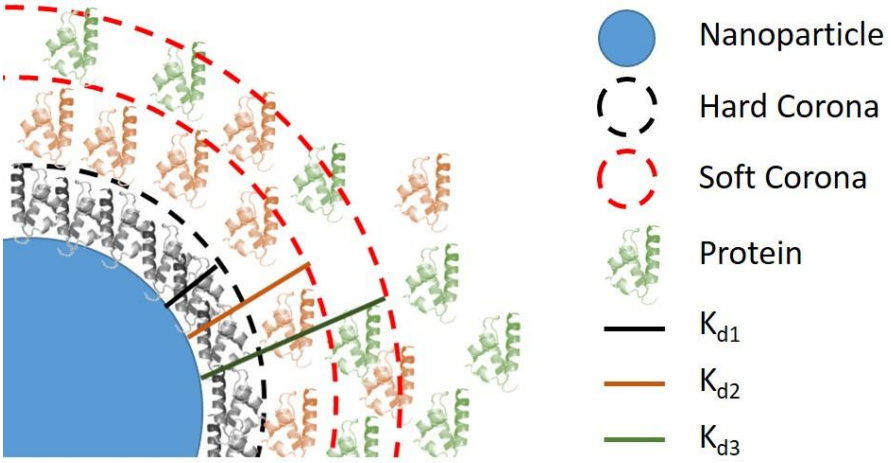

Figure 1.6 Model of PC NP based on the Vroman effect. The PC is made of several proteins layers characterized by their own dissociation constants (K_d). The inner layer is the hard corona (HC), the outer layers is the soft corona (SC).

Docter, Stauber and coworkers[99,100] developed a new model for protein corona evolution. Their new model is supported by recent studies in which are described PCs enriched with hundreds of proteins which evolve over time in quantity rather than quality[101]as it was assessed in Jansch's work. Furthermore, they found new kinetic trends for some proteins that do not follow Vroman effect and have "cup-shape" abundance trends with maximum or minimum adsorption at intermediate times.[101] In their model, the PC is formed within 30 seconds from the exposure to complex biological environment and it is made up of multi-layers of proteins. The inner layer is stable while the outer layers are more dynamic and exchange with the surrounding with kinetics both Vroman effect dependent and not. The proteins on the outer

layers could both weakly interact with the NP surface or establish weak protein-protein interactions with the HC proteins (Fig 1.5). Simberg and co-workers[102] introduced the concepts of "primary" and "secondary binders" to describe the interactions between a first layer of proteins strongly attached to the NP surface (primary binders) and an outer layer of proteins (secondary binders). In the model, secondary binders are relevant because they can change NPs coating properties and mask primary binders and NPs functionalities.

1.5.2 Intrinsic and extrinsic parameters affecting biomolecular PC

Coating, size and curvature of NPs can affect PC composition, but univocal correlation among all these factors has not been established yet. Sabuncu et al.[103] showed that Au NPs of different size in complete media formed stable proteins-NP complexes of comparable size, while in absence of proteins NPs aggregated. In another study, the analysis of PC compositions of silica NPs of different size revealed that the biomolecular corona was similar for all the NPs, while the relative amount of proteins varied.[104] Smaller NPs adsorbed more proteins (larger total surface area) and proteins with M_w below 50 kDa constituted of about 60-80% of the total PC, this was true especially for smaller NPs probably due to the more suitable curvature radius. On the contrary, PCs associated to larger NPs were more enriched with larger proteins (>100 kDa). Furthermore, a little influence of the surface charge on the adsorption of proteins with different isoelectric point was observed.[101] This observation correlates with the z-potential of PC NPs that generally slightly varies between -10 and -20 mV despite the charge of the pristine NPs. There are other interactions beyond the electrostatic ones that have been reported playing a role in PC composition (e.g. hydrogen bonding, London dispersion, hydrophobicity/hydrophilicity). Also charge can be distributed not homogeneously on both NP and protein surfaces promoting preferential interactions within specific domains.[105] NP shape, as the curvature, has a role in protein adsorption as it was shown by Mirsadeghi et al.[106] for sphere-like and rod-like gold NPs. Different PC patterns for the different NPs were described and the formation of the PC resulted in decrease of inhibit action on fibrillation of some proteins.

Surface coating of NPs can be modified to achieve a "stealth effect" reducing protein adsorption to limit interactions with macrophages and prolonging NPs circulation in blood. Polyethylene glycol is the most used anti-fouling coating agent and it has been shown that PEG grafting density and chain length modulate NP half-life in blood and interactions with target cells.[59,60,63,67,68]

There are factors that are independent of the NP and can affect corona formation and composition. Media composition is one of them. Colapicchioni and co-workers[107] analysed PCs originated from blood of both healthy and cancer donors. While the size of the PC complexes were very similar, quantitative and qualitative variations were found. Quantitative differences in the PCs were reported for donors within the same groups (healthy, breast, pancreatic, gastric cancers) and PCs from pancreatic cancer donors showed a much higher total protein content particularly enriched of immunoglobulins that reflects the pathology. This result is important in light of development of personalized medical treatments. A dynamic environment causes changes in the corona and in NPs colloidal status: for example, cells in culture secrete proteins and those proteins are able to alter PC composition and induce NPs aggregation. The situation is even more complicated because different cells secrete different proteins.[108]

As already mentioned, the PC formation is a dynamic process, thus time of exposure is a factor to carefully control during the experiments for obtaining comparable results. It has been shown many times that according to the exposure duration, HC composition does not change in quality but mainly in quantity. An extensive study performed by Tenzer and co-workers[101] revealed that a complex PC forms within half a minute upon exposure to media and major modifications happen at early times, while a PC fingerprint persists all along. Temperature influence on PC often is ignored, but it has been shown that temperature variations especially above 37°C can affect corona composition, structure and cells interaction.[109,110] In two recent studies, a PC formed in static conditions was compared to a PC formed in a dynamic environment keeping all the other parameters unvaried. Pozzi and co-workers[111] used a peristaltic pump to mimic abdominal aortic flow rate. Their findings highlighted differences between static and dynamic incubation of cationic liposomes with foetal bovine serum (FBS). The differences were in size evolution of the PC complexes and in composition. In particular, the dynamic incubation enriched corona with apolipoproteins instead of complement proteins with significant impact on targeting rather than interactions with macrophages. Another study examined differences in PC complexes structure and composition between bare, pegylated and targeted liposome after *in vitro* incubation with blood and *in vivo* circulation injecting NPs in mice. Overall, both *in vitro* and *in vivo* bare liposomes adsorbed the biggest amount of proteins. There were proteins common to all the PCs, but PCs of pegylated and targeted liposomes were enriched with unique proteins, especially for *in vivo* samples. Interestingly only *in vitro* PC-NPs complexes were characterized by peculiar fibrillary structures probably ascribed to the fibrinogen in the PC,

which has the ability to change conformation and form fibrils upon binding the NP surface.[112] Those two studies taken together say that *in vitro* studies on PC complexes can be a simplification of the actual *in vivo* situation and careful conclusions should be drawn.

It is evident the need of methodologies that consent the study of *in vivo* relevant PCs. However, the factors listed above can represent limitations in the choice of the protocol. There are many approaches that can be used,[93] but an optimum protocol should guarantee full recovery of complexes resembling *in vivo* PC NPs by minimum sample manipulation due to the PC dynamic nature. NPs' size and density and the fluids composition can limit the efficiency of some methodologies. For example, standard centrifugation is used routinely to obtain PC NPs, but partial sample recovery of NPs with density close to 1 mg/ml, and induced aggregation in presence of fluids particularly complex limit the efficiency of the process. Sucrose-gradient-based techniques and chromatography would guarantee to overcome these problems. The optimum approach should allow the separation of the multiple *in vivo* complexes in equilibrium among them, if they are present, but many techniques do not have the necessary resolution (e.g. centrifugation). Moreover, if needed for further applications, we should be able to recover high-volume samples of PC NPs and chromatography and centrifugation would not allow that in a short time.

1.5.3 Biomolecular-corona composition

Corona composition was examined in many studies through different techniques. Walkey and Chan[113] in a review, summarized the results of 26 works on the PC composition of 63 nanomaterials. They identified an "adsorbome" of 125 proteins that appear in the corona of at least one NP. They pointed out that all nanomaterials bind 2-6 proteins at higher amount, but they are not the same for all ENMs. In an interesting study,[87] it was shown that fibrinogen, whose concentration in 55% plasma is 10-27 μmol/L, was displaced from 200 nm silica NPs corona and histidine-rich glycoprotein became more abundant despite its low concentration (1-3 μmol/L). Hydrophobic sulfonated polystyrene NPs of the same size aggregated and it made difficult to determine corona composition, however it was composed mainly by albumin, fibrinogen and immunoglobulin that have affinity for hydrophobic regions and fibrinogen can enhance NPs clustering. In another study Jansch et al.[97] tested the effect of plasma concentration and incubation time on the formation of the PC for USPIONs: at low plasma concentration immunoglobulin chains and apolipoprotein A-1 were the most abundant; increasing the plasma concentration apolipoprotein A-1 abundance decreased and the PC enriched in fibrinogens. Albumin presence was not relevant although it is the most abundant

protein in plasma. This trend for albumin was confirmed by Clemments et al.[104] for silica NPs of various size and density in 10% FBS. It represented less than 4% of the complete PC. Serotransferrin, that is also very abundant in FBS, was completely absent in the PC. In Sakulkhu work[105] the investigation of HC and SC of USPION with positive, negative and neutral coatings did not give any correlation among all factors. PVA-coated USPION carried more proteins compared to dextran-coated, while most of proteins showed lower affinity for neutral coatings. A set of only four proteins was common to all HCs. Hydrophobicity and hydrophilicity of the NP plays a role in the PC composition.

So far, PCs derived from blood and serum proteins has been investigated. Just recently, the need to explore PC from other biological media has been stated.[99,114,115] That is mainly because the wide use of nanotechnology raised toxicological issues due to accumulation of NPs in the environment and inside the body through other pathways than intravenous. For example, if NPs are used in food and are ingested, the corona will depend on the food and evolve during digestive process. Gastrointestinal (GI) fluids are characterized by extreme conditions of pH, salts concentration and they are enriched of proteolytic enzymes. Those factors can affect NPs colloidal stability and toxicity.[116,117]

1.5.4 Impact of PC on NP properties and biological response

PC formation affects NP physical-chemical properties. For example, SPR bands of Au NPs experience a red-shift compatible with the change of the dielectric environment surrounding the NP surface.[106] Also magnetic properties of SPIONs are affected by the PC formation.[118] The immediate formation of the corona in some cases is exploited to stabilize charged NPs in high ionic strength conditions as in physiological and cell culture media.[119,120] In fact, the PC is able to provide steric stabilization.

Moreover, it has been reported that PC formation on silica and polystyrene NPs (PS) made them less cytotoxic and inhibits haemolytic effect on red blood cells.[101] Zinc oxide NPs[121] are widely employed in food industry and graphene oxide NPs[122] are emerging as interesting nano-objects. For both these kinds of NPs, toxicity is an issue although a pre-formed PC was shown to decrease their cytotoxicity. In the case of graphene nanosheets, the reduced cytotoxicity was related to a weaker interaction of the NPs with the cell membrane in the presence of the PC. In detail, PC reduced NPs uptake, in particular preventing penetration of the NPs in the cellular membrane, which caused lipids extraction and thus membrane defects. In other cases, although

PC is able to improve both colloidal stability and cytotoxicity, it has also been shown that its enzymatic degradation in lysosome might still induce cytotoxicity at different levels.[123]

The impact of PC on targeting efficiency and internalization processes can be either positive or negative. Serum albumin, for example, is adsorbed on nanoporous-polymer NPs with a change of conformation, this change enhanced uptake in macrophages but not in monocytes.[124] For polysorbate-stabilized solid lipid NPs, a selective adsorption of Apolipoprotein E from plasma has been found to facilitate the delivery of the drug to the brain improving the crossing of the blood brain barrier.[125] On the contrary, in many studies it has been highlighted that the adsorption of IgG, fibrinogen and complements (opsonins) on the NP surface promotes macrophage uptake and NPs removal from blood stream.[113] Apolipoproteins that are abundant in all coronas are involved in lipid and cholesterol transport in the membrane and consequently in internalization process in endothelial cells that implicates membrane proteins and lipid reorganization.[104] The binding of proteins to the NP surface can induce conformational changes in the protein as it has been already pointed out and these structural alterations can be either reversible[126] or irreversible, as it was reported for transferrin upon interaction with SPIONs.[127] The conformational changes can lead to the exposure of epitopes that can cause adverse effects.[128] For example, when fibrinogen binds poly (acrylic acid)-conjugated gold NPs is unfolded and interaction with the integrin receptor is promoted causing release of cytokines.

In silico approaches can help in elucidating NP-protein and NP-cell interactions for better predicting NPs behaviour in the biological environment in relation to their biological function. In this regard, Dell'Orco and co-workers[129] developed a model to predict how the PC composition affects cell targeting and uptake. They used experimentally derived kinetic rate constants, protein concentrations and geometrical factors to build a computational model. They concluded that it is possible to predict HC and SC compositions in good agreement with the experimental data. Experimentally derived stoichiometric and kinetic parameters, relative to specific NP-receptor interactions, are the starting set for building mathematical models and reproducing the experimental situation with good accuracy. However, in such a model no-cooperative effects among the proteins are introduced. Recently, quantitative structure–activity-relationship models (QSARs) have been applied to correlate NP-cell interactions to NP physical-chemical properties when NPs are coated by PC.[130] A dataset of 84 Au NPs described by 19 physical chemical features (hydrodynamic diameter, volume, Zp, NP surface area, etc.) was built and those NPs were characterized by coronas made of 129 proteins. The

correlation of all the factors listed above allowed identifying as main determinants for NPs-cell interactions some proteins such as apolipoproteins and some physical-chemical properties such as Zp. The best prediction accuracy got was of R^2 =0.895.

1.6 Project objective

Gold and Fe_3O_4 NPs have been largely studied in the past decades because of their biocompatibility and their peculiar physical-chemical properties that can be tuned by changing size, shape and coating.[74,75,78,131] They are ideal candidates to be used as theranostic nano-objects. Indeed, core properties at the nanoscale, such as optical properties for gold and magnetic qualities for magnetite, can be used as imaging tools and for thermal ablation therapy. The surface coating is modifiable through an organic shell, which enables targeting and imaging. The design of an ideal multifunctional nanocarrier relies on the understanding of its basic interactions with the biological matter in an environment resembling as much as possible *in vivo* conditions.

Keeping this in mind, the objective of this thesis was to investigate the interactions of model NPs, designed for biomedical applications, with biological membranes in the presence of a PC derived from various biologically relevant media.

This project was structured in four stages.

1- Two typologies of NPs were developed and fully characterized using various techniques. These techniques are described in *Chapter 2*. Au and Fe_3O_4 NPs were characterized following their synthesis in organic solvent, their transfer in water environment by amphiphilic polymer coating and the surface modifications by PEG and fluorescent molecules. This part is reported in *Chapter 3*.

2- The characterized NPs were studied in the presence of blood proteins. The formed PC complexes were isolated by sucrose-gradient ultracentrifugation (UC) and cycles of centrifugation/washing. The versatility and higher resolution of the methodology, compared to standard approach, were assessed applying it to several NPs (i.e. carboxylated and pegylated polymeric and core-shell Fe_3O_4 NPs). The physical-chemical characterization of the PC NPs and the influence of the approach used to isolate them on their biological response are illustrated in *Chapter 4*.

3- The interactions between NPs and cell membrane models were investigated. Quartz Crystal Microbalance with dissipation monitoring and Neutron Reflectometry were chosen to study supported lipid bilayers as model system of cell membranes. The effects of NP size,

surface charge and coating, as well PC formation on the interactions with the lipid bilayer were explored and outcomes are reported in *Chapter 5*.

4- The PC of Fe_3O_4 NPs derived from gastrointestinal fluids were studied. Sucrose-gradient ultracentrifugation was applied to recover PC complexes after gastric and duodenal *in vitro* digestion of NPs in the presence of food. An *in vitro* model of the small intestinal mucosa (Caco-2 cells monolayer) was used to investigate the biological response of the distinct PC complexes. Physical-chemical characterization of the complexes and their effect on Caco-2 cells are reported in *Chapter 6*.

1.7 Bibliography

(1) Desai, N. *The AAPS Journal* **2012**, *14*, 282.

(2) Shapira, A.; Livney, Y. D.; Broxterman, H. J.; Assaraf, Y. G. *Drug Resistance Updates*, *14*, 150.

(3) Feng, S.-S.; Chien, S. *Chemical Engineering Science* **2003**, *58*, 4087.

(4) Xie, J.; Lee, S.; Chen, X. *Advanced drug delivery reviews* **2010**, *62*, 1064.

(5) Peer, D.; Karp, J. M.; Hong, S.; Farokhzad, O. C.; Margalit, R.; Langer, R. *Nat Nano* **2007**, *2*, 751.

(6) Hafner, A.; Lovrić, J.; Lakoš, G. P.; Pepić, I. *International Journal of Nanomedicine* **2014**, *9*, 1005.

(7) Maeda, H. *Journal of Controlled Release* **2012**, *164*, 138.

(8) Xia, Q.; Yang, X.; Yang, X.; Qian, Z.; Wang, K. *Journal of Chinese Pharmaceutical Sciences* **2009**, *18*, 7.

(9) Yuan, M.; Qiu, Y.; Zhang, L.; Gao, H.; He, Q. *Drug Delivery* **2015**, 1.

(10) Korkusuz, H.; Ulbrich, K.; Welzel, K.; Koeberle, V.; Watcharin, W.; Bahr, U.; Chernikov, V.; Knobloch, T.; Petersen, S.; Huebner, F.; Ackermann, H.; Gelperina, S.; Kromen, W.; Hammerstingl, R.; Haupenthal, J.; Gruenwald, F.; Fiehler, J.; Zeuzem, S.; Kreuter, J.; Vogl, T.; Piiper, A. *Mol Imaging Biol* **2013**, *15*, 148.

(11) Dixit, S.; Miller, K.; Zhu, Y.; McKinnon, E.; Novak, T.; Kenney, M. E.; Broome, A.-M. *Molecular Pharmaceutics* **2015**, *12*, 3250.

(12) Kim, S.-S.; Rait, A.; Kim, E.; DeMarco, J.; Pirollo, K. F.; Chang, E. H. *Cancer Letters* **2015**, *396*, 250.

(13) Garcia-Bennett, A.; Nees, M.; Fadeel, B. *Biochemical Pharmacology* **2011**, *81*, 976.

(14) Hilgenbrink, A. R.; Low, P. S. *Journal of Pharmaceutical Sciences* **2005**, *94*, 2135.

(15) Lu, Y.; Klein, P. J.; Westrick, E.; Xu, L.-C.; Santhapuram, H. K. R.; Bloomfield, A.; Howard, S. J.; Vlahov, I. R.; Ellis, P. R.; Low, P. S.; Leamon, C. P. *The AAPS Journal* **2009**, *11*, 628.

(16) Guo, S.; Huang, F.; Guo, P. *Gene therapy* **2006**, *13*, 814.

(17) Li, X.; Tian, X.; Zhang, J.; Zhao, X.; Chen, X.; Jiang, Y.; Wang, D.; Pan, W. *International Journal of Nanomedicine* **2011**, *6*, 1167.

(18) Steichen, S. D.; Caldorera-Moore, M.; Peppas, N. A. *European Journal of Pharmaceutical Sciences* **2013**, *48*, 416.

(19) Weiner, L. M.; Surana, R.; Wang, S. *Nat Rev Immunol* **2010**, *10*, 317.

(20) Mi, Y.; Liu, X.; Zhao, J.; Ding, J.; Feng, S.-S. *Biomaterials* **2012**, *33*, 7519.

(21) Boohaker, R. J.; Lee, M. W.; Vishnubhotla, P.; Perez, J. M.; Khaled, A. R. *Current medicinal chemistry* **2012**, *19*, 3794.

(22) d'Angelo, I.; Casciaro, B.; Miro, A.; Quaglia, F.; Mangoni, M. L.; Ungaro, F. *Colloids and Surfaces B: Biointerfaces* **2015**, *135*, 717.

(23) Li, G.-H.; Li, W.; Mumper, R. J.; Nath, A. *The FASEB Journal* **2012**, *26*, 2824.

(24) Arosio, D.; Manzoni, L.; Araldi, E. M. V.; Scolastico, C. *Bioconjugate Chemistry* **2011**, *22*, 664.

(25) Kim, Y.-H.; Jeon, J.; Hong, S. H.; Rhim, W.-K.; Lee, Y.-S.; Youn, H.; Chung, J.-K.; Lee, M. C.; Lee, D. S.; Kang, K. W.; Nam, J.-M. *Small* **2011**, *7*, 2052.

(26) Dubey, P. K.; Singodia, D.; Verma, R. K.; Vyas, S. P. *Journal of Pharmacy and Pharmacology* **2011**, *63*, 33.

(27) Wang, F.; Chen, L.; Zhang, R.; Chen, Z.; Zhu, L. *Journal of Controlled Release* **2014**, *196*, 222.

(28) Li, K.; Zhang, Z.; Zheng, L.; Liu, H.; Wei, W.; Li, Z.; He, Z.; Larson, A. C.; Zhang, G. *Nanomedicine* **2015**, *10*, 2185.

(29) Danhier, F.; Breton, A. L.; Préat, V. *Molecular Pharmaceutics* **2012**, *9*, 2961.

(30) Chanda, N.; Kattumuri, V.; Shukla, R.; Zambre, A.; Katti, K.; Upendran, A.; Kulkarni, R. R.; Kan, P.; Fent, G. M.; Casteel, S. W.; Smith, C. J.; Boote, E.; Robertson, J. D.; Cutler, C.; Lever, J. R.; Katti, K. V.; Kannan, R. *Proceedings of the National Academy of Sciences* **2010**, *107*, 8760.

(31) Atefeh, J.; Mojtaba, S.; Saber Farjami, S.; Zahra, H.; Ahmad Bitarafan, R.; Komail, B.; Ali, N. *Nanotechnology* **2015**, *26*, 075101.

(32) Zhou, Z.; Qutaish, M.; Han, Z.; Schur, R. M.; Liu, Y.; Wilson, D. L.; Lu, Z.-R. *Nat Commun* **2015**, *6*, 7984.

(33) Kelly, K. L.; Coronado, E.; Zhao, L. L.; Schatz, G. C. *The Journal of Physical Chemistry B* **2003**, *107*, 668.

(34) Hotze, E. M.; Phenrat, T.; Lowry, G. V. *Journal of environmental quality* **2010**, *39*, 1909.

(35) CabralH; MatsumotoY; MizunoK; ChenQ; MurakamiM; KimuraM; TeradaY; Kano, M. R.; MiyazonoK; UesakaM; NishiyamaN; KataokaK *Nat Nano* **2011**, *6*, 815.

(36) Petros, R. A.; DeSimone, J. M. *Nat Rev Drug Discov* **2010**, *9*, 615.

(37) Kim, J. O.; Kabanov, A. V.; Bronich, T. K. *Journal of Controlled Release* **2009**, *138*, 197.

(38) Goldstein, J. L.; Brown, M. S.; Anderson, R. G. W.; Russell, D. W.; Schneider, W. J. *Annual Review of Cell Biology* **1985**, *1*, 1.

(39) Kettler, K.; Veltman, K.; van de Meent, D.; van Wezel, A.; Hendriks, A. J. *Environmental Toxicology and Chemistry* **2014**, *33*, 481.

(40) Zhu, J.; Liao, L.; Zhu, L.; Zhang, P.; Guo, K.; Kong, J.; Ji, C.; Liu, B. *Talanta* **2013**, *107*, 408.

(41) dos Santos, T.; Varela, J.; Lynch, I.; Salvati, A.; Dawson, K. A. *Small* **2011**, *7*, 3341.

(42) Lu, F.; Wu, S.-H.; Hung, Y.; Mou, C.-Y. *Small* **2009**, *5*, 1408.

(43) Chithrani, B. D.; Ghazani, A. A.; Chan, W. C. W. *Nano Letters* **2006**, *6*, 662.

(44) Neshatian, M.; Chung, S.; Yohan, D.; Yang, C.; Chithrani, D. B. *Colloids and Interface Science Communications* **2014**, *1*, 57.

(45) Huang, J.; Bu, L.; Xie, J.; Chen, K.; Cheng, Z.; Li, X.; Chen, X. *ACS Nano* **2010**, *4*, 7151.

(46) Bahrami, A. H.; Raatz, M.; Agudo-Canalejo, J.; Michel, R.; Curtis, E. M.; Hall, C. K.; Gradzielski, M.; Lipowsky, R.; Weikl, T. R. *Advances in Colloid and Interface Science* **2014**, *208*, 214.

(47) Nel, A. E.; Madler, L.; Velegol, D.; Xia, T.; Hoek, E. M. V.; Somasundaran, P.; Klaessig, F.; Castranova, V.; Thompson, M. *Nat Mater* **2009**, *8*, 543.

(48) Gao, H.; Shi, W.; Freund, L. B. *Proceedings of the National Academy of Sciences of the United States of America* **2005**, *102*, 9469.

(49) Chen, K. L.; Bothun, G. D. *Environmental Science & Technology* **2014**, *48*, 873.

(50) Zhang, S.; Gao, H.; Bao, G. *ACS Nano* **2015**, *9*, 8655.

(51) Dreaden, E. C.; Alkilany, A. M.; Huang, X.; Murphy, C. J.; El-Sayed, M. A. *Chemical Society Reviews* **2012**, *41*, 2740.

(52) Lee, K.-S.; El-Sayed, M. A. *The Journal of Physical Chemistry B* **2006**, *110*, 19220.

(53) Huang, X.; Teng, X.; Chen, D.; Tang, F.; He, J. *Biomaterials* **2010**, *31*, 438.

(54) Pantarotto, D.; Singh, R.; McCarthy, D.; Erhardt, M.; Briand, J.-P.; Prato, M.; Kostarelos, K.; Bianco, A. *Angewandte Chemie International Edition* **2004**, *43*, 5242.

(55) Shvedova, A.; Castranova, V.; Kisin, E.; Schwegler-Berry, D.; Murray, A.; Gandelsman, V.; Maynard, A.; Baron, P. *Journal of Toxicology and Environmental Health, Part A* **2003**, *66*, 1909.

(56) Park, J.-H.; von Maltzahn, G.; Zhang, L.; Schwartz, M. P.; Ruoslahti, E.; Bhatia, S. N.; Sailor, M. J. *Advanced materials (Deerfield Beach, Fla.)* **2008**, *20*, 1630.

(57) Singh, R.; Pantarotto, D.; Lacerda, L.; Pastorin, G.; Klumpp, C.; Prato, M.; Bianco, A.; Kostarelos, K. *Proceedings of the National Academy of Sciences of the United States of America* **2006**, *103*, 3357.

(58) Geng, Y.; Dalhaimer, P.; Cai, S.; Tsai, R.; Tewari, M.; Minko, T.; Discher, D. E. *Nat Nano* **2007**, *2*, 249.

(59) Pozzi, D.; Colapicchioni, V.; Caracciolo, G.; Piovesana, S.; Capriotti, A. L.; Palchetti, S.; De Grossi, S.; Riccioli, A.; Amenitsch, H.; Lagana, A. *Nanoscale* **2014**, *6*, 2782.

(60) Pelaz, B.; del Pino, P.; Maffre, P.; Hartmann, R.; Gallego, M.; Rivera-Fernández, S.; de la Fuente, J. M.; Nienhaus, G. U.; Parak, W. J. *ACS Nano* **2015**, *9*, 6996.

(61) Das, S.; Debnath, N.; Mitra, S.; Datta, A.; Goswami, A. *Biometals* **2012**, *25*, 1009.

(62) Kang, B.; Okwieka, P.; Schöttler, S.; Winzen, S.; Langhanki, J.; Mohr, K.; Opatz, T.; Mailänder, V.; Landfester, K.; Wurm, F. R. *Angewandte Chemie International Edition* **2015**, *54*, 7436.

(63) Jokerst, J. V.; Lobovkina, T.; Zare, R. N.; Gambhir, S. S. *Nanomedicine (London, England)* **2011**, *6*, 715.

(64) Singh, S.; Papareddy, P.; Mörgelin, M.; Schmidtchen, A.; Malmsten, M. *Biomacromolecules* **2014**, *15*, 1337.

(65) Essa, S.; Rabanel, J. M.; Hildgen, P. *International Journal of Pharmaceutics* **2011**, *411*, 178.

(66) Hu, Y.; Xie, J.; Tong, Y. W.; Wang, C.-H. *Journal of Controlled Release* **2007**, *118*, 7.

(67) Hak, S.; Helgesen, E.; Hektoen, H. H.; Huuse, E. M.; Jarzyna, P. A.; Mulder, W. J. M.; Haraldseth, O.; Davies, C. d. L. *ACS Nano* **2012**, *6*, 5648.

(68) Xu, Q.; Ensign, L. M.; Boylan, N. J.; Schön, A.; Gong, X.; Yang, J.-C.; Lamb, N. W.; Cai, S.; Yu, T.; Freire, E.; Hanes, J. *ACS Nano* **2015**, *9*, 9217.

(69) Verma, A.; Stellacci, F. *Small* **2010**, *6*, 12.

(70) Wang, J.; Byrne, J. D.; Napier, M. E.; DeSimone, J. M. *Small* **2011**, *7*, 1919.

(71) He, C.; Hu, Y.; Yin, L.; Tang, C.; Yin, C. *Biomaterials* **2010**, *31*, 3657.

(72) Huang, X.; El-Sayed, M. A. *Journal of Advanced Research* **2010**, *1*, 13.

(73) Lee, K.-S.; El-Sayed, M. A. *The Journal of Physical Chemistry B* **2005**, *109*, 20331.

(74) Huang, H.-C.; Barua, S.; Sharma, G.; Dey, S. K.; Rege, K. *Journal of Controlled Release* **2011**, *155*, 344.

(75) Doane, T. L.; Burda, C. *Chemical Society Reviews* **2012**, *41*, 2885.

(76) Vankayala, R.; Huang, Y. K.; Kalluru, P.; Chiang, C. S.; Hwang, K. C. *Small* **2014**, *10*, 1612.

(77) Huang, X.; El-Sayed, I. H.; Qian, W.; El-Sayed, M. A. *Journal of the American Chemical Society* **2006**, *128*, 2115.

(78) Cole, A. J.; Yang, V. C.; David, A. E. *Trends in biotechnology* **2011**, *29*, 323.

(79) Mody, V.; Cox, A.; Shah, S.; Singh, A.; Bevins, W.; Parihar, H. *Appl Nanosci* **2014**, *4*, 385.

(80) Kucheryavy, P.; He, J.; John, V. T.; Maharjan, P.; Spinu, L.; Goloverda, G. Z.; Kolesnichenko, V. L. *Langmuir* **2013**, *29*, 710.

(81) Tromsdorf, U. I.; Bigall, N. C.; Kaul, M. G.; Bruns, O. T.; Nikolic, M. S.; Mollwitz, B.; Sperling, R. A.; Reimer, R.; Hohenberg, H.; Parak, W. J.; Förster, S.; Beisiegel, U.; Adam, G.; Weller, H. *Nano Letters* **2007**, *7*, 2422.

(82) Tong, S.; Hou, S.; Zheng, Z.; Zhou, J.; Bao, G. *Nano letters* **2010**, *10*, 4607.

(83) Kim, H.-C.; Kim, E.; Jeong, S. W.; Ha, T.-L.; Park, S.-I.; Lee, S. G.; Lee, S. J.; Lee, S. W. *Nanoscale* **2015** , *7*, 16470.

(84) Lundqvist, M.; Stigler, J.; Elia, G.; Lynch, I.; Cedervall, T.; Dawson, K. A. *Proceedings of the National Academy of Sciences* **2008**, *105*, 14265.

(85) Cedervall, T.; Lynch, I.; Lindman, S.; Berggård, T.; Thulin, E.; Nilsson, H.; Dawson, K. A.; Linse, S. *Proceedings of the National Academy of Sciences* **2007**, *104*, 2050.

(86) Foroozandeh, P.; Aziz, A. A. *Nanoscale Research Letters* **2015**, *10*, 221.

(87) Monopoli, M. P.; Walczyk, D.; Campbell, A.; Elia, G.; Lynch, I.; Baldelli Bombelli, F.; Dawson, K. A. *Journal of the American Chemical Society* **2011**, *133*, 2525.

(88) Lesniak, A.; Fenaroli, F.; Monopoli, M. P.; Åberg, C.; Dawson, K. A.; Salvati, A. *ACS Nano* **2012**, *6*, 5845.

(89) Walczyk, D.; Bombelli, F. B.; Monopoli, M. P.; Lynch, I.; Dawson, K. A. *Journal of the American Chemical Society* **2010**, *132*, 5761.

(90) Aggarwal, P.; Hall, J. B.; McLeland, C. B.; Dobrovolskaia, M. A.; McNeil, S. E. *Advanced drug delivery reviews* **2009**, *61*, 428.

(91) Albanese, A.; Chan, W. C. W. *ACS Nano* **2011**, *5*, 5478.

(92) Maiolo, D.; Del Pino, P.; Metrangolo, P.; Parak, W. J.; Baldelli Bombelli, F. *Nanomedicine* **2015**, in Press.

(93) Sherwood, V.; Di Silvio, D.; Baldelli Bombelli, F. *Topics in Medicinal Chemistry* **2014**, 1.

(94) Monopoli, M. P.; Aberg, C.; Salvati, A.; Dawson, K. A. *Nat Nano* **2012**, *7*, 779.

(95) Vroman, L. *Nature* **1962**, *196*, 476.

(96) Pino, P. d.; Pelaz, B.; Zhang, Q.; Maffre, P.; Nienhaus, G. U.; Parak, W. J. *Materials Horizons* **2014**, *1*, 301.

(97) Jansch, M.; Stumpf, P.; Graf, C.; Rühl, E.; Müller, R. H. *International Journal of Pharmaceutics* **2012**, *428*, 125.

(98) Harnisch, S.; Müller, R. H. *European Journal of Pharmaceutics and Biopharmaceutics* **2000**, *49*, 41.

(99) Docter, D.; Westmeier, D.; Markiewicz, M.; Stolte, S.; Knauer, S. K.; Stauber, R. H. *Chemical Society Reviews* **2015**, *44*, 6094.

(100) Treuel, L.; Docter, D.; Maskos, M.; Stauber, R. H. *Beilstein Journal of Nanotechnology* **2015**, *6*, 857.

(101) Tenzer, S.; Docter, D.; Kuharev, J.; Musyanovych, A.; Fetz, V.; Hecht, R.; Schlenk, F.; Fischer, D.; Kiouptsi, K.; Reinhardt, C.; Landfester, K.; Schild, H.; Maskos, M.; Knauer, S. K.; Stauber, R. H. *Nat Nano* **2013**, *8*, 772.

(102) Simberg, D.; Park, J.-H.; Karmali, P. P.; Zhang, W.-M.; Merkulov, S.; McCrae, K.; Bhatia, S.; Sailor, M.; Ruoslahti, E. *Biomaterials* **2009**, *30*, 3926.

(103) Sabuncu, A. C.; Grubbs, J.; Qian, S.; Abdel-Fattah, T. M.; Stacey, M. W.; Beskok, A. *Colloids and Surfaces B: Biointerfaces* **2012**, *95*, 96.

(104) Clemments, A. M.; Botella, P.; Landry, C. C. *ACS Applied Materials & Interfaces* **2015**, *7*, 21682.

(105) Sakulkhu, U.; Mahmoudi, M.; Maurizi, L.; Salaklang, J.; Hofmann, H. *Sci. Rep.* **2014**, *4*, 5020.

(106) Mirsadeghi, S.; Dinarvand, R.; Ghahremani, M. H.; Hormozi-Nezhad, M. R.; Mahmoudi, Z.; Hajipour, M. J.; Atyabi, F.; Ghavami, M.; Mahmoudi, M. *Nanoscale* **2015**, *7*, 5004.

(107) Colapicchioni, V.; Tilio, M.; Digiacomo, L.; Gambini, V.; Palchetti, S.; Marchini, C.; Pozzi, D.; Occhipinti, S.; Amici, A.; Caracciolo, G. *The International Journal of Biochemistry & Cell Biology* **2015**, in Press.

(108) Albanese, A.; Walkey, C. D.; Olsen, J. B.; Guo, H.; Emili, A.; Chan, W. C. W. *ACS Nano* **2014**, *8*, 5515.

(109) Koshkina, O.; Lang, T.; Thiermann, R.; Docter, D.; Stauber, R. H.; Secker, C.; Schlaad, H.; Weidner, S.; Mohr, B.; Maskos, M.; Bertin, A. *Langmuir* **2015**, *31*, 8873.

(110) Mahmoudi, M.; Abdelmonem, A. M.; Behzadi, S.; Clement, J. H.; Dutz, S.; Ejtehadi, M. R.; Hartmann, R.; Kantner, K.; Linne, U.; Maffre, P.; Metzler, S.; Moghadam, M. K.; Pfeiffer, C.; Rezaei, M.; Ruiz-Lozano, P.; Serpooshan, V.; Shokrgozar, M. A.; Nienhaus, G. U.; Parak, W. J. *ACS Nano* **2013**, *7*, 6555.

(111) Pozzi, D.; Caracciolo, G.; Digiacomo, L.; Colapicchioni, V.; Palchetti, S.; Capriotti, A. L.; Cavaliere, C.; Zenezini Chiozzi, R.; Puglisi, A.; Lagana, A. *Nanoscale* **2015**, *7*, 13958.

(112) Hadjidemetriou, M.; Al-Ahmady, Z.; Mazza, M.; Collins, R. F.; Dawson, K.; Kostarelos, K. *ACS Nano* **2015**, *9*, 8142.

(113) Walkey, C. D.; Chan, W. C. W. *Chemical Society Reviews* **2012**, *41*, 2780.

(114) Lichtenstein, D.; Ebmeyer, J.; Knappe, P.; Juling, S.; Böhmert, L.; Selve, S.; Niemann, B.; Braeuning, A.; Thünemann Andreas, F.; Lampen, A. In *Biological Chemistry* **2015**, *396*, 1255.

(115) Nasser, F.; Lynch, I. *Journal of Proteomics* **2015**, in Press.

(116) Bergin, I. L.; Witzmann, F. A. *International journal of biomedical nanoscience and nanotechnology* **2013**, *3*, 163.

(117) Böhmert, L.; Girod, M.; Hansen, U.; Maul, R.; Knappe, P.; Niemann, B.; Weidner, S. M.; Thünemann, A. F.; Lampen, A. *Nanotoxicology* **2013**, *8*, 631.

(118) Amiri, H.; Bordonali, L.; Lascialfari, A.; Wan, S.; Monopoli, M. P.; Lynch, I.; Laurent, S.; Mahmoudi, M. *Nanoscale* **2013**, *5*, 8656.

(119) Dittrich, C.; Burckhardt, C. J.; Danuser, G. *Biomaterials* **2012**, *33*, 2746.

(120) Dobrovolskaia, M. A.; Patri, A. K.; Zheng, J.; Clogston, J. D.; Ayub, N.; Aggarwal, P.; Neun, B. W.; Hall, J. B.; McNeil, S. E. *Nanomedicine : nanotechnology, biology, and medicine* **2009**, *5*, 106.

(121) Yin, H.; Chen, R.; Casey, P. S.; Ke, P. C.; Davis, T. P.; Chen, C. *RSC Advances* **2015**, *5*, 73963.

(122) Duan, G.; Kang, S.-g.; Tian, X.; Garate, J. A.; Zhao, L.; Ge, C.; Zhou, R. *Nanoscale* **2015**, *7*, 15214.

(123) Ma, Z.; Bai, J.; Jiang, X. *ACS Applied Materials & Interfaces* **2015**, *7*, 17614.

(124) Yan, Y.; Gause, K. T.; Kamphuis, M. M. J.; Ang, C.-S.; O'Brien-Simpson, N. M.; Lenzo, J. C.; Reynolds, E. C.; Nice, E. C.; Caruso, F. *ACS Nano* **2013**, *7*, 10960.

(125) Goppert, T. M.; Muller, R. H. *Journal of drug targeting* **2005**, *13*, 179.

(126) Lundqvist, M.; Sethson, I.; Jonsson, B.-H. *Langmuir* **2004**, *20*, 10639.

(127) Mahmoudi, M.; Shokrgozar, M. A.; Sardari, S.; Moghadam, M. K.; Vali, H.; Laurent, S.; Stroeve, P. *Nanoscale* **2011**, *3*, 1127.

(128) Deng, Z. J.; Liang, M.; Monteiro, M.; Toth, I.; Minchin, R. F. *Nature nanotechnology* **2011**, *6*, 39.

(129) Dell'Orco, D.; Lundqvist, M.; Oslakovic, C.; Cedervall, T.; Linse, S. *PLoS ONE* **2010**, *5*, e10949.

(130) Liu, R.; Jiang, W.; Walkey, C. D.; Chan, W. C. W.; Cohen, Y. *Nanoscale* **2015**, *7*, 9664.

(131) Lu, W.; Xiong, C.; Zhang, G.; Huang, Q.; Zhang, R.; Zhang, J. Z.; Li, C. *Clinical Cancer Research* **2009**, *15*, 876.

Chapter 2. Materials and Methods

2.1 Introduction

Bioengineered nanoparticles (NPs) for nanomedicine are an interesting tool as are generally multifunctional objects able to carry out multiple tasks.[1] The need comes from the difficulty in treating certain diseases, like cancer, for which at the moment the current therapies are only effective in a narrow window of patients and at early stages of the illness. As extensively discussed in the previous chapter, NPs represent a versatile tool whose characteristics can be adapted to the need, tuning material, size, shape, charge and surface groups. In this scenario, core-shell NPs attract particular attention due to the possibility of exploiting both core and shell properties: for example, the inorganic core for imaging and diagnostic purposes and the outer shell for active targeting and drug transport.[2-6] For this reason, beyond the use of conventional NPs such as polystyrene and silica NPs, core-shell NPs based on magnetite (Fe_3O_4) and gold (Au) cores were also used in this project.

In this chapter, the procedures of synthesis and functionalization of core-shell Fe_3O_4 and Au NPs are described. Moreover, a theoretical background for all the techniques used during the project is provided. Given the multidisciplinary nature of this project, several techniques have been used for investigating NP physical-chemical characterization, their behaviour in the presence of biological fluids as well as with cell membrane models and cells.

Fe_3O_4 and Au cores were synthetized in organic solvent and coated with an amphiphilic polymer to achieve water transfer. Pegylation of the NP surface at various extents and drug loading were accomplished also. Other commercially available NPs were employed during the experiments to have a wider panel of materials and surface chemistries, namely polymeric polystyrene beads (PS) and silica NPs (SiO_2). Several techniques were used to characterize the colloidal properties of these NPs such as Transmission Electron Microscopy (TEM), Dynamic Light Scattering (DLS), Nanoparticle Tracking Analysis (NTA), agarose gel electrophoresis, Ultraviolet-visible spectroscopy (UV-vis), Inductively Coupled Plasma Atomic Emission spectroscopy (ICP-AES), Fourier Transform Infrared- Attenuated Total Reflectance (FTIR-ATR).

Size exclusion chromatography (SEC) and ultracentrifugation through sucrose gradient (UC) were used to purify NPs from the excess of polymer. The latter methodology was also applied to NPs when dispersed in complex biological environments to isolate protein-corona NPs. The PCs were further characterized by SDS-PAGE electrophoresis and liquid chromatography- mass spectrometry (LC-MS).

The interactions between NPs and cell membrane models were investigated through Quartz Crystal Microbalance (QCM-D) and Neutron Reflectometry (NR). Fluorescence microscopy was used in the presence of fluorescently labelled particles.

The last part of the project aimed to relate previous findings on cell model systems to NP-cell interactions *in vitro*. Several cell lines were used and NP uptake was assessed using fluorescence confocal microscopy.

2.2 Nanoparticles synthesis and functionalization

2.2.1 Polystyrene and Silica Nanoparticles

Polymeric carboxylated polystyrene beads (PS, Invitrogen) were labelled with a yellow- green dye (unless specified). Silica NPs (SiO_2) were purchased from Kisker. A summary of all the commercially available NPs used during the project is presented in Table 2.1. They were chosen because of their stability, biocompatibility, low density and the extensive characterization in the literature.[7,8]

Table 2.1 List of the commercially available NPs employed in the study (nominal size and surface groups are reported).

	d [nm]*	**Surface groups**
PS-COOH20	20	-COOH
PS-COOH100	100	-COOH
PS-COOH100NF**	100	-COOH
SiO_2	50	-OH

*provided by the manufacturer. **NF not fluorescently labelled

2.2.2 Magnetite Nanoparticles (Fe_3O_4)

Commonly magnetite NPs (Fe_3O_4) are prepared via co-precipitation of iron salts in alkaline water solutions in the presence of stabilizing agents and surfactants, but this method not always leads to crystalline and monodispersed NPs.[9,10] The synthetic protocol chosen for this work

was developed by Sun and coworkers[11] and it is based on thermal decomposition of an organic Fe salt that provides a better control on the size and size distribution producing small monodispersed nanocrystals.

Iron (III) acetylacetonate (2 mmol, Sigma Aldrich, 97%), 1, 2-tetradecanediol (10 mmol, Sigma Aldrich, 90%), oleic acid (6 mmol, Sigma Aldrich, 90%), oleylamine (6 mmol, Sigma Aldrich, 70%) dibenzyl ether (20 ml, Sigma Aldrich, 99%) were mixed and stirred magnetically under nitrogen flow. The mixture was heated gradually to 100°C in 45 min and kept at 100°C for other 45 min. Again, the temperature was raised to 200 °C in 40 min and kept constant for two hours. After that, the mixture was kept one hour at 300°C and then cooled to room temperature and left stirring overnight. It was transferred using a small amount of toluene in falcon tubes and centrifuged for 5 min to 360 rcf to eliminate insoluble aggregates. An excess of ethanol was added to the recovered solution and the black precipitate was separated via centrifugation (765 rcf, 30 min). The latter was dissolved in the minimum amount of toluene (Fluka) and filtered with a 0.22μm pores syringe filter.

2.2.3 Gold Nanoparticles (Au NPs)

The first scientific report describing a solution of colloidal gold (Au) solution was published in 1857 by Michael Faraday.[12] He used a two-phase method reducing an aqueous gold salt solution with phosphorus in carbon disulfide and obtained a ruby coloured water solution of dispersed gold particles. In 1994 Brust *et al.*[13] presented a two-phase method in which the growing nuclei were stabilized by thiols and the gold chloride was transferred in toluene using tetraoctylammonium bromide, a phase-transfer reagent. Tetraoctylammonium bromide was the phase-transfer agent used to move gold chloride from water to toluene and then reduced with aqueous sodium borohydride in the presence of dodecanethiol. In this work, dodecanethiol coated gold NPs were synthesised according to the Brust protocol with some changes.[14] The organic phase of tetraoctylammonium bromide in toluene (66 ml, 50 mM, Sigma Aldrich, 90%) was mixed with the aqueous phase of hydrogen tetrachloroaurate (III) in MQW (20.8 ml, 30 mM, Alfa Aesar, 99.9%) until the gold precursors were transferred into the organic phase forming the tetraoctylammonium-gold pairs. The nucleation of gold clusters in toluene was mediated by the reducing agent, sodium borohydride, dissolved in MilliQ water (20.8 ml, 0.4 M, Sigma Aldrich, 98%) with vigorous stirring. The excess of sodium borohydride was eliminated after one hour of further stirring by shaking with hydrochloric acid (20.8 ml, 0.01 M). Once the aqueous phase was removed, the organic one was washed

with sodium hydroxide (20.8 ml, 0.01 M), three times with sodium chloride (20.8 ml, 0.01 M), twice with MQW. Then, the organic phase was left until stirring for one day. The bromide ions were displaced by the addition of the solution of I-dodecanethiol (8.3 ml, Sigma Aldrich, 98%) and the mixture was then incubated at 65°C for two hours. After cooling the solution to room temperature, larger agglomerates were removed by centrifugation at 225 rcf for ten minutes. Methanol was added to the supernatant until the dispersion became cloudy and a precipitate was recovered by centrifuging for ten minutes at 725 rcf. The precipitate was dissolved in toluene and cold methanol was used again to precipitate NPs. After they were dissolved in 1.7 ml of toluene, a size-selective precipitation was carried out by adding 17 μl of cold methanol in order to improve sample polydispersity, followed by centrifugation (225 rcf, 15 minutes) to separate bigger particles and aggregates. The dodecanthiol-coated gold NPs were filtered with a 0.22 μm pores syringe filter.

2.2.4 Core-shell NPs coated by poly (maleic anhydride-alt-1-octadecene)

NPs in organic solvent were transferred into an aqueous solution to be suitable for biological applications. The transfer was achieved obtaining differently surface functionalized NPs. The most common mechanisms used for this procedure are the ligand exchange and the intercalation of amphiphilic polymers. While the choice of the right ligand to be exchanged depends on the nature of the inorganic core,[15] the second strategy is generally suitable to different NPs. The amphiphilic polymer intercalates with the bound stabilizer on the NP's surface through hydrophobic interactions and simultaneously exposes hydrophilic groups at the interface with the water molecules bringing the NPs in the solution.

For this reason, the intercalation method was chosen (Fig. 2.1) and poly (maleic anhydride-alt-1-octadecene) (PMAO, average M_n 30,000-50,000, Sigma Aldrich) was selected as intercalating agent on the base of previous studies where it showed to be a good coating agent.[16] PMAO is cheap and the octadecene chains can intercalate with the oleic and dodecane chains stabilizing the NP surface forming a stable coating,[17] the anhydride ring can be further cross-linked[18] and easily functionalized with any molecule terminated with an amine group through carbodiimide chemistry.[14]

In particular, 100 μl of core NPs in toluene (10^{15} NP/ml) were precipitated with ethanol and pelleted by centrifugation (765 rcf, 20 min). The precipitate was dried and re-solubilised in the minimum amount of chloroform. An excess of polymer (0.02 mmol monomer units) was dissolved stirring for 1 hour in chloroform (10ml). The solutions were mixed and the

chloroform slowly removed through evaporation under pressure control and gentle stream of nitrogen for 1 hour. An alkaline solution of water and tetramethyl ammonium hydroxide pentahydrate (TMAH, 0.13 mmol, Sigma Aldrich) or sodium hydroxide (0.1M, Sigma Aldrich) was used to solubilise the dried film sonicating for 15 min and leaving it to stir overnight. The solution was then filtered by 0.22μm pores syringe filters and concentrated by centrifugation with Amicon filter units with 50kDa cut-off (Millipore) at 405 rcf.[14]

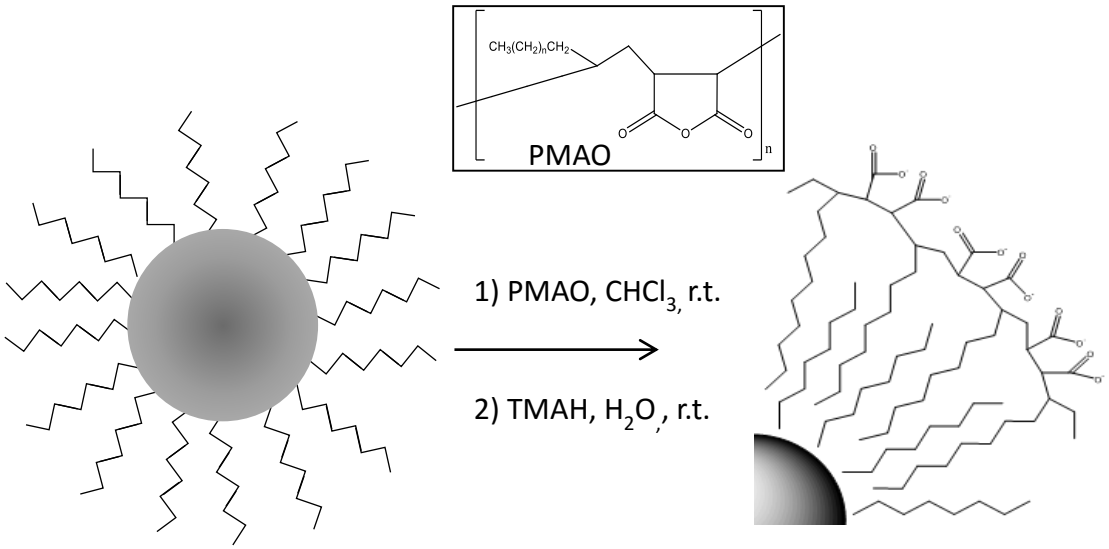

Figure 2.1 Schematic representation of the NP transfer in aqueous solutions. NPs in chloroform were mixed with an excess of PMAO in organic solvent (in the box the monomer structure) and slowly evaporated under controlled pressure. The dry film was dissolved in a basic aqueous solution.

2.2.5 PEG-functionalization

Biocompatibility of core-shell NPs through pegylation is nowadays a common practice: polyethylene glycol (PEG) coatings make NPs colloidal stable over a wide range of pH and salt concentrations, reduce unspecific binding of biological medium molecules, decreasing cytotoxicity and extending circulation time of NPs in the blood stream.[19-22]

Two strategies of pegylation were followed: partial pegylation of the NP surface was achieved using as ring-opening agent, Jeffamine M-1000 polyetheramine[15] that is a low molecular weight amino-PEG derivative. The terminal amino group acts as a nucleophile to open spontaneously the maleic anhydride rings on PMAO following the procedure described in paragraph *2.2.4* (0.25 mmol, Jeffamine M-1000 in MQW).

The second approach was a post-modification of the carboxylic groups exploiting N-(3-Dimethylaminopropyl)-N′-ethylcarbodiimide (EDAC, Sigma Aldrich) chemistry in the way

to get a higher degree of pegylation (almost 100% of the COOH groups based on Zp measurements). Normally, about 10^{12} NPs/ml were incubated overnight in PBS with 0.24 M EDAC and 6 mM Jeffamine. The excess of reagents was eliminated by 3-5 washings with centrifugal filters (Amicon 100kDa MWCO).

2.2.6 Fluorescent dye labelling

NPs were fluorescently labelled by functionalizing the polymer coating with a fluorescent dye. An amine-dye was used in low percentage to avoid macroscopic effects on the NPs coating density. The labelling was achieved with two strategies: in the first approach, the polymer was pre-labelled in organic solvent, while in the second the labelling was directly done on the NP surface in the aqueous solution.

Fluorescein-amine (FA, Sigma Aldrich) and BODIPY® FLEDA (Life Technologies) were used in the two methods, respectively. Both the approaches were performed to obtain theoretically a maximum of 2% of the total maleic anhydride rings labelled.

In the first strategy, a PMAO stock solution in Tetrahydrofuran (THF, 0.57 M in monomer units) was stirred for 30 min until complete dissolution. A stock solution of FA was prepared in THF and 10-fold diluted (1.15 mM). 50 µl of PMAO and 500 µl of FA were mixed and stirred overnight at room temperature. THF was evaporated under reduced pressure and the polymer film dissolved in chloroform ready to be incubated with the NPs.

In the second approach, core-shell NPs were first synthesized, coated by polymer and purified as described in the previous paragraphs and further fluorescently labelled. EDAC chemistry was used and in particular, a BODIPY dye was linked to the NP carboxylic groups forming amide bonds. Estimation of the dye amount needed was based on theoretical calculations to obtain 2% of the COOH groups labelled. The calculations were done considering the total volume of the polymer shell and the hydrodynamic volume occupied by a monomer unit carrying two carboxylic moieties. The shell volume was obtained considering the NP core diameter and assuming that the polymer coating increases the core diameter about 2 nm. These parameters were obtained by TEM images, while the volume occupied by a monomer unit was calculated by CHIMERA free software.

2.2.7 Drug loading

The hydrophobic nature of the shell surrounding the organic core of the NPs can be exploited to encapsulate small hydrophobic drugs, whose application in medicine is limited by their poor solubility in water, non-specific accumulation in the tumour site and toxicity for healthy tissues.[3,4,23] In this work, Leflunomide (Sigma) was choosen as small molecule to embed in the NP shell. It was shown to be an anti-rheumatic drug potentially good for melanoma treatment.[24] Two approaches were used to accomplish drug loading. In the first one, Leflunomide was prepared in chloroform (100 µl, 1.5 mg/ml) and added to the NPs (250 µl, 10^{15} NPs/ml) and the polymer in organic solvent. The mixture was left stirring for four hours and then the solvent evaporated as described in the previous paragraphs.

In the second route, the chloroform solution of drug (100 µl, 1.5 mg/ml) was added together at the water solution used to dissolve the dry film of NPs. After 15 minutes of sonication, the dispersion was left stirring overnight to evaporate the small amount of organic solvent. Purification was carried out dialysing against PBS for three days (membrane MWCO 100kDa) and performing size exclusion chromatography. In parallel, a control sample was prepared.

2.3 Characterization

Physical-chemical characterization of NPs is very important to understand and predict their behaviour *in vivo*. In fact, materials at the nanoscale act very differently from the corresponding bulk materials. NPs have intrinsically a huge chemical potential and environmental conditions can dramatically affect their physical and chemical state, and consequently bioavailability and uptake.[25] Generally, physical-chemical characterization implies the use of more than one technique to get a full picture of the nanosystem.[26]

2.3.1 Scattering techniques

Scattering techniques, being based on the interaction between incident radiations and particles, are very powerful to obtain quantitative information about size, shape and organization of colloids. In particular, in this study the nano-scale of the systems allowed performing a structural characterization by the use of visible light and neutrons.

2.3.1.1 Dynamic Light Scattering (DLS)

Dynamic Light Scattering (DLS), or Photon Correlation Spectroscopy, is one of the most used techniques to measure the size and the size distribution of particles in a suspension.[27,28]

According to the Rayleigh scattering theory, if particles are smaller than the incident light wavelength, they scatter the light in all directions due to their translational and rotational degrees of freedom. When a monochromatic and coherent light passes through a particle suspension, fluctuations of the scattering intensity are observed and they are time-dependent. In fact, particles are in Brownian motions and the distance between them changes continually. Constructive and destructive interferences occur, so scattering fluctuations over time carry information about the dynamics of the particles.[29]

In DLS, intensity fluctuations over time are recorded and correlated: it means that the scattered light at a time *t* is compared to itself at a time $t + \tau$, where τ is the correlation delay time. This procedure, repeated for a certain period, generates the autocorrelation function and its decay is related to the rate of diffusion of the particles in solution.

For a monodispersed system of perfectly spherical particles in Brownian motions, the field time-dependence autocorrelation function, g_2, decays exponentially with τ and can be represented as a single exponential equation:

$$g_2(\tau) = Ae^{-\frac{t}{\tau_c}} + B \quad (2.1)$$

where A is the amplitude, B the baseline and τ_c (s) is the relaxation time.

For particles in Brownian motions, the relaxation time depends on $\mathbf{q}^2$ according to:

$$\tau_c = \tfrac{1}{2} D\mathbf{q}^2 \quad (2.2)$$

With D the diffusion coefficient and **q** the modulus of the wave-vector transfer **Q**:

$$\mathbf{q} = \left| \mathbf{k_f} - \mathbf{k_i} \right| = \frac{4\pi n}{\lambda} sin(\frac{\theta}{2}) \quad (2.3)$$

Where θ is the angle between the incident and scattered wave-vectors $\mathbf{k_i}$ and $\mathbf{k_f}$, respectively, n is the refractive index of the medium and λ is the wavelength of the incident light. Assuming that the particles are spheres and do not interact with each other, it is possible to apply the Stokes-Einstein equation and hydrodynamic radius R_h is associated to the diffusion coefficient D:

$$D = k_B T / 6\pi\eta R_h \quad (2.4)$$

where η is the solvent viscosity, k_B is the Boltzmann constant (1.38×10^{-23} J/K), T the absolute temperature (K).

Often real colloidal systems are polydispersed and they can be represented by a distribution of particles that scatter in different ways and relax with different times. For a continue distribution, the first order correlation function can be expressed as follows:

$$g_1(\tau) = \int_0^\infty G(\Gamma)\exp(-\Gamma\tau)\,d\Gamma \tag{2.5}$$

Where Γ is the decay constant ($D\mathbf{q}^2$) for a size and G(Γ) is the relative intensity scattered by the population with decay constant Γ and will depend on the size and the volume fraction of the particles population.[30] Among the various mathematical approaches to analyse the autocorrelation function to extrapolate size information, two are particularly used. The Cumulant method is applied for monomodal samples. It assumes the expansion of the term *exp(–Γτ)* in eq. 2.5 considering a mean value for Γ:

$$\exp(-\Gamma\tau) = \exp(-\bar{\Gamma}\tau)\exp(-[\Gamma-\bar{\Gamma}]\tau) = \exp(-\bar{\Gamma}\tau)[1-(\Gamma-\bar{\Gamma})\tau + (\Gamma-\overline{\Gamma})^2\frac{\tau^2}{2!}+\cdots] \tag{2.6}$$

The contribution of terms with order higher than three are usually negligible. The second order eq. 2.6 can be substituted in 2.5 and assuming by definition the mean ($\bar{\Gamma}$) and the variance (μ_2) expressed as follow:

$$\bar{\Gamma} = \int_0^\infty G(\Gamma)\Gamma d\Gamma$$

$$\mu_2 = \int_0^\infty G(\Gamma)(\Gamma-\bar{\Gamma})^2 d\Gamma$$

Eq 2.7 is obtained:

$$g_1(\tau) = e^{-(\bar{\Gamma}t)}\left[1+\frac{\mu_2\tau^2}{2}\right] \tag{2.7}$$

If $\mu_2\tau^2 \ll 1$, eq. 2.7 becomes:

$$g_1(\tau) = e^{-\bar{\Gamma}t+\frac{\mu_2\tau^2}{2}} \tag{2.8}$$

In natural logarithm and adding a background factor (B), we get the final equation used in cumulant analysis:

$$ln[g1(\tau)] = ln\,B - \bar{\Gamma}\tau + \frac{\mu_2\tau^2}{2} \tag{2.9}$$

Fitting $ln[g1(\tau)]$ vs τ^2, the mean ($\bar{\Gamma}$) and the variance (μ_2) are obtained, and the ratio of the variance to the square of the mean defines the polydispersity index (PdI).

Another method to fit the autocorrelation function is through the CONTIN algorithm that uses the inverse Laplace transform, and is suitable to describe polydispersed systems. This fit is not always accurate, mostly when the autocorrelation function baseline is very noisy and the Laplace Transform inversion can lead to artefacts. Thus, a manual fitting can be done using either stretched mono-exponential decay functions or double exponential decay functions (eq. 2.10 and 2.11 respectively):

$$g_2(\tau) = Ae^{-\left(\frac{t}{\tau_c}\right)^{\beta}} + B \tag{2.10}$$

$$g_2(\tau) = A\left[C\, e^{-\frac{t}{\tau_{c1}}} + (1-C)\, e^{-\frac{t}{\tau_{c2}}}\right] + B \tag{2.11}$$

Where β is the stretching exponent, the coefficient A is the amplitude and B the baseline, C represents the weight of the population that relaxes earlier (the smaller); τ_{c1} and τ_{c2} are the relaxation times of the two populations in the sample. The stretching exponent takes into account the polydispersity of the system. When the stretched function does not fit well the autocorrelation function or the stretching coefficient is very different from one, the double exponential function fitting was applied instead and compared to the results obtained by CONTIN analysis.

In this study, the instrument used was a Malvern Zetasizer ZS Nano, with HeNe 5 mW laser (λ = 633 nm) and fixed collection angle (θ=173°). DLS was used throughout the thesis to monitor NPs size and eventual aggregation. Generally, three measurements were done on the same sample with an equilibration time of 120 seconds and each measurement was made up of 6 runs. Data were presented as averaged value with relative standard deviation.

2.3.1.2 Zeta-potential

The Z-potential (Zp) of a suspension is a key parameter for evaluating the stability of colloidal systems.[31] If the NPs have a net charge on their surface, this will affect the distribution of the ions in the solution at the interface, causing an increase in the counter-ion concentration close to the NPs surface. It means that an electrical double layer is formed around the NPs surface. This layer is formed by an inner region called “Stern layer”, where counter-ions are strongly bound to the surface and form a stable entity with the NP, then there is an outer part of diffuse

ions (counter ions and co-ions) that are weakly bound (Guoy-Chapman layer).[32] The potential at the interface between the Stern and the diffuse layer is the z-potential. NPs characterized by high negative or positive Zp are stable and have a lower attitude to agglomerate and flocculate.

When an electric field is applied, charged NPs tend to move toward the electrode with opposite charge and their velocity becomes constant when the equilibrium is reached. This velocity is called electrophoresis mobility and can be related to the Zp through the Henry equation:

$$U_E = 2\,\varepsilon\,Zp\,f(K_a)/\,3\,\eta \qquad (2.12)$$

where Zp is the zeta potential, U_E is the electrophoretic mobility, ε the dielectric constant, η the viscosity, and $f(K_a)$ is the Henry function that can be approximated to two values, 1.5 and 1.0, if Smoluchowski or Huckel approximations are used, respectively. In this work, electrophoretic mobility was measured by using Laser Doppler Velocimetry: this technique measures the velocity of small particles that move in a fluid under exposure to an electric field. The light scattered at an angle of 173° is combined to a reference beam and the originated fluctuating intensity signal is proportional to the NPs speed. Zeta potential measures are composed of two measurements, one in which the electric field is slowly reversed to avoid electrodes polarization and the other in which the field's turnaround is faster to allow particles to reach the terminal velocity.

Zp was measured to evaluate surface charge of NPs throughout the work and to monitor pegylation degree during pegylation optimization in Chapter 3. Measures were performed with the Malvern Zetasizer ZS Nano and the sample was injected in a "folded capillary cell", equipped with electrodes on both sides. Normally, three measurements of 10 runs each were made in 10 mM PBS at pH 7.4 and results were reported as averaged values with standard deviation.

2.3.1.3 Nanoparticle Tracking Analysis (NTA)

Nanoparticle Tracking Analysis (NTA) is based on the relationship between Brownian motions and particle size considering the movements of a single particle. In this technique, particles hit by a laser light thanks to their scattering can be live imaged *in situ* by a high-resolution camera. The movements of each particle are tracked in a certain number of frames by specific software. Particle trajectories and rates are related to the hydrodynamic radius of a sphere through the Stokes-Einstein equation.

NTA was used throughout the work as a complementary technique to DLS to determine NPs size. It was used to follow NPs separation by sucrose-gradient ultracentrifugation as alternative to DLS because dilution of a factor from 10 to 50 according to the initial concentration allowed to overcome limitation due to the sucrose refractive index (Chapter 4- 6). These measurements also provided the number of NPs in the sample.

Size and concentration of samples were obtained by Nanosight NS500 instrument. Samples were diluted with MQW to reach the ideal concentration of $1\text{-}3x10^{-8}$ particles/ml. With fluorescent particles, a fluorescent filter (λ=488 nm) was used. Three videos of sixty seconds were collected for each sample and analysed by NTA software. The mean size and standard deviation values obtained by the NTA software correspond to the arithmetic average calculated over the sizes of all the particles tracked by the software. Then, the data were averaged on three different measurements of the same sample.

2.3.1.4 Neutron Reflectometry (NR)

Neutrons are subatomic particles that, together with protons, constitute the nuclei of atoms. They are very useful to study biological samples because of the nature of their gentle interaction with the matter and to their intrinsic properties. In fact, they can penetrate deeply the bulk of the material under investigation in a non-destructive way. That is because neutrons are uncharged and they only interact with nuclei through strong short-range nuclear forces. Moreover, the incident neutron beam can scatter on a spin-based dipole-dipole interaction in case of magnetic nuclei having an unpaired orbital electron. Being neutrons interacting with the nuclei, the neutron scattering power (cross-section) does not depend on the atomic number of the elements (as for X-ray and electrons), but on the nuclei isotope composition and spin. It is possible to discriminate among isotopes, and elements close in the periodic table. Furthermore, since interaction with neutrons perturb the system very little, theoretical models work very well. Drawbacks in the use of neutrons are weakness of the scattering interaction, need of large volumes, long time of acquisition and access to the facilities.

Neutrons are mainly produced in two ways: either by nuclear fission in a reactor-based source or by spallation in an accelerator-based one. In the first case, thermal neutrons are absorbed by uranium-235 nuclei that, after collision, split in “daughter nuclei” generating a constant high-energy neutron flux. The energy of these neutrons needs to be thermalized and “hot neutrons” or “cold neutrons” can be made according to the moderator (in ILL self-heating graphite block at 2400K, and liquid deuterium at 25K respectively). In spallation sources,

neutrons are produced by collision of particles as H^+ generated from a high-power accelerator and a heavy metal target. In this way, pulses of high-energy protons and neutrons are generated with small heat dissipation and hence high neutron brightness compared to the reactor neutrons. Thermalization is achieved using hydrogenous moderator around the target and other sources to get the desired wavelength (in ISIS, water at 316K, liquid methane at 100K and liquid hydrogen 20K are used). The differences between the two sources is that the reactor is able to produce high time-averaged flux of neutrons compared to the pulsed source that instead can exploit the high brightness of the pulse through the time-of-flight technique to compensate.

Neutron reflectometry is a technique that exploits thermal neutrons and is useful to get structural information at molecular level about surfaces and thin films. Information such ast thickness, density, roughness at the interfaces in the normal direction to the reflecting surface can be inferred.[33-36]

2.3.1.4.1 Neutron reflectometry geometry

Figure 2.2a shows the geometry of a reflectometer: a beam of neutrons hits the surface with a grazing angle (θ_i). For elastic scattering the modulus of the reflected and incident wave vectors, $\mathbf{k_f}$ and $\mathbf{k_i}$, are the same and the angle of reflection, θ_f, is equal to the angle of incidence. In this case, the only component of the wave-vector transfer **Q** that can be considered is $\mathbf{k_z}$, the normal to the reflected plane and $\mathbf{Q_z}$ is the momentum transferred to the neutrons:

$$\mathbf{Q} = \mathbf{k_f} - \mathbf{k_i} \tag{2.13}$$

$$\left| \mathbf{k_f} \right| = \left| \mathbf{k_i} \right| = 2\pi / \lambda \tag{2.14}$$

$$\mathbf{Q_z} = 2\mathbf{k_z} = \frac{4\pi \sin\theta_i}{\lambda} \tag{2.15}$$

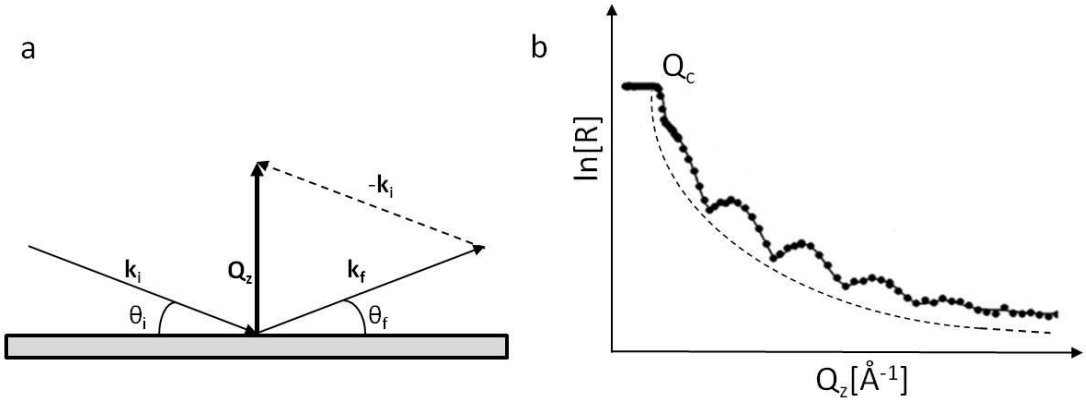

Figure 2.2 A) Geometry of a reflectometry experiment. Θ_i and θ_f are the incident and the reflected angles respectively and k_i and k_f the incident and reflected wave vectors. B) Typical profile for a surface in a reflectometry experiment: the solid line represented the best fit for the data collected.

In an experiment, either the beam wavelength or the angle of incidence can be varied keeping the other fixed. The resulting output will be the variation of the reflectivity profile, R, defined as the ratio of the reflected neutrons to the incident neutrons, in relation to $\mathbf{Q_z}$ as shown in Fig 2.3b.

The refractive index normal to the interface for any material can be defined as in equation 2.16:

$$n = 1 - A\lambda^2 + i\lambda C \tag{2.16}$$

Where $A = Nb / 2\pi$ and $C = N\sigma_{abs} / 4\pi$. N is the atomic number density in the medium (number of scattering nuclei in the volume unit), *b* is the atom coherent scattering length (scalar for the nuclear potential interaction between a nucleus and neutron that varies for elements and isotopes), σ_{abs} is the absorption cross-section that is often negligible for neutron reflection. The product N*b* is often presented as scattering length density, ρ (SLD), and for a material composed by M atoms or isotopes, it is:

$$\rho = \sum_{j=1}^{M} N_j \, b_j \tag{2.17}$$

For a single interface, at the critical angle, θ_c, for which total reflection happens, R(**Q**) is unity and $\mathbf{k_c}$, the component of the wave-vector normal to the surface at that particular angle, can be defined as follows and it results as a plateau in Fig. 2.3b for any $\theta \leq \theta_c$:

$$\boldsymbol{k_c} = 2\sqrt{\pi\rho} \tag{2.18}$$

$$\theta_c = \lambda\sqrt{\frac{\rho}{\pi}} \quad (2.19)$$

If $\theta > \theta_c$, R(**Q**) falls with $\mathbf{Q}^{-4}$ (dashed line in Fig. 2.2a). This is the so-called Frensel reflectivity. For more complex interfaces, e.g. when a film of a certain thickness is deposited on a substrate the R(**Q**) shows fringes whose frequency depends on the thickness of the film. The beam that hits the surface between two different substrates can be reflected and refracted. The refracted will be retarded by a phase compared to the reflected beam at the detector and this will originate interferences represented as maxima and minima points in the R(**Q**) curve. The distance between two minima can be related to the film thickness, *d*:

$$\Delta\mathbf{Q} = 2\pi / d \quad (2.20)$$

2.3.1.4.2 Neutron reflectometry profile for rough surfaces

The aim of a reflectometry experiment is to obtain a curve showing the SLD variation in the direction normal to the surface. That is achieved by comparing raw data with profiles generated by mathematical modelling.

As already mentioned above, during the experiments, the ratio between the incident and reflected neutron beams, R, as a function of the momentum transfer normal to the interface ($\mathbf{Q_z}$) is measured. In the Born approximation,[37] the reflectivity and the SLD perpendicular to the interface are linked by the following relationship:

$$R(\boldsymbol{Q_z}) \sim \frac{16\pi^2}{\boldsymbol{Q_z^2}} |\hat{\rho}(\boldsymbol{Q_z})|^2 \quad (2.21)$$

where $\hat{\rho}(\boldsymbol{Q_z})$ is the one-dimensional Fourier transform of $\rho(z)$ that carries information about the composition and structure of the each layer in which the original surface can be ideally divided. In the data analysis, commonly, each layer is characterized by an average SLD and thickness. These parameters, together with a roughness describing each layer, are used to plot a reflectivity profile model that is compared to the experimental data. The quality of the fit is evaluated by chi square (χ^2) and the parameters used in the model are adjusted by the least-squares method to minimize χ^2.

Complementary R($\mathbf{Q_z}$) profiles can be obtained for different components playing with the isotopes composition to tune the SLDs to highlight different parts of molecules or different constituent of the system of interest. It was already mentioned that coherent scattering lengths varies for isotopes. The difference between hydrogen and deuterium is significant (-

$0.3741x10^{-12}$ cm and $0.6671x10^{-12}$ cm, respectively) and it is particularly useful because it is exploited in the contrast matching technique. The ratio H_2O/D_2O can be adjusted to tune the SLD and match the SLD of parts of the sample making them "invisible" since their scattering would be indistinguishable from the buffer one. In Fig. 2.3, the graph shows how the SLDs of some macromolecules can be matched by a particular percentage of D_2O in the solvent.[38] This technique allows increasing the confidence in the models.

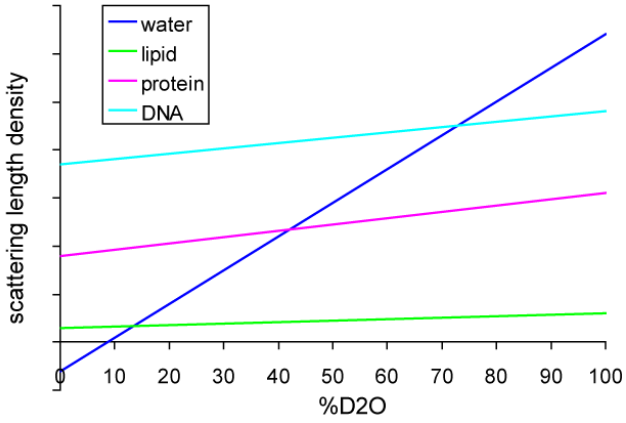

Figure 2.3 Scattering lengths densities of some macromolecules in relation to the mixture H_2O/D_2O composition. Intersection points give the percentage of D_2O in the solvent necessary to match contrast the SLDs of components of the system.

In this study, D17 reflectometer in ILL in Grenoble was used to study the structure of a SLB upon interaction with NPs in Chapter 5. D17 is a reflectometer with horizontal scattering geometry and a vertical surface operating in time-of-flight mode achieved by a double chopper using wavelengths in the range 2-20 Å. Two angles of incidence were used (θ = 0.8°-3°). A flow cell with a chamber of dimension 8x5x1 cm^3 was used and the surface was silicon oxide. It was cleaned by piranha solution (H_2SO_4: H_2O_2 3:1) for 20 minutes at 85°C and then it was washed extensively by MQW before assembling the cells and filling it with PBS buffer prepared with D_2O. Cells were kept at 37°C, aligned and the transmitted intensity measured (I_0). Silicon oxide surface was characterized in three contrast solutions: D_2O, H_2O and SMW (H_2O:D_2O 62:38) at the two angles of incidence. A lipid bilayer was formed injecting in the cell a 0.5 mg/ml 1,2-dioleoyl-sn-glycero-3-phosphocholine (DOPC) liposome dispersion. Briefly, to prepare the liposome dispersion the compound was weighted (20 mg) and suspended in 1 ml of chloroform; the solvent was quickly evaporated with a rotavapor and left to dry under vacuum overnight. The dry film was hydrated with 1 ml of PBS at pH 7.4 and agitated to form a homogeneous suspension. Five cycles of freeze and thaw were performed and then the solution was extruded twice through 200 nm and 100 nm pore diameter

membranes to obtain a monodispersed vesicle solution. The lipid bilayer was characterized in D_2O, 4MW (H_2O:D_2O 34:66), SMW (H_2O:D_2O 62:38), H_2O. The dispersion with NPs was injected and after 30 minutes of incubation, the lipid bilayer was characterized again in the four contrasts. The dispersion were at concentration respectively of 0.07 m^2/ml for PS-COOH20 in PBS, in 55% FBS and hard corona NPs; 0.055 m^2/ml for Fe_3O_4 and Fe_3O_4-PEG. Each experiment was conducted without replicates.

Motofit macro on Igor was used as software to fit the data collected[39]. It allows fitting simultaneously data sets describing the same system under different contrasts. The system under investigation is considered like a sum of layers. The first layer (L1) is the silicon oxide chip with SLD of 3.41 x 10^{-6} $Å^{-2}$ and thickness and roughness evaluated in a preliminary NR experiment in which the silicon block was characterized in H_2O and D_2O. In addition a bulk Si subphase (SLD of 2.07 x 10^{-6} $Å^{-2}$) and a bulk solvent superphase are present. The four matching solvent SLDs were 6.38 x 10^{-6} $Å^{-2}$, 4 x 10^{-6} $Å^{-2}$, 2.07x 10^{-6} $Å^{-2}$ and -0.56 x 10^{-6} $Å^{-2}$ respectively, for D_2O, 4MW, SMW and H_2O (although sometime values were adjusted due to inefficient solvent exchange). The lipid bilayer was modelled considering the lipid made of two discrete blocks: the head and the tail, each one characterized by a scattering length density, a thickness (t), a solvent penetration degree (φ) and a roughness (σ), which is treated as an error function. The resulting model consisted of five layers as represented in Fig. 2.4a. In this fitting model the layers parameters are fitted independently from each other. Another fitting model introduces constrains to describe lipids as shown in Fig. 2.4b. In this other model layers are described by a thickness (t_h and t_t for head and tail respectively), area per molecule (APM), head and tail volumes (V_h and V_t), roughness (σ_h and σ_t) and scattering lengths (b_h and b_t) that depend on the molecular composition of the groups. The SLDs for the head and tail layers is given by the ratio b/V. The volume fraction for the fragments are $V_{h,t}$ / A $t_{h,\,t}$. The volume occupied by water is 1-V/At. The SLD for the layer is then:

$$SLD_{h,t} = \frac{V_{h,t}}{A\,t_{h,t}} \times \frac{b_{h,t}}{A\,t_{h,t}} + \rho_{solv}\left(1 - \frac{V_{h,t}}{A\,t_{h,t}}\right) \tag{2.22}$$

The only parameters that vary during the fit are the area per molecule that is common to the two fragments of the lipid, the thickness and the roughness. The other values can be found in literature[40] and are tabulated in Table 2.2.

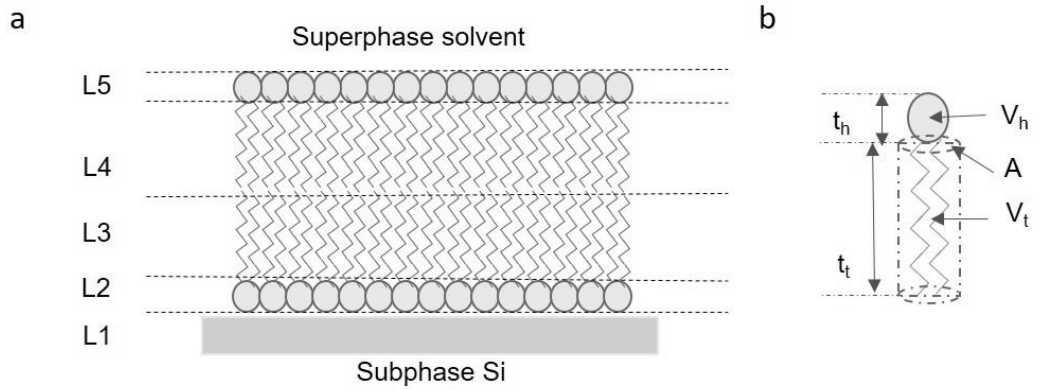

Figure 2.4 Supported lipid bilayer modelling. A) The SLB is modelled by 5 layers: L1 is the superficial SiO_2; L2 and L3 are the inner head and tail, respectively; L4 and L5 the outer tail and head respectively. A Si subphase and a solvent superphase are present in the model. B) Description of the lipid geometry: the head and the tail are defined by a thickness ($t_{h,t}$) and a volume ($V_{h,t}$), the area per molecule, A, is common to the two fragments.

Table 2.2 Parameters describing headgroup and tail fragments in DOPC lipid reported in Nagle et al.[40]

		DOPC
V_t [Å^3]	Tail volume	984
V_L [Å^3]	Lipid molecular volume	1303
APM [Å^2]	Area per molecule	72.5
D_c [Å]	Thickness of the hydrocarbon core	13.5
D_h [Å]	Headgroup thickness	9
b_h[1][Å]	Headgroup scattering length	$6x10^{-4}$
b_t[1] [Å]	Tail scattering length	$-2.1x10^{-4}$
SLD_h[2] [Å^{-2}]	Head scattering length density	$1.88x10^{-6}$
SLD_t[2] [Å^{-2}]	Tail scattering length density	$-0.21x10^{-6}$

[1] Calculated by http://sld-calculator.appspot.com/; [2] calculated by the ratio b/V.

2.3.2 Spectroscopic techniques

Spectroscopic techniques are based on light absorption and emission. Nanoparticles exhibit optical properties tuned by their geometry and composition. Material, shape, size and concentration are some of the parameters affecting optical behaviour of nanosystems.

2.3.2.1 UV-vis Spectroscopy (UV-vis)

UV-vis spectroscopy measures the interaction between matter and radiation in the range of ultraviolet and visible wavelengths of the electromagnetic spectrum (200-800nm). The energy associated to this region of the spectrum is comparable to the one involved in electronic transitions. Light in the UV or the visible spectra can be absorbed from molecules that contain π-electrons or non-bonding electrons. The light can excite those electrons to the higher non-bonding molecular orbitals. The wavelength absorbed depends on the entity of the energetic gap between the highest occupied molecular orbital (HOMO) and the lowest unoccupied molecular orbital (LUMO): the smaller the gap the lower is the energy needed for the transition, the longer is the wavelength that can be absorbed.[41]

In this work UV-vis spectroscopy was used to get information about the surface functionalization of NPs and measure the relative concentration exploiting the Lambert-Beer law (eq. 2.23), which links the absorbance (A) to the concentration (c) through the pathlength of the sample (l) and the molar absorptivity (ε):

$$A = c \times \varepsilon \times l \qquad (2.23)$$

In particular, in Chapter 3 and 4, UV-vis measures were exploit to follow NPs separation by size exclusion chromatography and sucrose-gradient ultracentrifugation; in Chapter 3, fluorescent and drug-loaded NPs adsorption profiles were presented in comparison to the starting NPs. The instrument used for UV-vis measurements was Hitachi U-3010 UV-vis spectrophotometer and quartz cuvettes with a path length of 10 mm were used. Spectra were corrected for solvent absorption automatically recording the baseline.

2.3.2.2 Fluorescence spectroscopy

After electrons jump to a higher energetic state absorbing light, they relax to the ground state either through small steps (non-radiative relaxation) or through fluorescence emitting photons. Emitted photons have smaller energy than the absorbed ones because of the non-radiative transitions, which bring electrons to the lower vibrational level of the excited state before to reach the ground state.

The instrument used to characterize fluorescent nanoparticles was Hitachi F-4500 with 150 watt Xe lamp. Fluorescence emission profiles were used in Chapter 3 to assess NPs labelling

efficiency by fluorescent dyes. Moreover, fluorescence emission was linked to NPs concentration and calibration curves were built to determine fluorescent NPs concentration.

2.3.2.3 Inductively coupled plasma- atomic emission spectroscopy (ICP-AES)

Inductively coupled plasma atomic emission spectroscopy (ICP-AES) is a spectroscopic technique and is used to determine sample composition. It is based on the emission of electromagnetic radiations from atoms and ions generated by inductively coupled plasma. Normally samples undergo an acid digestion to assure complete dissolution of the elements and destruction of the matrix. Afterwards the solution is dispersed into a gas phase where plasma electrons collide with ions that are further broken down and atoms excited. Atomic transitions are characteristic for a particular element and their intensity is related to the concentration of the specie through a calibration curve.[42,43] In this work, the instrument used was Varian Vista-PRO CCD Simultaneous ICP-AES Axial spectrometer with SPS5 Sample Preparation System. 100 µl of NP solutions were digested in *aqua regia* (HNO_3: HCl 1:3, 5ml) using a microwave reaction vessel for 40 min and then cooled at room temperature before the analysis. Au and iron atoms/ions concentrations were determined by ICP-AES for synthesized and purified batches of NPs and the obtained elements concentrations were linked to NPs concentration in solution by knowing density and size of the NPs as presented in Chapter 3. The batches concentrations obtained by ICP-AES data elaboration were used to build calibration curves by UV-vis and fluorescence measurements.

2.3.2.4 Attenuated total reflectance- Fourier transform infrared spectroscopy (ATR-FTIR)

Infrared spectroscopy is used to examine material at a molecular level. The absorption of light in the infrared region of the electromagnetic spectrum, from 4000 to 400 cm^{-1}, is associated to transition energies of rotational-vibrational modes of molecules. In order to be active in the IR the vibrational modes need to be coupled to a dipole change. Common vibrational modes that can occur in molecules are symmetric and asymmetric stretching, scissoring, rocking, wagging and twisting. Tables and references exist that summarize characteristic peaks wavelengths and intensities for common functional groups.

Fourier transform infrared spectroscopy (FTIR) is based on the use of an interferometer and allows the collection of interferograms that are converted in absorption spectrum through

Fourier transform approach. Attenuated total reflectance (ATR) is a coupled technique that makes easier the sample preparation. In fact, either solid or liquid samples are deposited on the ATR crystal and the IR light hits the crystal with a certain angle to reflect in it a certain number of times. The reflections generate evanescent waves that penetrate in the sample for 0.5 to maximum 2.5 micron. This techniques is particularly useful for nanoparticles because they can be just left to dry on the crystal surface without further preparation.

Nanomaterials can be characterized with this technique especially on the surface because any modification of functional groups leads to changes in the spectrum (as for example appearance or disappearance of bands).

In this work, ATR-FTIR spectra were used to monitor drug loading in NPs shell (Chapter 3). Spectrum BX spectrometer (Perkin Elmer, UK) fitted with a Golden Gate attenuated total reflectance (ATR) accessory (Specac Ltd, UK) was used. Spectrum software was used to process data. Samples were measured after placing a drop on the plate and left to dry at room temperature.

2.3.3 Microscopy

Microscopy is a straightforward method to obtain information about NPs size and shape. Optical microscopy is not very useful in nanotechnology due to diffraction effects that limit the resolution down to 1μm. Electromagnetic radiations, having shorter wavelengths, allow higher resolution and electron microscopy exploits that principle. In particularly, TEM uses transmitted electrons generated hitting the sample by an electron beam. Instead, conventional fluorescence microscopy exploits fluorescence to image objects (optical resolution) and becomes fundamental to image NPs in complex biological systems (i.e. cells).

2.3.3.1 Transmission electron microscopy (TEM)

Transmission electron microscopy (TEM) uses electron scattering to get a direct image of the sample down to the nanometer scale (0.1 nm). An electron beam is focused on a thin grid that contains a thin layer of the sample under high vacuum. From the interaction between the beam and the specimen, scattered (elastically and inelastically) and unscattered electrons originate.[44] Those are focused, magnified and projected on a detector on which a diffraction pattern is created. The image will be made up of darker and brighter regions according to the scattering of electrons. Weakly scattering materials (i.e. polymers) are transparent to TEM and additional treatments on the sample are necessary.

In this project, the microscope used was Joel 200EX with tungsten filament and acceleration voltage of 180kV to 200kV. Few drops of the sample solution, according the concentration, were deposited on thin copper carbon film grids and images were taken after solvent evaporation. Size distributions were obtained by analysing images of 100 to 500 NPs through ImageJ software; frequency and normal distribution of sizes were derived using Excel software. Polystyrene NPs were imaged by a Tecnai 20 TEM with AMT cameras, operating at an accelerating voltage of 200 kV (John Innes Centre). Particles were dried on carbon-coated 300 – mesh copper grids (Agar Scientific) and counterstained with 2 % uranyl acetate. Results are presented in Chapter 3.

2.3.3.2 Fluorescence microscopy

A fluorescence microscope exploits fluorescence from the samples to image them. It is an optical instrument in which the sample is illuminated with a light beam of a specific wavelength that is absorbed and photons are emitted to a longer wavelength. Filters and dichroic mirrors are used to select excitation and emission wavelengths of the beam depending on the fluorophore specifics.

In this work, fluorescence microscopy was used to evaluate fluorescent NPs absorption on QCMD chip surface (Chapter 5). The instrument Olympus BX60 microscope was used to reveal fluorescently labelled NPs. Blue filter block was chosen with an exciting filter wavelength of 470-490 nm and barrier filter wavelength of 515 nm. Images at several magnifications were captured.

2.3.3.3 Confocal microscopy

Marvin Minsky in the 1950s invented the confocal microscope that essentially differs from a normal fluorescence microscope for the presence of a screen with a pinhole. In Fig. 2.5 there is a scheme of how a confocal microscope works: there is a laser (blue line) directed to two dichroic mirrors that scan the light in the *xy* plane. The light passes through the objective and hits the sample. The fluoresced light (green line) goes back from the objective to the mirrors and passes through the pinhole hitting a detector. The screen with pinhole is able to screen the out of focus light reducing the background haze. At any instant, a thin section of the sample is imaged and the computer is able to reconstruct a 2D picture pixel by pixel and, combining several sections at different depths, a clear 3D image of the whole sample is obtained.

In this work, confocal microscopy was used to asses NPs uptake in cells and their location as reported in Chapters 4 and 6. Zeiss LSM510-META was used. It was equipped with a 63 x 1.30 NA oil immersion objective lens. The pinhole was set to one Airy. Cell's nucleus was excited using a 380 nm laser; NPs were excited with 488 nm laser and actin filaments with a 591 nm laser.

2.3.4 Separation techniques

As already mentioned, size and shape of NPs are some of the main determinants for their behaviour *in vivo* (i.e. toxicity)[46-48] and for this reason, it is important to obtain monodispersed homogenous NP samples. Many techniques may be applied to purify NP dispersions[46] and all of them have advantages and drawbacks. Thus, often it is necessary to apply a combination of them for obtaining a well-monodispersed NP distribution.

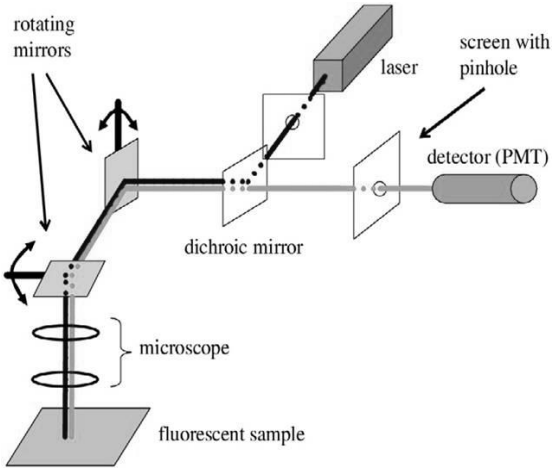

Figure 2.5 Schematic representation of a confocal microscope. The screen with the pinhole blocks the unfocused light. The rotating mirrors allow to scan the entire sample pixel by pixel.[45]

2.3.4.1 Size exclusion chromatography (SEC)

Size exclusion chromatography is one of the most used methodologies to separate NPs by size. It is based on the NP ability to move according to their hydrodynamic volume through a stationary phase constituted by pores of appropriate dimension. Smaller NPs will cross the pores and travel slower than bigger particles that can move through the accessible volume. NPs are collected and revealed by UV-vis or/and DLS.

In this work, SEC was used to remove aggregates and free polymer excess during the optimization of the purification protocol presented in Chapter 3: Sephacryl S-1000 SF was the stationary phase in a 98 cm long column of 2.5 cm diameter and Sephacryl S-500 HR in a 25

cm long column with the same diameter. The mobile phase was PBS buffer pH 7.4 that was previously filtered (0.22 μm) and degassed. Samples were loaded and the volume was 1% of the total column volume. An automated pump was used with a flux of 1.2 ml/min. Fractions were automatically collected (0.5 ml) and revealed by UV-detection at 320 nm and eventually scanned by DLS. Fractions with similar sizes were pooled together and concentrated by centrifugal concentrator (Amicon MWCO 50kDa, 405 rcf) prior to DLS analysis.

2.3.4.2 Density-gradient ultracentrifugation (UC)

Density gradient UC is a common technique exploited in biology and in colloidal science to separate objects according to their density and shape.

A particle in a centrifuge is subjected to three main forces: centrifugal (eq. 2.24), buoyant (eq. 2.25) and frictional (eq. 2.26):

$$F_c = \rho_{\mathrm{p}} V \omega^2 r \tag{2.24}$$

$$F_b = -\rho_{\mathrm{f}} V \omega^2 \tag{2.25}$$

$$F_f = -fv \tag{2.26}$$

With ρ_{p} and ρ_{f} the densities of particles and fluid, respectively, V the volume of a particle, ω the angular velocity, r the distance between the particle and the rotation axis, f the frictional coefficient usually dependent of shape and size of the particle and v the particle velocity. The particles will sediment at a constant velocity ($v = \frac{V(\rho_{\mathrm{p}} - \rho_{\mathrm{f}})\omega^2 r}{f}$) when forces are balanced ($F_{\mathrm{c}} + F_b = F_f$), so particles of different shape and size will move at different velocities. To improve the resolution of the separation, the medium can be constituted of layers of fluid at increasing density from the top to the bottom of the tube providing areas that apply fixed buoyant forces. Separation can be achieved through mainly two techniques: isopycnic and rate zonal centrifugation.

In the isopycnic one, separation is obtained only by matching the density of the NP with the buoyant density of a layer of the gradient, and a certain speed and time are necessary to allow the NPs to reach it. After that, further spinning does not cause any other change. The density of the NPs needs to be in between the lowest and highest densities of the chosen gradient.

In the zonal centrifugation, NP density is higher than the highest density of the gradient and time and speed of centrifugation are carefully chosen to allow separation of the objects within the gradient avoiding sedimentation of the sample that eventually occurs.

Centrifugation tubes of 13 ml were prepared carefully layering 1 ml solutions of sucrose in water from the most concentrated to the less one (10 solutions). These solutions were left to diffuse for an appropriate time to create a continuum gradient. 0.7 ml of sample was loaded on top of the so-formed gradient just before the centrifugation was started. In our experiments, the isopycnic technique was exploited and sucrose gradient range adjusted according to the NPs and medium (Table 2.3). One example of the procedure adopted to optimize the experimental conditions of NPs separation is reported in Chapter 8, paragraph 8.1. SW41 Ti rotor (Beckman Coulter) was used at 20°C. After the run, 1ml aliquots were collected and analysed by NTA to individuate NPs, diluting the sample in water up to 50 times in presence of sucrose. UC was part of the purification protocol as alternative to SEC to remove free polymer (Chapter 3) and it was used to obtain PC NPs isolation from several biological fluids in Chapters 4 and 6.

2.3.4.3 Electrophoresis: Agarose gel

Agarose gel electrophoresis is a separation technique used for DNA and proteins that are separated on the base of different size and charge. Recently, it has been used with NPs to determine hydrodynamic radius and surface charge density.[49] It has also been used to monitor pegylation status of the NPs after surface functionalization.[50]

In this work, we further characterized NP electrophoretic mobility relating it to NP size and surface charge. Moreover, it was useful to verify the absence of the free polymer after purification.[16] NPs were loaded in a 1.5% or 2% agarose gel in 0.5x TBE buffer and run at 100V for one hour. The gels were imaged by Molecular Imager ChemiDoc XRS System (BIORAD) and Image Lab software.

Table 2.3 Parameters used during ultracentrifugation through sucrose gradient for bare nanoparticles purified from the free polymer and for NPs *in situ* to isolate the hard corona.

	Sucrose density Δ [% w/w]	**Speed [RCF]**	**Time [min]**
Fe_3O_4/Au-PEG	6-66	187K	120
Fe_3O_4	2-66	187k	240
Au NPs	6-66	187k	120
PS-COOH100*	5-30	77k	60
PS-COOH20*	4-40	110k	120
PS-PEG*	3-30	60k	60
SiO_2*	3-30	12k	20
Fe_3O_4-PEG*	7-70	196k	120
Fe_3O_4*	7-70	196k	120

*NPs in FBS

2.3.4.4 Electrophoresis: SDS-PAGE

SDS-PAGE electrophoresis is one of the most important methodologies to analyse the PC composition of the NPs[51] and in this work was used to characterize PC made from serum and from complex digestive fluids.

Samples were added to SDS-PAGE loading buffer (10% Dithiothreitol, DTT), kept at 98°C for 5 min and 20 µl of samples were loaded in the wells of 12% or 10% Precast Gel NuPAGE (Life Technology). 5 µl of molecular ladder (Pageruler Broad Range, Biolabs, or Mark12 Unstained, Invitrogen) were loaded without any previous treatment. The running buffer used was MES buffer (NuPAGE 20x, Invitrogen) and the gels were run at 130V for 35 minutes. Gels were developed either by silver stain kit (Pierce) or Sypro Ruby Protein Stain (BIORAD) and imaged respectively by Molecular Imager ChemiDoc XRS System (BIORAD) and Biorad Pharos FX+ and Image Lab software.

2.3.4.5 Liquid chromatography- mass spectrometry (LC-MS)

Liquid chromatography-mass spectrometry (LC-MS) is an analytical technique used to detect and identify chemicals in complex mixtures. It combines the ability of liquid chromatography to separate molecules and the mass analysis of mass spectrometry. In this work, the bottom-up proteomic LC-MS approach was used to identify peptides from food digestion (Chapter 6).

According to the approach, proteins are first separated by electrophoresis, and then proteins from some selected bands are extracted from the gel, digested with an enzyme (e.g. trypsin) and the masses obtained for the peptides from LC-MS analysis are compared to those from peptides database. The identification of several peptides that belong to a single protein, leads to the identification of the protein itself.

The detailed procedure followed in this work was optimized in the Institute of Food Research. ProPick instrument was used to locate and cut bands from the gel. Bands were digested at 37°C for three hours by 10 mM Ammonium Bicarbonate 10 ng/µl Trypsin Gold (Promega, V528A in 50mM Acetic Acid) (prepared 01-May-14). 1% formic acid (Sigma) was added prior freezing samples and storing at -80°C. Samples were washed in 50% acetonitrile (Fisher), vortexed and dried out at the Low Drying setting (no heat) on a Speed Vac SC110 (Savant) fitted with a Refrigerated Condensation Trap and a Vac V-500 (Buchi). Samples were again stored at -80°C until ready for Orbitrap analysis. Protein identification was achieved by combining spectrum quality scoring obtained from a conventional database search program MASCOT (Matrix Science, London, England). Search parameters were: peptide mass and fragment mass tolerances of 5 ppm and 0.5 Da, respectively, a variable modification was oxidation (M), fixed modification carbamidomethyl (C), enzyme specificity was trypsin, two missed cleavage was allowed. All taxonomy database was searched.

2.3.5 Quartz Crystal Microbalance with Dissipation Monitoring (QCM-D)

The characterization of the interaction between NPs and cell membrane is important because the cell membrane is one of the first barriers encountered by the NPs *in vivo*. The nature and the extent of this interaction strongly depend on the NPs properties (size, charge, shape). There are different techniques to study the behaviour of NPs interacting with lipid membranes that simulate the cell surfaces.[52-62] One of these is the QCM-D that has been largely used for characterizing lipid bilayer structures mimicking cell membrane behaviour.[63-69] Moreover, it can give information about the surface adsorption and desorption of materials in real time. In fact, the change of resonance frequency of the crystal is associated to mass adsorption or desorption on the chip surface. The monitoring of the phase shift at different and higher harmonics allows, through mathematical model, to evaluate thickness and viscoelasticity of the attached layer.

When a radio frequency voltage is applied to the quartz crystal through the electrodes to a frequency close to its resonant one, it starts to oscillate at its fundamental resonance frequency

(f_0). A small change in mass (Δm) on its surface causes a proportional decrease in the oscillation frequency (Δf) (Fig. 2.6).

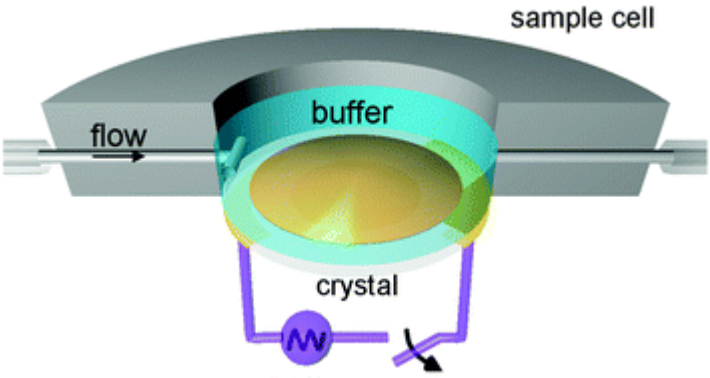

Figure 2.6 Scheme of a QCM-D cell.[70] The quartz crystal is placed between two gold electrodes. One electrode surface is exposed to solutions in flow. When AC is applied, the crystal oscillates and an adsorbed mass changes the frequency of oscillation. An exponential decay of frequency will result from the circuit opening.

If the deposited film is rigid and much thinner than the crystal, Δm, Δf and the overtone number (n=1, 3, 5...) are related from the Sauerbrey equation:

$$\Delta m = - (\rho_q \, l_q / f_0) (\Delta f / n) \qquad (2.27)$$

Δm is the hydrated mass (ng/cm^2), ρ_q (kg/m^3) and l_q (m) are respectively density and thickness of the crystal summarized in a constant of value 17.7 ng cm^{-2} Hz^{-1} at the fundamental frequency of 5 MHz.

If the film is not rigid, there is a deviation from the Sauerbrey equation and the adsorbed mass is underestimated due to the viscoelasticity of the system that oscillates with a phase shifted with respect to the crystal. The dissipation factor (D) is:

$$D = \frac{E_d}{2\pi E_s} = \frac{1}{\pi f t} \qquad (2.28)$$

Where E_d is the energy loss and E_s is the total energy stored in the system during one oscillation. ΔD is measured from the frequency exponential decay when the circuit is open. This decay is inversely proportional to t, the decay time constant. The energy dissipation change will be bigger for viscous film with respect to rigid ones because the ratio between the energy stored and the energy loss will be larger. If the film is represented in a continuum mechanics model by an elastic component in parallel with a viscous component (i.e. by a Voigt element), assuming no-slip conditions and homogenous thickness and density for each layer. A thickness (d_{eff}), density (ρ_{eff}), and complex shear modulus ($\mu+i\omega\eta$), where μ is the shear

elasticity, η is the shear viscosity, and ω = 2πf is the oscillation frequency, describe the viscoelastic model. By using multiple frequency measurements, the Voigt mass can be estimated as follows:

$$\Delta m = \rho_{eff} \times d_{eff} \quad (2.29)$$

In this work, the interaction between NPs and supported lipid bilayers (SLB) of different composition was studied as a function of NP concentration, surface functionalization and charge both in PBS buffer and in presence of serum.

Different compositions of the lipid bilayer were used: a) 100% 1,2-dioleoyl-*sn*-glycero-3-phosphocholine (DOPC); b) 75% 1,2-dioleoyl-*sn*-glycero-3-phosphocholine + 25% sphingomyelin (SM) (final concentration of lipids, 20 mg/ml).[71] The vesicle solution was prepared as described in paragraph *2.3.1.4.2*.

In the literature,[66] the process leading to the formation of the bilayer is described as a two-phase process: subsequently to the deposition of the vesicles on the sensor surface, a collapse into a bilayer occurs when a critical point is reached. The collapse can depend on the physical nature of vesicles (dimension, deformability and charge), their concentration, the solution ionic strength and temperature (Fig. 2.7). In all the experiments, conducted in triplicate, the solutions were kept at 37°C to avoid thermal shock upon contact with the sensor that is extremely sensitive.

2.4 Studies with cell lines

2.4.1 Caco-2

Caco-2 cell line is derived from colon carcinoma. In culture, cells become differentiated and polarized and mimic the enterocytes found in the small intestine. Usually they are used as *in vitro* model of the human small intestinal mucosa. These cells can be grown on membranes as cell monolayers forming tight junctions and are exploited to study the uptake and transport of ions and small molecules across this physical-chemical barrier. In this study, Transwell® Permeable Supports (Costar, Corning) were the devices used to grow cells in monolayer and study the transport of NPs across the membrane (Fig. 2.8). The polyester membrane had pores of 0.4 μm and the volumes used in the apical and basolateral chambers were 0.2 ml and 0.7 ml, respectively.

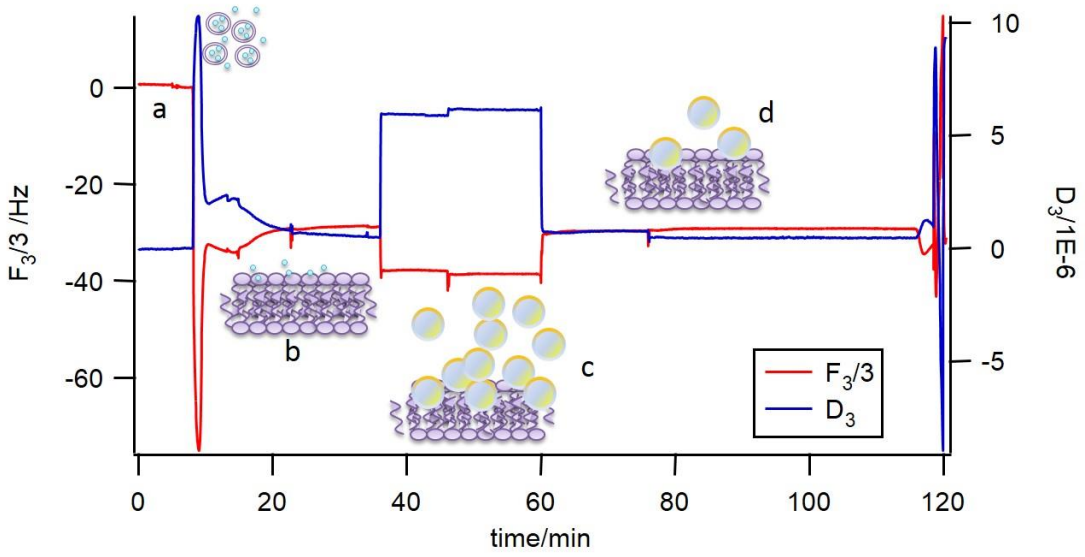

Figure 2.7 Example of QCM-D experiment output data. Frequency (red line) and Dissipation (blue line) at the third overtone were monitored over time because of the better signal/noise ratio. Before each stage, equilibrium of the system was reached. A vesicles solution in PBS buffer was injected (a). When the bilayer formed, solvation water was expelled from the vesicles core and it caused another significant change in both signals (b). After washings to get rid of the vesicles in excess, NPs solution was sent through (c) and other washings were performed (d).

Cells at the 12th passage were seeded at a concentration of 1.2x10^5 cells/ml per well. Cells were incubated in 37°C, 5% CO_2 / 95% air. Cells were cultured in RPMI-1640 supplemented with 10% heat-inactivated FBS used also for PC studies, 2 mM L-glutamine, 100 µg/ml penicillin and 100 µg/ml streptomycin all purchased Life Technologies (Carlsbad, CA). Medium was changed every two days and Trans Epithelial Electric Resistance (TEER) was measured just before changing the media to assess the integrity of the cell barrier. When the TEER values were above 300 Ω cm^{-1}, transport experiment was performed. The apical and basolateral chambers were filled with serum and phenol free media after PBS washings (x3) to remove phenol red and FBS proteins from the chambers and cells were allowed to equilibrate for one hour in the incubator prior NPs injection. Labelled magnetite NPs with and without PC were used (Chapter 6). 100 µl of basolateral medium were sampled at 30, 60, 120, 180 and 240 minutes and replaced with the same volume of fresh medium. TEER after 4 hours was measured again to assess the effect of the NPs on the cellular barrier integrity. NPs presence in the medium collected from the basolateral chamber was revealed by fluorescence using a plate reader exciting at 492 nm and collecting emission at 520 nm for all samples. Cells were washed by PBS three times and fixed by 5% formaldehyde for 10 minutes, then they were permeabilized by Triton-x 0.5% for 3 minutes and again washed for three times with PBS. F-Actin and nucleus staining were performed treating the cells with Texas-Red

Phalloidin (6.6µM, Invitrogen) and Hoechst 33258 (2 µg/ml, Sigma), respectively, for 30 minutes. After staining, the membranes were cut from the insert, placed on a glass slide and covered by a coverslip with mounting medium in between (Vectashield, Vector) and left overnight to dry before sealing by nail varnish. Zeiss LSM510-META confocal microscope was used to image cell monolayers and NPs using a multi-channel mode with three different excitation wavelengths for nuclei, actin and NPs.

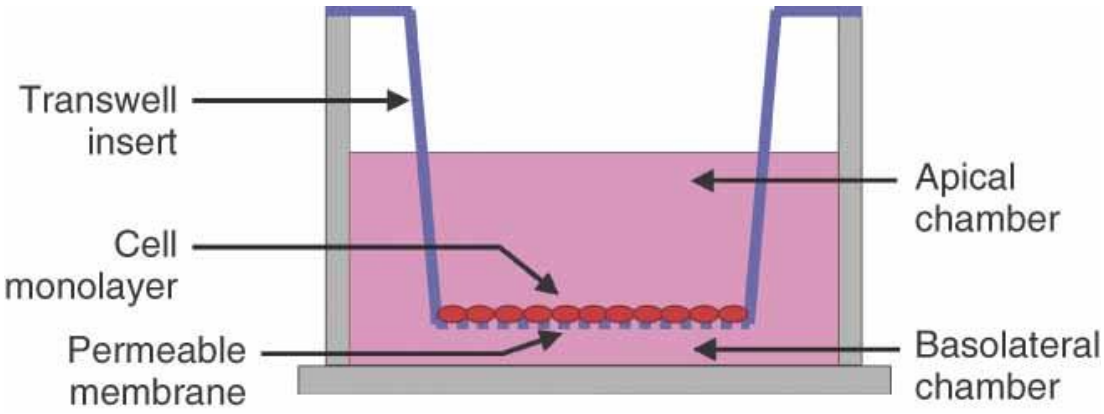

Figure 2.8 Diagram illustrating a Transwell Permeable Support device. Cells are grown in monolayer on a permeable membrane and two chambers, the apical and the basolateral are separated by the membrane and have independent access.

2.4.2 M2O2

M2O2 cells are adherent melanoma cells commonly used in our laboratory. Cells were incubated at 37°C, 5% CO_2 / 95% air and were cultured in RPMI-1640 (Life Technologies, Carlsbad, CA) supplemented with 10% heat-inactivated foetal bovine serum (FBS), 2 mM L-glutamine, 100 µg/ml penicillin and 100 µg/ml streptomycin all purchased Life Technologies, Carlsbad, CA. At P12 cells were trypsinized by 1ml trypsin 0.05%/ EDTA 0.5 mM for two minutes at 37°C, neutralized by 5ml of medium and centrifuged at 5 min at 1200xg. The supernatant was discharged and the pellet re-suspended in 1 ml of medium. Cells were seeded at a density of $4x10^4$ cells/ml on glass coverslips (18 mm) and left to adhere overnight. They were washed (PBS x3) and incubated with fluorescently labelled magnetite NPs without and with PC (Chapter 4). After incubation, the same procedure described above in paragraph *2.4.1* was used to wash, fix and stain cells. At the end, the coverslips were placed upside-down on microscope glass slides with 7 µl of mounting medium in between. They were left to dry overnight and sealed by nail varnish.

2.5 Bibliography

(1) Xie, J.; Lee, S.; Chen, X. *Advanced drug delivery reviews* **2010**, *62*, 1064.

(2) Gong, Y.; Dai, J.; Li, H.; Wang, X.; Xiong, H.; Zhang, Q.; Li, P.; Yi, C.; Xu, Z.; Xu, H.; Chu, P. K. *Journal of Biomaterials Applications* **2015**, *30*, 201.

(3) He, W.; Lv, Y.; Zhao, Y.; Xu, C.; Jin, Z.; Qin, C.; Yin, L. *International Journal of Pharmaceutics* **2015**, *484*, 163.

(4) Huang, W.-T.; Larsson, M.; Wang, Y.-R.; Chiou, S.-H.; Lin, H.-Y.; Liu, D.-M. *Molecular Pharmaceutics* **2015**, 12, 1242.

(5) Ming, W.; Da, Z.; Yongyi, Z.; Lingjie, W.; Xiaolong, L.; Jingfeng, L. *Nanotechnology* **2015**, *26*, 115102.

(6) Chatterjee, K.; Sarkar, S.; Jagajjanani Rao, K.; Paria, S. *Advances in Colloid and Interface Science* **2014**, *209*, 8.

(7) Loos, C.; Syrovets, T.; Musyanovych, A.; Mailänder, V.; Landfester, K.; Nienhaus, G. U.; Simmet, T. *Beilstein Journal of Nanotechnology* **2014**, *5*, 2403.

(8) Shirshahi, V.; Soltani, M. *Contrast Media & Molecular Imaging* **2015**, *10*, 1.

(9) Răcuciu, M. *Current Applied Physics* **2009**, *9*, 1062.

(10) Mürbe, J.; Rechtenbach, A.; Töpfer, J. *Materials Chemistry and Physics* **2008**, *110*, 426.

(11) Sun, S.; Zeng, H.; Robinson, D. B.; Raoux, S.; Rice, P. M.; Wang, S. X.; Li, G. *Journal of the American Chemical Society* **2003**, *126*, 273.

(12) Dreaden, E. C.; Alkilany, A. M.; Huang, X.; Murphy, C. J.; El-Sayed, M. A. *Chemical Society Reviews* **2012**, *41*, 2740.

(13) Brust, M.; Walker, M.; Bethell, D.; Schiffrin, D. J.; Whyman, R. *Journal of the Chemical Society, Chemical Communications* **1994**, 801.

(14) Lin, C.-A. J.; Sperling, R. A.; Li, J. K.; Yang, T.-Y.; Li, P.-Y.; Zanella, M.; Chang, W. H.; Parak, W. J. *Small* **2008**, *4*, 334.

(15) Lees, E. E.; Nguyen, T.-L.; Clayton, A. H. A.; Mulvaney, P. *ACS Nano* **2009**, *3*, 1121.

(16) Di Corato, R.; Quarta, A.; Piacenza, P.; Ragusa, A.; Figuerola, A.; Buonsanti, R.; Cingolani, R.; Manna, L.; Pellegrino, T. *Journal of Materials Chemistry* **2008**, *18*, 1991.

(17) Shtykova, E. V.; Huang, X.; Gao, X.; Dyke, J. C.; Schmucker, A. L.; Dragnea, B.; Remmes, N.; Baxter, D. V.; Stein, B.; Konarev, P. V.; Svergun, D. I.; Bronstein, L. M. *The Journal of Physical Chemistry C* **2008**, *112*, 16809.

(18) Pellegrino, T.; Manna, L.; Kudera, S.; Liedl, T.; Koktysh, D.; Rogach, A. L.; Keller, S.; Rädler, J.; Natile, G.; Parak, W. J. *Nano Letters* **2004**, *4*, 703.

(19) Godinho, B. M. D. C.; Ogier, J. R.; Quinlan, A.; Darcy, R.; Griffin, B. T.; Cryan, J. F.; O'Driscoll, C. M. *International Journal of Pharmaceutics* **2014**, *473*, 105.

(20) Hak, S.; Helgesen, E.; Hektoen, H. H.; Huuse, E. M.; Jarzyna, P. A.; Mulder, W. J. M.; Haraldseth, O.; Davies, C. d. L. *ACS Nano* **2012**, *6*, 5648.

(21) Essa, S.; Rabanel, J. M.; Hildgen, P. *International Journal of Pharmaceutics* **2011**, *411*, 178.

(22) Hu, Y.; Xie, J.; Tong, Y. W.; Wang, C.-H. *Journal of Controlled Release* **2007**, *118*, 7.

(23) Shen, Y.; Jin, E.; Zhang, B.; Murphy, C. J.; Sui, M.; Zhao, J.; Wang, J.; Tang, J.; Fan, M.; Van Kirk, E.; Murdoch, W. J. *Journal of the American Chemical Society* **2010**, *132*, 4259.

(24) White, R. M.; Cech, J.; Ratanasirintrawoot, S.; Lin, C. Y.; Rahl, P. B.; Burke, C. J.; Langdon, E.; Tomlinson, M. L.; Mosher, J.; Kaufman, C.; Chen, F.; Long, H. K.; Kramer, M.; Datta, S.; Neuberg, D.; Granter, S.; Young, R. A.; Morrison, S.; Wheeler, G. N.; Zon, L. I. *Nature* **2011**, *471*, 518.

(25) Cheng, L.-C.; Jiang, X.; Wang, J.; Chen, C.; Liu, R.-S. *Nanoscale* **2013**, *5*, 3547.

(26) Lin, P.-C.; Lin, S.; Wang, P. C.; Sridhar, R. *Biotechnology Advances* **2014**, *32*, 711.

(27) Lim, J.; Yeap, S. P.; Che, H. X.; Low, S. C. *Nanoscale Research Letters* **2013**, *8*, 381.

(28) Hackley, V. A.; Clogston, J. D. *Methods in Molecular Biology* **2011**, *697*, 35.

(29) Berne B. J.; Pecora R. *Dynamic Light Scattering: With Applications to Chemistry, Biology, and Physics* **1976**, 376.

(30) Hassan, P. A.; Rana, S.; Verma, G. *Langmuir* **2015**, *31*, 3.

(31) Felix, C.; Yaroshchuk, A.; Pasupathi, S.; Pollet, B. G.; Bondarenko, M. P.; Kovalchuk, V. I.; Zholkovskiy, E. K. *Advances in Colloid and Interface Science* **2014**, *211*, 77.

(32) Lyklema, J. *Fundamentals of Interface and Colloid Science* **1995**, *2*, 1.

(33) Heinrich, F.; Lösche, M. *Biochimica et Biophysica Acta (BBA) - Biomembranes* **2014**, *1838*, 2341.

(34) Torikai, N.; Yamada, N. L.; Noro, A.; Harada, M.; Kawaguchi, D.; Takano, A.; Matsushita, Y. *Polym. J* **2007**, *39*, 1238.

(35) Majewski, J.; Kuhl, T. L.; Wong, J. Y.; Smith, G. S. *Reviews in Molecular Biotechnology* **2000**, *74*, 207.

(36) Penfold, J.; Richardson, R. M.; Zarbakhsh, A.; Webster, J. R. P.; Bucknall, D. G.; Rennie, A. R.; Jones, R. A. L.; Cosgrove, T.; Thomas, R. K.; Higgins, J. S.; Fletcher, P. D. I.; Dickinson, E.; Roser, S. J.; McLure, I. A.; Hillman, A. R.; Richards, R. W.; Staples, E. J.; Burgess, A. N.; Simister, E. A.; White, J. W. *Journal of the Chemical Society, Faraday Transactions* **1997**, *93*, 3899.

(37) Wolf, E.; Born, M. *Principles of Optics* 7th ed.; Cambridge University Press, **1999**.

(38) Jacrot, B. *Reports on Progress in Physics* **1976**, *39*, 911.

(39) Nelson, A. *Journal of Applied Crystallography* **2006**, *39*, 273.

(40) Nagle, J. F.; Tristram-Nagle, S. *Biochimica et Biophysica Acta (BBA) - Reviews on Biomembranes* **2000**, *1469*, 159.

(41) Skoog D. A.; Holler, F. J.; Crouch S. R. *Principles of Instrumental Analysis*; 6th ed.; Thomson Brooks/Cole, **2007**.

(42) Mermet, J. M. *Journal of Analytical Atomic Spectrometry* **2005**, *20*, 11.

(43) Stefánsson, A.; Gunnarsson, I.; Giroud, N. *Analytica Chimica Acta* **2007**, *582*, 69.

(44) Williams D. B.; Carter, C. B. *Transmission Electron Microscopy: A Textbook for Materials Science*; Springer US, **2009**.

(45) Prasad, V.; Semwogerere, D.; Eric, R. W. *Journal of Physics: Condensed Matter* **2007**, *19*, 113102.

(46) Kowalczyk, B.; Lagzi, I.; Grzybowski, B. A. *Current Opinion in Colloid & Interface Science* **2011**, *16*, 135.

(47) Ivask, A.; Kurvet, I.; Kasemets, K.; Blinova, I.; Aruoja, V.; Suppi, S.; Vija, H.; Käkinen, A.; Titma, T.; Heinlaan, M.; Visnapuu, M.; Koller, D.; Kisand, V.; Kahru, A. *PLoS ONE* **2014**, *9*, e102108.

(48) De Jong, W. H.; Hagens, W. I.; Krystek, P.; Burger, M. C.; Sips, A. J. A. M.; Geertsma, R. E. *Biomaterials* **2008**, *29*, 1912.

(49) Hasenoehrl, C.; Alexander, C. M.; Azzarelli, N. N.; Dabrowiak, J. C. *ELECTROPHORESIS* **2012**, *33*, 1251.

(50) Sperling, R. A.; Pellegrino, T.; Li, J. K.; Chang, W. H.; Parak, W. J. *Advanced Functional Materials* **2006**, *16*, 943.

(51) Sherwood, V.; Di Silvio, D.; Baldelli Bombelli, F.; *Topics in Medicinal Chemistry* **2014**, 1.

(52) Torrano, A. A.; Pereira, Â. S.; Oliveira Jr, O. N.; Barros-Timmons, A. *Colloids and Surfaces B: Biointerfaces* **2013**, *108*, 120.

(53) Heikkilä, E.; Martinez-Seara, H.; Gurtovenko, A. A.; Vattulainen, I.; Akola, J. *Biochimica et Biophysica Acta (BBA) - Biomembranes* **2014**, *1838*, 2852.

(54) Christensen, M.; Rasmussen, J. T.; Simonsen, A. C. *Food Hydrocolloids* **2015**, *45*, 168.

(55) Klapetek, P.; Valtr, M.; Necas, D.; Salyk, O.; Dzik, P. *Nanoscale Research Letters* **2011**, *6*, 514.

(56) Block, S.; Glöckl, G.; Weitschies, W.; Helm, C. A. *Nano Letters* **2011**, *11*, 3587.

(57) Garnier, B.; Bouter, A.; Gounou, C.; Petry, K. G.; Brisson, A. R. *Bioconjugate Chemistry* **2009**, *20*, 2114.

(58) Wolny, P. M.; Banerji, S.; Gounou, C.; Brisson, A. R.; Day, A. J.; Jackson, D. G.; Richter, R. P. *The Journal of Biological Chemistry* **2010**, *285*, 30170.

(59) Baumann, M. K.; Swann, M. J.; Textor, M.; Reimhult, E. *Analytical Chemistry* **2011**, *83*, 6267.

(60) Buzhynskyy, N.; Golczak, M.; Lai-Kee-Him, J.; Lambert, O.; Tessier, B.; Gounou, C.; Bérat, R.; Simon, A.; Granier, T.; Chevalier, J.-M.; Mazères, S.; Bandorowicz-Pikula, J.; Pikula, S.; Brisson, A. R. *Journal of Structural Biology* **2009**, *168*, 107.

(61) Pera, H.; Nolte, T. M.; Leermakers, F. A. M.; Kleijn, J. M. *Langmuir* **2014**, *30*, 14581.

(62) Tatur, S.; Maccarini, M.; Barker, R.; Nelson, A.; Fragneto, G. *Langmuir* **2013**, *29*, 6606.

(63) Keller, C. A.; Kasemo, B. *Biophysical Journal* **1998**, *75*, 1397.

(64) Xu, D.; Hodges, C.; Ding, Y.; Biggs, S.; Brooker, A.; York, D. *Langmuir* **2010**, *26*, 18105.

(65) Kannisto, K.; Murtomäki, L.; Viitala, T. *Colloids and Surfaces B: Biointerfaces* **2011**, *86*, 298.

(66) Richter, R. P.; Brisson, A. R. *Biophysical Journal* **2005**, *88*, 3422.

(67) Grießinger, J.; Dünnhaupt, S.; Cattoz, B.; Griffiths, P.; Oh, S.; Gómez, S. B. i.; Wilcox, M.; Pearson, J.; Gumbleton, M.; Abdulkarim, M.; Pereira de Sousa, I.; Bernkop-Schnürch, A. *European Journal of Pharmaceutics and Biopharmaceutics* **2015**, *In Press*.

(68) Puhr, J. T.; Swerdlow, B. E.; Reid, D. K.; Lutkenhaus, J. L. *Soft Matter* **2014**, *10*, 8107.

(69) Alejo, T.; Merchán, M. D.; Velázquez, M. M. *Langmuir* **2014**, *30*, 9977.

(70) Benkoski, J. J.; Jesorka, A.; Edvardsson, M.; Hook, F. *Soft Matter* **2006**, *2*, 710.

(71) Cooper, G.M. *The Cell: A Molecular Approach. Structure of the plasma membrane*.; 2nd ed.; Sinauer Associates: Sunderland (MA), **2000**.

Chapter 3. Synthesis and characterization of core-shell NPs

3.1 Short outline of the chapter

In this chapter, synthesis and physical-chemical characterization of the NPs are described. As it was widely discussed in Chapter 1, shape, charge, surface properties, average size and size distribution are important determinants for NPs *in vivo* behaviour. A deep knowledge of those properties is important to predict the interaction of NPs with cellular membranes when dispersed in complex biological environments. This knowledge will allow researchers to design more effective nanoplatforms.

In this work, core-shell NPs were obtained by synthesizing organic cores according to well-established protocols. These NPs were stabilized in organic solvent functionalizing their surface with alkyl ligands. The hydrophobic NPs were then transferred into water dispersions coating their surface with an amphiphilic polymer. Their morphology, size and size distribution were monitored before and after polymer coating by transmission electron microscopy (TEM), dynamic light scattering (DLS), Nanoparticles Tracking Analysis (NTA) and inductively coupled plasma-atomic emission spectroscopy (ICP-AES). The coated NPs were also modified by pegylation and fluorescent labelling. Moreover, a hydrophobic drug was also successfully loaded inside the polymeric shell. UV-vis and attenuated total reflectance-Fourier transform infrared (ATR-FTIR) spectroscopies were used to confirm drug encapsulation. Size exclusion chromatography (SEC) and sucrose gradient ultracentrifugation (UC) were compared as purification methodologies to separate NPs from coating agent excess to obtain monodispersed stable NPs. Commercially available polystyrene and silica NPs were also characterized by size (DLS, NTA), Zeta-potential (Zp) and fluorescence.

3.2 Synthesis in organic solvent

Hydrophobic gold NPs (Au) and magnetite (Fe_3O_4) NPs were synthesized according to Brust *et al.*[1] and Sun *et al.*[2] respectively. The synthetic protocols described in detail in sections *2.2.2* and *2.2.*3 of this thesis, exhibited good reproducibility and produced monodispersed NPs: representative TEM and DLS measurements are reported in Fig. 3.1 and Fig. 3.2 respectively. Images collected by TEM were analysed by ImageJ and the size-distributions resulted in a diameter for both NPs below 10 nm (5.3±0.6 nm and 8.5±1.0 nm for Au NPs and Fe_3O_4, respectively). Diameters measured by DLS and TEM were slightly different due to the nature of the measured property: hydrodynamic diameters obtained by DLS include the solvation

sphere, while TEM (made on the dried sample) images the metal cores due to their electron contrast. For Fe_3O_4 NPs the stabilizing organic ligands are longer and, given the lower Fe contrast with respect to Au, the organic shell seems more visible. In Table 3.1, averaged TEM and DLS diameters are reported for both NPs.

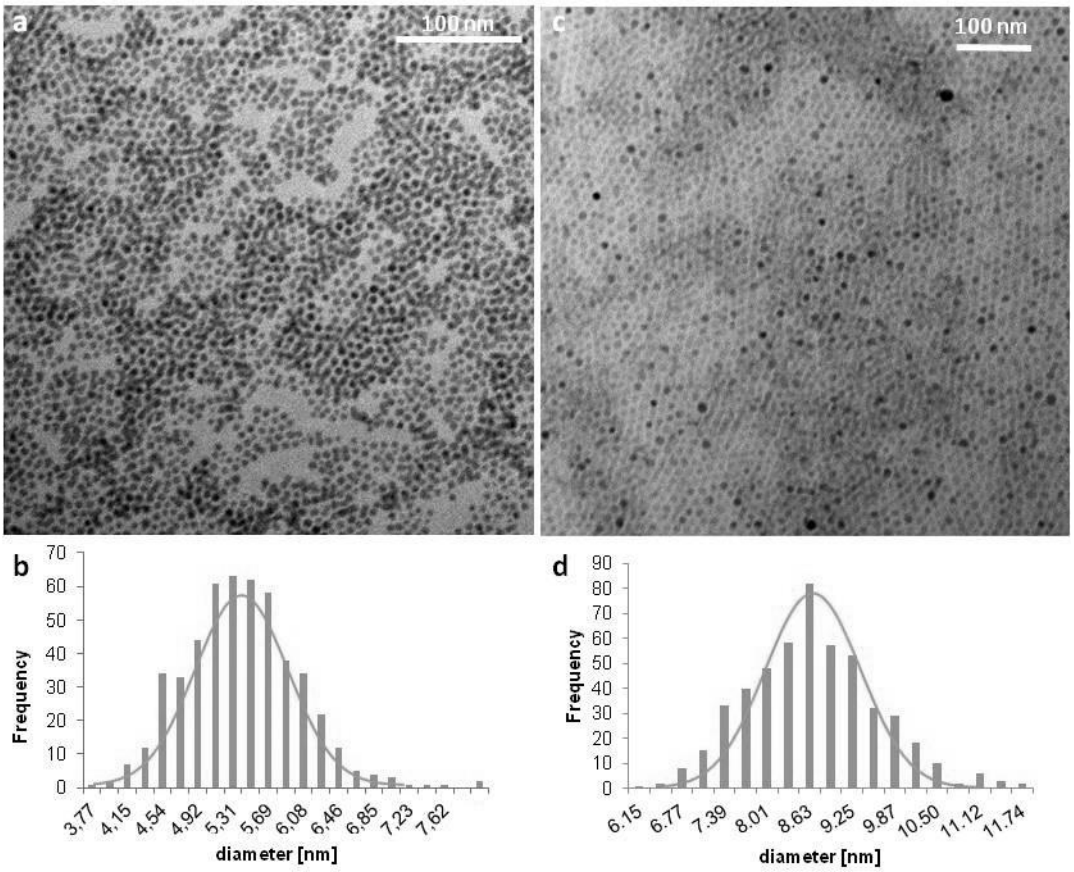

Figure 3.1 TEM images and size distributions obtained by TEM images. Images are at a magnitude of 50kx (a, Au NPs) and 40kx (c, Fe_3O_4). Statistic was done on about 500 NPs for each type of NP.

Table 3.1 Comparison of the averaged diameters measured by DLS[1] and TEM.

	DLS		TEM
	d_H [nm][2]	**PdI[3]**	**d [nm][4]$_{n=500}$**
Au NPs	8.2±0.1	0.18	5.3±0.6
Fe_3O_4	15.8±0.1	0.15	8.5±1.0

[1] DLS data were the average of three measurements and are presented with the relative standard deviation.
[2] Z-averaged hydrodynamic diameters (d_H) obtained by cumulant analysis of the auto-correlation functions
[3] Polydispersity indexes (PdI) obtained by cumulant analysis of the auto-correlation functions.
[4] TEM diameters were the average of 500 NPs' diameters measured by ImageJ.

ICP-AES was used to determine metal concentration of the NP dispersions in the organic solvent. Au spectrum was recorded at λ=267.594 nm and Fe at λ=240.489 nm. Data from three distinct syntheses are reported in Table 3.2. While for Au NPs the concentrations were very similar, Fe_3O_4 showed less reproducible results. This difference is due to the different synthetic protocol for magnetite NPs for which insoluble aggregates formed during the synthesis likely due to inappropriate thermal control and partial oxidation.

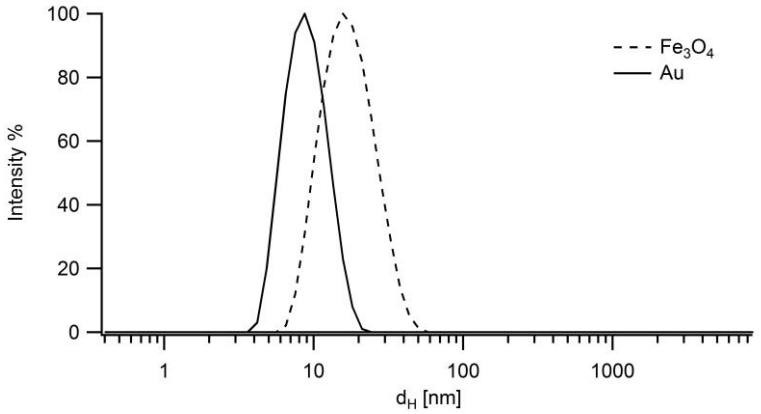

Figure 3.2 DLS Intensity-averaged size distributions of the hydrodynamic diameters for Au and Fe_3O_4 NPs. The original samples were diluted in toluene 20 times and the results are the average of three successive measurements.

Table 3.2 Parameters used to derive the concentration of particles in NPs/ml from the element concentration (mg/ml) in the dispersion derived from ICP- AES.

	d[a] [nm]	**Density [g/m³]**	**Volume [cm³]**	**Weight NP [g]**	**C_x[c] [mg/l]**	**NPs/ml**
Au NPs	5.3	19.3	$7.8x10^{-20}$	$1.5x10^{-18}$	1628	$1.1x10^{15}$
					1648	$1.1x10^{15}$
					1565	$1.0x10^{15}$
Fe_3O_4	8.5	5.2	$3.2x10^{-19}$	$1.7x10^{-18}$	5316	$3.1x10^{15}$
					3721	$2.2x10^{15}$
					836	$4.9x10^{14}$

a diameters from TEM statistics;
b volume was calculated assuming spherical geometry;
c x= Au or Fe from ICP-AES

3.3 Transfer of NPs in the aqueous environment

Biological application of these NPs requires their stabilization as aqueous dispersions. The strategy adopted here was based on the coating of the organic metal cores by poly (maleic anhydride alt- 1- octadecene) (PMAO), an amphiphilic polymer able to intercalate with the

alkyl chains stabilizing the organic core. This strategy was very convenient because it could be applied to both kind of NPs and offered a good starting point for further functionalization, providing the NPs surface with carboxylic groups after exposure to a basic solution. Moreover, the formation of a hydrophobic shell constituted a microenvironment to embed small molecules insoluble in water.[3-5] The applied protocol was described in paragraph *2.2.4*. The optimized molar ratios used for the reaction were established through an optimization protocol that also included purification steps after the coating process. The purification step is important for reducing the amount of free PMAO at the end of the reaction that could lead to the formation of polymer micelles and multi-core particles.[6,7] During the experiment the number of particles was kept constant (100 µl corresponding to 10^{15} NPs/ml), while the moles of PMAO and of tetramethyl ammonium hydroxide pentahydrate (TMAH) were varied. The TMAH is one of the strong bases chosen to solubilize the dry film of coated NPs. In Table 3 there is a summary of the different attempts where the PMAO/TMAH ratio was varied. Among those, *D* did not allow complete film solubilisation; *A* and *B* were both successful, while *C* showed a very slow kinetics. The results shown in this thesis were obtained with the PMAO/TMAH equal to ratio B reported in Table 3.3.

Table 3.3 Polymer coating optimization.

	PMAO monomer unit [mmol]	**TMAH [mmol]**
A	0.04	0.25
B	0.02	0.13
C	0.016	0.10
D	0.011	0.07

The slow evaporation of the organic solvent from a mixture of organic particles and PMAO guaranteed the wrapping of the polymer around the NPs surface. The polymer was used in large excess to limit the formation of multi-core particles. The polymer coating could be made more stable by cross-linking alkylic chains using diamines. Attempts with bis(6-aminohexyl)amine were performed[8], dissolving the cross-linker in chloroform together with the mixture of polymer and NPs. However, the need of cross-linking the polymer coating stabilizer around the NP was questionable because for long chain polymers the unwrapping from NPs surface is energetically unfavourable.[9] Moreover, to avoid inter-particles cross-linking during this process, it was necessary to operate in very dilute conditions. In these

conditions possible cross-linking of the co-existing polymeric micelles can occur making their removal and further NPs purification challenging. For these reasons and based on the good NP stability observed without cross-linking the polymeric shell, cross-linking was not performed.

Base-catalysed hydrolysis of the polymer coated NPs allowed their solubilisation in aqueous solution. Two strong bases were used: sodium hydroxide (NaOH) and TMAH. Both of them successfully transferred the hydrophobic NPs into aqueous dispersions (Fig. 3.3, Table 3.4). TEM images did not highlight aggregation or formation of multi-core particles as it can be seen in Fig. 3.4a and 3.4b. NPs stabilised by NaOH were shown to be less stable compared to those stabilized by TMAH and aggregation occurred within a few days. Statistics on the size distribution of these NPs was obtained measuring about 250 NPs by ImageJ software. Size values obtained for both coated NPs did not increase significantly compared to the cognate NPs in organic solvent. For Au NPs size changed from 5.3±0.6 nm to 5.7±1.0 nm, while for Fe_3O_4 was 10.2±1.6 nm compared to 8.5±1.0 nm in toluene. TEM mainly shows the organic cores (mostly for Au NPs), the polymer coating was difficult to visualize given the poor electron-density.

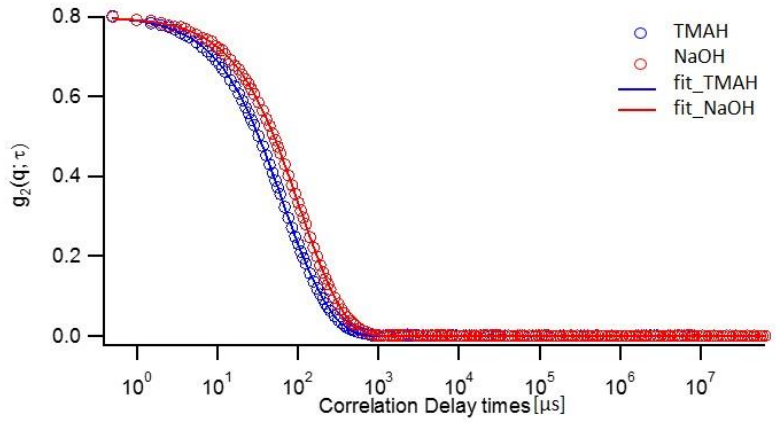

Figure 3.3 DLS auto-correlation functions of aqueous dispersions of Au NPs transferred by TMAH and NaOH. DLS curves were fitted by the double exponential equation 2.11.

Table 3.4 Comparison between hydrodynamic diameters obtained by cumulant analysis and by double-exponential fitting (eq. 2.11) of the auto-correlation functions for TMAH and NaOH stabilised NPs represented in Fig. 3.3.

	A[1]	**C**[2]	τ_{C1}[µs][3]	τ_{C2}[µs][3]	d_{H1} [nm][4]	d_{H2} [nm][4]	d_H [nm][5] (PdI)
TMAH	0.65	0.57	40.1	132.1	13.7	45.1	46.7±0.6 (0.41)
NaOH	0.58	0.48	56.3	167.8	19.2	57.3	73.4±1.0 (0.28)

[1] Amplitude; [2] weight-coefficient of the smaller population; [3] relaxation times obtained through equation 2.11; [4] hydrodynamic diameters derived from the Stokes-Einstein equation on fitted values; [5] hydrodynamic diameters derived from the Stokes-Einstein equation on cumulant results.

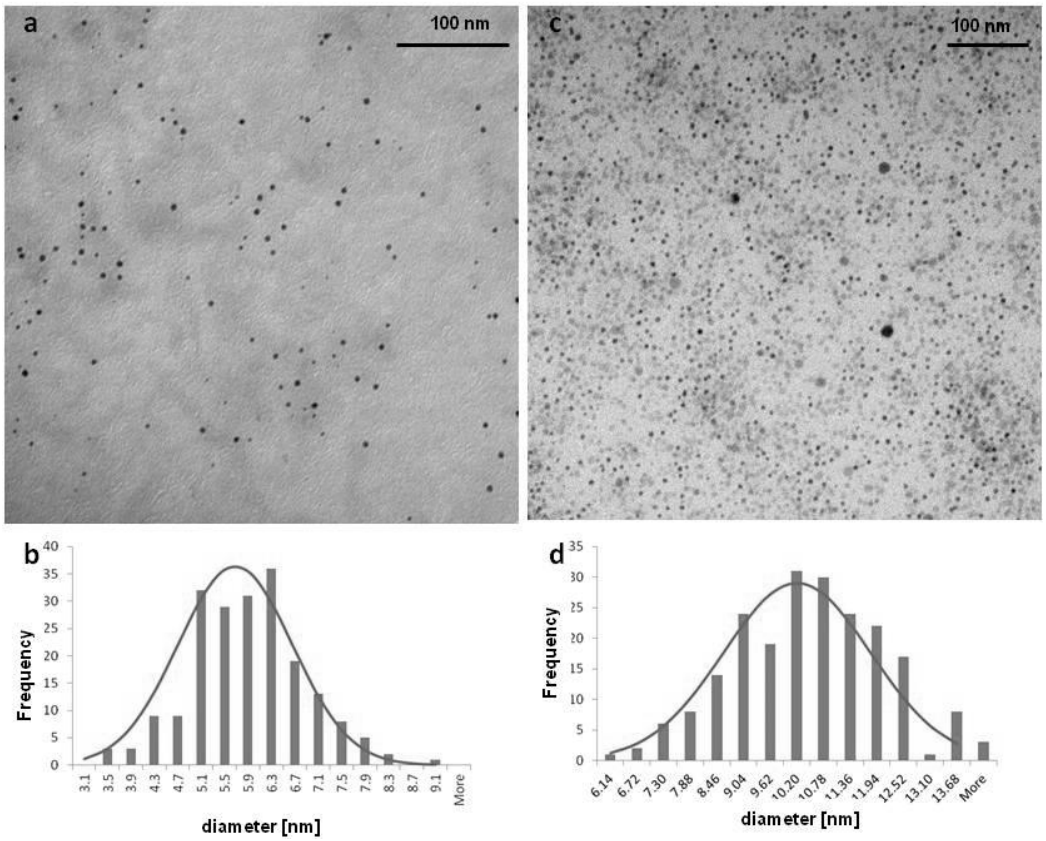

Figure 3.4 TEM images and histogram distribution of the carboxylated Au NPs and Fe_3O_4 (a and c respectively). Images are at a magnitude of 50kx. 250 particles were measured for each sample by ImageJ and the size distribution represented trough histograms (b and d, Au NPs and Fe_3O_4).

3.4 Purification of polymer coated NPs

NP coating was performed in the presence of excess of polymer so purification for removing the unbound polymer from the aqueous dispersion was needed.

NPs aqueous dispersions were dialysed against PBS for three days using a molecular cut-off of 100 kDa to slowly remove the excess of polymer used during the coating reaction. DLS size-distributions of NP dispersions after dialysis were characterized by lower polydispersity

as shown in Fig. 3.5a-b. The auto-correlation function of the dialysed sample showed a steeper slope as well as a size distribution centred at a lower hydrodynamic size (Fig. 3.5b).

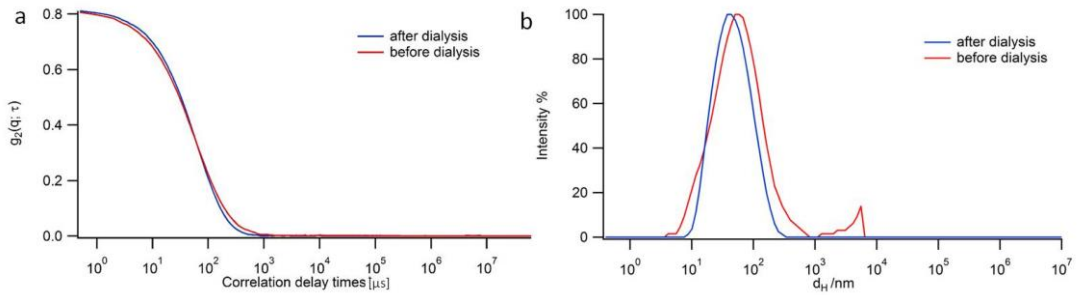

Figure 3.5 Auto-correlation data (a) and intensity-averaged size distributions (b) obtained by DLS of Fe_3O_4 NP aqueous dispersions before (red lines) and after (blue lines) dialysis.

3.4.1 Size exclusion chromatography

Size exclusion chromatography has been widely applied for NPs separation giving high reproducibility and resolution.[8,10] Although some examples are reported in literature where SEC was proved not to completely remove the excess of polymer from the NP dispersion,[6] in this work we tried to apply SEC after dialysis. The experimental procedure is extensively described in paragraph *2.3.4.1*. Briefly, we used two columns of one meter and 25 cm in length (same cross-sections) and filled with Sephacryl S-1000 SF and S-500 HR, respectively. NPs dispersions eluted through both columns were successfully separated by size with high resolution and the shorter column showed shorter time of analysis. Representative results are presented in Fig. 3.6a and 3.6b for Au and Fe_3O_4 NPs, respectively. Recovered fractions showing absorption at 320 nm were screened by DLS. While recovered Au NP fractions showed sharper size separation highlighting three main size populations (around 50, 25 and 16 nm), for Fe_3O_4 NPs a continuous trend was found. Fractions with a PdI above 0.25 were not pooled together, but filtration through syringe filter 0.22 μm pores was performed and samples measured again by DLS. Final batches of NPs were obtained pooling together fractions 10-20 (F1), 21-24 (F2) and 30-38 (F3) for Au and fractions 13-25 (F1) and 24-37 (F2) for Fe_3O_4, they were characterized by size and Zp and representative results are shown in Table 3.5. The main populations of Au and Fe_3O_4 NPs were characterized by a size of 23.1±1.5 nm and 46.1±0.4 nm. This purification approach worked better for gold NPs compared to magnetite ones as proved by the PdI values of 0.11 and 0.23, respectively. The smaller populations of 16 nm found in both samples showed a lower Zp (≈ -13 mV) with respect to the main populations (≈ -25/-20 mV): those samples contained such a low amount of metal that they were not suitable for ICP analysis. These fractions might have contained high

amounts of free polymer. In fact, TEM images on these three different fractions for Au NPs did not show particular alteration of the NP core (Fig. 3.7), with both morphology and size distributions appearing the same.

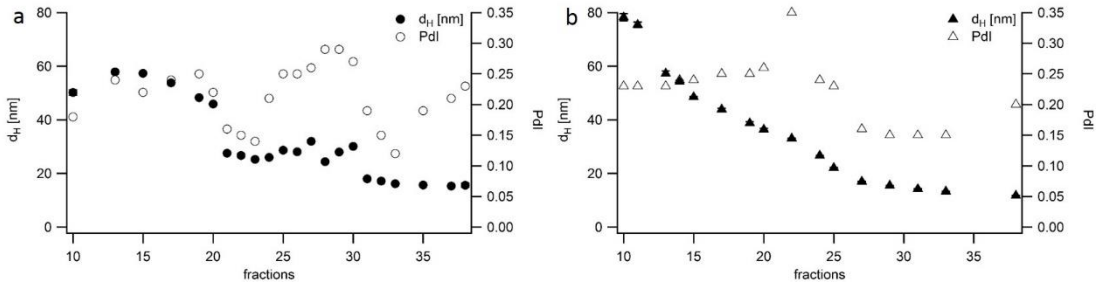

Figure 3.6 Trends for hydrodynamic diameters (d_H, full markers, left axis) and polydispersity indexes (PdI, empty markers, right axis) obtained from cumulant analysis of the auto-correlation functions of the fractions collected from Sephacryl S-500 SEC on Au (circles, a) and Fe_3O_4 NPs (triangles, b).

Table 3.5 DLS data[1] of purified Fe_3O_4 and Au NP dispersions obtained through size exclusion chromatography. Fe_3O_4 F1 (fractions 13-25), F2 (fractions 24-37); Au F1 (fractions 10-20), F2 (fractions 21-24), F3 (fractions 30-38).

	Fe_3O_4 F1	**Fe_3O_4 F2**	**Au NPs F1**	**Au NPs F2**	**Au NPs F3**
d_H [nm][2]	46.1±0.4	16.1±0.8	36.4±0.7	23.1±1.5	16.4±0.3
PdI[3]	0.23	0.16	0.14	0.11	0.19
Zp [mV]	-25.4±1.9	-12.6±3.4	-19.3±4.0	-28.5±4.6	-13.2±2.7

[1] DLS data were the average of three measurements and are presented with the relative standard deviation.
[2]Z-averaged Hydrodynamic diameters (d_H) obtained by cumulant analysis of the auto-correlation functions
[3]Polydispersity indexes (PdI) obtained by cumulant analysis of the auto-correlation functions.

3.4.2 Sucrose gradient ultracentrifugation

After performing SEC, NPs were subjected to agarose gel electrophoresis to prove the complete removal of the free polymer. The free polymer can be detected under UV light, while NPs can be detected under visible light.[6] In Fig. 3.8, panels *a* - *b* represent the same gel under visible and UV light detection, respectively. Bands 1, 2 and 3 are F_3O_4 before dialysis, after dialysis and after size exclusion chromatography, respectively. Fluorescent bands became narrower and fainter with the purification process, but free polymer was still present in band 3*. Although NPs bands were faint (dashed square in Fig. 3.8a and 3.8b), they could be distinguished from the polymer. Given the inefficiency of SEC-based purification, sucrose gradient UC was performed on dialysed NPs following the procedure described in paragraph *2.3.4.2*.

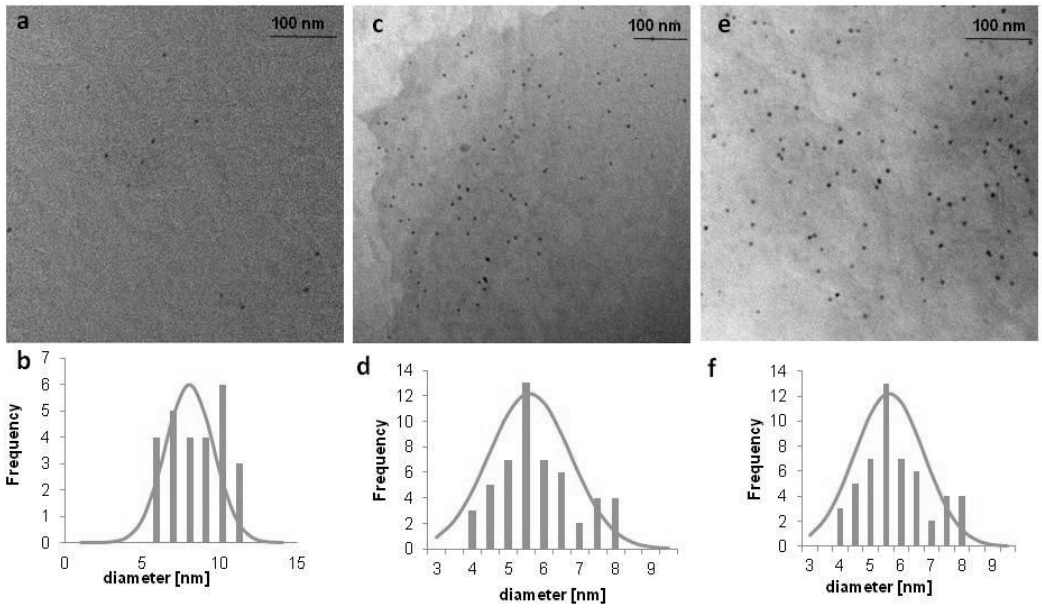

Figure 3.7 TEM images and histogram distribution of the three fractions collected by SEC of Au NP aqueous dispersions. a-b) Fraction 1; c-d) Fraction 2; e-f) Fraction 3 relative to the samples whose parameters are reported in Table 3.5. Images were at a magnification of 50kx (a, c) and 40kx (b).

In Fig. 3.8c, a picture of the UC tube after centrifugation was shown: NPs were localized in the coloured band in the centre. The transparent solution above the coloured band was sampled in 0.5 ml fractions from the top of the tube that were loaded on agarose gel (Fig. 3.8d). The detection of free polymer was from aliquots 2 to 7 and the corresponding bands became fainter progressing across the gradient (sucrose concentration 2-20% w/w). A band corresponding to NPs appeared from fraction 10 (sucrose concentration 33-50% w/w). The coloured band was isolated from the other uncoloured bands and dialysed against PBS (using a membrane with 2kDa cut-off) until complete elimination of sucrose. DLS confirmed the recovery of the main population previously isolated by SEC. NP dispersions purified through UC showed DLS size-distributions characterized by a lower polydispersity, passing from 0.23 to 0.16 (Fig. 3.9 and Table 3.6), and slightly lower Zp.

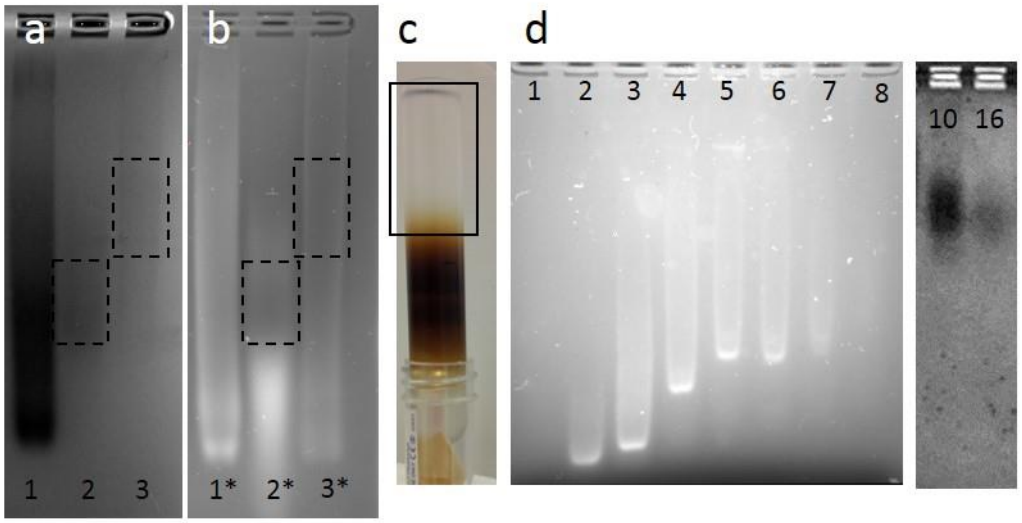

Figure 3.8 Polymer and NPs detection by 2% agarose gel. A gel was loaded with NPs before dialysis (lane 1, 1*), after dialysis (lane 2, 2*), after SEC (lane 3, 3*) and imaged under visible light (a) and UV filter (b). C) Picture of a tube loaded with Fe_3O_4 after UC. D) Gel loaded with aliquots collected from the top of the tube. Lanes 1-8 were imaged under UV filter while lanes 10 and 16 were imaged under visible light.

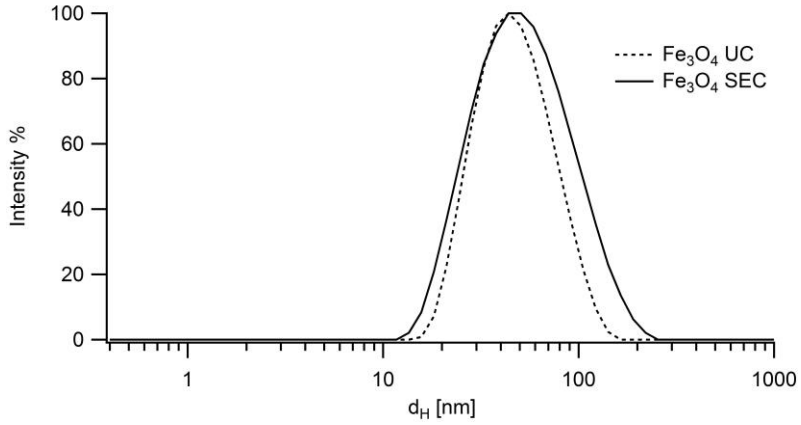

Figure 3.9 DLS intensity-averaged size distributions of Fe_3O_4 dispersions purified by UC (dotted line) and SEC (solid line).

Table 3.6 DLS data[1] of purified Fe_3O_4 obtained by SEC and UC. SEC sample is F1 (fractions 13-25), UC corresponds to sucrose concentration of 33-50% w/w.

	Fe_3O_4 SEC	**Fe_3O_4 UC**
d_H [nm][1]	46.1±0.4	42.9±0.1
PdI[2]	0.23	0.16
Zp [mV]	-25.4±1.9	-23.8±2.9

[1] DLS data were the average of three measurements and are presented with the relative standard deviation.
[2] Hydrodynamic diameters (d_H) from cumulant analysis of the auto-correlation functions.
[3] Polydispersity indexes (PdI) from cumulant analysis of the auto-correlation functions.

3.5 Surface functionalization

3.5.1 Pegylation

NP surface pegylation was performed exploiting two distinct routes to achieve two degrees of surface functionalization: partial and complete.

The partial pegylation was obtained using an excess of Jeffamine M1000 as nucleophile to open the maleic ring and disperse the polymer-NP film in the aqueous solution: this strategy allowed modification of 50% of the carboxylic groups by PEG. Pegylated NPs were imaged by TEM and showed a good size distribution of the cores without formation of multi-core NPs. The mean diameters obtained by statistical analysis of the NPs imaged by TEM (Fig. 3.10b-d and Table 3.7) were slightly larger than those obtained for the organic core NPs, although they were comparable to the carboxylated NPs. This is due to the contribution of the shell that unfortunately could not be clearly distinguished from the core due to instrumental limitations (Fig. 3.10a-c). The purification of NPs dispersions was done as previously described by UC and SEC. DLS and TEM results reported in Table 3.7 showed that NPs purified by SEC were characterized by higher polydispersity and larger diameters compared to those subjected to UC. Zp values were reduced by about 50% with respect to carboxylated NPs (from about -23 mV to -10 mV). Electrophoretic mobility of pegylated and carboxylated NPs in agarose gel was very different as it was expected (see Fig. 3.11). In particular, carboxylated Au NPs and Fe_3O_4, loaded in lanes *a* and *c* of the agarose gel reported in Fig. 3.11, respectively, showed a higher mobility with respect their pegylated counterparts (loaded in lanes *b* and *d* respectively).

The second strategy used to achieve complete pegylation of the surface carboxylic groups was done by a post-purification functionalization of the surface carboxylated groups by EDAC chemistry[11]. The optimal experimental conditions were found through several attempts where the molar ratio between EDAC and Jeffamine was systematically changed in order to avoid NP aggregation and flocculation. The optimal conditions were the following: incubating overnight 10^{12} NP/ml with a molar ratio EDAC/Jeffamine of 40 and then removing the excess of reagents washing 3-5 times by centrifugal filter, thus exchanging the buffer with water. The auto-correlation functions of the NPs in water and PBS dispersions are reported in Fig. 3.12. Their cumulant results are reported in Table 3.8: NPs in PBS are characterized by a larger hydrodynamic size and polydispersity. Some degree of aggregation and cross-linking could not be completely ruled out. Zp measured were close to 0 mV (Table 3.8) and confirmed a more extensive pegylation.

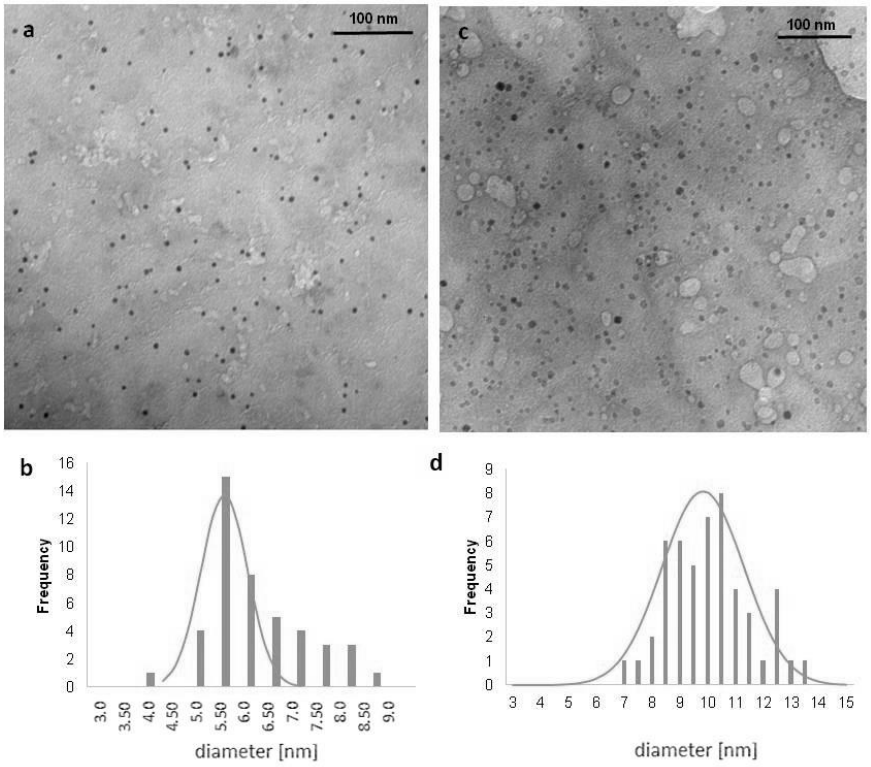

Figure 3.10 TEM images and relative histograms for pegylated Au NPs (a-b) and pegylated Fe_3O_4 (c-d). Images were at a magnification of 50kx and 40kx respectively (a-c). Statistics were done on 50 NPs.

Table 3.7 Hydrodynamic diameters, polydispersity indexes, z- potential and dry diameters of pegylated Au NPs and Fe_3O_4. DLS was done on dispersion purified by SEC and UC. TEM images were collected for samples after dialysis. Au-PEG NPs and Fe_3O_4-PEG isolated by UC corresponded to sucrose concentrations of 30-45% and 25-35% w/w respectively.

	DLS[1]				**TEM**
	d_H [nm][2] SEC (PdI)	Zp [mV]	d_H [nm][3] UC (PdI)	Zp [mV]	d[nm][4] TEM
Au-PEG NPs	42.1±0.4 (0.23)	-9.0± 2.3	26.1±0.2 (0.18)	-9.4± 1.0	5.9±0.9
Fe_3O_4-PEG	46.6±0.7 (0.16)	-10.4± 4.4	29.7±0.3 (0.15)	-10.3± 1.4	9.8±1.5

[1] DLS data were the average of three measurements and are presented with the relative standard deviation.
[2] Hydrodynamic diameters (d_H) from cumulant analysis of the auto-correlation functions.
[3] Polydispersity indexes (PdI) from cumulant analysis of the auto-correlation functions.
[4] Mean diameters from distribution analysis of NPs sampled by ImageJ.

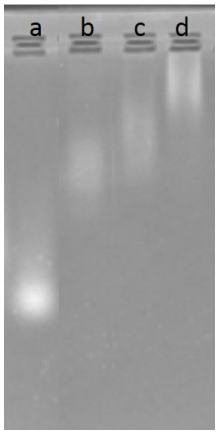

Figure 3.11 1.5% Agarose gel run at 100V for one hour. a) carboxylated Au NPs; b) pegylated Au NPs; c) carboxylated Fe_3O_4; d) pegylated Fe_3O_4.

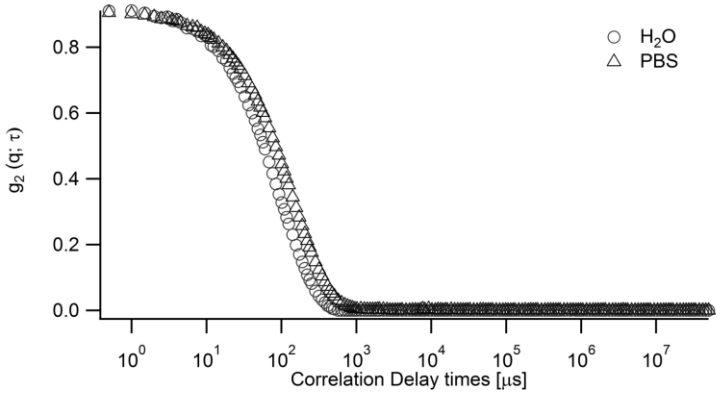

Figure 3.12 Auto-correlation data obtained by DLS comparing Fe_3O_4 dispersed in water (red circles) and PBS (blue triangle).

Table 3.8 Hydrodynamic diameters, polydispersity indexes and z-potential of pegylated Fe_3O_4 through EDAC coupling.

	Fe_3O_4-PEG in water[1]	**Fe_3O_4-PEG in PBS**
d_H [nm][2]	64.4±2.9	80.7±0.8
PdI[3]	0.19	0.21
Zp	-3.2±1.1	+1.6±0.3

Data were the average of three measurements and are presented with the relative standard deviation.
[1] The Zp was measured in a solution of NaCl 0.1 mM.
[2] Hydrodynamic diameters (d_H) from cumulant analysis of the auto-correlation functions.
[3] Polydispersity indexes (PdI) from cumulant analysis of the auto-correlation functions.

3.5.2 Fluorescent labelling of the NPs

Water-soluble NPs were further labelled with a fluorescent molecule to allow detection of the NPs through fluorescence spectroscopy and fluorescence microscopy. The labelling procedure was performed following two strategies: the first involved the labelling of PMAO in organic

solvent before the coating process, the second consisted in a fluorescent labelling of the core-shell NPs dispersed in aqueous solution post-purification.

Fluoresceinamine (FA, Sigma, chemical structure reported in Figure Fig. 3.13a) was used as fluorescent probe to modify the polymer. The coupling reaction between PMAO and FA was carried out in Tetrahydrofuran (THF) overnight (molar ratio of 50). The efficiency of the coupling was proved by fluorescence emission intensity increase of the labelled polymer [12] as conseguence of the coupling at the same dye concntration (Fig. 3.13b).

The labelled polymer was used to coat the NPs in organic solvent following the procedure described in the paragraph *2.2.6*. Briefly, NPs (10^{15} NPs) and polymer (0.02 mmol) were dissolved in chloroform and the solvent slowly eliminated by rotary evaporation. The dried film of coated NPs was then re-dispersed in an aqueous solution of TMHA (0.13 mmol).

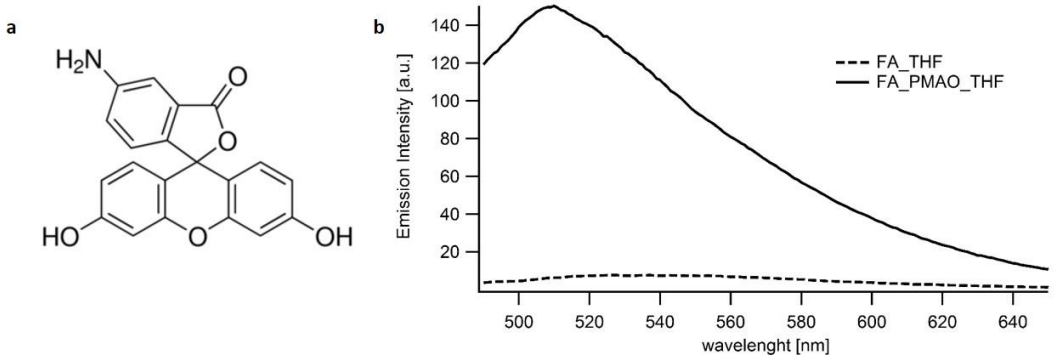

Figure 3.13 A) FA isomer. B) Emission spectra of FA in THF (dotted line) and PMAO modified with FA in THF (solid line). The concentration of the dye was 0.057 mM. The excitation wavelength was 430 nm.

Purification by sucrose gradient UC was applied to the coated fluorescent NPs after extensive dialysis against PBS. The sucrose gradient concentration used to purify the carboxylated NPs (i.e. 7-70%) did not result in a good separation of the NPs from the excess of polymer, thus the sucrose gradient was adjusted to concentration of 35-70%. After UC, twelve aliquots from the top to the bottom of the tube were taken. In Fig. 3.14a are reported the measured UV-vis and fluorescence intensities of these 12 fractions. NPs were detected at a wavelength of 231 nm and found from fractions 7 to 12. Fluorescence emission at 513 nm was used to detect the labelled polymer and its concentration (signal) was similar in all fractions except that in fractions 3 and 12. Aliquots were loaded in agarose gel and UV detection highlighted the presence of free polymer in the first four fractions. In fraction 12 the band corresponding to the free polymer was not detectable (Fig. 3.14b). Combining results from UV, fluorescence and agarose electrophoresis, we evaluated that labelled NPs were in fractions 7-12 (sucrose concentration of 54-70% w/w). Fraction 12 was characterized by a much higher fluorescence emission, but a similar absorbance to fractions 10 and 11 (sucrose concentration of 66-70%

w/w). It also presented some aggregates, thus to allow further characterization, it was sonicated before dialysis against PBS. Fractions 7-11 (sucrose concentration of 54-66% w/w) were pooled together and dialysed versus PBS. The two samples were characterized by UV-vis absorption, fluorescence and DLS.

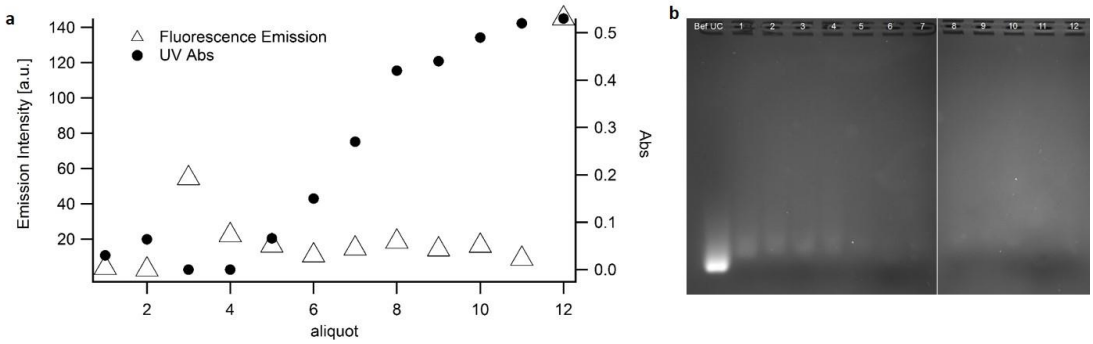

Figure 3.14 Analysis of the aliquots collected after UC of Fe_3O_4 coated with FA-PMAO. A) Fluorescence emission intensity (λ_{ecc}= 430 nm; λ_{em}= 513 nm) and UV absorption (λ_{abs}= 231 nm) of the 12 fractions collected from the top of the gradient to the bottom. B) 2% agarose gel of the sample before UC (first lane on the left) and the 12 fractions.

UV-vis spectra were recorded for labelled and unlabelled Fe_3O_4 NPs and are shown in Fig. 3.15a. NP dispersions were at a similar concentration ($2.5x10^{12}$ NPs/ml) and differences were observed at low wavelengths and in the region between 480-500 nm. In Fig. 3.15b fluorescence emissions of the same samples were recorded: while the spectrum of the labelled Fe_3O_4 NPs was characterized by a peak at wavelength of 518 nm, fluorescence emission of unlabelled Fe_3O_4 NPs was close to background. DLS characterization of these samples showed that coating the NPs with an excess of labelled polymer caused the formation of two populations as when the coating was performed by unlabelled polymer. The second population, mostly composed of polymer micelles, was eventually purified through dialysis and UC (Table 3.9). The presence of the dye on the polymer structure slightly affected the main population in terms of size (43 nm compared to 53 nm in diameters), while the z-potential was unchanged. The larger second population could be related either to the formation of multi-core coated NPs or to NP aggregation during UC. Overall, the procedure was successful but a considerable amount of material was lost during purification: NPs were not fully recovered

during the UC as well as a big excess of labelled polymer was needed. Thus, this procedure not appropriate when a more expensive fluorescent molecule was used.

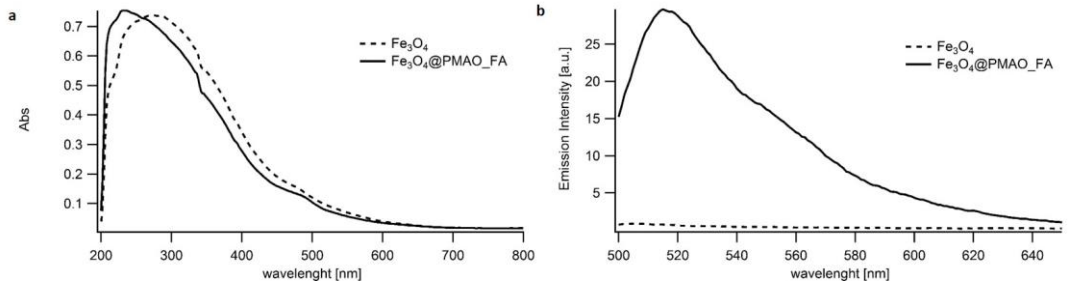

Figure 3.15 A) UV-vis spectra in PBS of unlabelled Fe_3O_4 (dotted line) and FA-labelled Fe_3O_4 (solid line). B) Emission spectra (λ_{ecc}= 430 nm) of unlabelled Fe_3O_4 (dotted line) and labelled ones (solid line).

Table 3.9 Hydrodynamic diameters, polydispersity indexes and z-potential measured by DLS[1] of FA-labelled and unlabelled Fe_3O_4. UC F7-11 and UC F12 corresponded to sucrose concentration of 54-66% and 70% w/w respectively.

	Fe_3O_4@ PMAO_FA bef dial	**Fe_3O_4@ PMAO_FA after dial**	**Fe_3O_4@ PMAO_FA UC F7-11**	**Fe_3O_4@ PMAO_FA UC F12**	**Fe_3O_4[2]**
d_H [nm][3]	147.6±2.9	110.5±1.1	54.6±0.9	113.7±1.3	43.6±0.2
PdI[4]	0.3	0.23	0.22	0.20	0.15
Zp [mV]	n.d.	n.d.	-24.4±0.9	-25.9±0.7	-26.7±2.6

[1] Data are the average of three measurements and are presented with the relative standard deviation.
[2] Fe_3O_4 were unlabelled carboxylated NPs purified by UC.
[3] Hydrodynamic diameters (d_H) from cumulant analysis of the auto-correlation functions.
[4] Polydispersity indexes (PdI) from cumulant analysis of the auto-correlation functions.

The second approach was based on 1-Ethyl-3-(3-Dimethylaminopropyl) carbodiimide (EDAC) coupling of an available amine of the fluorescent dye with the surface carboxylic groups on the coated NPs. The chosen dye was BODIPY®FLEDA (LifeTechnologies) whose chemical structure is reported in Fig. 3.16a and absorption and emission spectra in Fig. 3.16b. It belongs to a relatively new class of fluorescent dyes that show small Stokes shift with sharp peaks in absorption and emission, high quantum yield and photo-stability. Recently, it was used to label Fe_3O_4 NPs but the coupling was carried out in organic solvent.[13] The labelled NPs showed good magnetization properties and no cytotoxicity, but some aggregation was revealed by DLS and TEM. In our case, the coupling was performed in PBS buffer at pH 7.4 as described in paragraph *2.2.6*. The resulting dispersion was washed three times with PBS

using centrifugal filters (Amicon 50kDa MWCO) for removing the small amount of DMSO deriving from the stock solution of the dye as well as the excess of reagents. The recovered sample and its first washing were analysed by UV-vis absorption and fluorescence emission as shown in Fig. 3.17a and 3.17b and compared to the signal from the same concentration of unlabelled Fe_3O_4 NPs. In the absorption profile there was the appearance of a peak at 510 nm (the maximum was at 502 nm for the dye in methanol) while the remaining profile did not change. In the fluorescence emission spectrum the maximum was at 518 nm (511 nm for the dye in methanol), while no peaks were present either in the unlabelled Fe_3O_4 NP dispersions nor in the washings meaning that the dye was completely attached to the NPs surface.

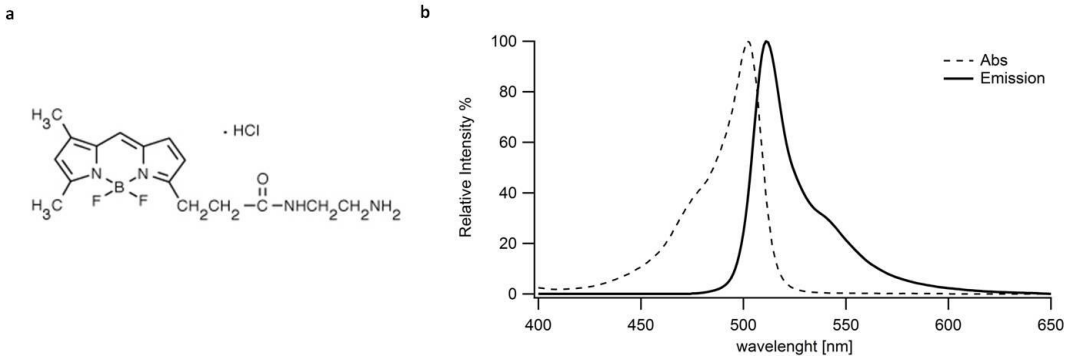

Figure 3.16 Chemical structure (a) and absorbance and emission spectra in methanol (b) of BODIPY®FL EDA from LifeTechnologies.com.

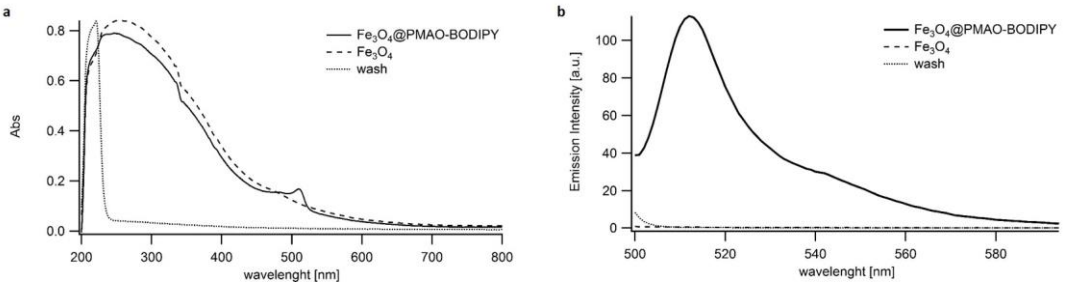

Figure 3.17 A) UV-vis spectra of BODIPY modified Fe_3O_4, unlabelled Fe_3O_4 and washing solution. B) Fluorescence emission spectra of the same samples at a Λ_{ecc}= 500 nm.

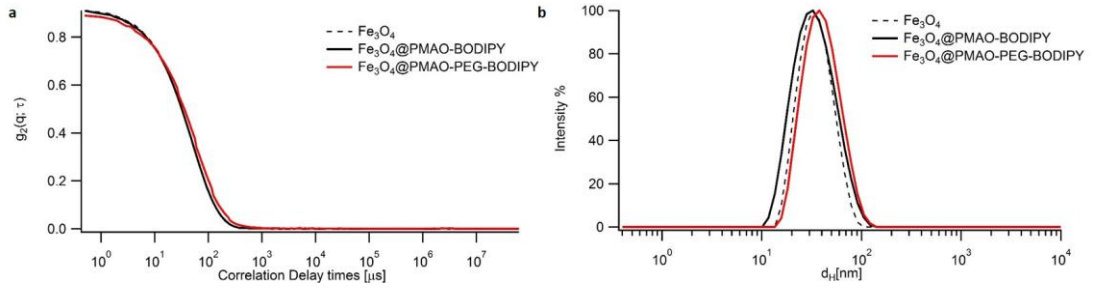

Figure 3.18 DLS auto-correlation data (a) and intensity-averaged size distributions (b) obtained from DLS of carboxylated unlabelled Fe_3O_4 (dashed line) and labelled carboxylated (black line) and pegylated (red line) Fe_3O_4.

Pegylation and fluorescence labelling could be simultaneously performed and, from a structural point of view, the differences from the original dispersion of pegylated NPs were negligible. DLS auto-correlation functions and relative size-distributions of unlabelled, labelled carboxylated and labelled pegylated NPs are reported in Figures 3.18a-b. Moreover, cumulant analysis of these auto-correlation functions showed an almost invariant polydispersity (PdI=0.18, 0.22 and 0.19 for unlabelled, labelled carboxylated, labelled pegylated, respectively) and a slight increase of the z-averaged hydrodynamic diameter passing from 30 nm to 34 nm and 39 nm for unlabelled, labelled carboxylated and labelled pegylated NPs respectively. Zp of the labelled NPs was still very negative for the carboxylated (-24±2 mV), while complete saturation of the COOH groups was not reached for the pegylated NPs as the Zp was still slightly negative (-6±2 mV).

3.6 Drug loading

Generally, the encapsulation of a hydrophobic drug in a nanocarrier exploits the tendency of the drug to spontaneously locate in the hydrophobic region of the NP. Previously, nanocapsules,[14] nano-gels[15] and polymeric NPs,[5] have been loaded with small hydrophobic molecules although the encapsulation efficiency varied.

In this study two approaches to encapsulate a model hydrophobic drug, leflunomide, were followed. The first one consisted in adding the drug in chloroform during the coating procedure. Leflunomide was prepared in chloroform (100 µl, 1.5 mg/ml) and added to the NPs (250 µl, 10^{15} NPs/ml) and the polymer in organic solvent. The mixture was left stirring for four hours and then the solvent evaporated under controlled pressure. The NPs film was dispersed in alkaline water and dyalisis and SEC purifications were performed. However, Fig. 19a shows that the final NPs were characterized by a wide size distribution and a mean hydrodynamic diameter of about 80 nm.

The second approach involved the addition of 100 µl of 1.5 mg/ml stock solution of Leflunomide in chloroform to 10 ml of an aqueous dispersion of the coated NPs at a concentration of $2.5x10^{13}$ NPs/ml. The mixture was left overnight to allow complete evaporation of chloroform. No precipitate was found in the dispersion and purification was carried out with dialysis and SEC. As shown in Fig. 3.19b a nicely monodispersed fraction was isolated by SEC and the hydrodynamic size was comparable to that of the unloaded sample. The hydrodynamic diameter of the loaded NPs was 21.2±0.1 nm (PdI = 0.18), while that of the unloaded ones was 18.1±0.1 nm (PdI = 0.21).

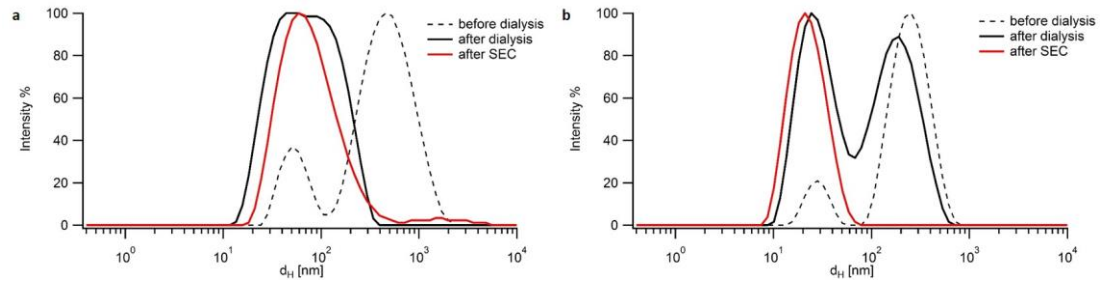

Figure 3.19 Hydrodynamic diameters by intensity percentage of Leflunomide loaded Au NPs with the two approaches. A) Drug in chloroform was added during the coating phase. B) The drug in chloroform was added after transfer of the NPs in water. Dialysis and SEC were performed to purify the final product.

TEM images confirmed that the incubation with the drug did not affect the overall morphology of the NPs although changes in the polymeric shell cannot be imaged and detected by TEM (Fig. 3.20).

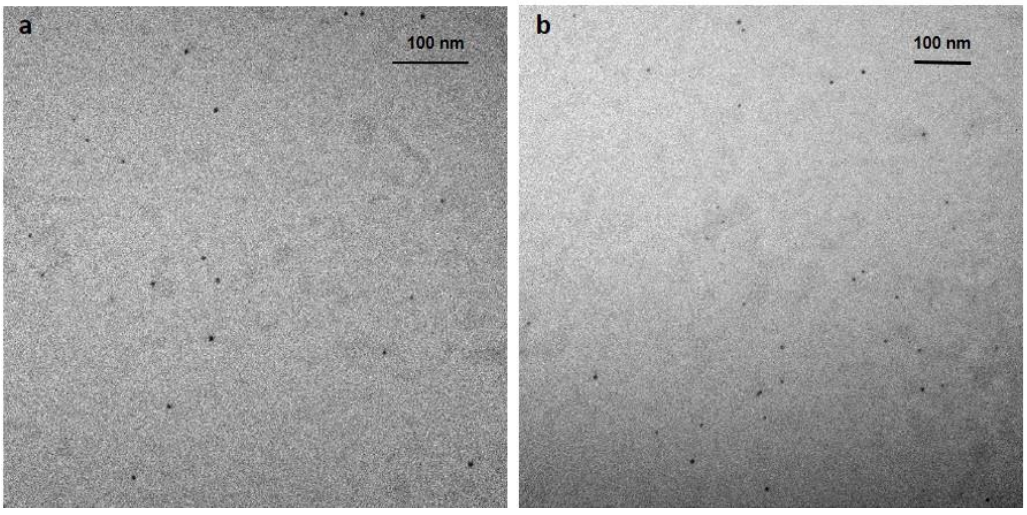

Figure 3.20 TEM images of Au NPs without drug (a) and with the drug (b). Magnification was 40kx and 60kx respectively.

The experimental evidence of the successful incorporation of the drug in the hydrophobic shell needed to be proved. UV-vis and ATR-FTIR spectroscopies were used to reveal Leflunomide

presence in the NPs shell. UV-vis spectra of the unloaded Au NPs, Leflunomide loaded NPs and Leflunomide in chloroform are shown in Fig. 3.21a. The presence of Leflunomide could be related to two features of the absorption spectra of the three samples. First of all, the different shape of the plasmon peak although the Au NP concentration was invariant for the two measurements.[16] Secondly, the appearance of a band at 260 nm that is characteristic of the Leflunomide but which is not present in the spectrum of the unloaded NPs.[17] Leflunomide ATR-FTIR spectrum from chloroform as well as the assignment of the vibrational modes are reported in Fig. 3.21b and in Table 3.10, respectively. ATR-FTIR spectra of Leflunomide loaded Au NPs and relative unloaded counterparts are presented in Fig. 3.22. Analysis of these spectra showed slight shifts or change in intensity of some analogous band of the two samples. Bands at 3298 cm^{-1} (amide N-H stretching), 2924 and 2850 (aromatic C-H stretching), 1658 cm^{-1} (amide C=O stretching), 1412 cm^{-1} (isoxazole ring stretching) and 858 cm^{-1} (aromatic =C-H para-substitution out-of-plan bending) were either slightly shifted or more intense in the loaded NPs spectrum. Furthermore, the band at 1046 cm^{-1} was very strong and it could be attributed to the combination of C-F stretching and C-H β-in-plane-bending for isoxazole. Extra peaks appeared at 1335 cm^{-1} (C-F asymmetry stretching), 1237 cm^{-1} (C-F stretching) and 926 cm^{-1} (isoxazole ring in-plane-bending). We could conclude that the hydrophobic molecule was successfully embedded in the polymeric shell but further optimization of the procedure needs to be done and a suitable methodology to quantify the drug in the shell needs to be found (for example by HPLC).

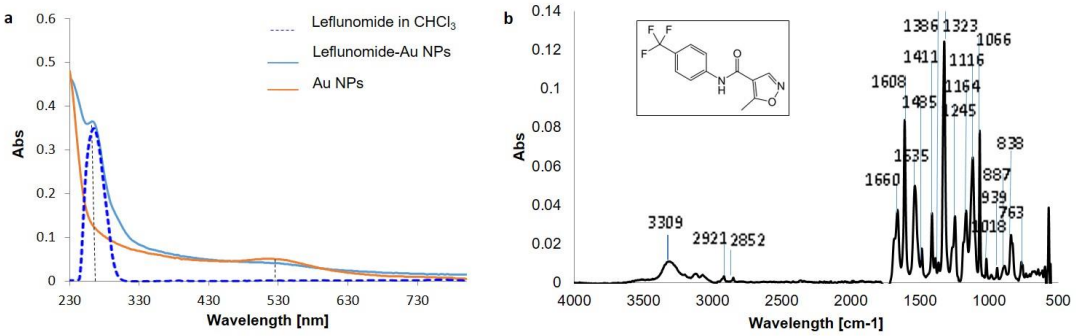

Figure 3.21 A) UV-vis spectra for Au NPs with and without drug and the drug in chloroform (5 μg/ml). The plasmonic resonance band at 516 nm and a peculiar peak for Leflunomide at 260 nm were marked with dashed black lines. B) ATR-FTIR spectrum of Leflunomide in chloroform. In the insert, the structure of the drug is reported. The frequencies of some peaks were highlighted and assignations were represented in Table 3.10.

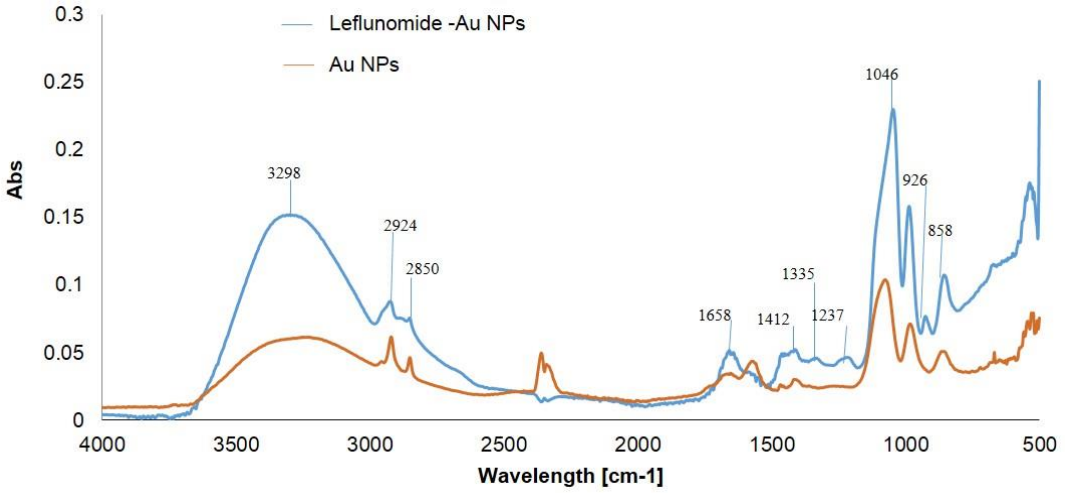

Figure 3.22 ATR-FTIR spectra of Leflunomide-loaded Au NPs (blue line) and unloaded NPs (red line). Relevant bands were labelled and the increase in intensity and shifts could be due to the additional vibration of drug in the polymeric shell.

3.7 Polystyrene and Silica NPs

Polystyrene and silica beads were used throughout this thesis as "standard" nanoparticles: they are extensively characterized in literature and available in a wide range of dimensions and surface groups showing good intrinsic stability and low cytotoxicity.[22-26]

In this study green-fluorescently labelled carboxylated polystyrene nanoparticles were used: nominally their diameters were 20 and 100 nm (PS-COOH20 and PS-COOH100). Unlabelled PS-COOH100 (PS-COOH100NF) and SiO_2 NPs were also tested. Size and surface charge were characterized by DLS and NTA in PBS buffer at pH 7.4 (Table 3.11). All the NPs were negatively charged (from -40 mV to -20 mV) and thus characterized by high colloidal stability. Moreover, DLS analysis of their dispersion resulted in narrow size distributions with PdI<0.1. Measured hydrodynamic diameters were slightly higher than the nominal sizes, except for SiO_2 NPs. NTA analysis gave slighly smaller avarage diameters than those obtained by DLS except for PS-COOH20.[27] PS-COOH20 size seemed to be twice larger from NTA analysis than in DLS, but the low refractive index of PS together with their small size make the analysis of these NPs at the resolution limit of the technique, thus the NTA measured sizes are considered less reliable than those obtained by DLS. A Tecnai 20 TEM with AMT cameras, operating at an accelerating voltage of 200 kV was used for imaging polystyrene NPs (PS-COOH100 and PS-COOH20). Particles were dried on carbon-coated 300–mesh copper grids (Agar Scientific) and counterstained with 2% uranyl acetate.The sizes were confirmed as shown in Fig. 3.23.

Table 3.10 Vibrational frequencies and relative assignments for ATR-FTIR spectra of Leflunomide in chloroform ($CHCl_3$) and after encapsulation in the NPs shell.

Vibrational modes	Vibrational frequencies [cm^{-1}]		Literature vibrational frequencies [cm^{-1}]
	In $CHCl_3$	In NP shell	
Amide N-H [1]	3309	3298	3500-3100[18]
Alkanes and aromatic C-H [1]	2921, 2852	2924, 2850	3000-2850[18]
Amide C=O [1]	1660	1658	1680-1630[18]
Aromatic C=C [1]	1608, 1535, 1485	----------	1600-1475[18]
Isoxazole ring [1]			1650-1610, 1580-1520, 1510-1470[19]
Isoxazole ring [1]	1411, 1386	1412	1430-1370[19]
C-F [2]	1323	1335	1332[20]
C-F [1]	1245	1237	1281-1218[21]
C-F [1]	1164	----------	1157[21]
C-F [1]	1116, 1066	1046	1097[21]
Isoxazole C-H [3]			1088[19]
Isoxazole ring [4]	1018	----------	1028-1000[19]
Isoxazole ring [3]	939	926	945-845[19]
CF_3 [5]	887	----------	909[21]
Aromatic =C-H [6]	838, 763	858	900-690[18]

[1] stretching; [2] asymmetry stretching; [3] β in-plane-bending; [4] breathing; [5] deformation; [6] out-of-plane bending vibrations for para-substituted benzene ring.

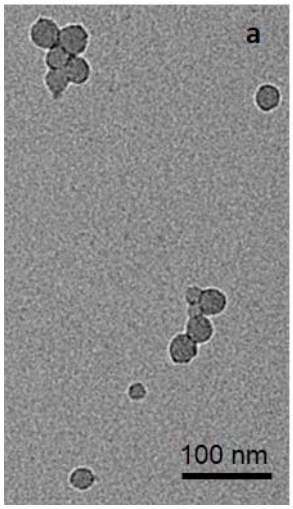

Figure 3.23 TEM images of PS-COOH20.Image was collected with a magnification of 29kx. Few drops of NPs' dispersions were placed on a copper grid and stained by uranyl acetate (picture taken by C. Webster).

Table 3.11 Size and z-potential characterization of polymeric NPs in PBS. DLS and NTA data are reported.

	PS-COOH20	**PS-COOH100**	**PS-COOH100NF**	**SiO_2**
d_H [nm][1]	64±21	78±3	97±5	37±4
SD [nm][2]	28±5	29±2	32±3	18±4
d_H [nm][3]	32.5±0.1	100.8±0.7	128.6±1.1	46.7±0.5
PdI[4]	0.10	0.01	0.05	0.02
Zp [mV]	-45.0±0.3	-33.6±1.2	-26.8±0.8	-22.3±4.0

[1] Hydrodynamic diameter (d_H) was calculated avaraging the hydrodynamic diameters of all NPs tracked in a particle-by-particle modality by NTA.
[2] SD is the standard deviation on all the hydrodynamyc diameters measured in a particle-by-particle modality by NTA.
[3]Hydrodynamic diameter (d_H) obtained by DLS from the cumulant analysis of the auto-correlation data.
[4] Polydispertity indexes (PdI) were obtained by DLS from the cumulant analisys of the auto-correlation data.
All data were presented as the avarage of three indipendent measurements with relative standard deviation.

PS-COOH20 and PS-COOH100 were pegylated through EDAC chemistry by Jeffamine M1000 following the procedure described in paraghraph *2.2.5*. In particular, pegylation on PS-COOH100 NPs was more effective than for PS-COOH20 NPs reaching a pegylation of 100% (evaluated by Zp measures) that made those NPs very stable. PS-COOH20 NPs instead showed less stability probably due to the higher chemical reactivity of the surface[28] and the reaction showed low reproducibility. The best results were achieved reacting $5.8x10^{13}$ NPs/ml of PS-COOH20 NPs with 13 mM Jeffamine and 120 mM EDAC. While purification of PS-PEG100 NPs was performed with five washings by centrifugal filters (Amicon MWCO

100kDa), that was not possible for PS-PEG20 for which aggregation occurred. These NPs were instead purified from excess of PEG through dialysis (MWCO 100kDa for two days). A summary of the features of the obtained particles was shown in Table 3.12.

Fluorescent PS nanoparticles were characterized by fluorimetry (Fig. 3.24) and no shift of the maximum of emission was recorded (515 nm) and concentration determination was possible building a calibration curve at this emission for both PS-COOH100 (Fig. 3.25a) and PS-COOH20 (Fig. 3.25b).

Table 3.12 Characterization by DLS and NTA of the pegylated PS NPs commercially available.

	PS-PEG20	**PS-PEG100**
d_H [nm][1]	80±36	125±1
SD [nm][2]	41±2	38±1
d_H [nm][3]	77.4±1.6	106.3±0.7
PdI[4]	0.19	0.04
Zp [mV]	-0.1±3.1	-0.1±2.2

[1] Hydrodynamic diameter (d_H) was calculated avaraging the hydrodynamic diameters of all NPs tracked in a particle-by-particle modality by NTA.
[2] SD is the standard deviation on all the hydrodynamyc diameters measured in a particle-by-particle modality by NTA.
[3]Hydrodynamic diameter (d_H) obtained by DLS from the cumulant analysis of the auto-correlation data.
[4] Polydispertity indexes (PdI) were obtained by DLS from the cumulant analisys of the auto-correlation data.
All data were presented as the avarage of three indipendent measurements with relative standard deviation.

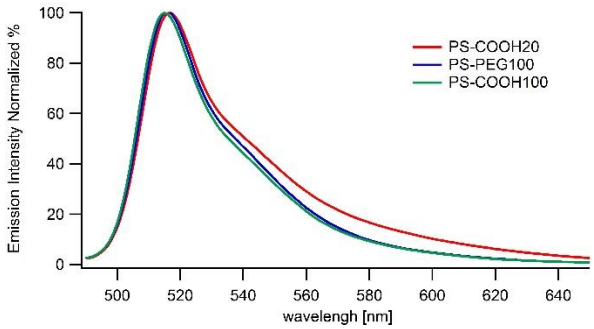

Figure 3.24 Emission intensities for PS NPs in PBS. The excitation wavelength was 490 nm.

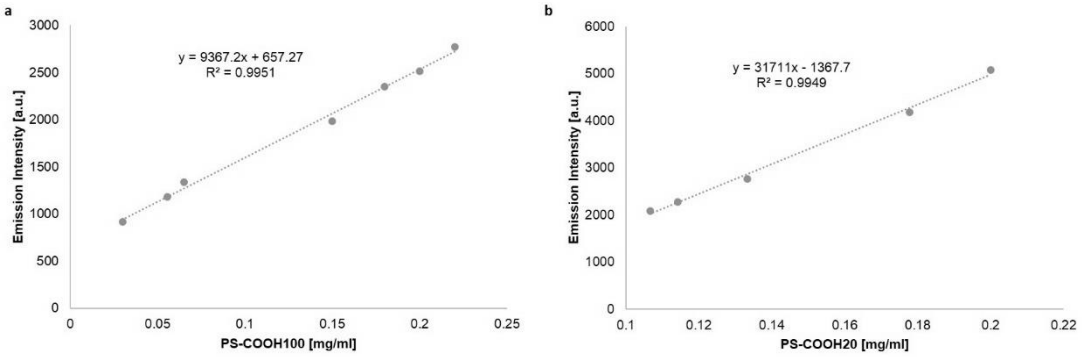

Figure 3.25 Concentration of PS NPs (mg/ml) versus emission intensity. The emission reported was for the maximum emission wavelength at 515 nm.

3.8 Conclusions

In this chapter synthesis, functionalization and physical-chemical characterization of NPs used in this thesis are described. A detailed description of these NPs was important for their further characterization in complex environmental conditions, for example when in contact with different types of biological fluids (e.g. blood and digestive fluids) and for the studies of the interactions with membrane models and cells.

Au and Fe_3O_4 core-shell NPs were synthetized in our laboratory according protocols well established in the literature.[1,2] In particular, the metallic cores of the NPs were synthetized in organic solvent and a polymer coating was introduced to allow them to be dispersed in water. The choice of PMAO, an amphiphilic polymer, as coating agent was convenient because it could be exploited for further surface functionalization (with PEG derivatives and fluorescent dyes) and for accommodating poorly water-soluble molecules in the hydrophobic shell. The optimization of a purification procedure based on dialysis and sucrose gradient UC was necessary to obtain monodispersed NPs free from the excess of reagents. SEC was shown to be not as effective as UC in accomplishing a complete purification. The resulting NPs were monodispersed (PdI <0.2) with hydrodynamic diameters around 50 nm. Surface charge could be controlled through pegylation and NPs that were negatively charged (Zp ≈ -20 mV), partially (Zp ≈ -10 mV) or fully pegylated (Zp ≈ 0 mV) were synthetized.

The properties listed above made our NPs suitable for nanomedicine applications. The cores can be exploited for different types of imaging, while pegylation of the surface made them stable in the biological environments. We confirmed the possibility of embedding a small hydrophobic drug in the polymer shell for drug delivery purposes and the ability to attach relevant molecules to the surface without macroscopic modification of the NPs. Furthermore,

some commercially available NPs were also characterized according their size, charge, morphology and spectroscopic properties. They will appear in the following chapters as standard NPs and compared to our “in house” made Fe_3O_4 NPs that were chosen over Au NPs to continue this work.

3.9 Bibliography

(1) Brust, M.; Walker, M.; Bethell, D.; Schiffrin, D. J.; Whyman, R. *Journal of the Chemical Society, Chemical Communications* **1994**, 801.

(2) Sun, S.; Zeng, H.; Robinson, D. B.; Raoux, S.; Rice, P. M.; Wang, S. X.; Li, G. *Journal of the American Chemical Society* **2003**, *126*, 273.

(3) Li, D.; Li, C.; Wang, A.; He, Q.; Li, J. *Journal of Materials Chemistry* **2010**, *20*, 7782.

(4) Karanikolopoulos, N.; Zamurovic, M.; Pitsikalis, M.; Hadjichristidis, N. *Biomacromolecules* **2010**, *11*, 430.

(5) Yan, H.; Hou, Y.-F.; Niu, P.-F.; Zhang, K.; Shoji, T.; Tsuboi, Y.; Yao, F.-Y.; Zhao, L.-M.; Chang, J.-B. *Journal of Materials Chemistry B* **2015**, *3*, 3677.

(6) Di Corato, R.; Quarta, A.; Piacenza, P.; Ragusa, A.; Figuerola, A.; Buonsanti, R.; Cingolani, R.; Manna, L.; Pellegrino, T. *Journal of Materials Chemistry* **2008**, *18*, 1991.

(7) Lin, C.-A. J.; Sperling, R. A.; Li, J. K.; Yang, T.-Y.; Li, P.-Y.; Zanella, M.; Chang, W. H.; Parak, W. J. *Small* **2008**, *4*, 334.

(8) Pellegrino, T.; Manna, L.; Kudera, S.; Liedl, T.; Koktysh, D.; Rogach, A. L.; Keller, S.; Rädler, J.; Natile, G.; Parak, W. J. *Nano Letters* **2004**, *4*, 703.

(9) Shtykova, E. V.; Huang, X.; Gao, X.; Dyke, J. C.; Schmucker, A. L.; Dragnea, B.; Remmes, N.; Baxter, D. V.; Stein, B.; Konarev, P. V.; Svergun, D. I.; Bronstein, L. M. *The Journal of Physical Chemistry. C, Nanomaterials and Interfaces* **2008**, *112*, 16809.

(10) Liu, F.-K. *ISRN Chromatography* **2012**, *2012*, 7.

(11) Sun, X.; Rossin, R.; Turner, J. L.; Becker, M. L.; Joralemon, M. J.; Welch, M. J.; Wooley, K. L. *Biomacromolecules* **2005**, *6*, 2541.

(12) Munkholm, C.; Parkinson, D. R.; Walt, D. R. *Journal of the American Chemical Society* **1990**, *112*, 2608.

(13) Topel, S. D.; Topel, Ö.; Bostancıoğlu, R. B.; Koparal, A. T. *Colloids and Surfaces B: Biointerfaces* **2015**, *128*, 245.

(14) Shen, Y.; Jin, E.; Zhang, B.; Murphy, C. J.; Sui, M.; Zhao, J.; Wang, J.; Tang, J.; Fan, M.; Van Kirk, E.; Murdoch, W. J. *Journal of the American Chemical Society* **2010**, *132*, 4259.

(15) He, W.; Lv, Y.; Zhao, Y.; Xu, C.; Jin, Z.; Qin, C.; Yin, L. *International Journal of Pharmaceutics* **2015**, *484*, 163.

(16) Liu, L.; Zhang, J.; Wu, C.; Zhao, H. *Macromolecular Rapid Communications* **2008**, *29*, 45.

(17) Yeniceli, D.; Dogrukol-Ak, D.; Tuncel, M. *Journal of Pharmaceutical and Biomedical Analysis* **2006**, *40*, 197.

(18) Pavia, D. L. L., G.M.; Kriz, G.S. *Introduction to Spectroscopy*; Third ed.; Harcourt College Publishers: Fort Worth, **2001**.

(19) Katritzky, A. R. R., C.A.; Joule, J.A.; Zhdankin V.V. *Handbook of Heterocyclic Chemistry*; Third ed.; Elsevier Ltd.: Oxford, **2010**.

(20) Liu, H.-Q.; Jiang, F.-C. *Guang Pu Xue Yu Guang Pu Fen Xi* **2007**, *27*, 2243.

(21) Andersen, M. P. S.; Hurley, M. D.; Ball, J. C.; Schneider, W. F.; Wallington, T. J.; Nielsen, O. J. *International Journal of Chemical Kinetics* **2003**, *35*, 159.

(22) Zauner, W.; Farrow, N. A.; Haines, A. M. R. *Journal of Controlled Release* **2001**, *71*, 39.

(23) Yin Win, K.; Feng, S.-S. *Biomaterials* **2005**, *26*, 2713.

(24) Fiorentino, I.; Gualtieri, R.; Barbato, V.; Mollo, V.; Braun, S.; Angrisani, A.; Turano, M.; Furia, M.; Netti, P. A.; Guarnieri, D.; Fusco, S.; Talevi, R. *Experimental Cell Research* **2015**, *330*, 240.

(25) Loos, C.; Syrovets, T.; Musyanovych, A.; Mailänder, V.; Landfester, K.; Nienhaus, G. U.; Simmet, T. *Beilstein Journal of Nanotechnology* **2014**, *5*, 2403.

(26) Shirshahi, V.; Soltani, M. *Contrast Media & Molecular Imaging* **2015**, *10*, 1.

(27) Filipe, V.; Hawe, A.; Jiskoot, W. *Pharmaceutical Research* **2010**, *27*, 796.

(28) Tiwari, A.; Mishra, A. K.; Kobayashi, H.; Turner, A. P. F. *Intelligent Nanomaterials*; Wiley, **2012**, *54*, 74.

Chapter 4. Isolation of protein corona complexes from blood serum

4.1 Introduction

Nanotechnologies are applied in many fields and it is fundamental to understand the potential impact of ENMs on human health. The characterization of NPs in relevant biological fluids is an important issue as NPs in biological fluids spontaneously adsorb proteins on their surface forming a PC.[1,2]

NP physical–chemical properties and size, medium composition and incubation time have been found to affect PC composition.[3-5] PCs have been shown to be dynamic structures composed of outer layers of proteins or soft corona (SC) that can exchange with the surrounding environment and an inner layer or hard corona (HC) strongly bound and stable if the experimental conditions are kept constant.[2,6-9] The HC is believed to provide the ultimate biological identity to the NP and determine the interactions with the surrounding biological material, while the impact of the SC is still debated. [10,11]

In this scenario, isolation and recovery of HC complexes are critical for studying their composition and relating it to possible biological responses. The main concern in this regard is to keep the HC as similar as possible to the *in situ* conditions. The most used approach to separate PC complexes from the excess of fluid is based on consecutive cycles of centrifugation/washing optimized according to NP and media properties.[12,13] Generally, this strategy is appropriate for most NPs and gives reliable results, but the equilibrium of the system can be altered by the presence of several steps and the PC can change during this process due to the different time-scales characterizing its dynamic nature.[14] Furthermore, NPs characterized by small diameters (about 5-20 nm) and/or low densities (close to 1 g/cm^3) may not be well-separated from loosely bound proteins. To overcome those limitations, high speeds and long times of centrifugation are often necessary with the promotion of extensive aggregation with respect to *in situ*. These effects are emphasized in the isolation of HC complexes for NPs that do not form rich coronas (for example pegylated NPs).

PC complexes exist simultaneously as monomers, dimers, trimers, etc. for which the actual composition is unknown. It is likely that those complexes have different biological activity being characterized by dissimilar sizes and proteins composition. Several techniques have

been used to achieve separation of *in situ* co-existing complexes: differential sedimentation centrifugation (DCS) permitted the analytical separation of different populations of HC complexes for different NPs and demonstrated that they were representative of those *in situ*. Other techniques are size-exclusion chromatography, magnetic separation through the use of magnetic columns MACS able to separate PC complexes of magnetic NPs,[15] and field-flow-field fractionation.[16,17] However, these techniques do not allow the recovery of the different populations of PC complexes for further studies.[2,18]

Density-gradient ultracentrifugation (UC) has been used to purify NPs from free coating agents[19] and to improve NPs size distributions.[20,21] Moreover, Docter, Tenzer and co-workers[22,23] and Werwie and co-workers[24] used a sucrose cushion as first step to remove unbound proteins followed by centrifugal washings to obtain HC complexes. However, also this approach involves a number of steps with the risk of altering the PC in terms of composition and structure.

In this chapter, a one-step procedure able to isolate and recover PC complexes from the biological environment with a less invasive effect on the structure of the PC NPs has been developed. In particular, sucrose-gradient UC was used to gently separate HC complexes from the excess of physiological fluids. In this case foetal calf serum (FBS) was chosen as model fluid. NPs of different size, material and surface coating were tested. The PC complexes isolated by conventional centrifugation methods and UC were analysed by size through Nanoparticle Tracking Analysis (NTA) and Dynamic Light Scattering (DLS). PC composition was investigated by SDS-PAGE. Finally, the effect of the two methodologies on the interactions between PC complexes and surrounding environment was investigated. PC complexes of magnetite NPs recovered from serum by both UC and conventional centrifugation methods were incubated on cells in serum free conditions to compare their NPs cellular uptake. Some of the results presented in this chapter are included in the work in the appendix.[25]

4.2 Overview of the methodology

In Fig. 4.1 a scheme, outlining the approach followed for this study, is presented. NPs were incubated in FBS for one hour at 37°C. Before progressing with the purification from unbound proteins, size was measured by DLS and NTA. One aliquot was subjected to sucrose-gradient UC according to the experimental protocols (sucrose gradient concentration, time and speed of centrifugation) described in paragraph *2.3.4.2*. Sucrose-

gradient concentration, time and speed of centrifugation are parameters that need to be adjusted according to the NP features. The same NPs incubated in serum were also isolated by the conventional methodology based on three centrifugations at 15500 rcf at 4ºC and re-suspension of the pellet in 500µl PBS pH 7.4. Recovered NPs were again characterized by size and Zp. PC complexes isolated by UC were first dialysed at 4°C overnight to remove sucrose and disperse them in PBS. SDS-PAGE was used to elucidate the corona composition. PC complexes isolated by standard centrifugation will be named from now "HC" while those isolated by sucrose gradient ultracentrifugation "UCx" ("x" indicates a number relative to the band position in the sucrose gradient, ascendant from zones from lower to higher densities).

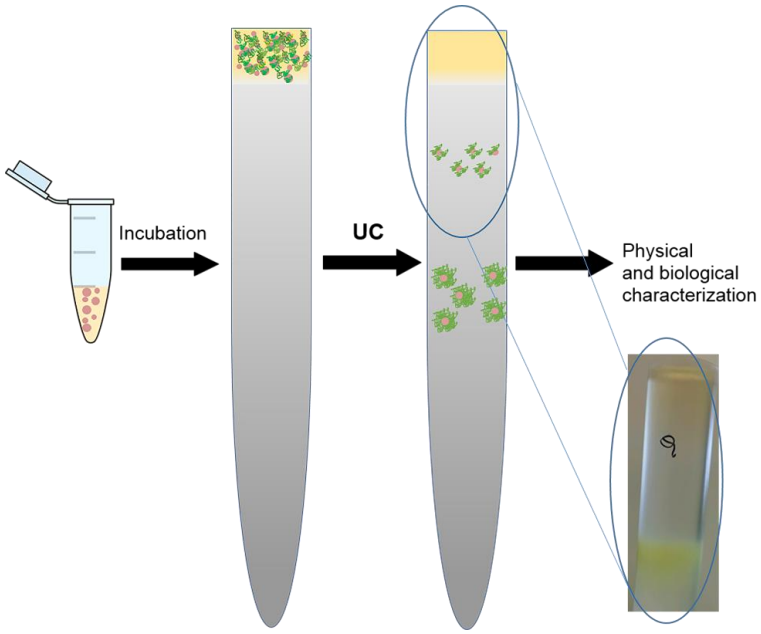

Figure 4.1 Scheme of the methodology to isolate and study HC NPs. NPs were incubated in biological fluid and then subjected to sucrose gradient UC. In the image of the vial on the far left pink dots are NPs and the yellow background is the biological medium. In the images of the UC tubes (middle images), green dots represent some proteins that form diverse coronas around the NPs and are separated by UC exploiting density differences.

4.3 Polystyrene NPs

4.3.1 Polystyrene NPs functionalized with carboxylic groups

PSCOOH NPs of a nominal size of 100 nm (PSCOOH100) were used to validate the UC procedure because PC complexes formed by polystyrene NPs have extensively been characterized in the literature.[3,26] PS-COOH100 NPs *in situ* in 55% and 90% FBS were shown to form rather monodispersed PC complexes with a hydrodynamic diameter of about 130 nm (Table 4.1). The isolation of such complexes by normal centrifugation at both FBS concentrations promoted limited aggregation leading to the formation of HC NPs with

hydrodynamic diameters of about 170 nm and characterized by higher PdI.

UC procedure allowed the recovery of two main bands for both FBS concentrations and the sizes of the recovered PC NPs differed between them about less than 10%. For example, PC complexes originated in 90% FBS differed by only of 7% in size (122 nm and 131 nm). Moreover, the isolated complexes were very similar in size to the *in situ* NPs. This indicated that with this procedure it was possible to separate in an one-step process HC complexes with a structure similar to those *in situ* and a high resolution in separation by size. In addition, the fully recovered NPs were analysed by SDS-PAGE and the composition of the PC was almost identical among the same sample and the two FBS concentrations (see Fig. 4.2a).

Table 4.1 DLS and NTA characterization of PS-COOH100 NPs in PBS, 55-90% FBS and of HC complexes isolated by centrifugation (HC) and ultracentrifugation (UC 1-2). The concentration of the sucrose gradient was 5-30% w/w: at 55% FBS, UC1 and UC2 corresponded to sucrose concentrations of 13% and 21% w/w respectively; at 90% FBS, UC1 and UC2 corresponded to sucrose concentrations of 13% and 21% w/w respectively.

	d_H [nm][1]	SD [nm][2]	d_H [nm][3]	PdI[4]	NPs/ml
PS-COOH[5]	78±3	29±2	100.8±0.7	0.01	$7x10^{12}$
PS-COOH 55% *in situ*	126±3	38±2	130.2±1.8	0.05	$3x10^{12}$
PS-COOH 55% HC	193±6	61±4	177.1±4.9	0.25	$8x10^{11}$
PS-COOH 55% UC1	115±4	33±2	122.3±1.4	0.03	$1x10^{12}$
PS-COOH 55% UC2	131±8	36±1	135.7±0.8	0.15	$1x10^{12}$
PS-COOH 90% *in situ*	130±1	31±1	128.1±0.9	0.03	$3x10^{12}$
PS-COOH 90% HC	154±3	52±7	168.0±0.9	0.26	$7x10^{12}$
PS-COOH 90% UC1	117±1	34±1	122.2±1.7	0.01	$5x10^{10}$
PS-COOH 90% UC2	126±2	35±1	131.4±1.6	0.01	$1x10^{12}$

[1] Hydrodynamic diameter (d_H) was calculated avaraging the hydrodynamic diameters of all NPs tracked in a particle-by-particle modality by NTA.
[2] SD is the standard deviation on all the hydrodynamic diameters measured in a particle-by-particle modality by NTA.
[3]Hydrodynamic diameter (d_H) obtained by DLS from the cumulant analysis of the auto-correlation data.
[4] Polydispertity indexes (PdI) were obtained by DLS from the cumulant analisys of the auto-correlation data.
All data were presented as the avarage of three indipendent measurements with relative standard deviation.
[5]in PBS pH 7.4

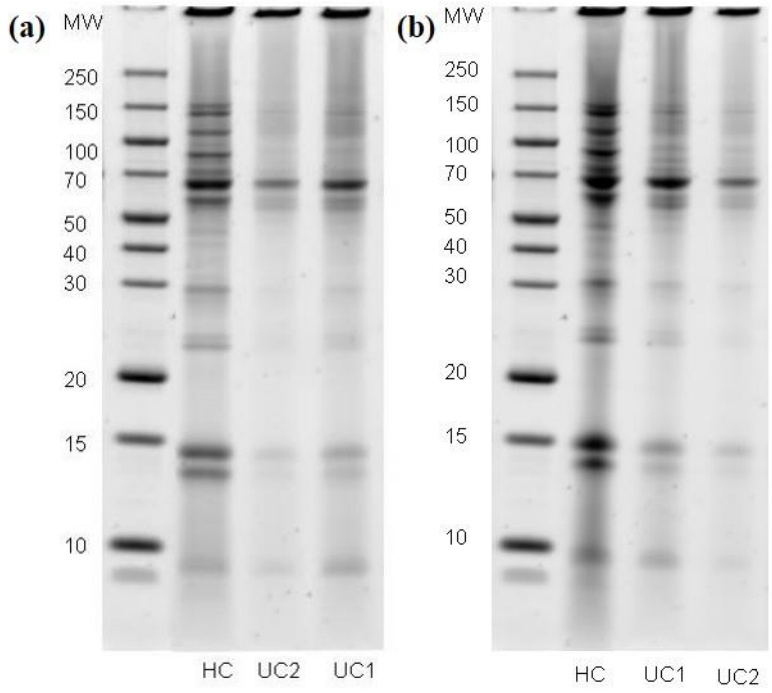

Figure 4.2 HC complexes of PS-COOH100**.** SDS-PAGE gel of the HC complexes of PS-COOH100 NPs in 90% (a) and 55% (b) FBS, isolated by conventional centrifugation methods (hard corona, HC) and sucrose ultracentrifugation (UC) respectively, as indicated by the label below the tracks of the gel. The concentration of the sucrose gradient was 5-30% w/w: at 55% FBS, UC1 and UC2 corresponded to sucrose concentrations of 13% and 21% w/w respectively; at 90% FBS, UC1 and UC2 corresponded to sucrose concentrations of 13% and 21% w/w respectively.

Smaller NPs such as 20 nm PSCOOH NPs exhibited a lower tendency than 100 nm carboxylated NPs to pellet by centrifugation as it is shown in Fig. 4.3, where fluorescence emissions of the supernatant solutions after centrifugation are reported for the three polymeric NPs. The loss of material is higher for the 20 nm PSCOOH, for which 50% of material is lost during the first centrifugation. An increase of time and speed of centrifugation for enhancing sedimentation of the HC complexes did not work effectively, especially for the NPs incubated in 90% FBS. These NPs showed extensive aggregation and loss of material as indicated by the hydrodynamic diameter of about 250 nm with PdI over 0.5 (Table 4.2). In fact, incubation of these NPs in 90% FBS caused the formation of aggregates with an averaged hydrodynamic diameter of 65 nm *in situ* compared to 30 nm of the bare NPs in PBS. Clearly, centrifugation promoted aggregation of these PC NPs.

The use of UC allowed us not only to avoid this aggregation, but also to separate the different populations of complexes. In particular, the presence of a small population of large aggregates of about 240 nm was highlighted. This population was mainly formed by proteins, as indicated by the low density of the sucrose layer (UC1, sucrose concentration of 8% w/w) where they accumulated compared to that of UC2 and UC3 (sucrose concentration

of 20% and 36 w/w, respectively), containing most of the PC complexes. This was also confirmed by the concentrations revealed by NTA analysis for NPs in UC2 and UC3 sucrose layers, which was comparable to that of the NPs *in situ*. Moreover, the hydrodynamic sizes of the complexes recovered from UC2 and UC3 layers were comparable to those of the *in situ* samples and characterised by a lower PdI related to the separation from the larger protein aggregates as shown in Fig. 4.4a. The lower sizes detected by NTA for the HC and UC1 samples confirmed the presence of big protein aggregates in these samples, whose lower sizes were likely due to a partial disaggregation by dilution (required for measuring NTA). SDS-PAGE analysis of those samples, reported in Fig. 4.4b, showed that fractions UC2 and UC3 were very similar in protein composition, while UC1 was enriched with proteins of Mw=60-70 kDa and 150 kDa (possibly BSA and IgG). When the NPs were incubated with a lower concentration of FBS (55% v/v), only one UC fraction was isolated containing PC NPs similar in size to those present *in situ* (Table 4.2) at a sucrose concentration of 28% w/w. For this sample, significant differences in the PC composition (mostly in high Mw proteins) between PC NPs isolated by HC and UC were detected (Fig. 4.4c).

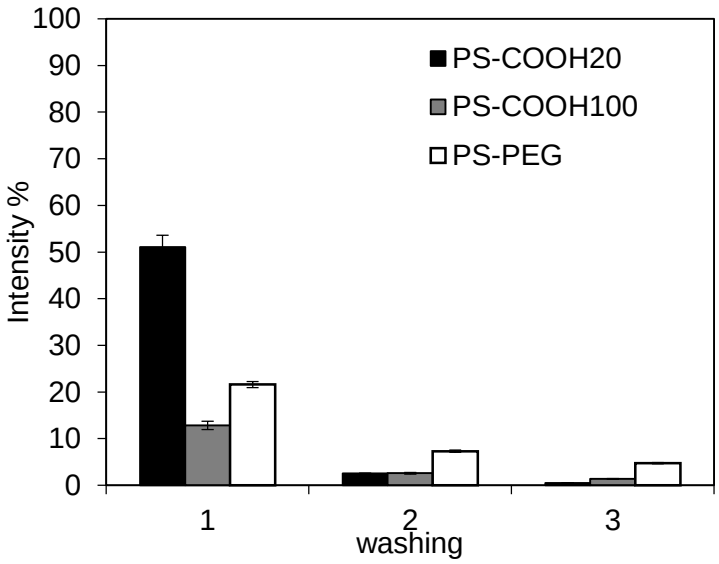

Figure 4.3 Fluorescence intensity emissions of the supernatant solutions compared to that of the initial stock solutions when centrifugal washings are performed on *in situ* samples of PS NPs incubated in 90% FBS. The excitation and emission wavelengths were 490 nm and 515 nm, respectively.

Table 4.2 DLS and NTA characterization of PS-COOH20 NPs in PBS, 55-90% FBS and of HC complexes isolated by centrifugation (HC) and ultracentrifugation (UC 1-2-3). The concentration of the sucrose gradient was 4-40% w/w: at 55% FBS, UC corresponded to sucrose concentrations of 28% w/w; at 90% FBS, UC1, UC2 and UC3 corresponded to sucrose concentrations of 8%, 20% and 36% w/w respectively.

	d_H [nm][1]	SD [nm][2]	d_H [nm][3]	PdI[4]	NPs/ml
PS-COOH20 [5]	64±21	28±5	32.5±0.1	0.10	$3x10^{12}$
PS-COOH20 55% *in situ*	83±2	44±3	67.6±1.2	0.31	$5x10^{12}$
PS-COOH20 55% HC	142±8	57±3	135.8±2.1	0.34	$1x10^{10}$
PS-COOH20 55% UC	78±1	38±1	83.6±0.8	0.16	$3x10^{12}$
PS-COOH20 90% in *situ*	81±3	38±6	67.6±0.7	0.31	$8x10^{12}$
PS-COOH20 90% HC	186±18	66±6	247.3±7.6	0.65	$6x10^{11}$
PS-COOH20 90% UC1	86±5	59±4	259.5±4.6	0.43	$7x10^{11}$
PS-COOH20 90% UC2	58±1	26±1	68.2±.1.9	0.16	$1x10^{13}$
PS-COOH20 90% UC3	73±3	35±3	91.1±1.9	0.18	$9x10^{12}$

[1] Hydrodynamic diameter (d_H) was calculated avaraging the hydrodynamic diameters of all NPs tracked in a particle-by-particle modality by NTA.
[2] SD is the standard deviation on all the hydrodynamic diameters measured in a particle-by-particle modality by NTA.
[3]Hydrodynamic diameter (d_H) obtained by DLS from the cumulant analysis of the auto-correlation data.
[4] Polydispertity indexes (PdI) were obtained by DLS from the cumulant analisys of the auto-correlation data.
All data were presented as the avarage of three indipendent measurements with relative standard deviation.
[5]in PBS pH 7.4

4.3.2 Polystyrene NPs functionalized with pegylated groups

Conventional centrifugation methods are not very effective in isolating HC complexes for NPs with lower affinity for binding proteins, *e.g.* pegylated NPs. When this low affinity is coupled with the low density of the NPs, it can be even more challenging to isolate representative PC NPs for investigating their properties in further experiments.

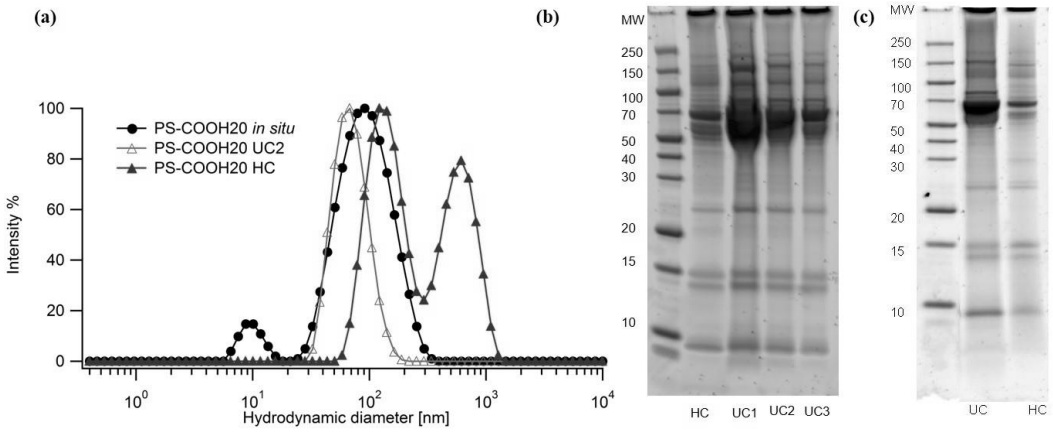

Figure 4.4 HC complexes of PS-COOH20. a) Intensity averaged size distribution of 20 nm PS NPs in situ in 90% FBS (dots), relative HC complexes isolated by centrifugation (HC, full triangles) and ultracentrifugation (UC2, empty triangles). B-C) SDS-PAGE gel of the complexes in 90% and 55% FBS, respectively, isolated by conventional centrifugation methods (hard corona, HC) and ultracentrifuge (UC1-2-3) as indicated by the label below the tracks of the gel. The concentration of the sucrose gradient was 4-40% w/w: at 55% FBS, UC corresponded to sucrose concentrations of 28% w/w; at 90% FBS, UC1, UC2 and UC3 corresponded to sucrose concentrations of 8%, 20% and 36% w/w respectively.

UC was used to separate liposomes by size[27] and recently Pozzi and co-workers[28] showed that liposome pegylation could be exploited to reduce protein adsorption, limiting macrophages uptake, and to enrich the residual corona with apolipoproteins that bind specifically some receptors of prostate cancer cells. Pegylated polystyrene NPs (100 nm size) were incubated in 55% and 90% FBS and characterized by DLS and NTA (Table 4.3).

Their dynamic properties did not change significantly with respect to those in PBS indicating a weak interaction with the environmental proteins and no significant changes in the structure of the bare NPs, although protein adsorption could not be completely ruled out. HC complexes isolated by centrifugation were aggregated with respect to those *in situ* and some loss of material occurred (Table 4.3). A well-defined single sucrose band enriched in NPs was isolated by UC at a sucrose concentration of 15% w/w. The recovered NPs were analysed by DLS and NTA and results were very similar to those *in situ*. DLS, unlike NTA, showed an increase in diameter and PdI with respect to *in situ* sample (Fig. 4.3a) and a slight loss of NPs likely due to the very similar density to the proteins. The corona composition of the complexes isolated through the two methods was compared by SDS-PAGE (see Fig. 4.5b and 4.5c) and some differences could be seen for high molecular weight proteins indicating that aggregation and loss of material can ultimately affect the properties of the HC. Thus, UC was shown to be a promising method for recovering HC complexes of pegylated nanomaterials and it allows their further characterization and biological response.

Table 4.3 DLS and NTA characterization of PS-PEG NPs in PBS, 55% and 90% FBS and of HC complexes isolated by centrifugation (HC) and ultracentrifugation (UC). The concentration of the sucrose gradient was 3-30% w/w: both at 55% and 90% FBS, UC corresponded to sucrose concentration of 15% w/w.

	d_H [nm][1]	SD [nm][2]	d_H [nm][3]	PdI[4]	NPs/ml
PS-PEG[5]	125±1	38±1	106.3±0.7	0.04	$3x10^{12}$
PS-PEG 55% *in situ*	148±3	48±5	103.4±0.6	0.10	$3x10^{12}$
PS-PEG 55% HC	167±2	52±7	149.4±1.4	0.31	$7x10^{11}$
PS-PEG 55% UC	129±2	42±2	133.2±1.5	0.18	$2x10^{12}$
PS-PEG 90% *in situ*	136±1	42±2	105.9±0.5	0.10	$4x10^{11}$
PS-PEG 90% HC	123±10	36±8	155.7±2.5	0.22	$1x10^{11}$
PS-PEG 90% UC	118±6	34±1	137.1±0.1	0.22	$7x10^{10}$

[1] Hydrodynamic diameter (d_H) was calculated avaraging the hydrodynamic diameters of all NPs tracked in a particle-by-particle modality by NTA.
[2] SD is the standard deviation on all the hydrodynamic diameters measured in a particle-by-particle modality by NTA.
[3]Hydrodynamic diameter (d_H) obtained by DLS from the cumulant analysis of the auto-correlation data.
[4] Polydispertity indexes (PdI) were obtained by DLS from the cumulant analisys of the auto-correlation data.
All data were presented as the avarage of three indipendent measurements with relative standard deviation.
[5]in PBS pH 7.4

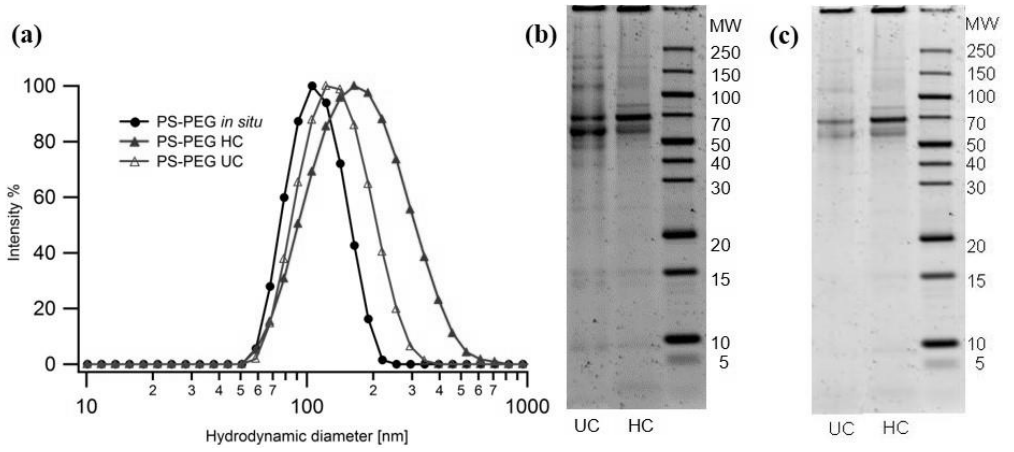

Figure 4.5 HC complexes of PS-PEG. a) Size distribution by intensity percentage of PS-PEG NPs in situ in 90% FBS (dots), HC complexes isolated by centrifugation (HC, full triangles) and ultracentrifugation (UC, empty triangles). B-C) SDS-PAGE gel of the HC complexes of PS-PEG NPs in 90% an 55% FBS respectively, isolated by ultracentrifugation (UC) and conventional centrifugation methods (HC), as indicated by the label below the tracks of the gel. The concentration of the sucrose gradient was 3-30% w/w: both at 55% and 90% FBS, UC corresponded to sucrose concentration of 15% w/w.

4.4 Silica NPs

In the literature it has been reported that PCs of SiO_2 NPs (diameter of 50 nm) strongly depends on the proteins concentration in the biological fluids.[18] They tend to form larger aggregates (dimer, trimer, etc.) at low proteins concentrations (< 20%), while higher proteins concentrations seem to stabilize smaller and more monodispersed complexes. For this reason, two concentrations of proteins were compared in this study: 10% FBS (proteins concentration 0.0036 g/ml) and 90% FBS (proteins concentration 0.032 g/ml).

For the lower proteins concentration, conventional centrifugation induced extensive aggregation as shown in Table 4.4, furthermore it was impossible to separate PC complexes simultaneously present *in situ*. In fact, DLS of the *in situ* NPs showed a broad distribution with an average diameter size of 140 nm, while complexes isolated by conventional centrifugation were bigger (over 200 nm). In contrast, UC resulted in successful separation and recovery of two equivalent fractions (in terms of number of NPs) of NP-proteins complexes. They were characterized by hydrodynamic diameters of 110 and 180 nm, respectively localized in bands at sucrose concentration of 15-18% and 21-24% w/w. SDS-PAGE showed a slight different pattern of proteins for the two fractions highlighting the different nature of these complexes that might interact differently with the biological matter (Fig. 4.6a). For the sample incubated in 90% FBS, HC and UC samples showed a very similar protein composition but DLS and NTA results indicated that PC-NPs complexes isolated by UC retained a structure more representative of that *in situ*. Size distributions obtained both by NTA and DLS are narrow and similar for *in situ* and HC complexes isolated by UC (about 100 nm), while HC complexes isolated by centrifugation are bigger (80% size increase) and more polydispersed. The possibility of isolating complexes without altering their physical properties is clearly important for studying their biological response in more detail.

4.5 Polymer coated magnetite NPs

4.5.1 Fe_3O_4

The possibility of isolating PC complexes without altering their physical properties is clearly important for studying their biological response in more detail. Fe_3O_4 NPs coated by PMAO polymer incubated in 55% FBS showed a high tendency to agglomerate. Larger NPs-proteins complexes were observed *in situ* by DLS together with the proteins background (peak at 10-15 nm) as illustrated by the size distribution reported in Fig. 4.7a. HC samples showed extensive aggregation and the pellet obtained by centrifugation was difficult to dissolve.

Table 4.4 DLS and NTA characterization of silica NPs in 10% and 90% FBS. The concentration of the sucrose gradient was 3-30% w/w: at 10% FBS UC1 and UC2 corresponded to sucrose concentrations of 15-18% and 21-24% w/w; at 90% FBS one single band at 12% w/w of sucrose concentration was isolated.

	d_H [nm][1]	SD [nm][2]	d_H [nm][3]	PdI[4]	NPs/ml
SiO_2[5]	37±4	18±4	46.7±0.5	0.02	$6x10^{12}$
SiO_2 10% *in situ*	211±13	65±8	141.5±0.2	0.19	$1x10^{13}$
SiO_2 10% HC	157±2	73±1	291.0±3.9	0.36	$1x10^{11}$
SiO_2 10% UC1	98±3	43±8	123.5±1.7	0.23	$3x10^{10}$
SiO_2 10% UC2	153±21	41±9	179.1±0.9	0.30	$4x10^{10}$
SiO_2 90% *in situ*	108±5	36±4	81.1±0.3	0.20	$1x10^{13}$
SiO_2 90% HC	174±13	75±15	129.7±4.4	0.27	$1x10^{12}$
SiO_2 90% UC	101±4	38±1	80.2±1.1	0.22	$9x10^{10}$

[1] Hydrodynamic diameter (d_H) was calculated avaraging the hydrodynamic diameters of all NPs tracked in a particle-by-particle modality by NTA.
[2] SD is the standard deviation on all the hydrodynamic diameters measured in a particle-by-particle modality by NTA.
[3]Hydrodynamic diameter (d_H) obtained by DLS from the cumulant analysis of the auto-correlation data.
[4] Polydispertity indexes (PdI) were obtained by DLS from the cumulant analisys of the auto-correlation data.
All data were presented as the avarage of three indipendent measurements with relative standard deviation.
[5]in PBS pH 7.4

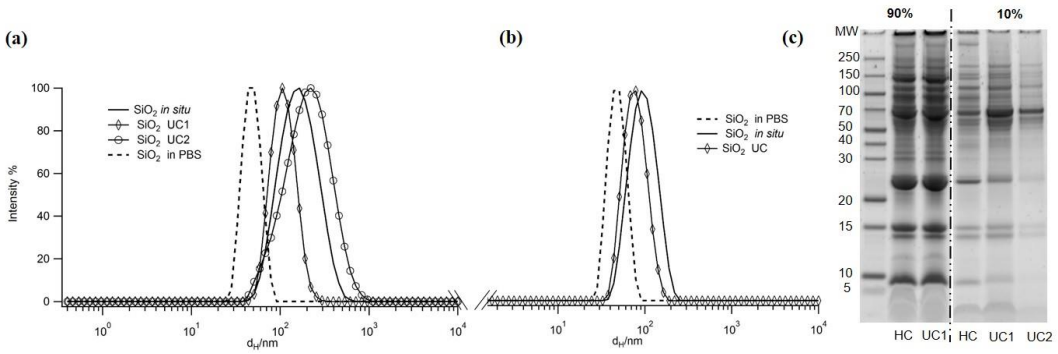

Figure 4.6 Characterization of SiO_2 NPs. In graph a) and b) are reported size distributions by intensity percentage of SiO_2 NPs in 10% and 90% FBS respectively, compared to NPs in PBS (dashed line). C) SDS-PAGE gel of the hard corona complexes of SiO_2 NPs in 10% and 90% FBS isolated by ultracentrifugation (UC) and conventional centrifugation methods (HC), respectively, as indicated by the labels below the tracks of the gel. The concentration of the sucrose gradient was 3-30% w/w: At 10% FBS UC1 and UC2 corresponded to sucrose concentrations of 15-18% and 21-24% w/w; at 90% FBS one single band at 12% w/w of sucrose concentration was isolated.

In contrast, UC samples were successfully isolated and recovered in two NP-protein fractions containing structures of about 77 nm and 140 nm, respectively, which seem to correspond to the species in the *in situ* sample (Table 4.5). The proteins patterns were

analysed by SDS-PAGE and they qualitatively seemed to be very similar indicating that in this case NP-proteins complexes of different diameters (monomer and dimers) were enriched with similar proteins. Fe_3O_4 NPs incubated in 90% FBS had a very similar behaviour to the NPs incubated in 55% FBS. It is confirmed by the PC pattern in Fig. 4.7b and hydrodynamic sizes analysed by DLS and NTA.

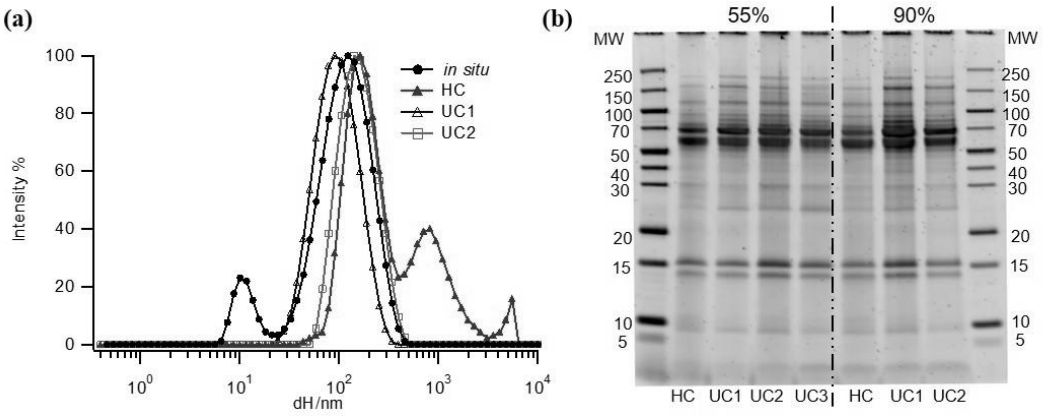

Figure 4.7 Characterization of Fe_3O_4 NPs. In graph a) are reported size distributions by intensity percentage of the NPs in 55% FBS in situ and HC complexes isolated by centrifugation (HC) and by ultracentrifuge (UC1-2). B) SDS-PAGE gel of the hard corona complexes in 55% and 90% FBS isolated by ultracentrifugation (UC) and conventional centrifugation methods (HC), respectively, as indicated by the labels below the tracks of the gel. The concentration of the sucrose gradient was 7-70% w/w: At 55% FBS UC1, UC2 and UC3 corresponded to sucrose concentrations of 35%, 56% and 63% w/w; at 90% FBS the two enriched bands were localized at 42% and 63% w/w of sucrose concentration.

4.5.2 Fe_3O_4-PEG

Pegylated Fe_3O_4 NPs were prepared by the post-purification approach as described in paragraph *2.2.5* and PC formation was studied in 55% FBS. As for pegylated PS NPs, less proteins were adsorbed on the NP surface and UC induced a slight aggregation of the PC NPs as shown by the results reported in Table 4.6 and Fig. 4.8a compared to *in situ* NPs. However, UC allowed a better separation of the PC NPs from the excess of proteins if compared to the standard centrifugation method that promoted the formation of several aggregates (large PdI value). We run SDS PAGE for these samples and we speculated that PC was mainly composed of albumin (65 kDa) and IgG (50 kDa) for the UC sample, while the one isolated by centrifugation was enriched in transferrin (75 kDa)[29] and globulins (120 kDa). Again, we showed that the procedure to isolate the HC can ultimately modify its composition.

Table 4.5 DLS and NTA characterization of Fe_3O_4 NPs in 55% and 90% FBS. The concentration of the sucrose gradient was 7-70% w/w: At 55% FBS UC1, UC2 and UC3 corresponded to sucrose concentrations of 35%, 56% and 63% w/w, UC2 and UC3 were pooled together; at 90% FBS the two enriched bands were localized at 42% and 63% w/w of sucrose concentration.

	d_H [nm][1]	SD [nm][2]	d_H [nm][3]	PdI[4]
Fe_3O_4[5]	93±7	42±12	51.4±0.3	0.17
Fe_3O_4 55% *in situ*	157±3	51±4	63.1±1.8	0.50
Fe_3O_4 55% HC	n.d.	n.d.	251.8±9.5	0.55
Fe_3O_4 55% UC1	90±1	33±1	77.4±0.2	0.26
Fe_3O_4 55% UC2	139±3	47±2	147.1±4.3	0.20
Fe_3O_4 90% *in situ*	201±12	65±5	86.3±1.2	0.48
Fe_3O_4 90% HC	n.d.	n.d.	327.6±3.8	0.45
Fe_3O_4 90% UC1	87±3	41±1	76.1±0.4	0.17
Fe_3O_4 90% UC2	136±4	38±3	153.7±3.9	0.20

[1] Hydrodynamic diameter (d_H) was calculated avaraging the hydrodynamic diameters of all NPs tracked in a particle-by-particle mode by NTA.
[2] SD is the standard deviation on all the hydrodynamic diameters measured in a particle-by-particle mode by NTA.
[3]Hydrodynamic diameter (d_H) obtained by DLS from the cumulant analysis of the auto-correlation data.
[4] Polydispertity indexes (PdI) were obtained by DLS from the cumulant analisys of the auto-correlation data.
All data were presented as the avarage of three indipendent measurements with relative standard deviation.
[5]in PBS pH 7.4

Table 4.6 DLS and NTA characterization of pegylated Fe_3O_4 NPs in 55% FBS. The concentration of the sucrose gradient was 7-70% w/w: One band enriched in PC complexes was isolated and corresponded to sucrose concentrations of 42% w/w.

	d_H [nm][1]	SD [nm][2]	d_H [nm][3]	PdI[4]	Zp[5] [mv]
Fe_3O_4-PEG[6]	136±7	50±3	59.8±0.9	0.18	-3±2
Fe_3O_4-PEG *in situ*	120±9	63±1	26.4±0.2	0.51	n.d.
Fe_3O_4-PEG HC	n.d.	n.d.	117.7±2.1	0.44	-6±1
Fe_3O_4-PEG UC	125±4	48±2	93.4±2.3	0.22	-8±1

[1] Hydrodynamic diameter (d_H) was calculated avaraging the hydrodynamic diameters of all NPs tracked in a particle-by-particle modality by NTA.
[2] SD is the standard deviation on all the diameters measured in a particle-by-particle mode by NTA.
[3]Hydrodynamic diameter (d_H) obtained by DLS from the cumulant analysis of the auto-correlation data.
[4] Polydispertity indexes (PdI) were obtained by DLS from the cumulant analisys of the auto-correlation data.
All data were presented as the avarage of three indipendent measurements with relative standard deviation.
[5]Zp was measured in 0.1mM NaCl
[6]in MQW

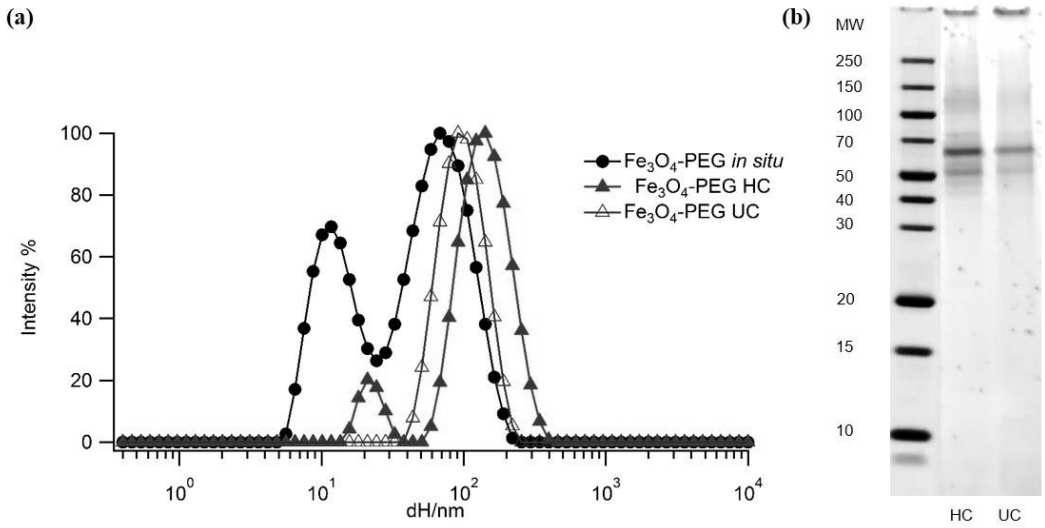

Figure 4.8 Characterization of pegylated Fe_3O_4 NPs. In graph a) are reported size distributions by intensity percentage of the NPs in 55% FBS *in situ* and HC complexes isolated by centrifugation (HC) and by ultracentrifuge (UC). B) SDS-PAGE gel of the hard corona complexes in 55% isolated by ultracentrifugation (UC) and conventional centrifugation methods (HC), respectively, as indicated by the labels below the tracks of the gel. The concentration of the sucrose gradient was 7-70% w/w: One band enriched in PC complexes was isolated and corresponded to sucrose concentrations of 42% w/w.

4.6 Effect on cell uptake of the HC complexes isolated by ultracentrifugation and centrifugation

Fe_3O_4 NPs were covalently labelled with a fluorescent dye as described in paragraph *2.2.6* following the second approach based of EDAC coupling. SDS-PAGE of the isolated PC complexes by UC and standard centrifugation demonstrated the low impact of the labelling on the corona composition. Comparing the SDS PAGE gels reported in Fig. 4.9 and Fig. 4.7b, proteins patterns in 55% FBS are very similar. While the PC has already been shown to affect cells uptake,[3,18,30] we investigated the uptake of the HC NPs isolated by UC and standard centrifugation. Cells were stained for actin filaments and nuclei. In Fig. 4.10 representative images of cells incubated for two hours with PC samples in serum-free conditions are reported. A different fluorescent pattern between PC NPs isolated by conventional centrifugation methods (Fig. 4.10a) and those obtained by UC (Fig. 4.10b and 4.10c) can be observed. In fact, the images show that samples treated with HC NPs are characterized by large fluorescent aggregates hardly taken up by the cells, while those treated with the PC complexes from UC fractions are more monodispersed in size and showed a much higher cell uptake. No significant differences were observed in NPs cell uptake from the two UC fractions indicating that, in this case, differently structured PC complexes are "seen" similarly by the cells. This is also in agreement with the PC patterns observed in the SDS-PAGE (see Fig. 4.9). Uptake experiments using different times of

incubation, 4 hours and 24 hours, did show increased aggregation in all samples, included UC1 and UC2 NPs, especially after 24 hours. Nevertheless, uptake is still higher for UC1 and UC2 NPs than for HC NPs, which mainly accumulated on the outside of the membrane (Fig 4.11, HC 4h and HC 24h).

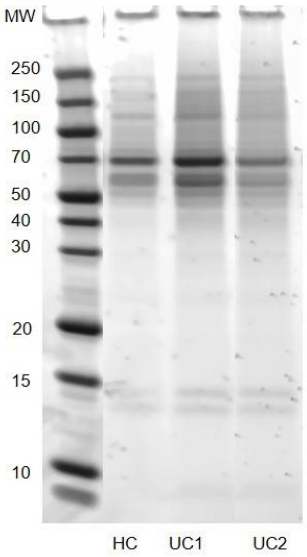

Figure 4.9 SDS-PAGE gel of the hard corona complexes in 55% formed by fluorescently labelled Fe_3O_4 NPs isolated by ultracentrifugation (UC) and conventional centrifugation methods (HC), respectively, as indicated by the labels below the tracks of the gel. The concentration of the sucrose gradient was 7-70% w/w: Two bands enriched in PC complexes, UC1 and UC2, were isolated and corresponded to sucrose concentrations of 35% and 56-63% w/w.

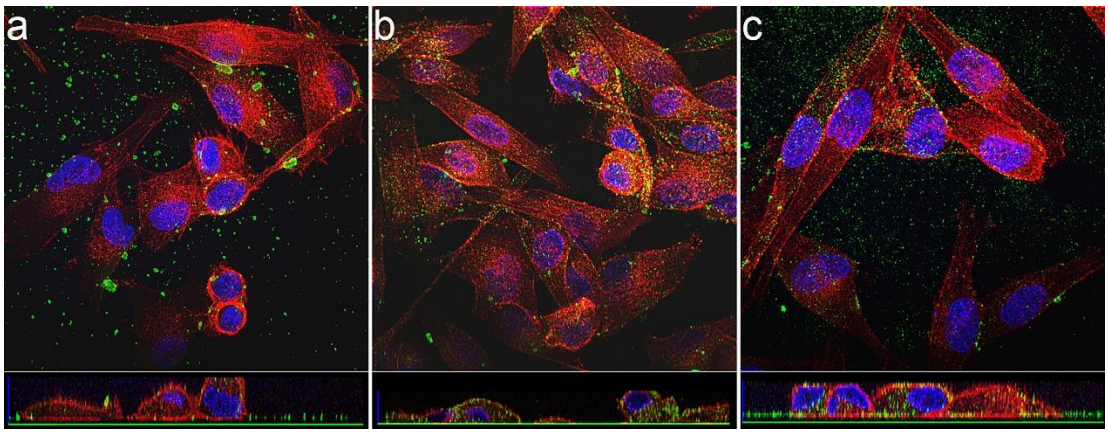

Figure 4.10 Fe_3O_4 PC uptake. Confocal images of M202 cells after 2 hours of incubation with Fe_3O_4 PC complexes (10^{12} NPs/ml) isolated a)by centrifugation (HC), and (b) and (c) by ultracentrifugation. Actin filaments were stained by Texas Red®-X Phalloidin (red channel), nuclei by Hoechst33342 (blue channel) and NPs by BODIPY FL EDA (green channel).

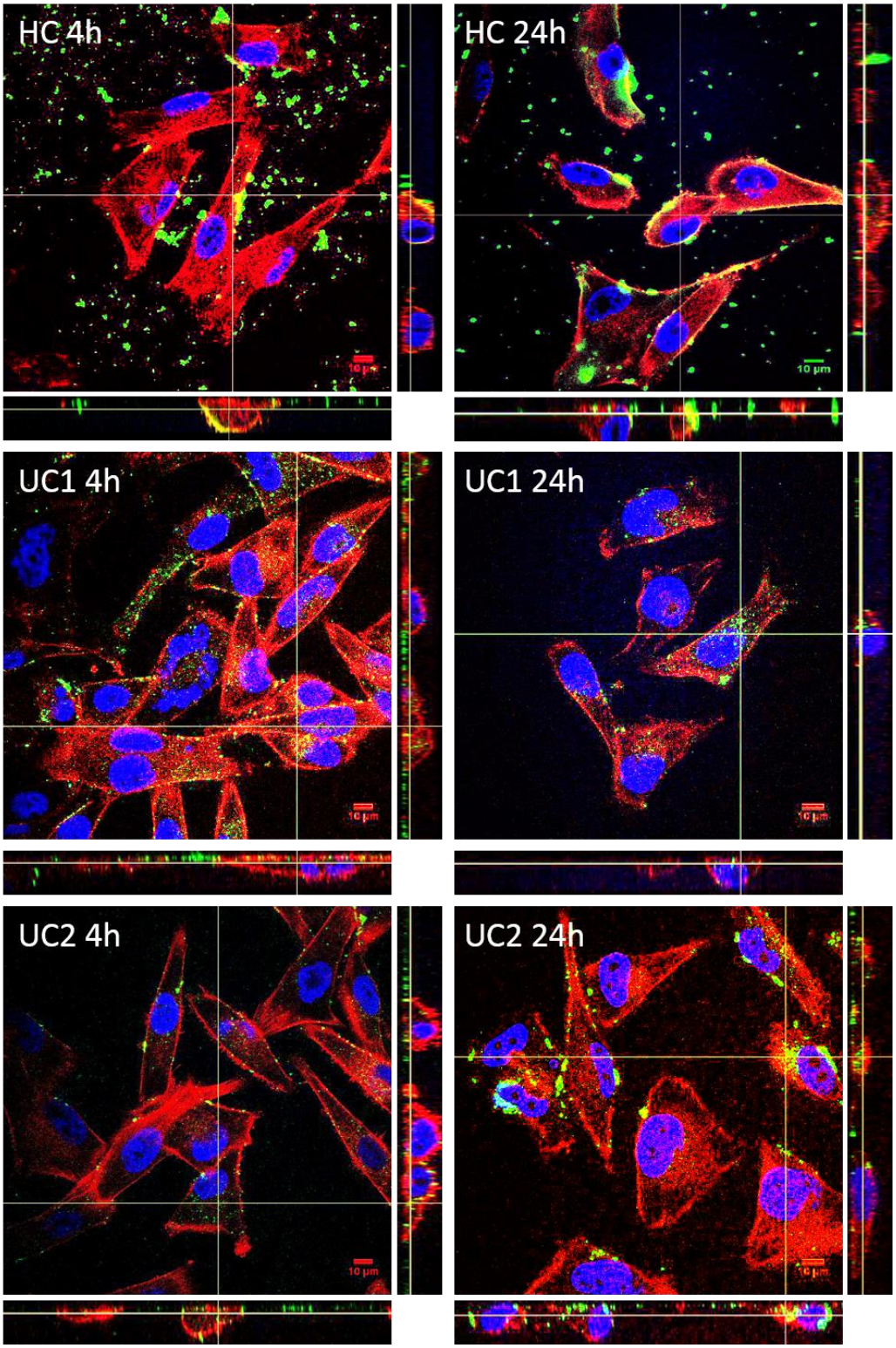

Figure 4.11 Fe_3O_4 PC uptake. Confocal images of M202 cells after 4 hours and 24 hours of incubation with Fe_3O_4 PC complexes (10^{12} NPs/ml) isolated a)by centrifugation (HC), and (b) and (c) by ultracentrifugation. Actin filaments were stained by Texas Red®-X Phalloidin (red channel), nuclei by Hoechst33342 (blue channel) and NPs by BODIPY FL EDA (green channel).

4.7 Conclusions

In this chapter, we have demonstrated that sucrose gradient UC is an effective technique to isolate PC complexes from biological media without affecting their structure and composition with respect to those *in situ*. We showed that this approach could be applied to a wide range of NPs by simply tuning the experimental conditions (sucrose-gradient concentration, centrifugation rate, time). Moreover, it proved to be a less invasive method than the conventional one, keeping the structure and composition intact while limiting aggregation of the PC complexes. The methodology has higher resolution in terms of size separation compared to conventional approaches allowing the fine isolation of PC complexes simultaneously present in the biological environment. NPs characterized by low density were fully recovered from the environment, and the structure of the resulting NPs–proteins complexes was more representative of that *in situ*.

Isolated PC complexes were incubated with cells and those recovered by the UC methodology showed less aggregation and a higher uptake with respect to those recovered by conventional methods. The ability to isolate and recover different NPs–proteins complexes from complex biological media in a stable form with such a high size resolution may have a significant impact on the interpretation of the role of the protein corona in the interaction with cellular mechanisms. However, the biological relevance of these different complexes remains to be investigated.

4.8 Bibliography

(1) Cedervall, T.; Lynch, I.; Lindman, S.; Berggård, T.; Thulin, E.; Nilsson, H.; Dawson, K. A.; Linse, S. *Proceedings of the National Academy of Sciences* **2007**, *104*, 2050.

(2) Walczyk, D.; Bombelli, F. B.; Monopoli, M. P.; Lynch, I.; Dawson, K. A. *Journal of the American Chemical Society* **2010**, *132*, 5761.

(3) Lundqvist, M.; Stigler, J.; Elia, G.; Lynch, I.; Cedervall, T.; Dawson, K. A. *Proceedings of the National Academy of Sciences* **2008**, *105*, 14265.

(4) Casals, E.; Pfaller, T.; Duschl, A.; Oostingh, G. J.; Puntes, V. *ACS Nano* **2010**, *4*, 3623.

(5) Kreyling, W. G.; Fertsch-Gapp, S.; Schäffler, M.; Johnston, B. D.; Haberl, N.; Pfeiffer, C.; Diendorf, J.; Schleh, C.; Hirn, S.; Semmler-Behnke, M.; Epple, M.; Parak, W. J. *Beilstein Journal of Nanotechnology* **2014**, *5*, 1699.

(6) Lynch, I.; Dawson, K. A. *Nano Today* **2008**, *3*, 40.

(7) Milani, S.; Baldelli Bombelli, F.; Pitek, A. S.; Dawson, K. A.; Rädler, J. *ACS Nano* **2012**, *6*, 2532.

(8) Wang, J.; Jensen, U. B.; Jensen, G. V.; Shipovskov, S.; Balakrishnan, V. S.; Otzen, D.; Pedersen, J. S.; Besenbacher, F.; Sutherland, D. S. *Nano Letters* **2011**, *11*, 4985.

(9) Vogler, E. A. *Biomaterials* **2012**, *33*, 1201.

(10) Mahmoudi, M.; Meng, J.; Xue, X.; Liang, X. J.; Rahman, M.; Pfeiffer, C.; Hartmann, R.; Gil, P. R.; Pelaz, B.; Parak, W. J.; del Pino, P.; Carregal-Romero, S.; Kanaras, A. G.; Tamil Selvan, S. *Biotechnology Advances* **2014**, *32*, 679.

(11) Walkey, C. D.; Chan, W. C. W. *Chemical Society Reviews* **2012**, *41*, 2780.

(12) Sherwood, V.; Di Silvio, D.; Baldelli Bombelli, F.; *Topics in Medicinal Chemistry* **2014**, 1.

(13) Saptarshi, S. R.; Duschl A Fau - Lopata, A. L.; Lopata, A. L. *Journal of Nanobiotechnology* **2013**.

(14) Pino, P. d.; Pelaz, B.; Zhang, Q.; Maffre, P.; Nienhaus, G. U.; Parak, W. J. *Materials Horizons* **2014**, *1*, 301.

(15) Sakulkhu, U.; Mahmoudi, M.; Maurizi, L.; Salaklang, J.; Hofmann, H. *Sci. Rep.* **2014**, *4*.

(16) Böhmert, L.; Girod, M.; Hansen, U.; Maul, R.; Knappe, P.; Niemann, B.; Weidner, S. M.; Thünemann, A. F.; Lampen, A. *Nanotoxicology* **2013**, *8*, 631.

(17) Ashby, J.; Schachermeyer, S.; Pan, S.; Zhong, W. *Analytical Chemistry* **2013**, *85*, 7494.

(18) Monopoli, M. P.; Walczyk, D.; Campbell, A.; Elia, G.; Lynch, I.; Baldelli Bombelli, F.; Dawson, K. A. *Journal of the American Chemical Society* **2011**, *133*, 2525.

(19) Planken, K. L.; Colfen, H. *Nanoscale* **2010**, *2*, 1849.

(20) Kanokwan, N.; Vinayak, R.; Jeffrey, A. F.; Vytas, R. *Nanotechnology* **2013**, *24*, 155701.

(21) Moore, K. E.; Pfohl, M.; Hennrich, F.; Chakradhanula, V. S. K.; Kuebel, C.; Kappes, M. M.; Shapter, J. G.; Krupke, R.; Flavel, B. S. *ACS Nano* **2014**, *8*, 6756.

(22) Docter, D.; Distler, U.; Storck, W.; Kuharev, J.; Wünsch, D.; Hahlbrock, A.; Knauer, S. K.; Tenzer, S.; Stauber, R. H. *Nat. Protocols* **2014**, *9*, 2030.

(23) Tenzer, S.; Docter, D.; Kuharev, J.; Musyanovych, A.; Fetz, V.; Hecht, R.; Schlenk, F.; Fischer, D.; Kiouptsi, K.; Reinhardt, C.; Landfester, K.; Schild, H.; Maskos, M.; Knauer, S. K.; Stauber, R. H. *Nat Nano* **2013**, *8*, 772.

(24) Werwie, M.; Fehr, N.; Xu, X.; Basché, T.; Paulsen, H. *Biochimica et Biophysica Acta (BBA) - General Subjects* **2014**, *1840*, 1651.

(25) Di Silvio, D.; Rigby, N.; Bajka, B.; Mayes, A.; Mackie, A.; Baldelli Bombelli, F. *Nanoscale* **2015**, *7*, 11980.

(26) Jansch, M.; Stumpf, P.; Graf, C.; Rühl, E.; Müller, R. H. *International Journal of Pharmaceutics* **2012**, *428*, 125.

(27) Sánchez-López, V.; Fernández-Romero, J. M.; Gómez-Hens, A. *Analytica Chimica Acta* **2009**, *645*, 79.

(28) Pozzi, D.; Colapicchioni, V.; Caracciolo, G.; Piovesana, S.; Capriotti, A. L.; Palchetti, S.; De Grossi, S.; Riccioli, A.; Amenitsch, H.; Lagana, A. *Nanoscale* **2014**, *6*, 2782.

(29) Winzen, S.; Schoettler, S.; Baier, G.; Rosenauer, C.; Mailaender, V.; Landfester, K.; Mohr, K. *Nanoscale* **2015**, *7*, 2992.

(30) Lesniak, A.; Fenaroli, F.; Monopoli, M. P.; Åberg, C.; Dawson, K. A.; Salvati, A. *ACS Nano* **2012**, *6*, 5845.

Chapter 5. Interactions between NPs and lipids membrane

5.1 Introduction

The extensive use of NPs in many aspects of human life means voluntary and involuntary exposure to them.

If one of the main advantages of using NPs is the possibility to confer targeting abilities, targeting is not always effective. Moreover, NPs accumulation in the body can cause adverse effects inducing toxicity. Therefore, understanding of the interactions between NPs and biological environments, especially cells, is important to design safer and more efficient NPs.

As already discussed in the introduction, physical chemical properties of NPs,[1,2] such as size,[3-6] charge[7,8] and surface chemistry[9-12] are the main factors modulating NP-membrane interactions. They also influence the formation of a PC around the NPs that constitutes the ultimate interface with the biological surroundings.[13] Proteins in the environment have been found to change NP surface properties and thus NP-membrane interactions with membrane models[14-17] and cells.[4,14,18-21]

The study of these interactions is complicated by the heterogeneity of the cell membranes and their complex structure.[4] The use of membrane models composed of biologically relevant lipids allows the study of NP-membrane interactions using a simplified system for which composition can be controlled and structure elucidated without the effects of cell metabolism and growth.[22]

Supported lipid bilayers (SLBs) represent one of the most used and versatile models for biological membranes. They are planar and can be formed upon deposition and collapse of vesicles on interfaces with defined surface area.[23] Non-specific interactions with NPs can alter SLB structure and elasticity.[22] NPs can adhere to the lipid bilayer and cause changes in the lipid phase,[24] induce formation of lipid domains[25,26] or pores and extract lipids[27] inducing lipid bilayer disruption.[3,7]

Commonly, a combination of techniques is used to get insight into NP-membrane model interactions. Among them, quartz crystal microbalance with dissipation (QCM-D) has been extensively used to characterize lipid bilayers interactions with drugs, proteins and NPs.[23,28-31] Frequency and dissipation changes of the quartz crystal can be monitored and the adsorbed mass and the viscoelasticity of the layer can be assessed. Measures are in real time, and small volumes of solutions are used.

Neutron reflectometry (NR) studies can be coupled to QCM-D measurements through mathematical models, allowing investigation of the effect of small molecules, peptides and NPs on the lipid bilayer at a molecular level.[31-35] In particular, a qualitative description of the lipid bilayer is possible discriminating between hydrophobic tail and hydrophilic head regions. The design of a NR experiment is similar to a QCM-D one with the use of a flow chamber in which dispersions of vesicles and/or NPs can be injected, performing buffer washings on the SLB between each step.

In this chapter, QCM-D and NR are employed to study the interactions between polystyrene and Fe_3O_4 NPs and SLBs. Size, charge and surface chemistry as main determinants of biological responses to NPs are investigated. Moreover, the effect of the proteins is studied, using both *in situ* and HC conditions.

5.2 Supported lipid bilayers

Supported lipid bilayers were formed by flowing a solution of lipid vesicles into the chambers of QCM-D and NR instruments. Liposomes made of DOPC (1, 2-Dioleoyl-sn-glycero-3-phosphocholine) and SM (sphingomyelin), DOPC 100% and DOPC:SM 75:25 were prepared as described in paragraphs *2.3.1.4.2*. These formulations were chosen because they partially mimic the endothelial composition. Briefly, lipids were dissolved in chloroform and a dry film was obtained evaporating the solvent by rotary evaporation under vacuum. The film was hydrated in buffer and uniform unilamellar vesicles were obtained by freeze/thaw cycles and extrusion through 200 and 100 nm porous membranes. Highly monodispersed vesicles of similar size and neutral surface charge were obtained in both formulations (Fig. 5.1 and Table 5.1). Both lipids are zwitterionic, hence, neutral surface is expected.

In Fig. 5.2a and Fig. 5.2b, the formation of the supported lipid bilayer is followed by frequency and dissipation variations over time. Initially the system is in equilibrium with the buffer (step 1 in Fig. 5.2), the injection of vesicle solution causes a quick frequency and dissipation change (both increase in absolute value) (step 2 in Fig. 5.2). When saturation of the surface is reached, vesicles start to spontaneously collapse and a loss of mass is registered and corresponds to the release of water from the inside of the liposomes[36] (step 3 in Fig. 5.2). At the same time, the decrease of dissipation highlights the loss of vesicles elasticity. The system again reaches a situation of equilibrium and washings with buffer are performed to remove the excess of vesicles that can further deposit on the formed bilayer (step 4 in Fig. 5.2). The final bilayer is rigid (dissipation between 0 and 2) with frequency variation of about -25 Hz (step 5 in Fig. 5.2). The kinetics of collapse of vesicles is slower for the DOPC:SM formulation (step 2 in

Fig. 5.2a). Although the frequency variations characterizing the two SLBs are the same (step 5 in Fig. 5.2a), the dissipations are different. The DOPC:SM SLB is more rigid than the DOPC one, as pointed out by the smaller value of dissipation. The slower collapse kinetics and the higher rigidity of the DOPC:SM SLB can be ascribed to the higher transition temperature of sphingomyelin with respect to DOPC and the tendency to stipulate strong intermolecular interactions that promote the formation of domains in the membrane.[37]

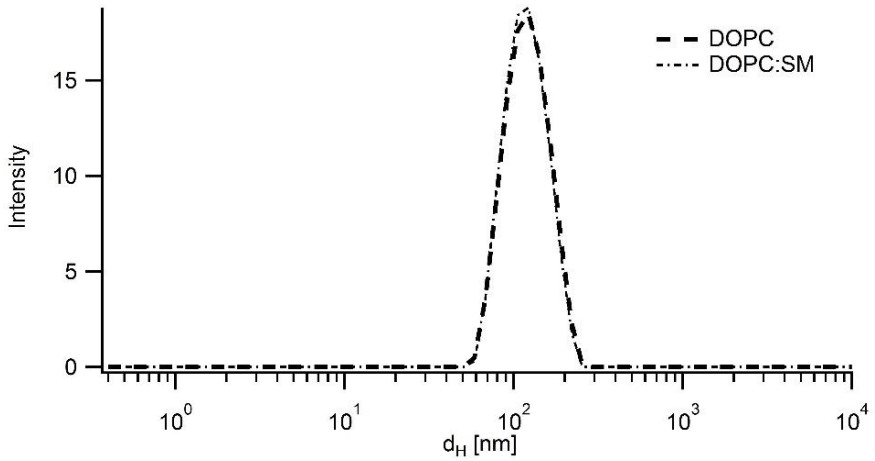

Figure 5.1 DLS Intensity-averaged size distributions of the hydrodynamic diameters for DOPC and DOPC:SM 75:25 liposomes. The initial solution (20mg/ml) was diluted 50 times.

Table 5.1 DOPC and DOPC:SM 75:25 liposomes after extrusion.

	d_H [nm][1]	**PdI[2]**	**Zp [mV]**
DOPC	116.3±3.4	0.04	-3.6±0.2
DOPC:SM	113.2±1.5	0.05	-2.0±0.3

DLS data were the average of three measurements and are presented with the relative standard deviation.
[1]Z-averaged Hydrodynamic diameters (d_H) obtained by cumulant analysis of the auto-correlation functions
[2]Polydispersity indexes (PdI) obtained by cumulant analysis of the auto-correlation functions.

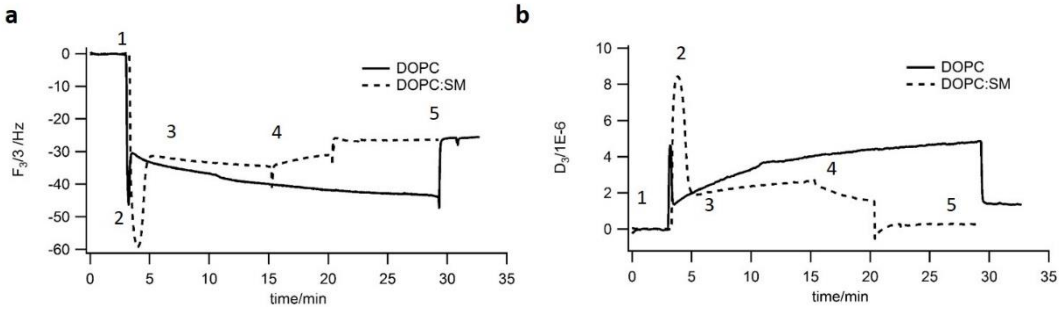

Figure 5.2 Frequency (a) and dissipation (b) profile obtained from the formation of DOPC (full line) and DOPC:SM (dashed line) SLB. In step 1, vesicles are injected in the chamber; at 2, vesicles start to collapse until a SLB is formed (3). Buffer washings are performed (4) to obtain the final SLB (5). Profiles represent frequency and dissipation at the third overtone.

Table 5.2 summarizes frequency ($\Delta f_3/3$), dissipation (ΔD_3), hydrated mass (Δm) and thickness (T) for DOPC and DOPC: SM SLBs. Values for hydrated mass and thickness were obtained applying the Sauerbrey equation for rigid film to the third overtone (eq. 2.27). An average density of 1100 Kg/m^3 was set. Data confirmed that similar adsorbed masses generated bilayers of similar thickness but different viscoelasticity in agreement with the literature.[36] The formulation DOPC:SM is more representative of the outer leaflet of the endothelial cells membrane and no significant differences were found in QCM-D experiments with the two formulations. It needs to be pointed out that the hydration mass includes the coupled water that is the solvent layer between the sensor and the lipid bilayer and it was estimated to have a mass of about 102 ng/cm^2 [38].

Table 5.2 QCM-D derived parameters measured and calculated for vesicles of different composition after collapsing in a lipid bilayer.

	$\Delta f_3/3$ [Hz]	**ΔD_3 [10^{-6}]**	**Δm^1[ng cm^{-2}]**	**T^1 [nm]**
DOPC	-(29.3±3.4)	1.3±0.3	514.1±59.4	4.7±0.5
DOPC:SM	-(30.6±2.2)	0.6±0.2	536.4±39.5	4.9±0.4

QCM-D data were the average of 21 measurements and are presented with the relative standard deviations.
[1]Values were derived applying the Sauerbrey equation to the frequency variation for the third overtone.

5.3 NP – SLB interactions in physiological buffer

Once the SLB has been formed and washed from the excess of vesicles, NPs in PBS are flowed into the chamber in two steps and, when the system reached the equilibrium, two flushes with buffer were performed. In Table 5.3, sizes and Z-potentials in PBS are reported for NPs used in the experiments. We employed carboxylated polystyrene NP of 20 nm and 100 nm of nominal diameter (PS-COOH20, PS-COOH100 and PS-COOH100NF, unlabelled), carboxylated Fe_3O_4 NPs (when not specified in the labelled they are assumed fully

carboxylated), pegylated polystyrene and magnetite NPs (PS-PEG and Fe_3O_4-PEG). The wide range of NPs allowed exploring the effect of size, charge and surface functionalities on the SLB.

5.3.1 Size effect

Size of NPs contributes to determine the pathway through which the NPs enter the cells.[39] Many computational studies on NP-membrane interactions investigated the behaviour of NPs whose diameter was similar or smaller than the SLB thickness. In these studies, it was demonstrated that NP size together with hydrophobicity could lead to NPs embedding in the SLB[6,12] while semi-hydrophobic NPs could be adsorbed.

Table 5.3 NPs employed in QCM-D experiments described by size distributions and Z-potential in PBS.

	d_H[1] [nm]	**PdI[2]**	**Zp [mV]**
PS-COOH20	32.3±0.4	0.10	-42.3±0.6
PS-COOH100	100.2±0.7	0.04	-33.7±1.4
PS-COOH100NF[3]	125.6±1.3	0.05	-26.2±0.8
PS-PEG	108.3±0.6	0.08	-2.1±1.0
F_3O_4[4]	48.5±0.8	0.18	-22.3±1.4
F_3O_4-PEG1	34.1±1.4	0.15	-9.6±0.5
F_3O_4-PEG2	46.3±2.1	0.19	-1.2±2.3

DLS data were the average of 3 measurements and are presented with the relative standard deviation.
[1]Hydrodynamic diameter (d_H) obtained by DLS from the cumulant analysis of the auto-correlation data.
[2]Polydispertity indexes (PdI) were obtained by DLS from the cumulant analisys of the auto-correlation data.
[3]PS-COOHNF are carboxylated polystyrene nanospheres not fluorescently labelled.
[4] Unless specified otherwise, Fe_3O_4 NPs are functionalized by carboxylic groups.

Carboxylate NPs of different diameters and core material were used to assess the effect of size on NP-SLB interactions. Comparison involved polystyrene NPs of hydrodynamic diameters of 30 and 100 nm and Fe_3O_4 NPs of about 50 nm (Table 5.3). Z-potential values were comparable and effects of the surface charge can be excluded. Two concentrations of NPs 0.1 m^2/ml and 0.02 m^2/ml were tested. Only the higher of the two (0.1 m^2/ ml) is reported as no significant differences were recorded, probably because the saturation of the lipid surface available is reached by both concentrations. Fig.5.3a shows frequency shifts during the different phases of the QCM-D experiments. The formation of the SLB is associated with the negative frequency of about -30 Hz. After NPs injections, a significant shift towards a more negative value is recorded only for PS-COOH100. This shift is associated with a significant dissipation increase that indicates a viscoelastic system (Fig. 5.3b). PS-COOH20 seemed to

adsorb in a smaller amount on the SLB, while after washing there was a slight increase the Δf (less negative value in WASH2 compared to SLB). Carboxylated Fe_3O_4 NPs seemed to not affect the SLB at all. The unperturbed rigidity of the SLB upon PS-COOH20 and Fe_3O_4 NPs application, allowed the use of the Sauerbrey equation to translate Δf in adsorbed mass and eventually layer thickness. The decrease in hydrated mass of the bilayer, which was exposed to PS-COOH20 is about 46 ng, roughly 10% of the initial adsorbed mass. These considerations cannot be applied to PS-COOH100 because the large change in dissipation would cause an underestimation of absorbed mass.[40,41]

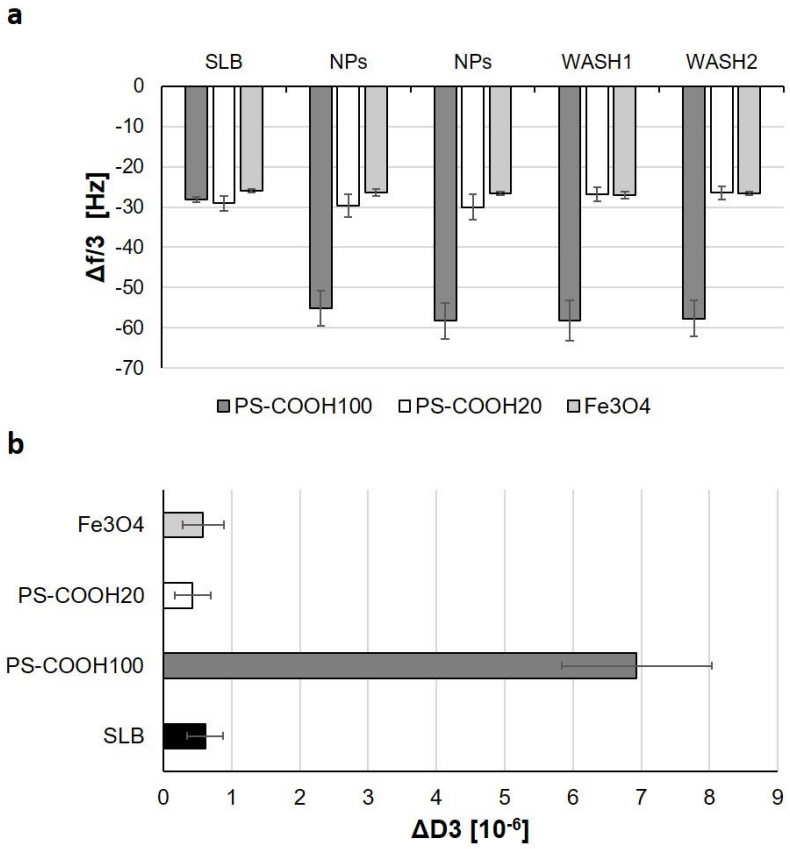

Figure 5.3 Frequency and dissipation variations during QCM-D experiments for interactions between DOPC: SM SLB and PS-COOH100, PS-COOH20, Fe_3O_4. A) Frequency shifts during the different steps of the experiments: the SLB after washings (SLB), the two NPs injections (NPs) and the two washings (WASH1-2). B) Dissipations of the SLB before the NPs injections (SLB) and at the end of the experiments. Experiments were done in triplicates.

Previously, it has been highlighted that polystyrene NPs might be too light (1.05 g/cm^3) to cause an appreciable frequency shift during QCM-D experiments. For this reason, PS-COOH20 effect on the SLB has been tested increasing the NPs concentration. No significant differences were reported among the samples as is illustrated in Fig. 5.4. From a structural point of view, FRET studies on interactions between NPs and GUVs (giant unilamellar

vesicles)[24,42] and mathematical modelling[43] demonstrated that anionic NPs below 20 nm are able to adsorb on neutral membranes and induce local rigidity. The VdW interactions between the polar heads of the lipids and the carboxylic groups on the NP surface induce a change in the tilt angle of the lipid heads bringing to a reorganization of the neighbouring lipids. As consequence of NPs effect, the LB would exist in different phases with patches that are more fluid and more rigid. Our data can be interpreted in two ways: either as membrane shrinkage with loss of water as a consequence of the NPs binding to the SLB, or as lipids extraction caused by NPs without any major perturbation of the SLB (unchanged dissipation).

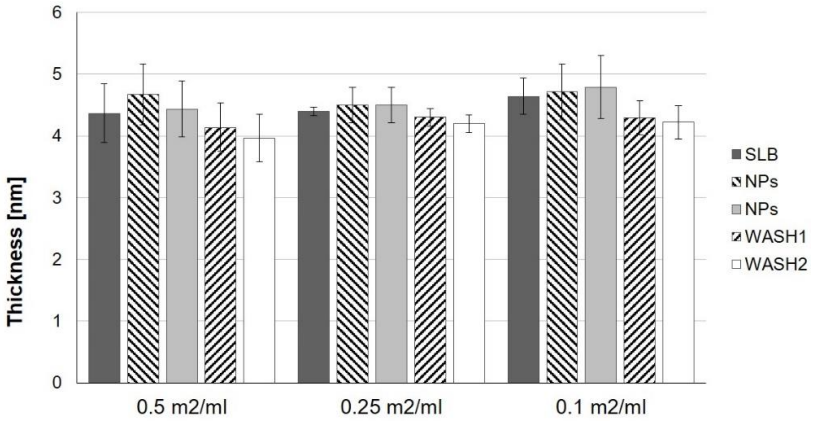

Figure 5.4 Thickness variations during each step of QCM-D experiments on pristine PS-COOH20 at different concentrations. Experiments were done in triplicates.

On the contrary, it has been reported a great and irreversible association of PS-COOH100 to POPC membranes.[14] Hou and co-workers[44] analysed the distribution of anionic Au NPs on solid-supported lipid membranes coated on 10 μm silica spheres. Their study suggested that in conditions of similar mass concentration, bigger NPs (>50 nm) distributed to a larger amount on the membrane due to mass concentration accumulation at the membrane interface, instead, smaller NPs (<50 nm) distributed at a faster rate due to a larger number of NPs in solution. In another work, 40 nm anionic Au NPs seemed to induce lipid extraction from the phosphatidylcholine SLB with a mass decrease of about the 20%.[45] Not many studies have characterized the kind of association between NPs bigger than 10 nm with SLBs as it is not trivial to interpret the eventual changes.

The results shown above, i.e. frequency shifts towards more negative values and increased dissipations, can represent a complex situation in which lipid extraction, NPs adsorption and

partial NPs envelopment can take place at the same time leading to an overall mass increase and dissipation change that describe a softer system with respect to the starting SLB.

5.3.2 Charge and surface coating effect

Neutral charge and hydrophilic coatings such as PEG coatings reduce interactions with cell membrane of both macrophages and other cell lines.[2,9,46,47] Pegylation provides steric hindrance to the binding of large molecules, mostly to opsonins that trigger macrophage recognition. Liu *et al.* monitored the effect of functionalized silica NPs on tethered lipid bilayer resistance and found that pegylation caused small increases compatible with the formation of small pores.[48]

In our study, PS-COOH100 NPs were fully pegylated, while Fe_3O_4-PEG NPs were both partially and fully functionalized (Fe_3O_4-PEG1 and Fe_3O_4-PEG2, respectively). In fact, PEG grafting density and polymer chain length can change PEG conformation on the NP surface (brush or mushroom conformations). In particular, low grafting density favours a mushroom conformation, while a high density favours the brush one.[11,49,50] These properties played an important role in the uptake of pegylated NPs. In Fig. 5.5 QCM-D, data for pegylated PS and Fe_3O_4 NPs are compared to the correspondent ones for carboxylated NPs. PS-PEG NPs application to the SLB is characterized by a slightly more negative shift, while Fe_3O_4-PEG2 is characterized by a slightly more positive shift (Fig. 5.5a). PS-PEG perturbed the rigidity of the SLB in a smaller amount than PS-COOH100, but still made it softer, while Fe_3O_4-PEG NPs reduced dissipation index. In the latter case, lipid extraction might take place but not enough to perturb the general structure of the SLB. Only experiments using Fe_3O_4-PEG2 NPs are reported from now on because there were not differences between the two magnetite NPs. If any, the differences were too small to be detected by QCM-D.

Another batch of carboxylated PS NPs of nominal diameter of 100 nm was tested. PS-COOH100NF NPs differed from PS-COOH100 NPs as they were not fluorescently labelled. However, despite a similar zeta-potential in PBS, charge densities were quite dissimilar: in particular, PS-COOH100NF had a charge density twenty times smaller than PS-COOH100 (0.018 meq/g and 0.32 meq/g, respectively, supplied by the manufacturer). The frequency shift produced by PS-COOH100NF NPs was –683±1 Hz with a dissipation of (153±91) $x10^{-6}$. The disruption of the SLB, accumulation and clustering of NPs on the sensor was speculated in this case.

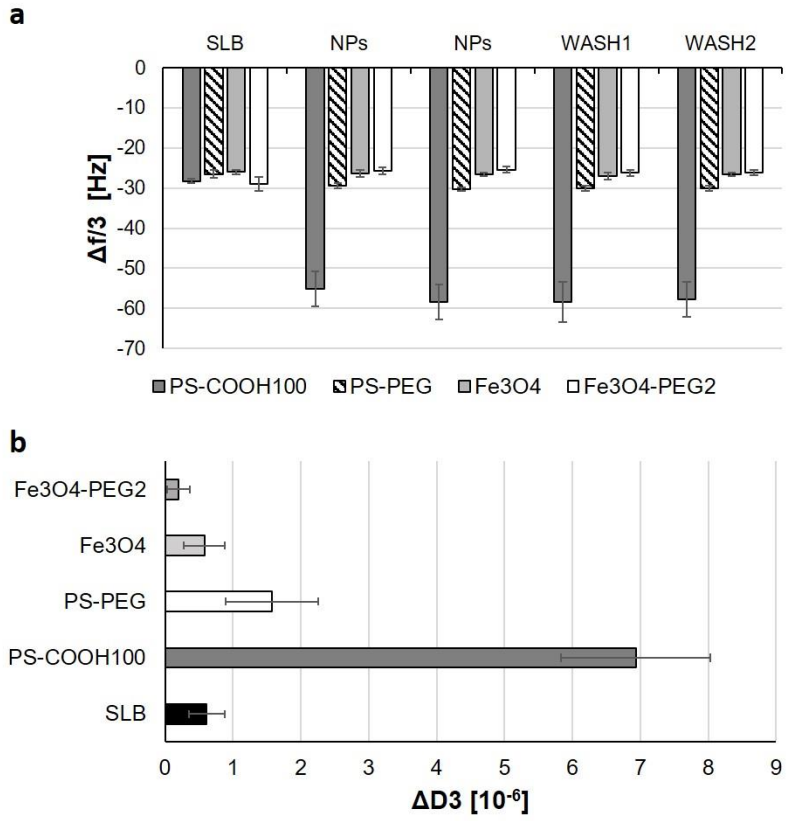

Figure 5.5 Frequency and dissipation variations during QCM-D experiments for interactions between DOPC: SM SLB and carboxylated and pegylated PS andFe_3O_4 NPs. A) Frequency shifts during the different steps of the experiments: the SLB after washings (SLB), the two NPs injections (NPs) and the two washings (WASH1-2). B) Dissipations of the SLB before the NPs injections (SLB) and at the end of the experiments. Experiments were done in triplicate.

5.4 Proteins effect

The SLB was also characterized in presence of FBS proteins. A 55% v/v FBS solution in PBS was injected on DOPC and DOPC:SM SLBs and after that the system reached the equilibrium, washings with buffer were performed. In Fig. 5.6, frequency and dissipation variations caused by FBS are shown. A soft layer of proteins deposited on the SLB until saturation was reached. The interactions between proteins and lipids were weak and reversible. In fact, during PBS washings, proteins were progressively removed without visibly affecting the viscoelastic properties of the SLB. Eventually, when the equilibrium between protein-SLB was reached, NPs in PBS or in FBS were added to the system. However, as reported in the literature, proteins generally mask interactions with NPs.[14] For example, in Fig. 5.7 is showed that when Fe_3O_4 NPs in PBS were added to the FBS coated bilayer, they could remove proteins from the SLB, while *in situ* Fe_3O_4 NPs, i.e. NPs dispersed in free and loosely bound proteins medium, did not add any mass to the protein layer (striped bar) and PBS washing detached proteins. Based on

the results, we decided to design the PC experiments adding directly to the SLB equilibrated in PBS either *in situ* NPs (in 55% FBS) or isolated HC NPs. The *in situ* NPs were incubated at 37°C to favour the formation of the HC but the excess of free and loosely bound proteins was not removed from the dispersion added on the SLB.

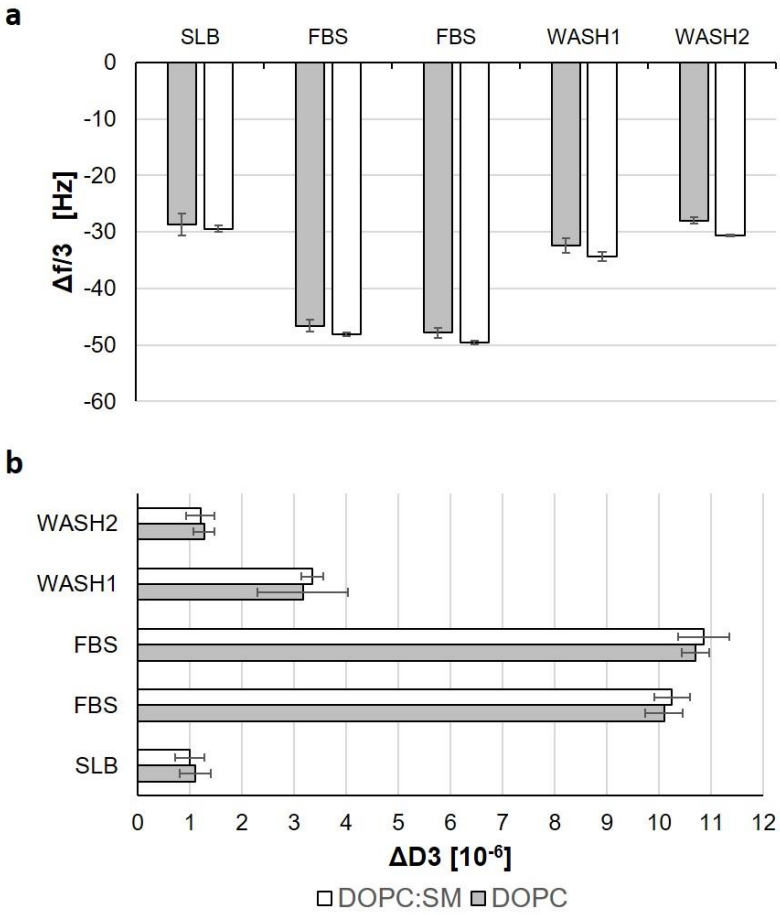

Figure 5.6 Frequency and dissipation variations during QCM-D experiments for interactions between DOPC and DOPC:SM SLB and FBS 55% v/v. A) Frequency shifts during each steps of the experiments: the SLB after washings (SLB), the two FBS injections (FBS) and the two washings (WASH1-2). B) Dissipations of the SLB before during all the phases of the experiments. Experiments were done in triplicate.

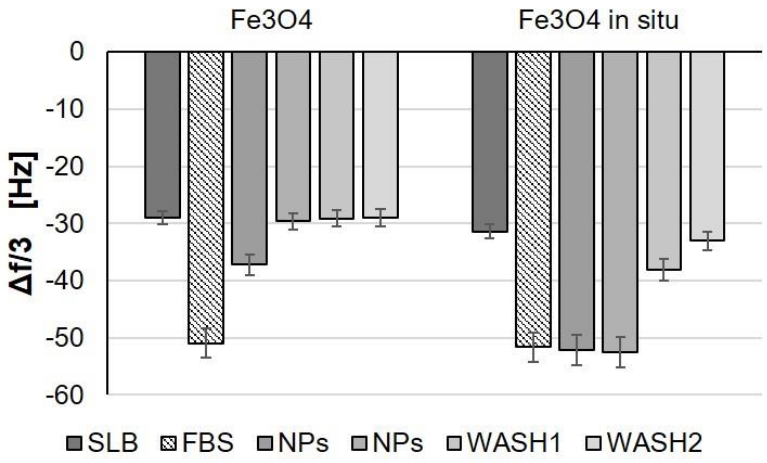

Figure 5.7 Frequency shifts associated to each phases of QCM-D experiments in which Fe_3O_4 are injected on SLB covered by FBS proteins (striped bar). In PBS and *in situ* NPs were compared. Experiments were done in triplicate.

5.4.1 *In situ* NP – SLB interactions

In situ NPs were incubated one hour at 37°C in 55% FBS and DLS was used to verify that aggregation did not occur before and after incubation with the SLB (Table 5.4). Polystyrene NPs were monodispersed after incubation and only PS-COOH20 showed some aggregation after recovery from the SLB. NPs after the QCM-D measurements were on average slightly bigger than the starting samples and magnetite NPs improved in polydispersity probably because unbound proteins stayed adsorbed on the SLB more easily than the NPs.

Table 5.4 NPs employed in QCM-D experiments described by size distributions of *in situ* NPs after incubation for one hour at 37°C and after injection on the SLB.

	Before injection		**After injection**	
	d_H[1] [nm]	PdI[2]	d_H[1] [nm]	PdI[2]
PS-COOH20	67.6±0.7	0.18	68.7±0.3	0.31*
PS-COOH100	139.0±0.4	0.02	150.1±0.2	0.05
PS-COOH100NF[3]	167.4±0.5	0.16	173.7±3.6	0.13
PS-PEG	101.4±0.7	0.12	106.4±0.9	0.12
F_3O_4	32.6±0.3	0.50**	31.0±0.7	0.23
F_3O_4-PEG1	25.0±0.3	0.43***	52.3±0.5	0.23

DLS data were the average of 3 measurements and are presented with the relative standard deviation. Samples were diluted 1:5 in PBS.
[1]Hydrodynamic diameter (d_H) obtained by DLS from the cumulant analysis of the auto-correlation data.
[2]Polydispertity indexes (PdI) were obtained by DLS from the cumulant analisys of the auto-correlation data.
[3]PS-COOHNF are carboxylated polystyrene nanospheres not fluorescently labelled.
*Bimodal size distribution: the main population was 104.4±2.9 nm, the second one was 11.8±0.3 nm.
** Bimodal size distribution: the main population was 46.1±2.7 nm, the second one was 12.5±0.8 nm.
*** Bimodal size distribution: the main population was 44.7±1.9 nm, the second one was 9.4±0.5 nm.

All samples, PS-COOH20, Fe_3O_4 and Fe_3O_4-PEG NPs that did not show any tendency to bind the SLB in PBS and PS-COOH100 and PS-COOH100NF that, on the contrary, attached irreversibly to the SLB, showed the same trend *in situ* in FBS: an initial adsorption on the SLB until its surface was saturated and successive removal of adsorbed mass by PBS washing. Proteins mediated the interactions with the SLB making the NP-membrane interaction much less strong than was observed for pure FBS (Fig. 5.8 compared to Fig. 5.6). However, some adsorbed mass seemed to stay attached to the membrane with respect to the experiments with only FBS for PS-PEG and PS-COOH20 NPs. It is remarkable that the only sample out of the trend was PS-COOH100NF for which we observed a frequency shift less negative at the end of the experiment compared to the SLB. Probably the high surface free energy of the PS-COOH100NF NPs was still high enough to induce disruption in the SLB. Dissipation trend is comparable for all NPs to the one showed in Fig. 5.6b for FBS alone. Although we can speculate that interactions with cell are more complex due to the structure of the cell membrane and the presence of uptake mechanisms, two parameters as excess of proteins, that reduce NPs surface free energy,[14,51] and shear flow,[52] seem to influence adhesion to lipid membrane when unspecific interactions are predominant.

5.4.2 HC NPs

Hard corona complexes were isolated applying standard centrifugation methodology (PS-COOH100, PS-PEG, PS-COOH100NF) and UC (PS-COOH20, Fe_3O_4, Fe_3O_4-PEG). In Table 5.5, DLS characterization of the complexes is reported before and after passage over the SLB. All NPs after the passage on the SLB were characterized by a bigger size and higher polydispersity. The variation of frequency shifts after HC NPs were injected was minimal (Fig 5.9). However, the general trend was a small increase in mass except for PS-COOH100NF, which was expected considering the *in situ* experiment outcome, and Fe_3O_4-PEG NPs. Dissipation was unchanged considering the standard deviations. The same conclusions on the HC effect hindering membrane adhesion were drawn by Lesniak and co-workers.[14] Montis and co-workers[42] described in more detail the effect of PC NPs on membrane models. They showed that HC NPs induced a mild structural reorganization of GUVs' lipid bilayer.

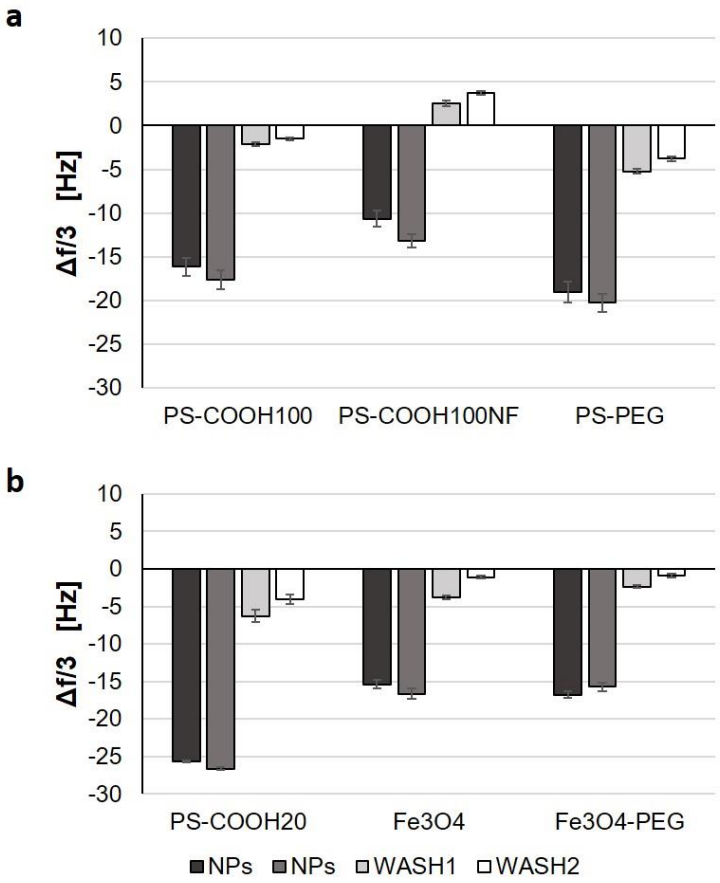

Figure 5.8 Frequency shifts reported to the SLB shift following *in situ* NPs injections and washings. NPs were added in excess of FBS proteins after one hour of incubation at 37°C, left to equilibrate on the SLB and washed by PBS. A) 100 nm diameter PS NPs; b) diameter < 50 nm NPs. Experiments were done in triplicate.

Table 5.5 HC NPs employed in QCM-D experiments described by size distributions. NPs were incubated for one hour at 37°C and subjected to centrifugation or ultracentrifugation as was described in Chapter 4. The HC complexes were analysed before and after transit through QCM-D.

	Before injection		**After injection**	
	d_H[1] [nm]	PdI[2]	d_H[1] [nm]	PdI[2]
PS-COOH20	69.2±1.5	0.11	85.1±1.3	0.23
PS-COOH100	173±2.9	0.20	177.2±4.1	0.22
PS-COOH100NF[3]	217.7±3.9	0.18	239.4.±5.6	0.23
PS-PEG	108.3 0.7	0.07	156.8±0.8	0.24
F_3O_4	51.5±0.4	0.19	61.03±1.3	0.23
F_3O_4-PEG1	93.4±2.3	0.23	101.1±1.6	0.23

DLS data were the average of 3 measurements and are presented with the relative standard deviation. Samples were suspended in PBS at 0.1 m^2/ml.
[1]Hydrodynamic diameter (d_H) obtained by DLS from the cumulant analysis of the auto-correlation data.
[2]Polydispertity indexes (PdI) were obtained by DLS from the cumulant analisys of the auto-correlation data.
[3]PS-COOHNF are carboxylated polystyrene nanospheres not fluorescently labelled.

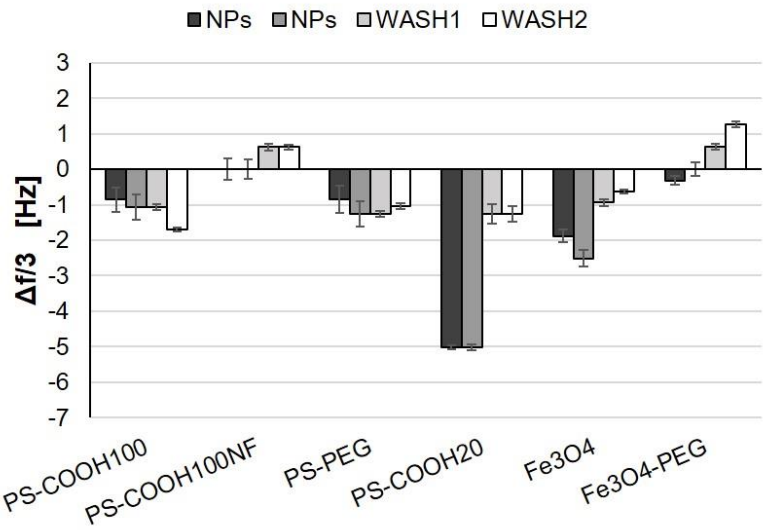

Figure 5.9 Frequency shifts reported to the SLB shift following HC NPs injections and washings. NPs were at concentration of 0.1 m^2/ml. PS-COOH100, PS-COOH100NF and PS-PEG were isolated by centrifugation; PS-COOH20, Fe_3O_4 and Fe_3O_4-PEG were isolated by ultracentrifugation, dialysed against PBS and concentrated by Amicon MWCO 50kD. Experiments were done in triplicate.

It needs to be pointed out that the protein composition of the HC complexes were very diverse from each other as shows in Chapter 4. Interaction with the SLB might affect corona composition and SDS-PAGE was used to spot differences between the HC composition before and after the passage on the SLB both in experiments with HC and *in situ* NPs. We verified the hypothesis examining the PC composition of carboxylated PS NPs in Fig. 5.10. The comparison was between the HC before the experiment (HC), the HC recovered from the *in situ* sample after having flowed over the SLB (F_IS) and the HC recovered from the HC sample after having flowed over the SLB (F_HC). Samples were prepared from the same batch of *in situ* NPs. Although the SDS-PAGE resolution is quite limited, some differences can be seen in the HCs. In PS-COOH100, some differences can be noticed in the block of proteins around 70 kDa (HC and F_HC in Fig. 5.10a are similar while F_IS is not). For the sample PS-COOH20, F_IS has a band missing at 150 kDa (Fig. 5.10b). In PS-COOH100NF, the HC seems to lose the entire block of proteins at high MW, F_IS more than F_HC but it might be due also to the sample concentration (Fig. 5.10c).

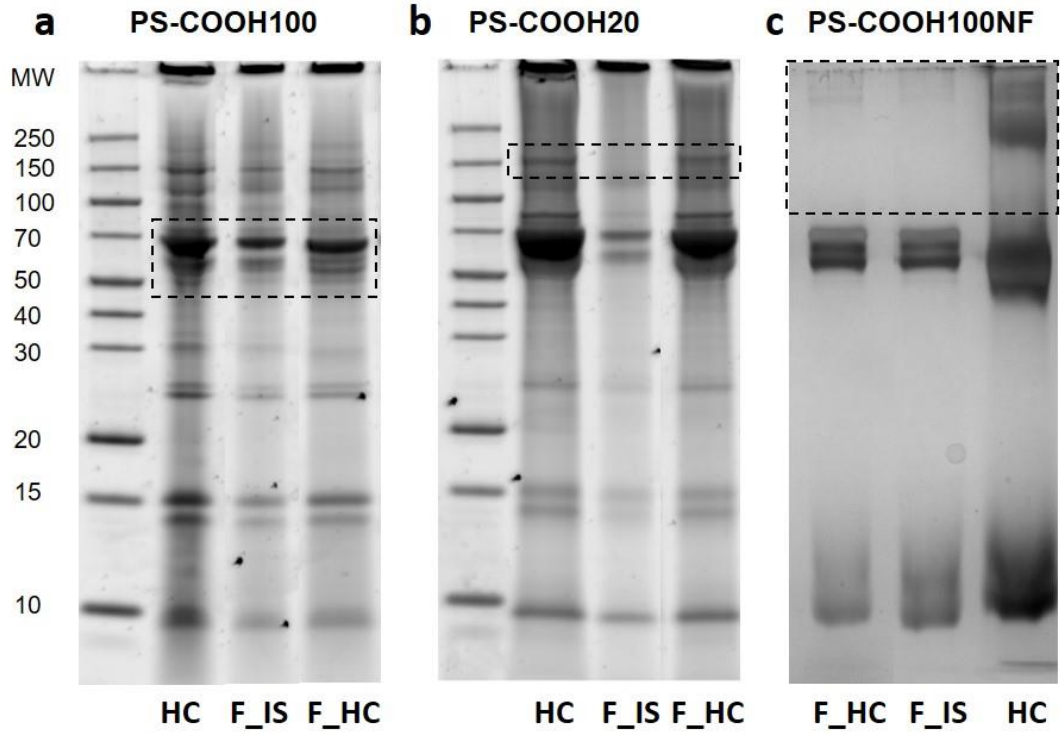

Figure 5.10 Hard corona composition is reported for carboxylated PS NPs. A) PS-COOH100; B) PS-COOH20; C) PS-COOH10NF. Lanes are named: HC (stock of HC NPs before QCM-D experiment); F_IS (*in situ* NPs were recovered after they were added on the SLB and HC was obtained by centrifugation or ultracentrifugation); F_HC (the HC NPs were recovered after QCM-D experiment and analysed by SDS-PAGE).

5.5 Fluorescence imaging of QCM-D chips

QCM-D experiments revealed a clear strong adsorption on the SLB only for pristine PS-COOH100 and PS-COOH100NF NPs. The other NPs caused little effects in terms of frequency shifts and dissipation changes so that it was hard to interpret if any adhesion took place. QCM-D technique might be not sensitive enough to detect NPs adhesion. Polystyrene NPs are notably "light" NPs having a density of 1.05 g/cm^3, while magnetite NPs, despite the denser core (5.1 g/cm^3), are probably too small in size (diameter of 8.5 nm by TEM, Chapter 3) to induce a detectable effect when present in small amounts. Therefore, QCM-D chips were explored by fluorescence microscopy to detect any NPs presence. Although real size estimation could not be achieved, some general conclusion could be drawn from Fig. 5.11: adsorption for PS-COOH100 and PS-COOH20 was confirmed and it was quite extensive for *in situ* and HC samples. For PS-PEG NPs small adhesion to the SLB was confirmed for the pristine NPs in PBS, while proteins (*in situ* and HC NPs) seemed to slightly increase the adhesion. Sensors treated by Fe_3O_4 NPs, both carboxylated and pegylated, showed a lower

fluorescence emission than PS NPs that might be correlated to a lower adhesion tendency compared to polystyrene NPs and few clusters were found mainly on the edge of the chips.

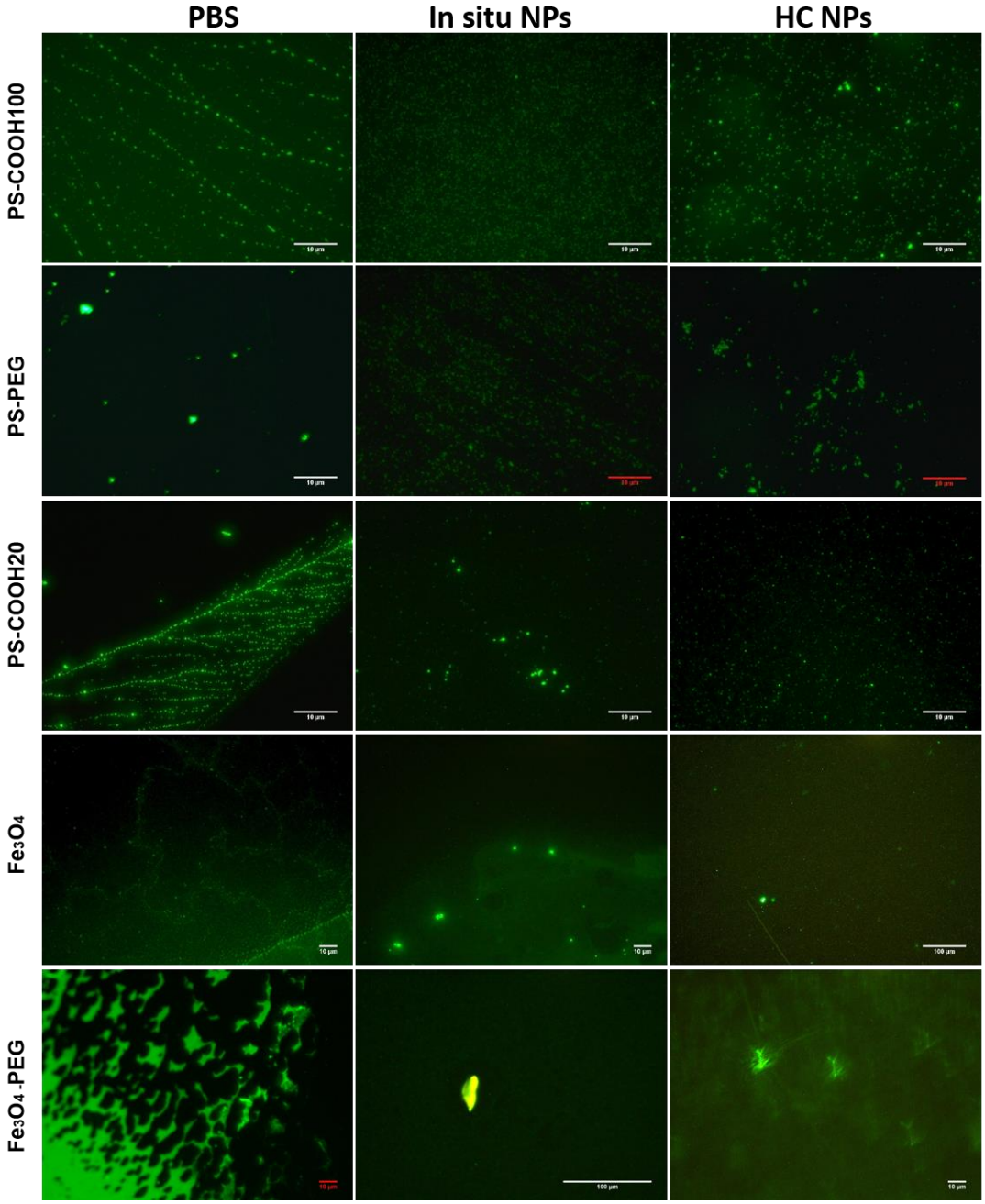

Figure 5.11 Fluorescence micrographs of QCM-D chips after experiments. Near blue filter was used to captured images at several magnification and a scale bar is provided. Samples were kept hydrated but a certain amount of dryness and aggregation, induced during the imaging process, cannot be excluded.

The presence of proteins clearly affects the spatial arrangement of the NPs. They appear to be generally less aggregated and more homogeneously distributed on the sensor surface, especially polystyrene NPs in presence of proteins. Moreover, in PS-COOH20 micrographs, the brighter aggregates of NPs present in the *in situ* sample could not be found in the HC sample indicating the successful UC purification of the HC complexes. In conclusion, all particles exhibit some adsorption on the SLB and QCM-D, that gives an average quantitative description of the systems, does not always provide a response that highlights it.

5.6 Probing NPs- SLB interactions by Neutron Reflectometry

5.6.1 Insight into internal structure of SLB

Neutron Reflectometry (NR) is a technique that allows the structural investigation of films at the nanoscale. It exploits the reflection of neutrons at the interface with two regions with different neutron scattering length densities (SLD) and it is able to provide an average description, down to Ångstrom resolution, of the structure normal to the direction of the film. As already described in Chapter 2, the output of a NR experiment is a plot of the reflectivity, R, intensity of the specularly reflected beam divided by the intensity of the incident beam, as a function of the momentum transfer, **Q**. The SLD is directly related to the composition of the film as it is a continuous function of the depth of a film in the z- direction and it is the sum of the neutron scattering lengths of all the atoms in the layer, divided by the layer volume. The reflectivity profile obtained during experiments is modelled to extrapolate a SLD profile of the system. The model is based on a design of the lipid bilayer as composed of homogeneous layers characterized by their own thickness, SLD, roughness.

NR experiments were not replicate due to the difficult experimental set up, but for each serie we completely characterized the pure SLB made of 100% DOPC. This lipid composition was chosen to reduce variables during the fitting process due the use of two lipids with different structural properties (i.e. SM and DOPC). Moreover, DOPC SLB are well characterized in literature.[53-56] The SLBs prepared by collapsing DOPC vesicles on the chips, were reproducible as can be seen in Fig. 5.12, in which all the NR in buffer in D_2O perfectly overlap. Small discrepancies were found at high values of **Q** were noise was higher. Each SLB was characterized in three different contrast conditions (100% D_2O; 38% D_2O or SMW; 100% H_2O; when NPs are added one more contrast was measured 4MW, 66% D_2O). In Fig. 5.13a the experimental curves at the three contrasts with the relative fits are displayed. The minimum between 0.15 and 0.2 $Å^{-1}$ was ascribed to the thickness of the bilayer, due to interferences arising between the reflected waves at the top and the bottom of the SLB.

The experimental curves were fitted by two models that are described in paragraph *2.3.1.4.2*. One named shortly "Rfit" depicts the SLB by 5 layers each one defined by its own scattering length density (SLD), thickness (t), roughness (σ) and solvent penetration degree (φ). These parameters are independent from each other. The second model, named "Gfit", characterizes the inner and the outer leaflets of the SLB by means of an area per molecule (APM), common to both tail and head of the same leaflet, thicknesses for head and tail, and a general roughness for all the fragments. In Fig. 5.13b the SLD profiles originated from the Gfit fitting reported in Fig. 5.13a as solid curves are shown. Resulting structural parameters obtained by the two fitting models for the SLB NR experiments shown in Figure 5.13a are reported in Table 5.6. The parameters describing the SiO_2 layer, except for the hydration, were fixed in both fitting procedures. Defects in the SLB can be evaluated from the amount of hydration water in the hydrophobic tails region of the SLB. The averaged value of tail hydration was less than 2% (1.6±1.4%) meaning that the overall coverage of the silicon chamber was 98% (the complement to 100%).

The thickness of the SLBs agreed with the QCM-D data (4.6±0.5 nm, reported in Table 5.2) and the averaged size was 4.7±0.8 nm (model without constrains) and 4.6±1.4 nm (model with constrains). The thickness of the hydrophobic tail region was 29.1±0.7 Å (without constrain, with constrains it was 28.5±0.8 Å) slightly higher than the data provided by Nagle *et al.*[54] (27.1 Å at 30°C). The outer polar head region was 6.2±0.3 Å while the inner headgroup region was 11.5±0.4 Å (without constrains, with constrains they were respectively 6.3±0.1 Å and 11.6±0.9 Å). The asymmetry of the profiles can be due to the different distribution of the hydration water and to the thermal motions that affect the thickness of the head regions at the interfaces.[55-57] Moreover, the two leaflets, the inner (L2-3) and the outer (L4-5) experienced different environment and the inner leaflet was in direct contact with the SiO_2 layer (L1).[33]

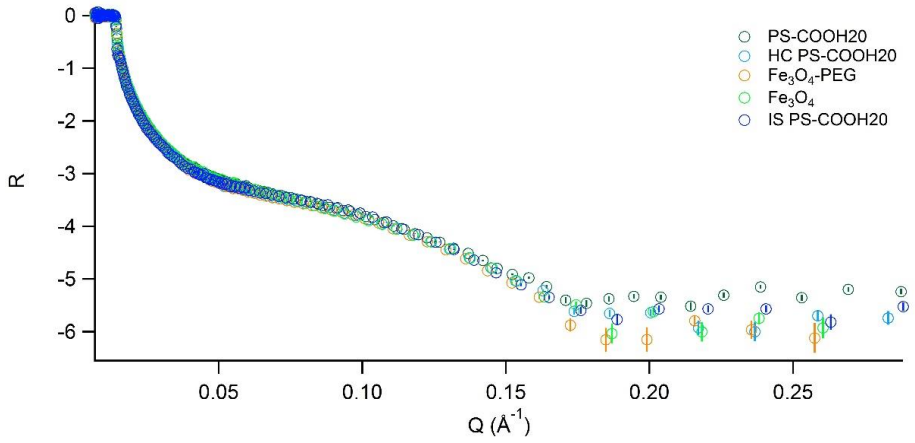

Figure 5.12 NR profiles for all the DOPC SLBs prepared. Data were collected in D_2O contrast. Raw data are reported as $\log_{10}$ R as function of the momentum transfer **Q**. The NP used during the experiment names each SLB. PS-COOH20, Fe_3O_4 and Fe_3O_4-PEG were used in PBS, while HC PS-COOH20 were HC NPs isolated by UC and IS PS-COOH20 were NPs in 55% FBS.

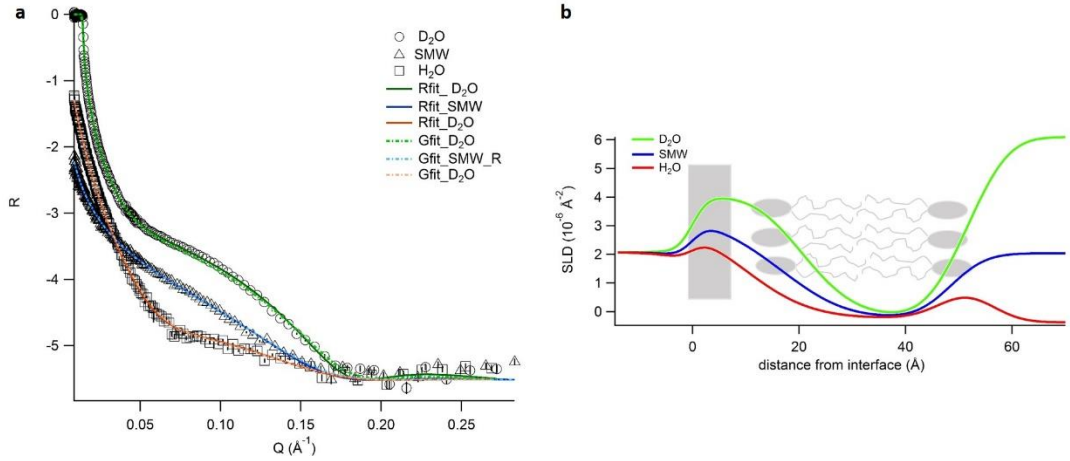

Figure 5.13 A) Neutron reflectometry profiles for DOPC SLB plotted as $\log_{10}$ R as function of the momentum transfer **Q**. Raw data and fits for the three contrasts are reported: circles and green lines for D_2O, triangles and blue lines for SMW, squares and red lines for H_2O. Solid and dashed lines are respectively fits with models without (Rfit) and with constrains (Gfit). B) Correspondent SLD profiles in the three contrasts for the fittings.

Table 5.6 Parameters acquired from the modelling of NR profiles of DOPC SLBs by models with (Gfit) and without constrains (Rfit). Gfit parameters are obtained applying equations in paragraph *2.3.1.4.2*. Data are referred to the experiment named HC PS-COOH20 and plots in Fig. 5.13.

Layer (L)	t [Å]		σ [Å]		Φ	
	Rfit	Gfit	Rfit	Gfit	Rfit	Gfit
1	8.5	8.5	2.1	2.1	5.3	14.9
2	11.6	11.5	8.8	7.1	69.4	61.2
3	14.3	14.0	8.8	7.1	0.4	1.6
4	14.3	14.5	5	7.1	0.4	1.8
5	6	6.1	5	7.1	27.1	24.7

Layer 1 is the SiO_2 layer. Layer 2 is the inner head group; Layer 3 is the inner tail group; Layer 4 is the outer tail group; Layer 5 is the outer head group. t is the thickness; σ is the roughness between each layer and the following one or the bulk; φ is the solvent penetration degree.

5.6.2 Effects of pristine NPs on the SLB

Overall, QCM-D results for PS-COOH20, Fe_3O_4 and Fe_3O_4-PEG did not highlight either a disruption of the SLB or a major adsorption of NPs that could be revealed by a significant change of mass on the quartz sensor. Instead, in the case of PS-COOH20 and Fe_3O_4-PEG, small changes in the dissipation profile were registered (Fig. 5.3 and Fig. 5.5). Changes in the lipid organization including possible removal of some molecule could be speculated and NR experiments NPs were in fact performed to clarify the effect of such NPs on the SLB structure. In Fig. 5.14, the raw data comparing the NR profiles before and after the injection of NPs are displayed for different NPs. The plot is displayed in R $\mathbf{Q}^4$ vs **Q** and it allows negative data points (where background subtraction gives rise to noise) to be correctly represented. The curves are in SMW contrast. Different effects on the SLBs were evident, mostly for Fe_3O_4-PEG NPs for which a small compression of the curve was observed (Fig. 5.14b). While the NR curve of the SLB treated with PS-COOH20 NPs showed the minimum at about **Q** = 0.15 $Å^{-1}$ shifted at higher Q values with respect to the pristine SLB (5.14a). In addition, for the SLB treated with Fe_3O_4 NPs NR curves mostly differed in the high **Q** region (in Fig. 5.14c). The NR profiles of the three SLBs after NPs flow did not evidence any LB disruption as it was revealed by QCM-D. However, a structural reorganization of the SLB at molecular level could be speculated. To evidence these changes, NR profiles were fitted with the same model used for the starting SLB (5-layers model with and without constrains) and with a model made up of 6-layers fitted without constrains that assumes a certain adsorption of NPs on the SLB surface. Penetration was excluded because the size of the NPs was too large to allow it. Moreover, the fittings of the raw data with a model of a whole bilayer gave better results.

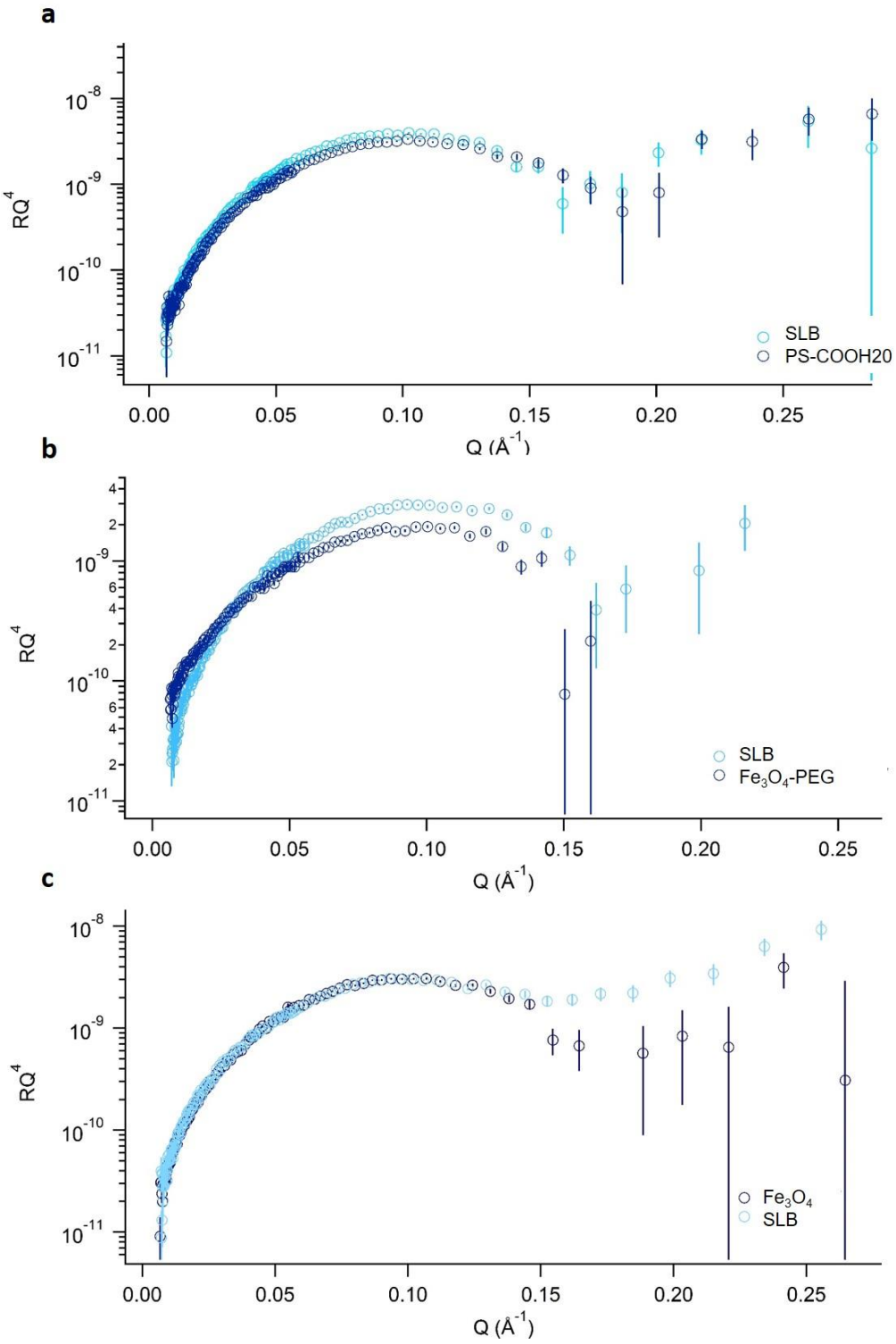

Figure 5.14 NR curves for pristine NPs: a) PS-COOH20, b) Fe_3O_4-PEG, c) Fe_3O_4. Plots are in R **Q^4 vs Q.** Data refer to SMW contrasts and NR profiles of the SLB before (light blue circles) and after (dark blue circles) the injection of NPs are reported.

5.6.2.1 PS-COOH20

PS-COOH20 NPs were applied to SLB. In Fig. 5.15, the fittings of the NR raw data are presented. The experimental NR curves of the SLB after NP injection were well fit by the 5-layers model (Fig. 5.15b), while the 6-layers model (Fig. 5.15c) did not work well, especially for the H_2O contrast. Fit parameters extracted from these fittings are reported in Table 5.7. All regions increased in thickness and solvent penetration degree post NPs addition. The effect was bigger for the hydrophobic tails. Moreover, we analysed the APM that was reported to be 72 $Å^2$ for a pure DOPC SLB at 30°C.[55] During the fitting analysis we constrained the minimum value of APM to 72 $Å^2$ and only in one case, it changed to 74.6 $Å^2$, i.e. for the outer leaflet of the SLB upon NPs application. QCM-D results for PS-COOH20 NPs were interpreted with either a SLB shrinkage and consequent loss of water or by lipid removal from the SLB (paragraph *5.3.1*). The hypothesis of lipids removal seems to be the most reliable because it would lead to a decrease of lipids packing that is inversely proportional to the APM. A higher APM describes a more fluid lipids organization that should lead to a thinner bilayer.[58] In this regard, the small increase of the overall thickness (from 4.5 nm to 4.8 nm) could be explained by a small swelling due to hydrophobic region hydration. This effect on the tail region is visible in the SLD profiles in Fig. 5.16. The wider spacing among curves at the level of the tails in Fig. 5.16b with respect to 5.16a indicates higher solvation. Other studies on carboxylated polystyrene NPs referred other effects on lipid bilayers: Negoda and co-workers[59] reported the formation of pores in DOPC LB upon exposure to NPs, however the bilayer was formed on a Delrin cup and not on a support that makes them more resistant. In another study, fluorescence correlation spectroscopy showed that adsorption of the same NPs on LUVs (large unilamellar vesicles) was able to induce local gelation of the lipids,[24] resulting in vesicles water content reduction, shrinking of the membrane and decrease of the APM which it was not observed in our system. This different behaviour might be ascribed to the diverse experimental setting and NPs charge density.

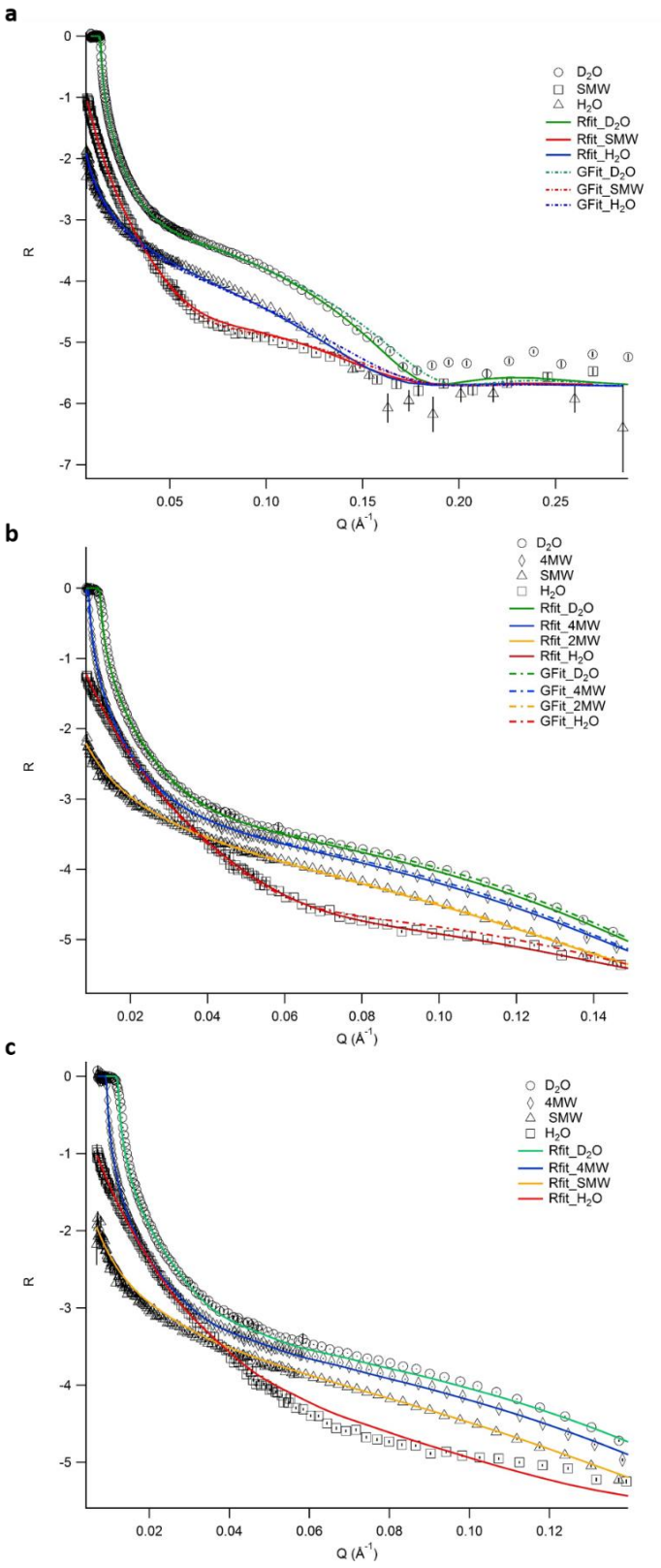

Figure 5.15 Plots of log (R) (reflected intensity divided by incident intensity) vs **Q** for SLB treated with PS-COOH20 NPs. A) SLB raw data with correspondent fittings; SLB after NPs injection fitted with 5-layers model (B) and 6-layers model (C).

Table 5.7 PS-COOH20 induced structural changes on SLB. Model with constrains (Gfit) was applied. The parameters describing the SiO_2 layer and the roughness of the layers were kept constant to evaluate the effects on thicknesses (t) and solvent penetration degrees (φ). Gfit parameters are obtained applying equations in paragraph *2.3.1.4.2*.

Layer (L)	t [Å]		Φ	
	SLB	NPs	SLB	NPs
2	11.6	12.4	61.7	64.4
3	13.7	14.8	0.3	7.6
4	13.7	14.8	0.3	10.7
5	6.4	6.6	30.4	34.9

Layer 2 is the inner head group; Layer 3 is the inner tail group; Layer 4 is the outer tail group; Layer 5 is the outer head group. t is the thickness; φ is the solvent penetration degree.

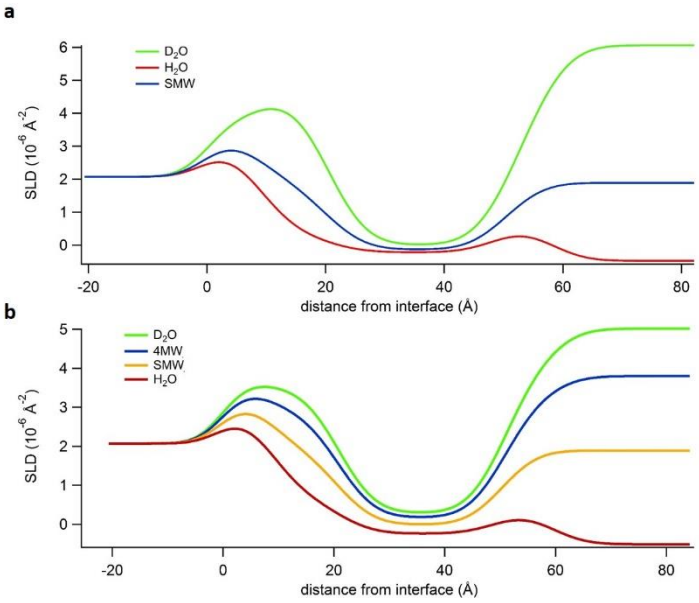

Figure 5.16 SLD profiles describing the original SLB (a) and the SLB after NPs flowing (b). The profiles are obtained by the raw data fittings displayed in Fig. 5.15a-b.

5.6.2.2 Fe_3O_4

Carboxylated Fe_3O_4 NPs did not seem to induce any perturbation of the SLB when it was characterized by QCM-D. On the contrary, the analysis of NR profiles highlighted some effects on the SLB. We found alterations in NR profiles at high **Q** (Fig. 5.14c).

The 6-layers model, describing a highly solvated layer of NPs on top the SLB, did not perfectly fit as shown in Fig. 5.17c. The 5-layers model was able to reproduce the raw data trend. Looking at the resulting parameters reported in Table 5.8, thickness and solvation increases are evident and the inner head region was the less affected by the NPs. These general findings on the SLB reflect what we reported for PS-COOH20. However, some differences can be pointed out. First of all, the SLB thickness increased from 4.5 nm to 5.2 nm, the 15.5%

compared to the growth of the 6.7% of the SLB treated by PS-COOH20. The biggest difference involved the outer polar heads whose thickness and hydration doubled. We could speculate that carboxylated Fe_3O_4 NPs exert a stronger influence over the outer leaflet compared to PS-COOH20. Interestingly, in the fitting process, the APM of both leaflets remained fixed at 72 $Å^2$ while the outer leaflet of the SLB previously subject to PS-COOH20 NPs increased to 74.6 $Å^2$. While in the previous experiment all the signs were well explained with lipid removal, in the current one the constant APM does not directly correlates with the lipid removal. We demonstrated a striking effect on the outer polar head. We can speculate that significant modification of the head tilt angle[8,60] occurred as consequence of the different surface chemistry characterizing Fe_3O_4 NPs compared to PS NPs. For the latter, such alterations could happen but they were not as evident as here.

In addition, although we did not use the 6-layers model, little adsorption of NPs cannot be completely ruled out. Some effects can manifest even at very low concentration as reported in a recent computational study[6] where Au NPs in a small concentration were able to induce lipid packing even in a site far from the place of interaction. We need to keep in mind that NR offers an average description of the system and the cell vertical geometry and gravitational forces acting on NPs can cause inhomogeneities in the environment and the inhomogeneities affect differently the SLB according the NP specie.

Table 5.8 Fe_3O_4 induced structural changes on SLB. Model with constrains (Gfit) was applied. The parameters describing the SiO_2 layer and the roughness of the layers were kept constant to evaluate the effects on thicknesses (t) and solvent penetration degrees (φ). Gfit parameters are obtained applying equations in paragraph *2.3.1.4.2*.

Layer (L)	t [Å]		φ	
	SLB	**NPs**	**SLB**	**NPs**
2	10.3	10.7	57.1	58.5
3	14.1	15.1	3.1	9.8
4	14.1	15.1	3.0	9.7
5	6.4	11.0	31.3	59.7

Layer 2 is the inner head group; Layer 3 is the inner tail group; Layer 4 is the outer tail group; Layer 5 is the outer head group. t is the thickness; φ is the solvent penetration degree.

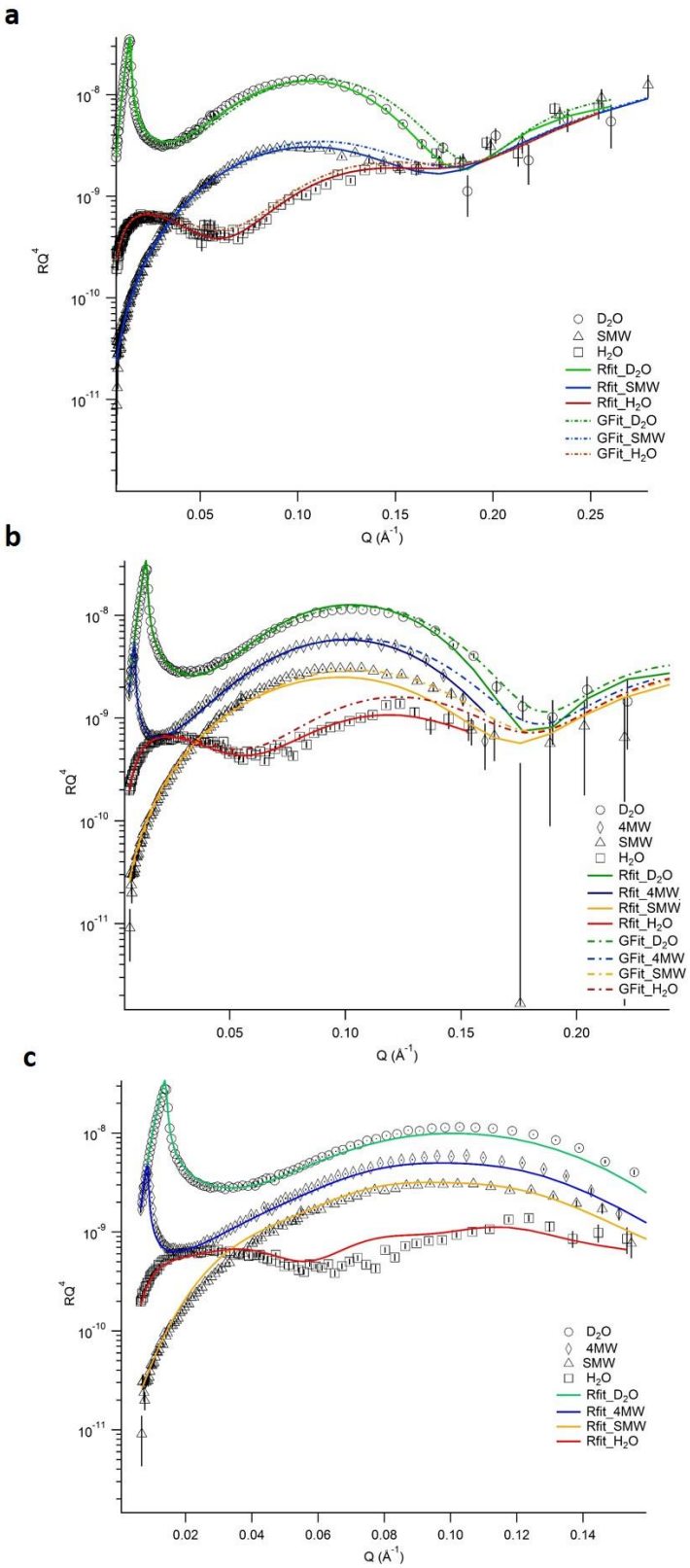

Figure 5.17 NR profiles for DOPC SLB (a) treated by Fe_3O_4 NPs and modelled by 5-layers (b) and 6-layers models (c). Data are presented as R**Q**^{4} vs **Q**.

5.6.2.3 Fe_3O_4-PEG

QCM-D characterization of SLB exposed to pegylated magnetite NPs evidenced a small but significant modification of the dissipation compared to the SLB (Fig. 5.5). The examination of the raw data in Fig.5.14b allowed us to appreciate some effect caused by the NPs on the SLB. The fitting goodness of the 5-layers models is shown in Fig. 5.18a-b while the 6-layers model was not as good as the 5-layers one (Fig 5.18c). From a first look at the SLD profiles of the SLB before and after NPs injection (respectively Fig. 5.18d-e derived from fitting in Fig. 5.18a-b), any evident change in solvation of the tails region could be seen. A careful examination of the fitting parameters, listed in Table 5.9, emphasises the decrease in thickness and dehydration of the polar segments of the LB. That correlates with the extra stiffening of the membrane underlined by QCM-D. PEG moieties are highly hydrophilic and the cumbersome hydration shell that surrounds the molecules hinders interactions with proteins[61] and membranes. The interactions with the hydrophobic tail region are repulsive and the proximity of NPs to the membrane causes a reduction of the chains mobility and unfavourable entropic contribution to the total energy of the system.[50] Measures of electrical resistance on DOPC SLB showed that pegylated silica NPs did not disrupt the SLB.[48]

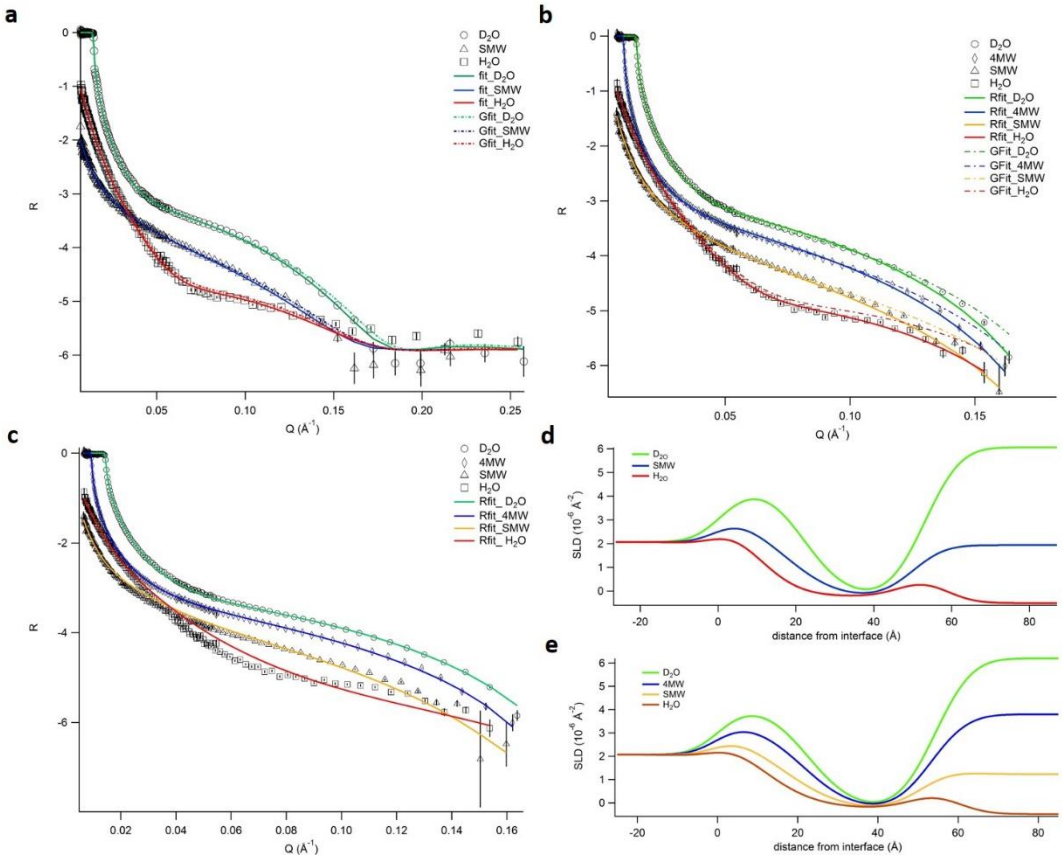

Figure 5.18 NR profiles for DOPC SLB (a) treated by Fe_3O_4 -PEG and modelled by 5-layers (b) and 6-layers models (c). Data are presented as log (**R)** vs **Q**. D-E) SLD profiles for SLB before and after NPs injection obtained from fittings in a-b) respectively.

Table 5.9 Fe_3O_4-PEG induced structural changes on SLB. Model with constrains (Gfit) was applied. The parameters describing the SiO_2 layer and the roughness of the layers were kept constant to evaluate the effects on thicknesses (t) and solvent penetration degrees (φ). Gfit parameters are obtained applying equations in paragraph *2.3.1.4.2*.

Layer (L)	t [Å]		Φ	
	SLB	NPs	SLB	NPs
2	12.0	9.6	63.0	54.2
3	14.3	14.3	4.7	4.4
4	14.3	14.3	4.6	4.3
5	6.3	6.1	30.2	27.6

Layer 2 is the inner head group; Layer 3 is the inner tail group; Layer 4 is the outer tail group; Layer 5 is the outer head group. t is the thickness; φ is the solvent penetration degree.

5.6.2.4 Short summary of pristine NPs impact on SLB

To summarize, we saw two opposite effects induced by pristine NPs on SLBs. We observed either a dehydration with shrinking of the SLB or a hydration with swelling of the SLB. Disruption of the SLB did not occur in any of the cases examined.

Pegylated Fe_3O_4 NPs, as described in paragraph *5.6.2.4*, caused a general dehydration and small decrease of the thickness of the outer layer formed by the polar heads. The layer of hydrophobic tails was instead unchanged, meaning that these modifications of the outer layer did not involve a rearrangement of the hydrophobic moiety of the bilayer.

Carboxylated NPs promoted an increase of the SLB thickness with hydration of the tails region. In the case of PS-COOH20 NPs, also an increase of the APM of the outer leaflet lead us to the conclusion that some lipids were removed from the SLB with further reduction of the lipid packing, which promoted solvation of the polar head groups (paragraph *5.6.2.2*). Carboxylated Fe_3O_4 NPs had the strongest impact on the outer leaflet of the polar head region that showed values of thickness and hydration doubled with respect to the starting SLB. This remarkable change, accompanied by a constant APM value, was ascribed to a different nature in the interaction between the functional groups on the NP surface and the polar heads of the lipid, in fact despite the presence of carboxylated groups PSCOOH and Fe_3O_4 NPs were characterized by a completely different surface in terms of chemical composition. Also, in this case lipid removal cannot be ruled out but it is not likely the predominant effect (paragraph *5.6.2.3*).

Adsorption of NPs was not satisfyingly supported by fitting the SLB profiles with a 6-layers model. However, the presence of a highly solvated layer of NPs, not evenly distributed on the SLB, cannot be completely ruled out given the vertical geometry of the chamber.

5.6.3 Proteins effect on the SLB: *In situ* PS-COOH20

As explained above, the pure interaction between proteins and SLB showed to be unspecific and weak. Solvent exchange in QCM-D chamber was able to remove most, if not all, proteins adsorbed on the SLB (paragraph *5.4*).

However, we compared the effects on the SLB caused by pure FBS (55% v/v) and *in situ* PS-COOH20 NPs. Examining Fig. 5.19, a decrease of intensity of the fringe at 0.1 $Å^{-1}$ can be observed, and the effect is enhanced by NPs presence. A similar effect was observed by Le Brun and co-workers related to proteins adsorption.[62] They studied the interactions of some fragments of the prion proteins with zwitterionic and anionic SLBs. They did not see any interactions with the neutral SLB, while they attributed a highly solvated layer of peptide (0.15 volume fraction) to be adsorbed on the anionic SLB. They performed a deep analysis on the structural SLB reorganization upon peptides interaction, which unluckily is not applicable for

the heterogeneity of the medium: proteins of different size and charge compose FBS that interact dissimilarly with lipids. FBS-induced destabilization of SLBs was reported by Peetla *et al.*[27] who observed a small decrease of surface pressure when they treated a DPPC lipid bilayer with 10% FBS. The decrease of surface pressure is a sign for lipid condensation and it was attributed to either proteins embedding in the SLB that reduced the APM of the lipids or electrostatic interactions between proteins and polar heads that decreased repulsive forces between lipids inducing compression.

In our case, two opposite effects were seen when the SLB was exposed to FBS or NPs in FBS. Also, in this case SLBs were modelled with the 5-layers model to focus the attention on the SLB structural changes. In Fig 5.20, SLD profiles derived from a 5-layers model are plotted. The increasing water content in the tails region is evident in comparison to the original SLB, both with FBS and *in situ* NPs (Fig. 5.20a-b-c respectively). The extracted fitting parameters, reported in Table 5.10, showed that the addition of FBS induced a slight dehydration of the outer head groups (φ goes from 35% to 27%). On the contrary, for *in situ* NPs, the tail and the outer polar head regions of the SLB exhibited a higher hydration which was reflected by the splitting of the curves in the range 25-45 Å in Fig. 5.20c. We can speculate that SLB modifications are a consequence of a lipid-protein exchange with NP PCs.

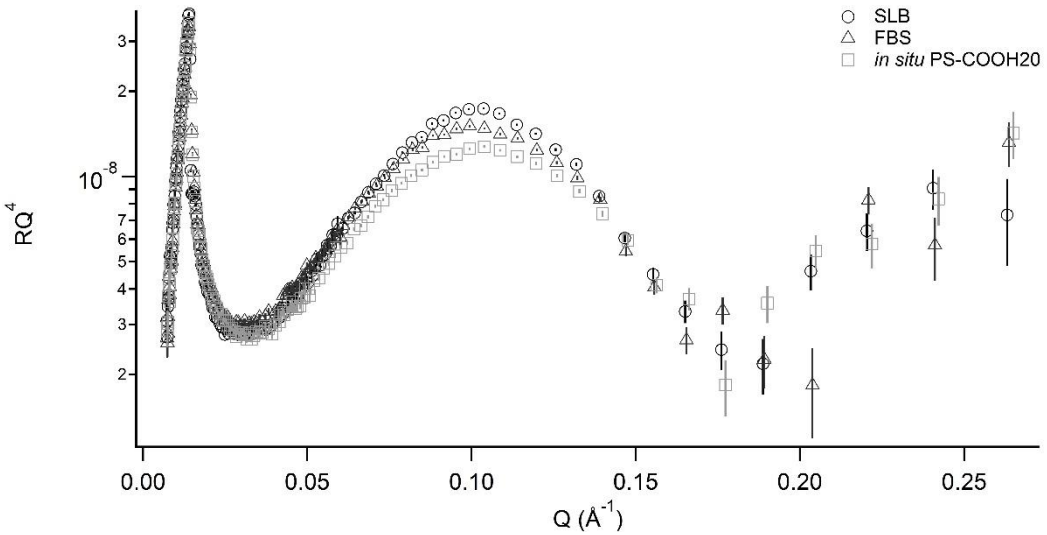

Figure 5.19 NR profiles for SLB (SLB), SLB after proteins injection (FBS) and after injection of *in situ* NPs. Data are presented as R $\mathbf{Q}^4$ vs **Q**.

Table 5.10 Proteins induced structural changes on SLB. Model without constrains (Rfit) was applied. The parameters describing the SiO_2 layer and the roughness of the layers were kept constant to evaluate the effects on thicknesses (t) and solvent penetration degrees (φ).

Layer (L)	t [Å]			Φ		
	SLB	FBS	IS NPs	SLB	FBS	IS NPs
2	11.7	12.7	12.4	56.0	61.4	61.6
3	14.3	14.1	14.5	2.8	2.8	8.8
4	14.3	14.1	14.5	2.8	2.8	8.8
5	6.6	6.4	7.1	35.1	27.0	43.6

IS NPs are PS-COOH20 NPs in 55% FBS initially in D_2O; Layer 2 is the inner head group; Layer 3 is the inner tail group; Layer 4 is the outer tail group; Layer 5 is the outer head group. t is the thickness; φ is the solvent penetration degree.

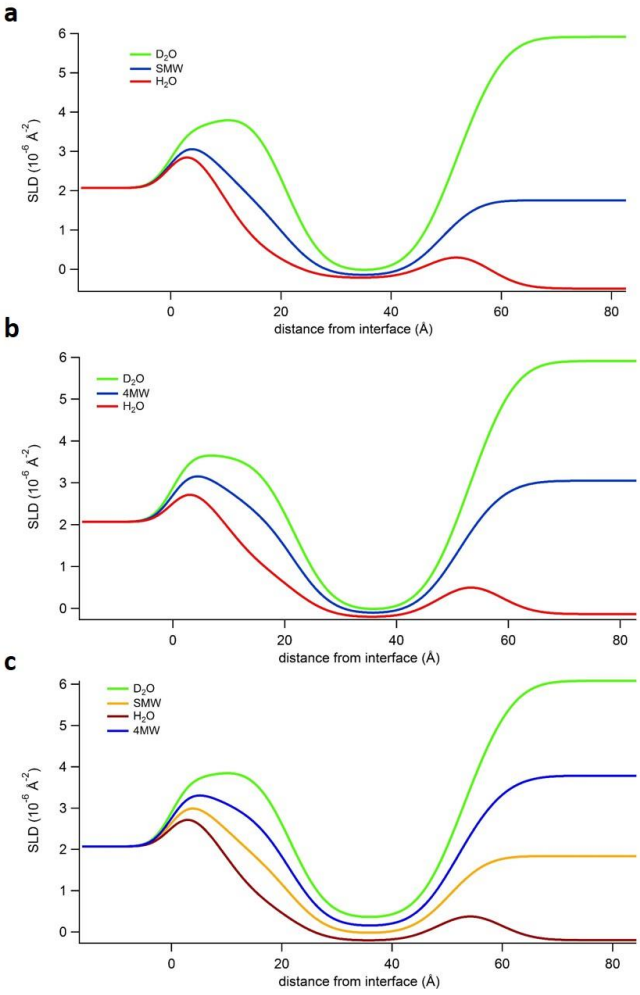

Figure 5.20 SLD profiles derived from fitting the raw data with a 5-layers model without constrains. A) SLB; b) SLB after addition of FBS; c) SLB after addition of *in situ* PS-COOH20.

Attempts in fitting the NR data with a 6-layers model were performed. Since FBS proteins are very heterogeneous, Albumin was taken as reference being the most abundant protein in the blood. During the fitting, Albumin thickness was varied in the range of 50-70 Å (the Albumin

shell was found to vary from 3 to 6 nm according to the salinity of the solvent[63]). SLD was calculated for the different solvent compositions (*http://psldc.isis.rl.ac.uk/Psldc/*). The sequence used was Q56G89 (UniProt) and 90% of hydrogen-exchange was considered for a variation of the SLD of 10% in the fitting. Fittings were good and compatible with a hydrated layer of proteins (Fig. 5.21). Given the small protein presence, the characteristics of the bilayers were mostly unvaried compared to 5-layers fittings (Table 5.11). However, the proteins presence justified the general dehydration and packing of lipids when FBS was added.[27] When in situ NPs were added, the SLB was subject to hydration and this could be ascribed to NPs corona that could exchange lipids with the bilayer or interact strongly with the outer leaflet inducing defects in the SLB.

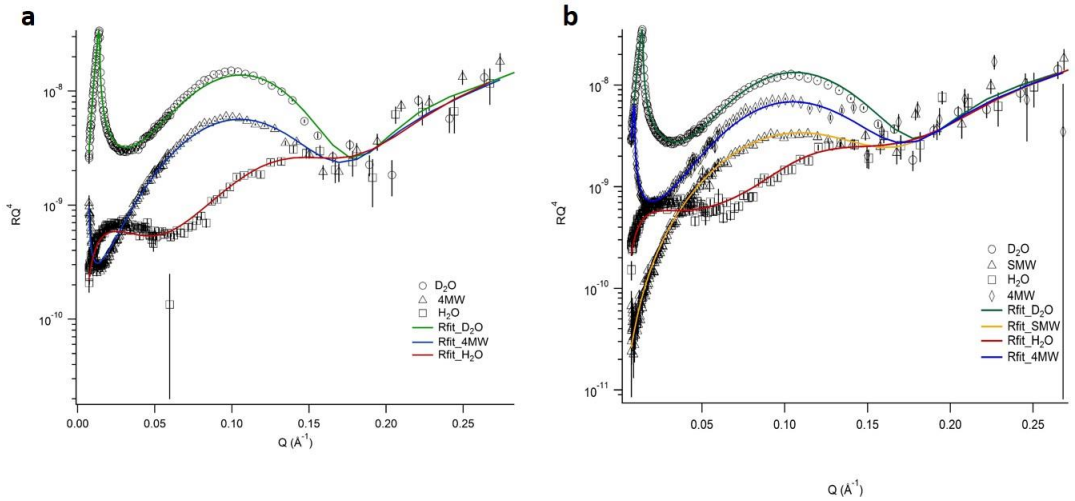

Figure 5.21 NR data describing the SLB after FBS flow (a) and *in situ* PS-COOH20 (b). Markers represent raw data, solid lines their simultaneous fittings by 6-layers model. The proteins layer exposed to the bulk phase was simplified assuming FBS composed by Albumin molecules.

Table 5.11 Proteins induced structural changes on SLB. Model without constrains (Rfit) was applied. The parameters describing the SiO_2 layer and the roughness of the layers were kept constant to evaluate the effects on thicknesses (t) and solvent penetration degrees (φ).

Layer (L)	t [Å]			Φ		
	SLB	FBS	IS NPs	SLB	FBS	IS NPs
2	11.7	12.8	12.6	56.0	41.9	49.3
3	14.3	13.9	14.3	2.8	1.9	6.9
4	14.3	13.9	14.3	2.8	1.9	6.9
5	6.6	6.4	6.3	35.1	20.0	33.6
6	---	50.1	62.9	---	98	98

IS NPs are PS-COOH20 NPs in 55% FBS initially in D_2O; Layer 2 is the inner head group; Layer 3 is the inner tail group; Layer 4 is the outer tail group; Layer 5 is the outer head group. SLDs (10^{-6} Å^{-2}) for L6 were in both experiments FBS and IS NPs: 2.3 (D_2O), 2.1 (4MW), 1.8 (SMW), 1.7 (H_2O); t is the thickness; φ is the solvent penetration degree.

5.6.4 Proteins effect on the SLB: HC PS-COOH20

The effect on SLB structure of HC PS-COOH20 NPs was also studied. HC NPs were isolated by UC according to the procedure described in Chapter . QCM-D measures did not highlight any change due to HC NPs, neither in the frequency shift nor in dissipation (paragraph *5.4.2*). NR study did not point out any relevant effect on the SLB, it can be seen on the raw data (Fig. 5.22) and in Table 5.12 where parameters describing fittings in Fig.5.23a-b. Only a small perturbation of the outer polar head can be seen from the fitting parameters. We can speculate that since the HC proteins constitute a resistant and stable shell around NPs characterized by low total surface free energy, any interaction with the SLB would be unfavourable and hence very limited. This result compared to FBS and *in situ* NPs data could suggest that the presence of a soft corona could in fact have a decisive role on the NPs interaction with lipid membranes.

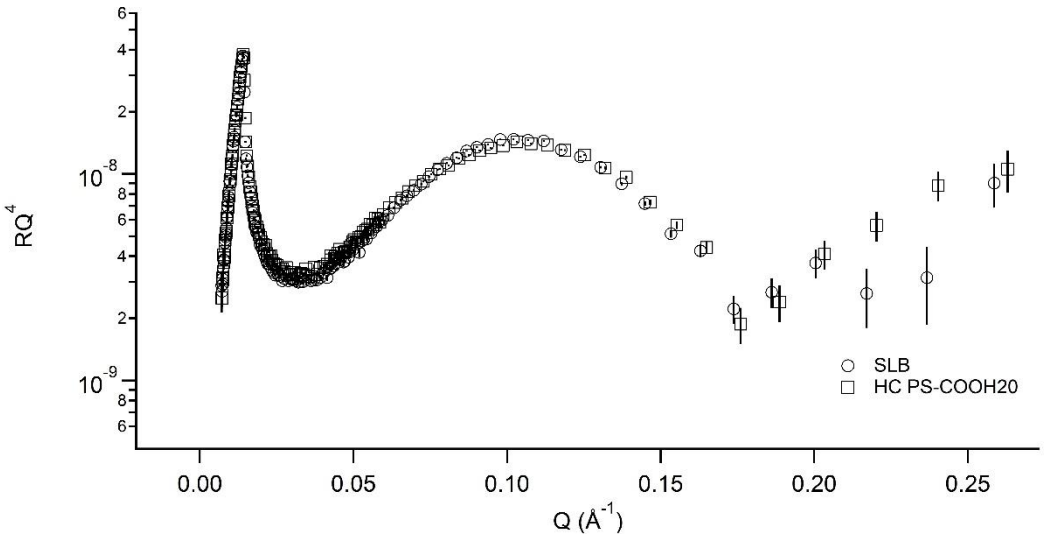

Figure 5.22 NR profiles for SLB (SLB) and the SLB after HC PS-COOH20. Data are presented as R $\mathbf{Q}^4$ vs **Q**.

Table 5.12 HC PS-COOH20 induced structural changes on SLB. Model with constrains (Gfit) was applied. The parameters describing the SiO_2 layer and the roughness of the layers were kept constant to evaluate the effects on thicknesses (t) and solvent penetration degrees (φ). Gfit parameters are obtained applying equations in paragraph *2.3.1.4.2*.

Layer (L)	t [Å]		φ	
	SLB	NPs	SLB	NPs
2	11.7	11.9	62.0	62.7
3	13.7	13.7	0.6	0.4
4	13.7	13.7	0.5	0.3
5	6.0	6.4	26.3	30.5

Layer 2 is the inner head group; Layer 3 is the inner tail group; Layer 4 is the outer tail group; Layer 5 is the outer head group. t is the thickness; φ is the solvent penetration degree.

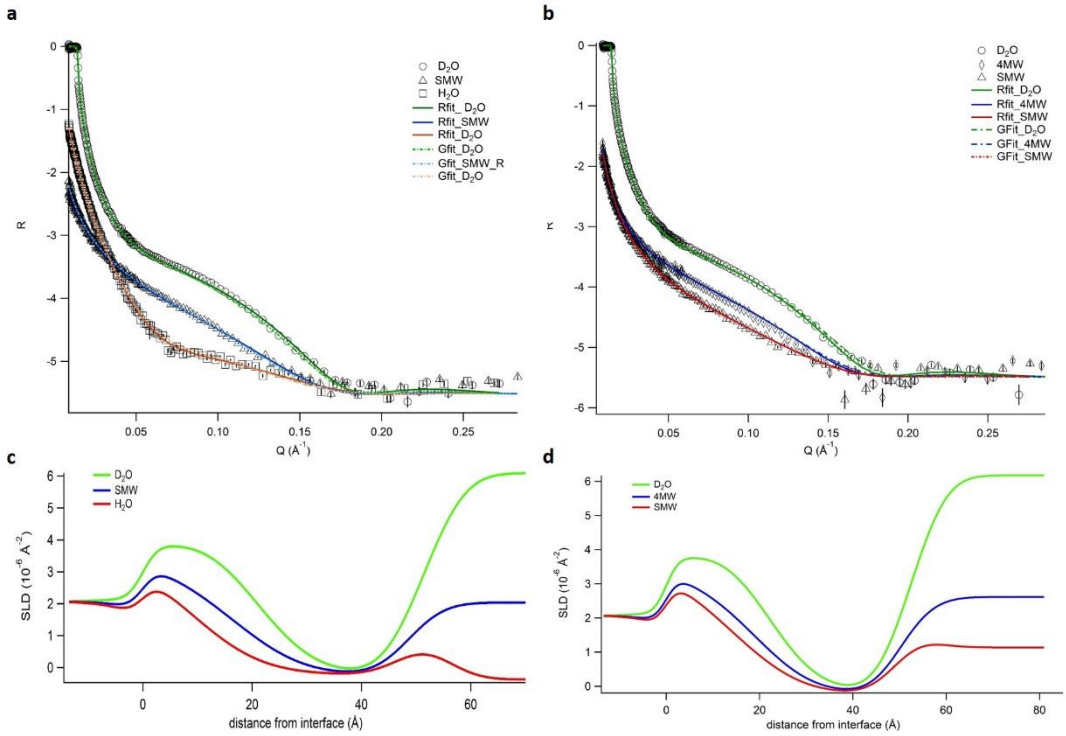

Figure 5.23 NR profiles for DOPC SLB (a) treated by HC PS-COOH20 and modelled by 5-layers model (b). Data are presented as log **(R)** vs **Q**. C-D) SLD profiles for SLB before and after NPs injection obtained from fittings in a-b) respectively.

5.7 Conclusions

In this chapter, NPs-membrane interactions were investigated. Supported lipid bilayers were used as model of cell membrane and in-flow experiments were performed to study the NPs effects on the film structure.

The first technique employed was QCM-D and several NPs in absence and presence of proteins were tested. Among pristine NPs only bigger carboxylated polystyrene NPs induced a permanent effect on the SLB. Due to consistent changes in SLB viscoelasticity properties, disruption was speculated as possible outcome. Smaller and pegylated NPs, both made by polystyrene and magnetite, did not significantly alter the SLB structure. The presence of proteins levelled the behaviour for all NPs, inducing a weak and unspecific adsorption on the SLB. The HC NPs seemed to do not interact with the SLB. However, imaging the QCM-D supports by fluorescence microscopy revealed a certain amount of fluorescence for all the samples.

The QCM-D technique proved to be not enough sensitive to describe the effect of certain NPs on the SLB. For this reason, neutron reflectometry study on the SLB was carried out. NR is a

powerful technique for characterizing films at the interfaces and it guarantees a resolution down to Angstrom level. Moreover, the setting up of the experiment is similar to that in QCM-D experiments making the comparison among the results more reliable. It was possible to discriminate different structural reorganizations of the lipids caused by the pristine NPs: SLB incubation with carboxylated PS-COOH20 NPs led to tails hydration and increase of APM, while for SLB treated with Fe_3O_4 NPs tails hydration with further swelling of the bilayer was observed. On the contrary, pegylated Fe_3O_4 NPs induced dehydration and shrinking of the bilayer. Pure FBS was found to induce dehydration and compression of the lipid packing as described in literature, but the presence of NPs in FBS generally caused increase of the SLB thickness with mild bilayer solvation. HC NPs did not induce any relevant change in the SLB structure. Proteins in the HC showed to have a lower attitude to interact with the SLB, while soft corona proteins, being loosely bound to NPs surface, were more incline to interact. Moreover, the little changes that were reported, although significant might have been affected by the intrinsic resilience of SLB formed on SiO_2 surface.

Overall, QCM-D results were not conclusive and coupling with other technique was necessary. Agreement between QCM-D and NR results was found, but NPs adsorption pointed out by fluorescence microscopy was not confirmed either by NR. That might be ascribed both to the vertical geometry of the chamber and the extensive solvent exchanges performed to characterize the same bilayer in several contrasts. We can conclude that careful evaluation of the experimental conditions is necessary when studying phenomena that produce effects at a scale smaller than nanometer. The next step would be elaborating membrane models closer to cell membrane (for example include in the SLB formulation cholesterol and membrane proteins) and then find a correlation between the results obtained with membrane models and endothelial cells to evaluate which effects seen on models are relevant in biological systems.

5.8 Bibliography

(1) Cheng, L.-C.; Jiang, X.; Wang, J.; Chen, C.; Liu, R.-S. *Nanoscale* **2013**, *5*, 3547.

(2) Verma, A.; Stellacci, F. *Small* **2010**, *6*, 12.

(3) Chen, Y.; Bothun, G. D. *Langmuir* **2011**, *27*, 8645.

(4) dos Santos, T.; Varela, J.; Lynch, I.; Salvati, A.; Dawson, K. A. *Small* **2011**, *7*, 3341.

(5) Shang, L.; Nienhaus, K.; Nienhaus, G. U. *Journal of Nanobiotechnology* **2014**, *12*, 5.

(6) Mhashal, A. R.; Roy, S. *PLoS ONE* **2014**, *9*, e114152.

(7) Leroueil, P. R.; Berry, S. A.; Duthie, K.; Han, G.; Rotello, V. M.; McNerny, D. Q.; Baker, J. R.; Orr, B. G.; Banaszak Holl, M. M. *Nano Letters* **2008**, *8*, 420.

(8) Li, Y.; Gu, N. *The Journal of Physical Chemistry B* **2010**, *114*, 2749.

(9) Kim, S. T.; Saha, K.; Kim, C.; Rotello, V. M. *Accounts of Chemical Research* **2013**, *46*, 681.

(10) Jing, B.; Zhu, Y. *Journal of the American Chemical Society* **2011**, *133*, 10983.

(11) Pelaz, B.; del Pino, P.; Maffre, P.; Hartmann, R.; Gallego, M.; Rivera-Fernández, S.; de la Fuente, J. M.; Nienhaus, G. U.; Parak, W. J. *ACS Nano* **2015**, *9*, 6996.

(12) Rocha, E. L. d.; Caramori, G. F.; Rambo, C. R. *Physical Chemistry Chemical Physics* **2013**, *15*, 2282.

(13) Walczyk, D.; Bombelli, F. B.; Monopoli, M. P.; Lynch, I.; Dawson, K. A. *Journal of the American Chemical Society* **2010**, *132*, 5761.

(14) Lesniak, A.; Salvati, A.; Santos-Martinez, M. J.; Radomski, M. W.; Dawson, K. A.; Åberg, C. *Journal of the American Chemical Society* **2013**, *135*, 1438.

(15) Dell'Orco, D.; Lundqvist, M.; Cedervall, T.; Linse, S. *Nanomedicine: Nanotechnology, Biology and Medicine* **2012**, *8*, 1271.

(16) Hirano, A.; Yoshikawa, H.; Matsushita, S.; Yamada, Y.; Shiraki, K. *Langmuir* **2012**, *28*, 3887.

(17) Hirano, A.; Uda, K.; Maeda, Y.; Akasaka, T.; Shiraki, K. *Langmuir* **2010**, *26*, 17256.

(18) Fleischer, C. C.; Payne, C. K. *The Journal of Physical Chemistry B* **2014**, *118*, 14017.

(19) Jiang, W.; Lai, K.; Wu, Y.; Gu, Z. *Arch. Pharm. Res.* **2014**, *37*, 129.

(20) Ritz, S.; Schöttler, S.; Kotman, N.; Baier, G.; Musyanovych, A.; Kuharev, J.; Landfester, K.; Schild, H.; Jahn, O.; Tenzer, S.; Mailänder, V. *Biomacromolecules* **2015**, *16*, 1311.

(21) Safi, M.; Courtois, J.; Seigneuret, M.; Conjeaud, H.; Berret, J. F. *Biomaterials* **2011**, *32*, 9353.

(22) Chen, K. L.; Bothun, G. D. *Environmental Science & Technology* **2014**, *48*, 873.

(23) Jing, Y.; Trefna, H.; Persson, M.; Kasemo, B.; Svedhem, S. *Soft Matter* **2014**, *10*, 187.

(24) Wang, B.; Zhang, L.; Bae, S. C.; Granick, S. *Proceedings of the National Academy of Sciences* **2008**, *105*, 18171.

(25) Schulz, M.; Olubummo, A.; Binder, W. H. *Soft Matter* **2012**, *8*, 4849.

(26) Ouberai, M. M.; Wang, J.; Swann, M. J.; Galvagnion, C.; Guilliams, T.; Dobson, C. M.; Welland, M. E. *Journal of Biological Chemistry* **2013**, *288*, 20883.

(27) Peetla, C.; Labhasetwar, V. *Molecular Pharmaceutics* **2008**, *5*, 418.

(28) Choi, S. Y.; Jeong, S.; Jang, S. H.; Park, J.; Park, J. H.; Ock, K. S.; Lee, S. Y.; Joo, S.-W. *Toxicology in Vitro* **2012**, *26*, 229.

(29) Dabkowska, A. P.; Michanek, A.; Jaeger, L.; Rabe, M.; Chworos, A.; Hook, F.; Nylander, T.; Sparr, E. *Nanoscale* **2015**, *7*, 583.

(30) Garnier, B.; Bouter, A.; Gounou, C.; Petry, K. G.; Brisson, A. R. *Bioconjugate Chemistry* **2009**, *20*, 2114.

(31) Hellstrand, E.; Grey, M.; Ainalem, M.-L.; Ankner, J.; Forsyth, V. T.; Fragneto, G.; Haertlein, M.; Dauvergne, M.-T.; Nilsson, H.; Brundin, P.; Linse, S.; Nylander, T.; Sparr, E. *ACS Chemical Neuroscience* **2013**, *4*, 1339.

(32) Arteta, M. Y.; Berti, D.; Montis, C.; Campbell, R. A.; Eriksson, C.; Clifton, L. A.; Skoda, M. W. A.; Soltwedel, O.; Koutsioubas, A.; Baglioni, P.; Nylander, T. *Soft Matter* **2015**, *11*, 1973.

(33) Belicka, M.; Gerelli, Y.; Kucerka, N.; Fragneto, G. *Soft Matter* **2015**, *11*, 6275.

(34) Kurniawan, J.; Kuhl, T. L. *Langmuir* **2015**, *31*, 2527.

(35) Shen, H.-H.; Lake, V.; Le Brun, A. P.; James, M.; Duff, A. P.; Peng, Y.; McLean, K. M.; Hartley, P. G. *Biomaterials* **2013**, *34*, 8361.

(36) Richter, R.; Mukhopadhyay, A.; Brisson, A. *Biophysical Journal* **2003**, *85*, 3035.

(37) Slotte, J. P. *Progress in Lipid Research* **2013**, *52*, 424.

(38) Zwang, T. J.; Fletcher, W. R.; Lane, T. J.; Johal, M. S. *Langmuir* **2010**, *26*, 4598.

(39) Zhang, S.; Gao, H.; Bao, G. *ACS Nano* **2015**.

(40) Keiji Kanazawa, K.; Gordon, J. G. *Analytica Chimica Acta* **1985**, *175*, 99.

(41) Dixon, M. C. *Journal of Biomolecular Techniques : JBT* **2008**, *19*, 151.

(42) Montis, C.; Maiolo, D.; Alessandri, I.; Bergese, P.; Berti, D. *Nanoscale* **2014**, *6*, 6452.

(43) Li, Y.; Chen, X.; Gu, N. *The Journal of Physical Chemistry B* **2008**, *112*, 16647.

(44) Hou, W.-C.; Moghadam, B. Y.; Corredor, C.; Westerhoff, P.; Posner, J. D. *Environmental Science & Technology* **2012**, *46*, 1869.

(45) Bailey, C. M.; Kamaloo, E.; Waterman, K. L.; Wang, K. F.; Nagarajan, R.; Camesano, T. A. *Biophysical Chemistry* **2015**, *203–204*, 51.

(46) Zahr, A. S.; Davis, C. A.; Pishko, M. V. *Langmuir* **2006**, *22*, 8178.

(47) Nativo, P.; Prior, I. A.; Brust, M. *ACS Nano* **2008**, *2*, 1639.

(48) Liu, Y.; Zhang, Z.; Zhang, Q.; Baker, G. L.; Worden, R. M. *Biochimica et Biophysica Acta (BBA) - Biomembranes* **2014**, *1838*, 429.

(49) Pozzi, D.; Colapicchioni, V.; Caracciolo, G.; Piovesana, S.; Capriotti, A. L.; Palchetti, S.; De Grossi, S.; Riccioli, A.; Amenitsch, H.; Lagana, A. *Nanoscale* **2014**, *6*, 2782.

(50) Li, Y.; Kröger, M.; Liu, W. K. *Biomaterials* **2014**, *35*, 8467.

(51) Monopoli, M. P.; Walczyk, D.; Campbell, A.; Elia, G.; Lynch, I.; Baldelli Bombelli, F.; Dawson, K. A. *Journal of the American Chemical Society* **2011**, *133*, 2525.

(52) Gonzalez-Rodriguez, D.; Barakat, A. I. *PLoS ONE* **2015**, *10*, e0122097.

(53) Vandoolaeghe, P.; Rennie, A. R.; Campbell, R. A.; Nylander, T. *Langmuir* **2009**, *25*, 4009.

(54) Nagle, J. F.; Tristram-Nagle, S. *Biochimica et Biophysica Acta (BBA) - Reviews on Biomembranes* **2000**, *1469*, 159.

(55) Wiener, M. C.; White, S. H. *Biophys J* **1992**, *61*, 434.

(56) Hristova, K.; White, S. H. *Biophys J* **1998**, *74*, 2419.

(57) Kučerka, N.; Nagle, J. F.; Sachs, J. N.; Feller, S. E.; Pencer, J.; Jackson, A.; Katsaras, J. *Biophysical Journal*, *95*, 2356.

(58) Buehler, L. *Cell Membranes*; Taylor & Francis Group, 2015.

(59) Negoda, A.; Liu, Y.; Hou, W.-C.; Corredor, C.; Moghadam, B. Y.; Musolff, C.; Li, L.; Walker, W.; Westerhoff, P.; Mason, A. J. *International Journal of Biomedical Nanoscience and Nanotechnology* **2013**, *3*, 52.

(60) Wei, X.; Jiang, W.; Yu, J.; Ding, L.; Hu, J.; Jiang, G. *Journal of Hazardous Materials* **2015**, *287*, 217.

(61) Kettler, K.; Veltman, K.; van de Meent, D.; van Wezel, A.; Hendriks, A. J. *Environmental Toxicology and Chemistry* **2014**, *33*, 481.

(62) Le Brun, A. P.; Haigh, C. L.; Drew, S. C.; James, M.; Boland, M. P.; Collins, S. J. *Biophys J* **2014**, *107*, 2313.

(63) Caruso, F.; Möhwald, H. *Journal of the American Chemical Society* **1999**, *121*, 6039.

Chapter 6. Isolation of protein corona NPs from digestive fluids

6.1 Introduction

In Chapter 4, the protein corona (PC) of different NPs incubated in plasma or serum was investigated. Many studies on the PC isolated from blood have in fact been done due to the biomedical applications of most NPs that are administrated through the systemic route. In contrast, PCs formed in fluids other than blood, such as gastrointestinal (GI), have been less investigated even though they are of great interest for pharmacological and toxicological reasons.[1-3] However, the oral route is one of the most used for drug administration in clinics and it might be a probable route for the entrance of NPs in the human body given the large use of engineered nanomaterials (ENMs) also in food industry, as additives (flavour, texture, stability improvements)[4] and in packaging.[1,5,6]

The GI tract is a complex environment characterized by pH ranging from two to eight, high electrolyte concentrations, enzymes and food matrix that change dynamically. All those elements can affect NPs colloidal stability [7-9] and PC composition with consequences on bioavailability and toxicity.[10] Recently, core-shell gold NPs were shown to be subject of proteolytic enzymes and pH conditions in lysosomes when internalized by macrophages and endothelial cells. The shell was partially removed and PC was affected by the altered coating.[11] Moreover, Docter et al. in a recent review [12] highlighted the lack of reports about the influence of PC complexes on the GI tract albeit some studies revealed that upon NP exposure gut homeostasis was altered. This is mainly due to the experimental difficulty in isolating PC NPs from such a dynamic environment without modifying their properties. For example, Jahn *et al.*[13] studied the uptake of hemin-coupled iron hydroxide NPs on Caco-2 cells and speculated a strong effect due to the colloidal instability of such NPs in the medium, but they did not perform any stability study. Pereira *et al.*[14] found that Fe(III)-oxo hydroxide NPs formed ferrihydrite-like complexes after a simulated *in vitro* digestion. In this study PC NPs could not be isolated from GI fluids without promoting aggregation, so they used the approach to synthesize ferrihydrite complexes *ex novo* for studying their biological response on Caco-2 cells, bypassing the isolation of such NPs from digestive fluids. Finally Yang *et al.*[7] studied the behaviour of iron oxide NPs in GI fluids and observed their tendency to aggregate if specific surface coating (citrate ions) was not performed.

Several models have been proposed to simulate the digestion process. *In vivo* mammalian models have been used, but *in vitro* models are generally preferred because they are more versatile, less expensive and do not require ethical approval (The Organization for Economic Co-operation and Development, OECD, 2010). *In vitro* models can be dynamic when physical processing of the food and temporal changes of the gastrointestinal conditions (pH changes, enzymes and electrolytes concentrations) mimic the *in vivo* digestive process. They can be static when there are synthetic fluids that reproduce chemically and enzymatically the environmental conditions encountered in the distinct areas of the GI tract and the ratio meal/enzymes is kept constant.

The gap between *in vivo* and *in vitro* studies can be partially covered by cell culture models. Cell monolayers are often used to assess epithelial permeability of compounds. Immortalized Caco-2 cell lines are commonly used because they are able to form an adherent monolayer that shows some characteristics of the gut epithelium. Thus, translocation studies can be performed when they are grown on semi-permeable membranes mimicking the transport of substances from the gut lumen to the basolateral side.[2] Other models are based on Caco-2 co-culture with other cells that are able to express mucus.[15]

There are many studies on translocation of NPs across Caco-2 monolayers[2], but most of them deal with *in situ* NPs. Walczak *et al.*[16] investigated polymeric NP translocation in different *in vitro* models taking into account the formation of a corona upon exposure to complete cell medium. Afterwards, the same group showed that NPs, if subject of *in vitro* digestion, expressed a different corona upon contact with cell culture medium compared to pristine NPs.[17] On the other hand, Lichtenstein and co-workers [18] studied the impact of food on silver NPs digestion. They modified the *in vitro* digestion model of Bohmert et al. [9] by adding food components to the digestive fluid. They found that the corona originating from food digestion was able to stabilize NPs in full cell medium, while NPs digested without food extensively aggregated. They showed also that the NPs digested with food had similar uptake to undigested NPs, while those digested without food showed less uptake.

In this part of the thesis, we evaluated the PC originating from skimmed milk powder and common bread. We adopted a static *in vitro* model following INFOGEST recommendations as described in detail in paragraph *6.2*. The INFOGEST COST action network aimed to give some recommendations to achieve standard conditions for static *in vitro* digestion to allow comparison of results among research groups. [19] First, we verified if sucrose gradient UC was a suitable technique to recover the PC complexes from digestive fluids when a food matrix was added. Secondly, we optimized a protocol that aimed to mimic the *in vivo*

conditions in which NPs were subject of a complete simulated digestion in the presence of a bread matrix. The recovered PC complexes were characterized by size, surface charge and corona composition by Dynamic Light Scattering (DLS), Nanoparticles Tracking Analysis (NTA), SDS-PAGE and liquid chromatography- mass spectrometry (LC-MS). When it was possible, the traditional centrifugation protocol to recover PC NPs was applied and results compared. Finally, the effect of the PC on NP uptake and translocation through a Caco-2 monolayer was investigated in serum free environment to stress on the role of the PC formed during digestion. Confocal microscopy was used to assess eventual morphological alterations in the monolayer. Some of the results presented in this chapter are included in manuscripts attached in the appendix.[20]

6.2 INFOGEST protocol and stability of NPs in digestive fluids

The *in vitro* model to simulate digestion adopted in this work is based on INFOGEST recommendations.[19] The protocol aims to mimic the *in vivo* conditions that characterize oral, gastric and small intestinal phases, which are distinguished by a specific pH, electrolyte concentrations and particular enzymes. In Table 6.1, a summary of the electrolyte final concentrations in the simulated salivary fluid (SSF), simulated gastric fluid (SGF) and simulated intestinal fluid (SIF) is reported. The pH during the digestion was adjusted to pH 3 and pH 7 for SGF and SIF, respectively. The calcium salt solution was added to the final mixture of each phase to avoid precipitation in the electrolyte solutions.

Table 6.1 Electrolytes final concentrations in SSF, SGF, SIF according to INFOGEST recommendations.[19]

	SSF [mmol/l]	**SGF [mmol/l]**	**SIF [mmol/l]**
KCl	15.1	6.9	6.8
KH_2PO_4	3.7	0.9	0.8
$NaHCO_3$	13.6	25	85
NaCl	-	47.2	38.4
$MgCl_2(H_2O)_6$	0.15	0.1	0.33
$(NH_4)_2CO_3$	0.06	0.5	-
$CaCl_2(H_2O)_2$*	1.5	0.15	0.6

* It was added in the final mixture to avoid precipitation

The digestive simulation was performed at 37°C under magnetic stirring. The oral phase lasted for two minutes and α-amylase was not added to the mixture.[21] The gastric phase lasted for two hours: SGF and Porcine Pepsin (final activity 2000 U/ml, Sigma Pepsin, P7012) were added. In the duodenal phase SIF, bile salts (160 mM) and Pancreatin from porcine pancreas (final trypsin activity 100 U/ml, Sigma, P7545) were added to the mixture. Pancreatin in SIF formed a fibrous precipitate that was centrifuged at 4°C for one minute. Negligible loss of activity was assessed using the p-toluene-sulfonyl-L-arginine methyl ester (TAME) assay for trypsin activity.[22]

Carboxylated fluorescently labelled Fe_3O_4 NPs were used in this study. Their stability was tested in the simulated digestive fluids prior the addition of enzymes and food, thus before to be coated by a PC.

In Fig. 6.1, hydrodynamic size distribution trends are reported for Fe_3O_4 NPs in PBS, SSF and SGF. NPs in SIF immediately precipitated likely due to the high electrolyte concentration that shields NPs surface negative charge.[7,8,23,24,25] In SSF, the averaged hydrodynamic sizes of the NPs mostly increased with respect to those in PBS during the first hour of incubation, reaching a plateau with an average size almost double with respect to that of the starting NPs in PBS. PdI values were comparable to those in PBS. In SGF NP hydrodynamic sizes appeared to slowly increase over time to reach an average value almost three times larger than the starting one. On the other hand, PdI values appeared invariant with time. Overall, these results showed that when the NPs reach the gastric environment they form agglomerates of uniform dimensions.

6.3 Skimmed milk powder digestion

Skimmed milk powder (SMP) was used as food model to optimize hard corona (HC) recovery from digestion. Milk proteins represent a considerable proportion of human dietary proteins and for this reason the products of their GI digestion are well characterized.[26]

6.3.1 Simulated oral digestion

Simulated digestion was run using an AT-700 pH Stat Kyoto Electronic Manufacturing Company. SMP at a concentration of 34 mg/ml was mixed with SSF and $CaCl_2$ and diluted with ultrapure water to get the appropriate electrolyte concentration as described in Table 1. The mixture was kept under constant magnetic stirring at 37°C and the pH continuously monitored. After two minutes, an aliquot of digested chyme was sampled and incubated at 37°C with NPs to get a concentration of $1.5x10^{13}$ NPs/ml for one hour. Part of the mixture was

then separated by UC through a sucrose gradient 35-70% w/w run at 20°C for two hours at 188k rcf. Part of the mixture was centrifuged and washed for three times at 15.5k rcf at 4ºC and re-suspended in 500µl PBS at pH 7.4.

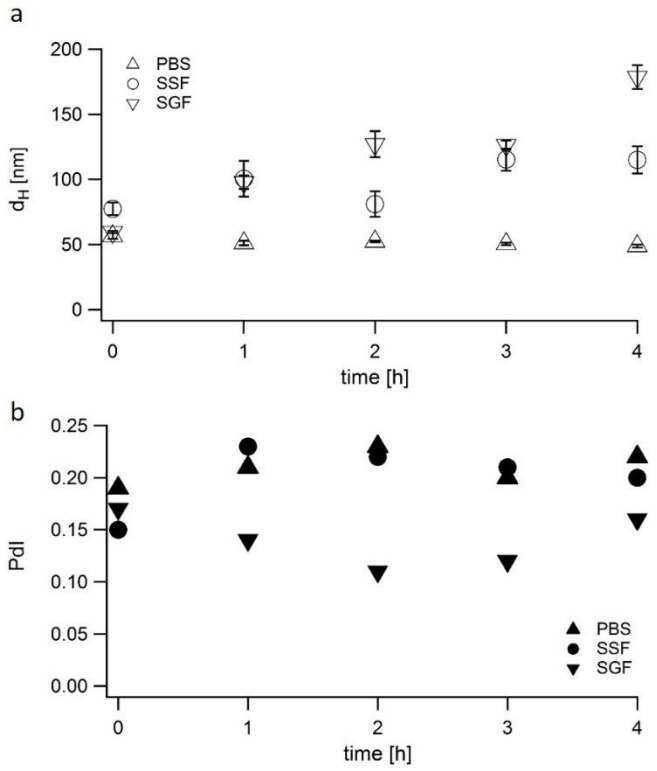

Figure 6.1 A) Hydrodynamic diameters variation by time for Fe_3O_4 NPs incubated in PBS (triangle), in SSF (circle) and SGF (upside-down triangle) at 37°C. B) PdI variation for the same samples. Hydrodynamic diameters and PdI were obtained by DLS from cumulant analysis of the auto-correlation data.

In Fig. 6.2 NPs recovered from UC (Fe_3O_4 S UC) and from conventional centrifugation (Fe_3O_4 S HC) are compared to the NPs *in situ.* Screening of UC aliquots by NTA showed that UC allowed the separation of protein-NP complexes from the digestion environment limiting NP agglomeration with respect to those recovered by conventional centrifugation/washing procedure (see Fig. 6.2). Although hydrodynamic diameters were very different for the two PC NPs, SDS-PAGE showed that the corona composition was very similar. In Fig. 6.3a, lanes named UC and HC present a very similar protein pattern especially at high molecular weights (MWs). Some bands are selectively found only in the UC isolated corona (40 and 12 kDa) but not in the HC sample or in the corresponding fractions from a control experiment run without NPs (1*-5* Fig. 6.3a).

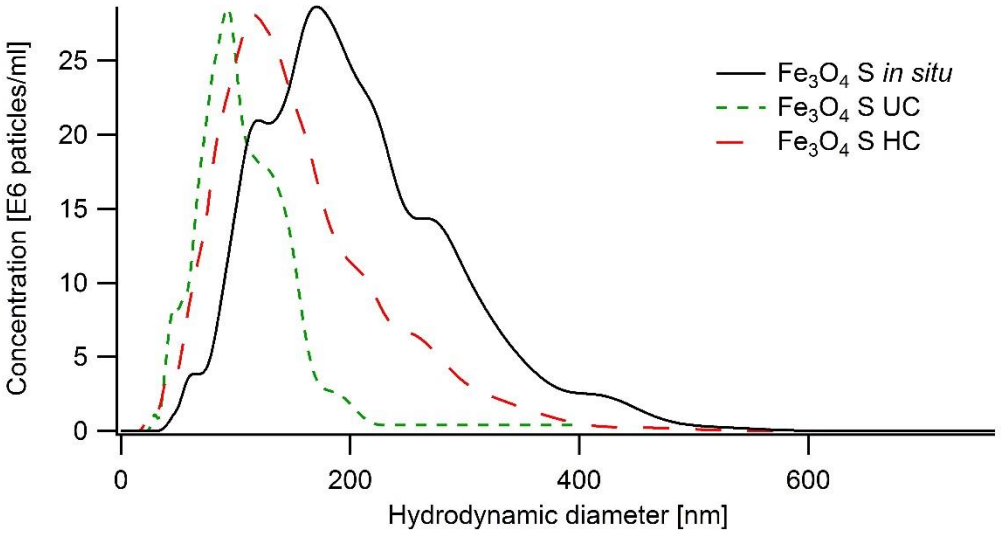

Figure 6.2 Hydrodynamic diameter distributions measured by NTA on NPs incubated in salivary mixture (black line), after UC (green dashed line) and after three centrifugation/washing steps (red dashed line).

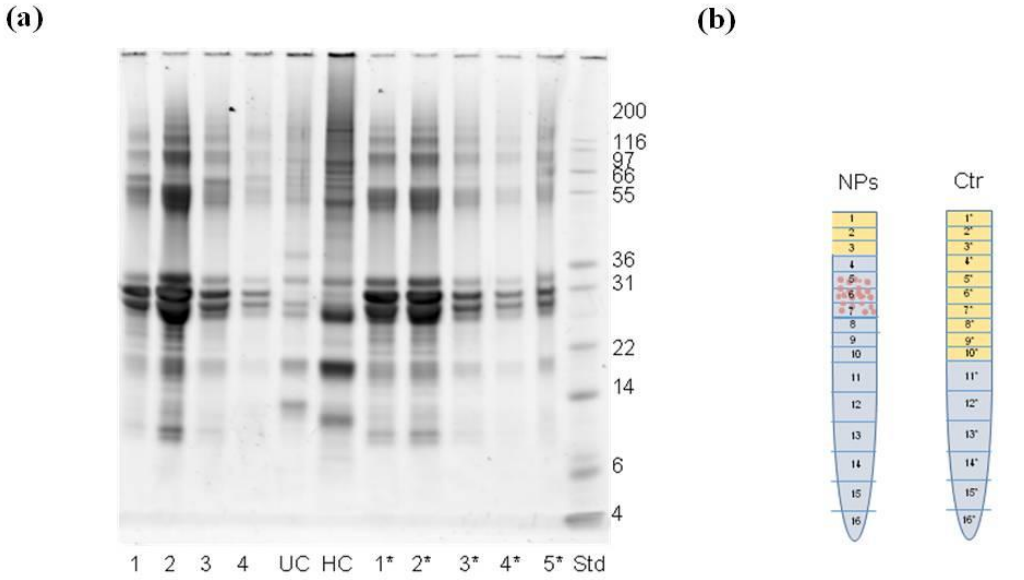

Figure 6.3 Fe_3O_4 NPs in simulated salivary fluid. a) SDS-PAGE of fractions 1;4 and 5-7 (joined together from UC, HC NPs isolated by centrifugation and 5 fractions from a control UC experiment without NPs (1*-5*). b) Schematic drawing of the sucrose layers arrangement in the UC tube showing where NPs and proteins were located in samples with NPs (NPs) and without NPs (Ctr).

6.3.2 Simulated gastric digestion

Gastric phase was started after two minutes of the oral phase by addition of SGF, 0.03 M $CaCl_2$, pepsin and pH was adjusted to 3 and monitored to assure stability. After two hours, an aliquot of digested chyme was taken and the enzymes were inactivated increasing the pH and

thus stopping the gastric digestion. NPs were added ($1.5x10^{13}$ NPs/ml) to the mixture and the incubation at 37°C for one hour promoted the corona formation. UC (188k rcf for 2 hours at 20°C, sucrose gradient 35-70% w/w) and standard centrifugation were performed on the mixture of NPs and digested food. In this case, both techniques led to isolation of complexes comparable in size between them and to *in situ* proteins-NPs complexes, as shows in Fig. 6.4a and resembling the NPs status *in situ.* However, PC composition as determined by SDS-PAGE, showed a quite different pattern. During standard centrifugation protocols, co-sedimentation of protein agglomerates and/or NP-protein aggregates can cause the presence of additional proteins not present in the PC in the recovered pellet loaded in the SDS-PAGE gel. Thus, the presence of additional proteins in the PC associated to the NPs recovered by normal centrifugation is likely due to this effect. While the UC procedure on sucrose gradient was able to separate protein agglomerates from PC NPs due to the different density of such complexes.

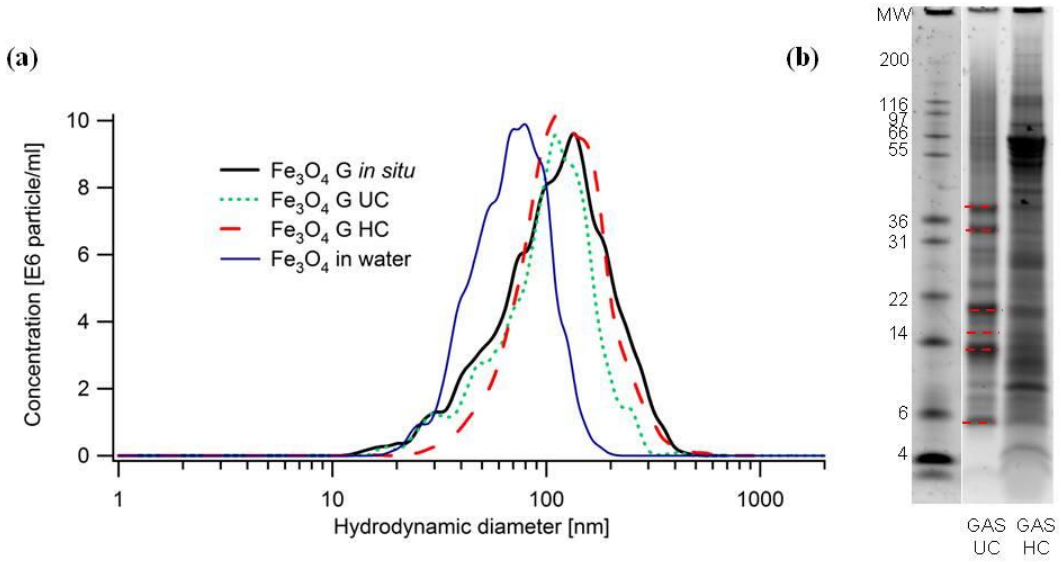

Figure 6.4 Fe_3O_4 NPs in simulated gastric fluid. a) Size distributions obtained from NTA for Fe_3O_4 NPs incubated with gastric fluids and relative PC complexes isolated by ultracentrifugation (UC) and centrifugation (HC). b) SDS-PAGE of the samples isolated by ultracentrifugation (UC) and conventional centrifugation (HC) methods, respectively, as indicated by the labels below the tracks of the gel. Red dashed lines on the gel highlighted bands analysed by LC-MS.

LC-MS analysis of UC isolated PC showed that they were mainly composed of pepsin (34 kDa), some selected peptides from β-casein hydrolysis at very low molecular weight (6 kDa),[27,28] α-lactalbumin (14.4 kDa) and β-lactoglobulin (18.4 kDa). HC protein pattern was characterized by some stronger bands at high MWs, consisting in a number of hydrolysed

fragments that were not easily identifiable[29] probably due to artefacts promoted by the centrifugation procedure such as induced aggregation and longer exposure times.[30-32]

6.4.3 Simulated duodenal digestion

The last phase of the simulated digestion is the one mimicking the small intestine. The environment is characterized by neutral pH, presence of bile salts and pancreatic enzymes. They are added as a mixture of extract of porcine pancreatin. After two hours of digestion, chyme was sampled and incubated with NPs ($1.5x10^{13}$ NPs/ml) at 37°C for one hour. In contrast to the other phases, conventional centrifugation methods did not allow the recovery of a population of PC complexes that could be well characterized. The rich environment composed of enzymes (trypsin, 23 kDa, and chymotrypsin, 25 kDa) and some persistent peptide agglomerates led to strong NP-protein aggregates that were hard to disperse after centrifugation (Fe_3O_4 D HC in Fig. 6.5). PC complexes could be isolated through UC (188k rcf for 2 hours at 20°C, sucrose gradient 35-70% w/w). In Fig. 6.5 NTA revealed that the *in situ* sample contained a wide range of particulates ranging from 200 nm to micron size. UC fractions containing PC complexes showed a small and relatively narrow population.

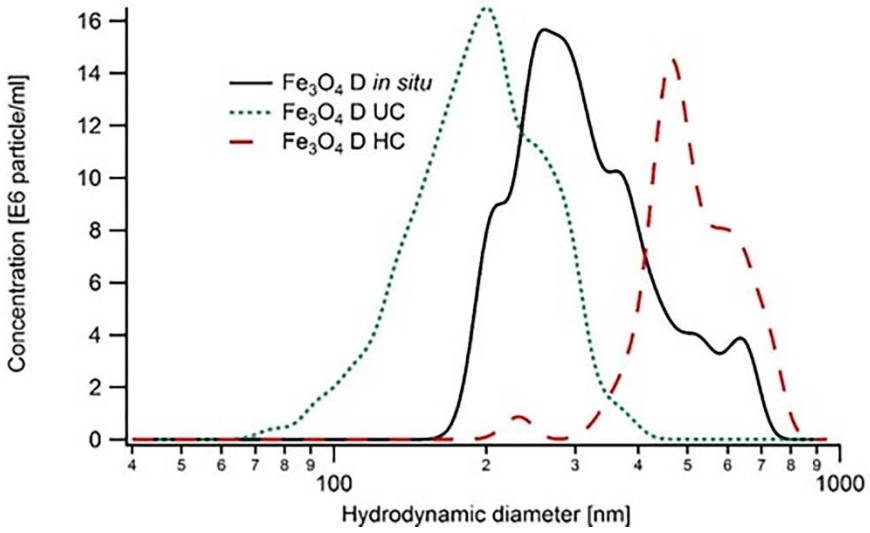

Figure 6.5 Fe_3O_4 NPs in SIF. Size distributions obtained from NTA analysis for NPs incubated with intestinal fluids for one hour and relative PC complexes isolated by ultracentrifugation (UC) and centrifugation (HC).

In Fig. 6.6, the PC is defined by SDS-PAGE. Two sucrose gradients were run, the first containing NPs in duodenal juice (Fig. 6.6a), the second only containing the digestive fluid (Fig. 6.6b and 6.6c). Sucrose layers arrangement is schematically reported in Fig. 6.6d. The first two sucrose fractions of both tubes (with and without NPs) contained the proteins and bile salts and the composition was similar with and without NPs (lanes 1-2, Fig. 6.6a and lanes 1*-

2*, Fig. 6.6b). In the sample without NPs protein bands started to be fainter going through the gradient from lower to higher density (3*-11*). In contrast, the gradient with NPs, lane 8 (Fig. 6.6a) was enriched with proteins. This band was brown indicating the presence of Fe_3O_4 NPs. Hard and soft PCs obtained by centrifuging the incubated NPs once and three times, respectively, were similar (lane HC and SC of Fig. 6.6a), but significantly different from the PC isolated by UC. The latter presented some notable bands at 21 kDa persistent from the gastric phase and chymotrypsin at 25 kDa. In the PC isolated from UC some bands at higher MWs were more pronounced compared to HC and SC isolated by centrifugation. According to the assigned molecular weights, being equally spaced it can be speculated that they are oligomers of a smaller fragment and SDS-PAGE allows separation of oligomers at high resolution.[33] The fragment might be the one at 4.9 kDa. In intestinal fluids bile salts are present and it has been reported that they cause desorption of proteins depending on their concentration and exposure time.[30,34,35] Therefore, the immediate separation between PC complexes and excess of fluid obtained by sucrose gradient UC is fundamental to prevent changes in the protein composition that instead occurred in standard centrifugation for which experimental time was longer.

6.4 Bread simulated digestion

The isolation of PC NPs complexes originating from NPs co-digested with bread is very interesting but challenging. In fact, bread is a common food in the daily diet but as all cereal-based foods it is a very complex matrix.[36] During a simulated digestion of bread, insoluble protein aggregates are formed particularly in the gastric phase. Hydrolysis converts them into low molecular weight peptides and small food particulates.

Recently, Lichtenstein and co-workers[18] performed simultaneous digestion of NPs, bread and other food. They studied the size and aggregation of *in situ* complexes by SAXS at the end of the duodenal phase, but HC NPs were not isolated and characterized in terms of composition and evolution over time. In this section, we have focused on the evolution of the NPs during the different phases of digestion with particular attention to the characterization of the structure and composition of the PC. The methodology based on sucrose gradient UC was exploited for successfully recovering PC-NP complexes from both gastric and duodenal phases. In particular, 0.5 g of minced bread was hydrated with 250 µl of Fe_3O_4 NPs ($5x10^{13}$ NPs/ml), SSF and 0.3 M $CaCl_2$.

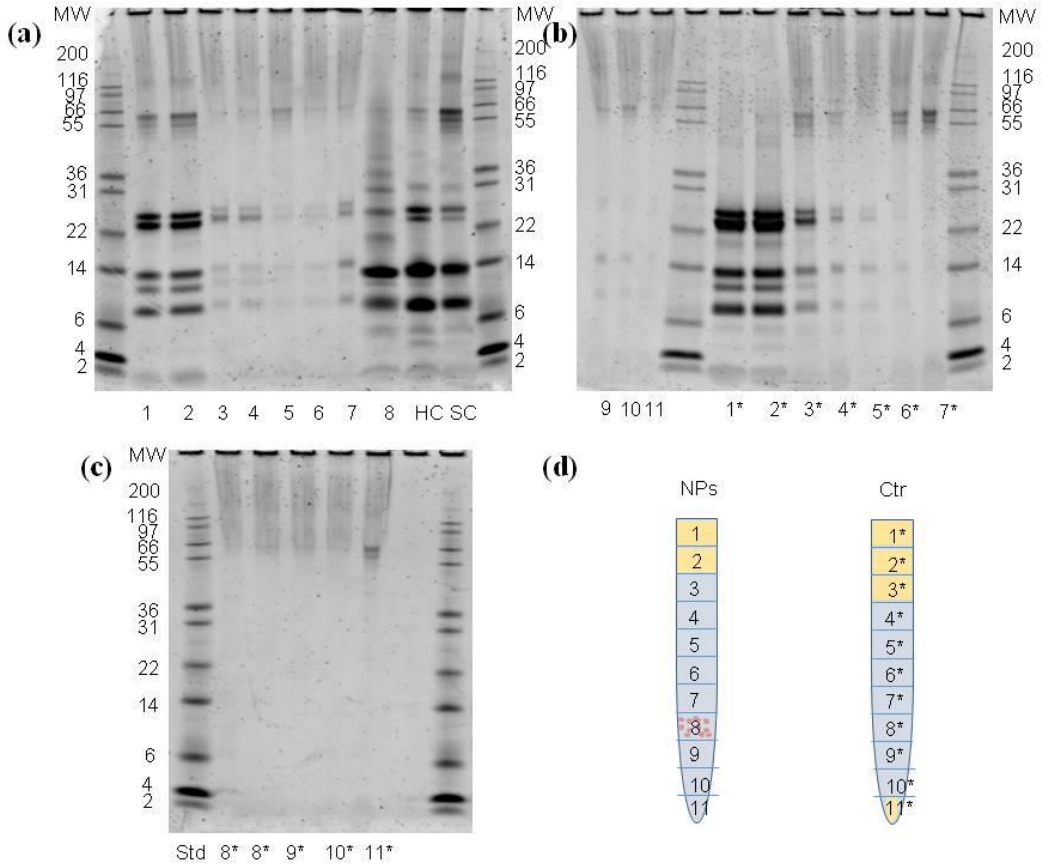

Figure 6.6 SDS-PAGE of Fe_3O_4 NPs in SIF. A) SDS-PAGE gel containing UC fractions of the sample of NPs incubated in intestinal fluids. Lane 8 contains the PC complexes; lanes labelled HC and SC contained SC and HC complexes, respectively, isolated by conventional methods. B-C) Control samples without NPs to show no contaminations from free proteins in the lanes with the PC complexes. D) Schematic drawing of the sucrose layers arrangement in the UC tube showing where NPs and proteins were located in samples with NPs (NPs) and without NPs (Ctr).

6.4.1 Simulated gastric digestion

The chyme was subjected to gastric digestion as described in paragraph 6.3 after two minutes of oral phase. An aliquot of the dispersion was taken and run through sucrose gradient by UC. The gradient was 6.6-66% w/w in sucrose and was run for one hour at 20°C at a speed of 48k rcf. The gradient density was optimized (wide sucrose concentration, slow speed and short time of centrifugation) to avoid co-localization of PC NPs and starch particulates. PC NPs were located at the top of the gradient correspondent to a sucrose concentration between 10% and 20% w/w (pink zone in Fig. 6.7a), while starch residues were spread in the gradient at higher densities (blue zone). Standard centrifugation protocols were attempted with different experimental conditions for separating PC NPs from starch residues without success. PC NPs recovered by UC were characterized by a hydrodynamic size about three/four time larger

compared to the size of the equivalent NPs in PBS as it is shown in Table 6.2. During digestion, NPs density decreased as can be inferred from NPs location in the sucrose gradient. Indeed, while pristine NPs moved to about 40% w/w sucrose concentration, the PC NPs reached the area between 10% and 20%. This is likely due to the formation of multi-particle protein agglomerates stabilized by the PC, which are characterized by a lower overall density depending on the partial specific volume and the frictional coefficient variations of the complexes.[37]

PC composition was determined by SDS-PAGE and LC-MS. In Fig. 6.7b the lane labelled as G-NP corresponds to the UC fractions where NPs subject of gastric digestion were found (fractions 2-5). This sample was clearly enriched with proteins when compared to the same fractions of the control without NPs (3G*, 5G*). Some bands of the PC around at 36-40 kDa (probably a mixture of polypeptides from albumins and globulins) were also found in the analogue lanes of the control sample (1G*-5G*), thus they might be contaminants from the environment and not associated to the corona.

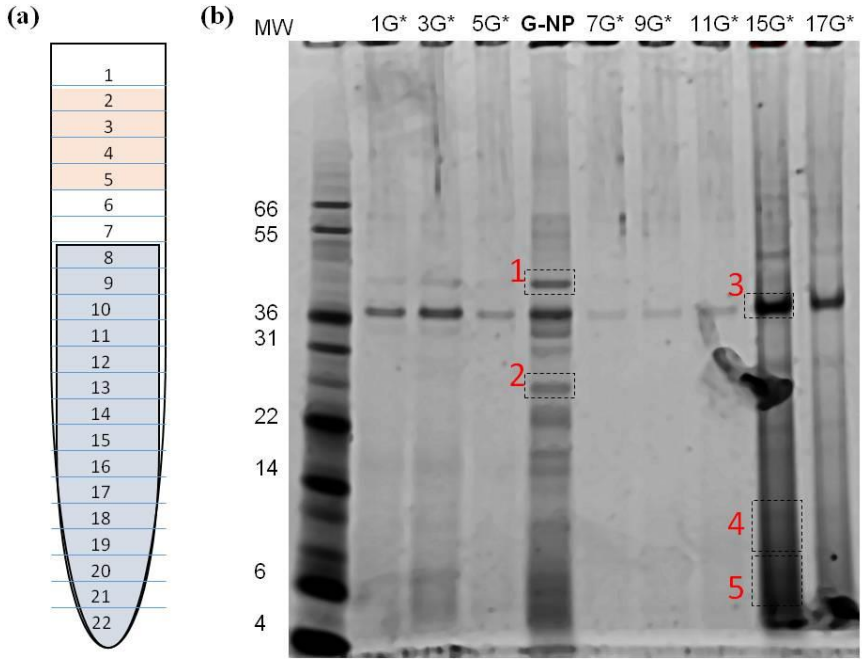

Figure 6.7 Simulated gastric digestion in presence of bread. A) Schematic drawing of the sucrose layers arrangement in the UC tube showing where NPs and proteins were located. Pink fractions (2-5) contained NPs while blue fractions contained floating starch residues. A control experiment only on digested bread without NPs underwent UC and it was sampled with the same modality. B) SDS-PAGE of PC-NPs obtained pooling together fractions 2-5 (G-NP lane) and some bands from the digestion run without NPs (lanes marked with* symbol). Some bands are framed with dashed lines and numbers and they were characterized by LC-MS.

Table 6.2 Characterization by DLS and NTA of Fe_3O_4 in PBS before undergoing digestion and PC complexes isolated by UC after dialysis (G-NPs).

	Fe_3O_4	**G-NPs**
d_H [nm][1]	73±8	245±13
SD [nm][2]	32±18	60±17
d_H [nm][3]	46.9±0.9	199.2±0.2
PdI[4]	0.20	0.26
Zp [mV]	-21.6±1.5	-4.3±0.2

[1] Hydrodynamic diameter (d_H) was calculated avaraging the hydrodynamic diameters of all NPs tracked in a particle-by-particle modality by NTA.
[2] SD is the standard deviation on all the hydrodynamic diameters measured in a particle-by-particle modality by NTA.
[3]Hydrodynamic diameter (d_H) obtained by DLS from the cumulant analysis of the auto-correlation data.
[4] Polydispertity indexes (PdI) were obtained by DLS from the cumulant analisys of the auto-correlation data.
All data were presented as the avarage of three indipendent measurements with relative standard deviation.

A characteristic protein pattern at M_W lower than 36 kDa is observed in the G-NP lane but not in the analogue lanes of the control (1G*-3G*-5G*). A similar protein pattern, but much more diffuse, appeared in the control sample in the higher density fractions where starch residues were clearly visible (15G*). Table 6.3 contains information about significant peptides recognized by LC-MS. Bands from control aliquots and the PC NPs were analysed. A mixture of peptides was present in each band. Peptides with high scores were listed. The score represents the probability that the match found is a random event; so the higher it is the more likely is the match. The corona was particularly enriched with albumins and globulins. Serpin-Z1a was found in band 1 (localized at a molecular weight of 43 kDa) and band 2 (localized at 25 kDa). Peptides from proteins with a lower M_W indicated the formation of peptide aggregates: GSP-1 Grain Softness Protein (17 kDa), albumin-2 (26 kDa) and Avenin-like A1 (19k Da). Lectin (26 kDa) was exclusively found in band 2. Legumin, Granule-bound Starch Synthase 1 and GSP-1 Grain Softness Protein were also revealed. Band 3 contained Pepsin and many peptides from yeast proteins. Band 4 and 5 mainly showed peptides from beta-amylase and 0.19 dimeric alpha-amylase inhibitor, albumin-2 and Serpin. Those wide bands were not present in the first 4 fractions of the control, but they can be seen in those of the PC NPs.

Table 6.3 Identification of protein bands extracted from gel shown in Fig.6.7b.

Name	Taxonomy	Coverage[1]	Score[2]	Nominal mass
		B1		
Serpin-Z1a	triticum aestivum	35	404	43262
Albumin-2	pisum sativum	58	276	26393
GSP-1 Grain Softness Protein	triticum aestivum	35	223	17494
Vicilin 47k	pisum sativum	37	188	49542
LegA class - Q9T0P5	pisum sativum	23	115	59153
Avenin-like a1	triticum aestivum	35	91	19513
		B2		
Serpin-Z1a	triticum aestivum	23	284	43262
Lectin	cicer arietinum	48	265	26363
Legumin	pisum sativum	26	265	59633
Vicilin 47k	pisum sativum	34	172	49542
GSP-1 Grain Softness Protein	Triticum turgidum	20	115	18701
		B3		
12S seed storage globulin 1	Triticum urartu	33	363	64230
Serpin-Z1a	triticum aestivum	27	313	43262
Adh1p	S. cerevisiae	51	322	37296
Malate dehydrogenase	triticum aestivum	37	315	35805

Name	Taxonomy	Coverage[1]	Score[2]	Nominal mass
Transaldolase	S. cerevisiae	53	299	37127
Ade1p	S. cerevisiae	69	255	34639
Phosphoglycerate kinase	S. cerevisiae	49	293	44768
Pepsine	Sus Scrofa	4	136	41635
	B4			
Beta amylase	Triticum urartu	49	1216	58995
0.19 dimeric alpha-amylase inhibitor	Aegilops tauschii	77	792	13881
Serpin-Z1a	Triticum aestivum	37	482	43262
Sucrose synthase 1	Aegilops tauschii	31	366	44300
Glucose-1-phosphate adenylyltransferase	Triticum aestivum	47	403	52400
Alpha amylase inhibitor CM3	Triticum durum	57	363	18893
Thioredoxin	S. cerevisiae	66	286	11311
	B5			
Beta amylase	Triticum urartu	52	772	58995
Albumin-2	pisum sativum	74	759	26393
0.19 dimeric alpha-amylase inhibitor	Aegilops tauschii	70	343	13881
Serpin-Z1a	Triticum aestivum	25	303	43262
Vicilin 47k	pisum sativum	47	264	49542

[1]Sequence coverage is calculated by dividing the number of amino acids observed by the protein amino acid length
[2]The score is a probability based score. The total score is the probability (P) that the observed match is a random event. Score = -10 x LOG_{10} (P)

6.4.2 Simulated duodenal digestion

Neutralization of the pH, addition of bile salts and porcine pancreatin according to the modality described in paragraph 6.3 determined the start of the duodenal digestion. The texture of the digestive mixture after two hours became liquid without solid residues. The agglomerates formed by NPs and peptides in the gastric phase partially disaggregate under duodenal conditions. UC on intestinal aliquots was performed for one hour at 195k rcf. After it, a brown band (D2-NPs) was visible at high sucrose concentration (fractions 14 to 16 at about 55% w/w sucrose concentration) as shown in Fig. 6.8a. NTA screening of all the fractions disclosed another population of PC NPs (D1-NPs) located from fraction 4 to 9. Bile and unbound low-density peptides were located at the top of the gradient. The two PC NPs populations were characterized by hydrodynamic diameters smaller than 150 nm: D1-NPs were about 20% smaller in hydrodynamic size compared to D2-NPs, but they had a sensibly different density. Both complexes were characterized by negative Zp, possibly because of the absorbance of bile salts on the surface (Table 6.4).

Table 6.4 Characterization by DLS and NTA of Fe_3O_4 in PBS before undergoing digestion and PC complexes isolated by UC after dialysis (D1- and D2-NPs).

	Fe_3O_4	**D1-NPs**	**D2-NPs**
d_H [nm][1]	73±8	116±14	143±17
SD[nm][2]	32±18	55±9	48±9
d_H [nm][3]	46.9±0.9	85.7±2.9	116.6±5.2
PdI [nm][4]	0.20±0.01	0.21±0.02	0.23±0.01
Zp [mV]	-21.6±1.5	-24.2±0.4	-16.1±1.2

[1] Hydrodynamic diameter (d_H) was calculated avaraging the hydrodynamic diameters of all NPs tracked in a particle-by-particle modality by NTA.
[2] SD is the standard deviation on all the hydrodynamic diameters measured in a particle-by-particle modality by NTA.
[3]Hydrodynamic diameter (d_H) obtained by DLS from the cumulant analysis of the auto-correlation data.
[4] Polydispertity indexes (PdI) were obtained by DLS from the cumulant analisys of the auto-correlation data.
All data were presented as the avarage of three indipendent measurements with relative standard deviation.

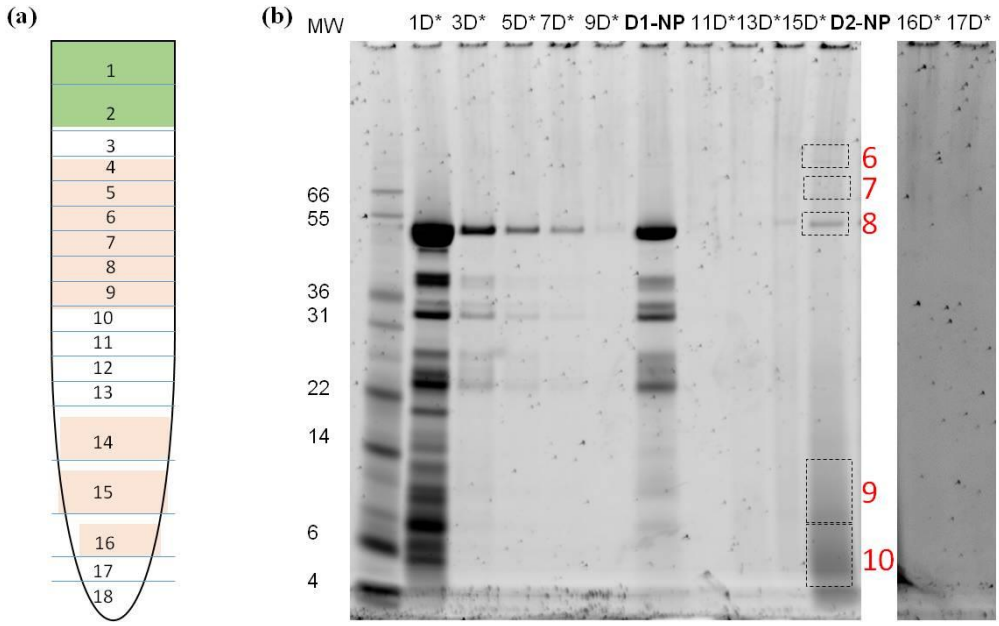

Figure 6.8 Duodenal simulated digestion in presence of bread. A) Schematic drawing of the sucrose layers arrangement in the UC tube showing where NPs and proteins were located. Green fractions contained bile salts and low density peptides. Pink fractions (4-9 and 14-16) contained NPs. A control experiment only on digested bread without NPs was also measured and investigated. B) SDS-PAGE of PC-NPs obtained pooling together fractions 4-9 and 14-16 (D1-NP and D2-NPs lanes respectively). Lanes labelled with* symbol contained aliquots from a control UC run without NPs. Some bands are framed with dashed lines and numbers and they were characterized by LC-MS.

In Fig. 6.8b PC profiles are shown. As expected many peptides were found in the first fraction and their presence in the sucrose tube decreases with increasing sucrose density and no peptides were detected in high-density sucrose bands (11D*- 17D*). The PCs associated with the complexes extracted by the two different fractions are completely different. The D1 PC was mainly composed of pancreatin enzymes (lipase and amylase at 55 kDa, trypsin and chymotrypsin at 24 kDa) as it can be expected based on the composition of the duodenal environment. The D2 PC was instead enriched with uncharacteristic proteins such as the band at 55 kDa and some other bands at higher Mws. Moreover, the diffuse band observed in the gastric sample seemed to be protected from digestion, while in the control sample without NPs the same bands in high-density fractions (15*-16*-17*D) were not detected.

According to LS-MS, the bands from B6 to B8 contained lipase and amylase, but also Adh1p and Phosphoglycerate kinase from yeast, lectin and vicilin 47k that were protected from duodenal digestion. The bottom bands B9 and B10 were rich in yeast enzymes, carrying peptides from gastric digestion that were not present in the control: albumin-2, amylase inhibitor, vicilin 47k and thioredoxin (Table 6.5). To the best of our knowledge, this is the first time that proteomic analysis of PC from food containing digestive juices has been described.

Moreover, the reported incomplete digestion of some proteins could have important biological implications considering that some of those peptides were recognized to be allergens[38] and could induce prolonged adverse reactions in the gut.

Table 6.5 Identification of protein bands extracted from gel shown in Fig.6.8b.

Name	Taxonomy	Coverage[1]	Score[2]	Nominal mass
		B6		
Enolase	S. cerevisiae	22	129	46830
Phosphoglycerate kinase	S. cerevisiae	27	126	44783
vicilin 47k	pisum sativum	18	109	49922
Lectin	Cicer arietinum	37	102	26363
Adh1p	S. cerevisiae	19	94	37296
		B7		
Adh1p	S. cerevisiae	20	98	37296
		B8		
Amylase	Sus Scrofa	45	824	20733
ATP synthase alpha chain	S. cerevisiae	43	434	55530
Pancreatic lipase	Sus Scrofa	52	328	52446
Adh1p	S. cerevisiae	38	156	37296
Phosphoglycerate kinase	S. cerevisiae	34	141	44768
Por1p	S. cerevisiae	20	116	30524

Name	Taxonomy	Coverage[1]	Score[2]	Nominal mass
		B9		
Phosphoglycerate kinase	S. cerevisiae	63	829	44768
Enolase	S. cerevisiae	44	707	46830
Tdh3p	S. cerevisiae	52	610	35825
Pyruvate kinase	S. cerevisiae	51	531	54909
Adh1p	S. cerevisiae	54	361	37296
Dimeric alpha-amylase inhibitor	triticum dicoccoides	29	213	15904
Legumin a2	pisum sativum	26	268	59633
Thioredoxin	S. cerevisiae	53	260	11311
		B10		
Phosphoglycerate kinase	S. cerevisiae	57	1008	44768
Eno 2	S. cerevisiae	51	957	46993
Pyruvate kinase	S. cerevisiae	61	86	54909
Tdh3p	S. cerevisiae	59	743	358825
Adh1p	S. cerevisiae	56	676	37296
Dimeric alpha-amylase inhibitor	triticum dicoccoides	49	215	15666
Pancreatic colipase	Sus Scrofa	45	287	12702
Thioredoxin	S. cerevisiae	66	277	11311

[1]Sequence coverage is calculated by dividing the number of amino acids observed by the protein amino acid length
[2]The score is a probability based score. The total score is the probability (P) that the observed match is a random event. Score = -10 x LOG_{10} (P)

6.4.3 Caco-2 transport experiment

There are many articles about uptake and translocation of NPs through monolayers of Caco-2 cells[13,39] or co-cultures that produce mucus.[40] Brun *et al.*[41] described titanium oxide NPs uptake in Caco-2 mono and co-cultures and in mice, studying the PC composition of NPs incubated in 10% serum proteins and subjected of simulated digestion. However, all these studies did not report detailed description of isolated PC NPs from digestive juices. Also Walczak *et al*.[16,17] highlighted the role of the PC, formed upon exposure to complete cell medium, on Caco-2 uptake. Lichtenstein and co-workers, [18] on the other hand, pointed out the importance of a food matrix during NPs *in vitro* digestion showing that the formation of the PC imparted colloidal stability to the NPs in the GI fluids.

In the previous paragraphs, we showed the successful recovery of PC complexes from bread after *in vitro* simulated digestion. They differed by hydrodynamic size, Zp and PC composition. Uptake and translocation of those complexes were studied and compared to those of the pristine Fe_3O_4 NPs using Caco-2 monolayer grown in transwell dishes.

6.4.3.1 NPs translocation through a transwell dish without cells

The pore size of the membrane on the transwell dish was 0.4 μm, thus some of the PC NPs could be too large to cross it or also Van der Waals attractive forces could limit their transmembrane diffusion.[42,43] Hence, the ability of the PC complexes to pass through the membrane of the transwell dish was first investigated. Moreover, small molecules such as carboxyfluorescein (CF) and fluoresceinamin (FA) were used to assess the integrity of the membrane.

The transwell dish was treated as if there were cells present: it was pre-incubated with full medium for one hour at 37°C. It was washed with PBS before adding NPs. All samples were prepared diluting 1:1 with serum free medium (SFM) to avoid additional effects of the FBS proteins. Several concentrations of NPs were tested (Fe_3O_4 $2x10^{12}$ NPs/ml, G-NPs $3x10^{12}$ NPs/ml, D1-NPs $2x10^{11}$ NPs/ml, D2-NPs $5x10^{11}$ NPs/ml), while FA and CF were loaded at 10^{-3} mg/ml.

In Fig. 6.9 fluorescence emission of aliquots from the basolateral chamber at 1, 2, 3, 4 hours of incubation and from the apical solution at the beginning and at the end of the experiment are reported.

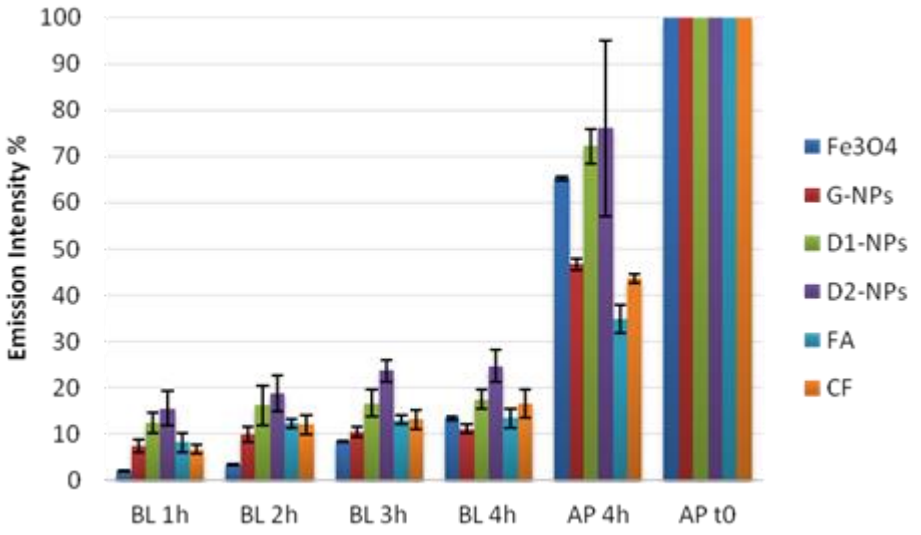

Figure 6.9 Fluorescence emission intensities for samples from the basolateral chambers after 1, 2, 3, and 4 hours of incubation (BL 1h, 2h, 3h, 4h) and for the apical chambers at the beginning of the experiment (AP t0) and after 4 hours (AP 4h). Fluorescence emission was measured with a plate reader with excitation wavelength at 492 nm and emission at 520 nm. Data are the average of three different replicates and they are normalized to AP t0.

Fluorescence emission of the apical chamber solutions decreased after 4 hours for all samples, while emissions from the basolateral chamber increased over time. PC NPs were able to translocate through the membrane with different rates of translocation also in comparison to the controls (CF and FA) that were in contrast similar. Interesting is the case of the gastric PC NPs (G-NPs) that, although characterized by the largest hydrodynamic sizes, showed the highest fluorescent intensity decrease after 4 hours in the apical chamber compared to duodenal PC complexes. That might be due to the structure of the G-NPs complexes that could be particularly flexible and enhance the ability to cross the basal membrane: in fact, the complexes were characterized by low density (see Fig. 6.7) and we can speculate that they were enriched in proteins. The two duodenal samples had similar translocation. In Table 6.6 are reported the vectorial transport ratios defined as the ratio between the apical and basolateral chambers amounts of NPs and molecules. Concentrations were evaluated by fluorescence calibrations curves (reported in appendix). Vectorial ratios resulted close to the unit for controls (CF and FA), slightly lower than the unit for G-NPs and D1-NPs, while D2-NPs was characterized by a value of 0.6. A vectorial ratio of 1 means that after four hours, equilibrium between the two chambers was reached. Values lower than the unity means a shift towards the basolateral chamber that was more pronounced for D2-NPs probably due to higher sedimentation.

Table 6.6 Vectorial transport ratio obtained from the molar ratio or the number of NPs ratio (Fe_3O_4, G-NPs, D1-NPs, D2-NPs) measured in the apical and basolateral chambers.

	CF	FA	Fe_3O_4	G-NPs	D1-NPs	D2-NPs
Vectorial transport ratio	1.06±0.03	1.08±0.01	0.83±0.12	0.93±0.04	0.95±0.08	0.61±0.22

6.4.3.2 NPs translocation through a Transwell dish with Caco-2 monolayer

Cell monolayer was grown as described in paragraph *2.4.1*. NPs were incubated at a concentration of $2x10^{12}$ NPs/ml for four hours and the electrical integrity of the monolayer was tested at the beginning and at the end of the experiment. As it is shown in Fig. 6.10, the decrease of TEER values in all samples is comparable to the control (PBS in Fig. 6.10) and it was not enough to suggest either disruption of the tight junctions or cell death as already observed in previous NP uptake experiments on Caco-2 monolayers.[18]

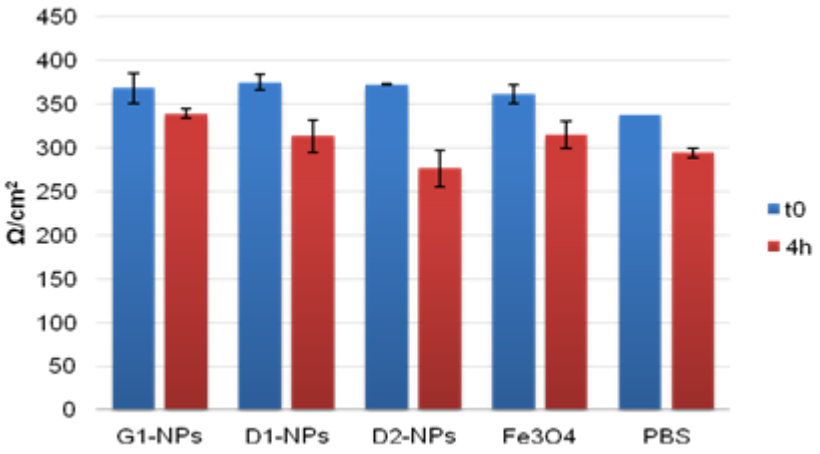

Figure 6.10 Changes of TEER values before and after incubation of NPs for 4 hours.

Fluorescence detection of the NPs in the basolateral chambers was not possible. The measured fluorescence values were similar to the background. Since we showed the passage of NPs through the membrane without cells, the adhesion of NPs to the support membrane can be excluded. However, NPs can agglomerate inside the cells and can be transcytosed in larger aggregates that would not pass through membrane pores.[44,45]

Fluorescence measurements on the apical media recovered after the incubation did not allow reliable NPs quantification. The fluorescence emissions were higher than the starting values

even for the control without NPs. Several parameters could affect the fluorescence signal of the apical media such as loosely adherent cells floating in the recovered solutions, NPs aggregates and fluorescence emission due to molecules in the media or excreted by the cells (e.g. riboflavin).[46]

6.4.3.3 Confocal imaging of Caco-2 monolayer

Fluorescence measurements on NPs incubated with the Caco-2 monolayer were not able to clarify whether uptake took place. TEM is the technique that gives better results in terms of morphology resolution allowing direct visualization of the inside of the cells with sub-cellular organelles and the apical surface with microvilli,[18,41,44,45], but sample preparation is very laborious and can lead to artefacts. Confocal microscopy can give a qualitative picture of the system,[47,48] elucidating NPs localization inside or outside cell membrane, as well as their passage through the pores of the insert membrane. For these reasons we decided to image the samples through confocal microscopy.

In Fig. 6.11, an overview of Caco-2 monolayers is displayed. F-Actin filaments were stained with phalloidin (red colour). Nuclei were stained in blue with Hoechst dye. Control samples incubated with PBS and CF were characterized by normal cell architecture with integrity of actin skeleton and tight junctions. Slight alterations of the actin network were acknowledged in the sample treated with pristine NPs (Fe_3O_4), while aberrations in membrane morphology were evident for all the samples treated with PC NPs.

In Fig. 6.12, the uptake of pristine Fe_3O_4 NPs in PBS is shown. The morphology of nuclei and actin filaments delimiting cells seems similar to the control, although invaginations in the membrane appeared (Fig. 6.12b). NPs seemed to accumulate at the intersections among adjacent cells and induce alteration in the membrane tight junctions. The amount of NPs taken up is quite low and some clusters are visible in the upper part of the cytoplasm.

Figure 6.13 is a collection of images highlighting features of the monolayer treated with G-NPs. TEER measurements did not highlight disruption of the tight junctions, but their integrity seems compromised and many vesicles appeared in the apical membrane (Fig. 6.13a and 6.13b). NPs were quite dispersed and big clusters inside the cytoplasm were not found. Many NPs accumulated between the basal membrane of the cells and the polyester membrane support. In Fig. 6.13c, a high density of NPs clusters is observed with a view from the bottom of the basal membrane and in Fig. 6.13d, the passage of NPs through the porous channels is

confirmed with a 3D rendering of a stack in the orthogonal direction from the top of the cells going through the support membrane.

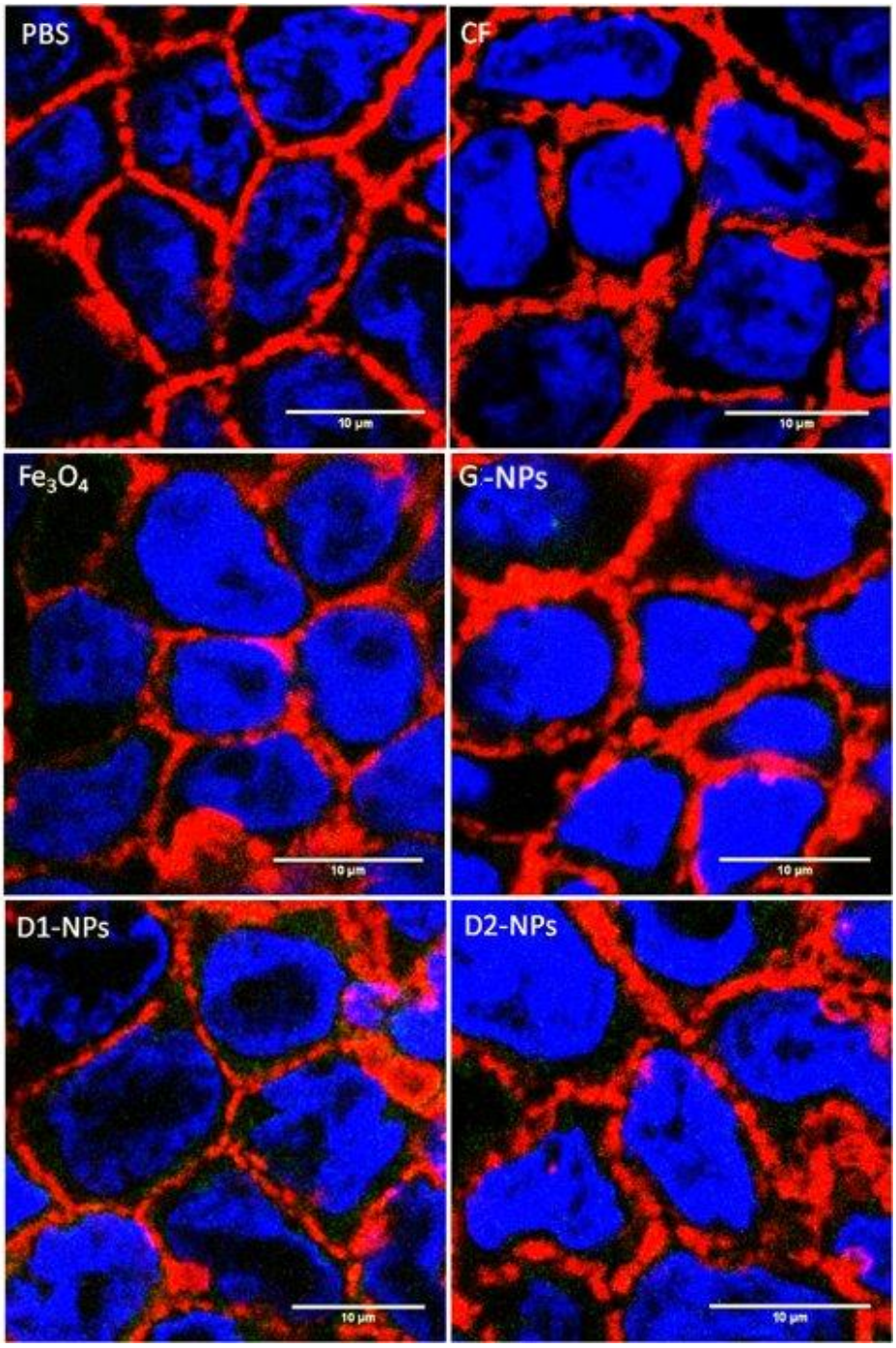

Figure 6.11 Confocal snapshots of Caco-2 monolayer after four hours of incubation with SFM:PBS 1:1 (PBS), Carboxyfluorescein (CF), bare Fe_3O_4 (Fe_3O_4), PC complexes isolated from gastric (G-NPs) and duodenal digestion (D1-NPs and D2-NPs). F-Actin filaments were stained by Phalloidin- Texas Red (591/608 nm) and nuclei by Hoechst 33342 (350/461 nm). Fe_3O_4 NPs were labelled by BODIPY FL-EDA (500/510 nm). Images were rendered using ImageJ.

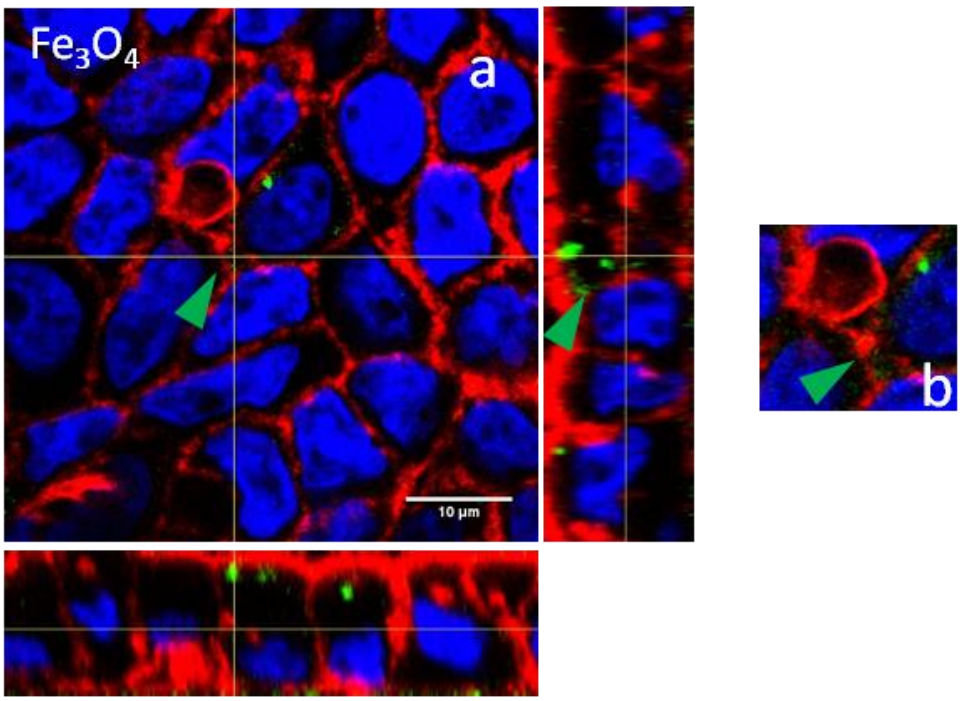

Figure 6.12 Confocal stacks of pristine NPs incubated monolayer. A) Orthogonal stacks of the cells. B) Zoomed detail highlighted by green arrow. Actin filaments were stained by Phalloidin- Texas Red (591/608 nm) and nuclei by Hoechst 33342 (350/461 nm). Fe_3O_4 NPs were labelled by BODIPY FL-EDA (500/510 nm). Images are rendered by ImageJ.

D1-NPs were present in the cells mainly as clusters enclosed in vesicles formed from the apical membrane as showed in Fig 6.14a and 6.14c with an orthogonal stack and a top view of the monolayer, respectively. However, most of the NPs are located between the basal and the support membranes and at the top of the porous channels (Fig. 6.14b). Likely, in this case channels were blocked by the formation of clusters larger than pore nominal size. Fluorescent green regions were mainly located in the upper part of the support and not in the lower part.

In Fig. 6.15, D2-NPs incubated cells are shown in detail. Big clusters were found in vesicles between cells (layer 4 of Fig 6.15d-e-f) and on the bottom of the cells as shown in Fig. 6.15b and 6.15c. A peculiar feature of D2-NPs treated cells was the presence of vesicles and invaginations found at level of the basal membrane highlighting trancytosis. For this sample, the orthogonal view in Fig. 6.15a displays the status of the membranes very close to the insert membrane and in Fig.15d clusters that co-localize with those vesicles at the level of the basal membrane are shown (Fig. 6.15d, layer 19d-f).

Those kinds of alterations could not be revealed by TEER as the values did not change significantly [18] as shown in Fig. 6.10. Brun and co-workers [41] showed that also titanium oxide

NPs did not affect TEER values for monolayers indicating membrane integrity and unaffected paracellular transport of cells, but they also showed for the same samples metabolic abnormalities, oxidative stress and DNA damage.[9,25,49] PC composition might have a role in the morphological alterations encountered: some peptides found in the corona of G-NPs such as serpin, alpha-amylase inhibitor, and lectin were digestion-protected and were found in the corona of D2-NPs. Those proteins were recognized to be allergens[38] and the presence of gliadin-derived peptides cannot be excluded. Gliadins are the gluten water-soluble component and the derived peptides have been proved to induce cytotoxicity and apoptosis in Caco-2 cells with particular effect on membrane proteins and redox activities.[50,51] However, more studies are necessary to investigate these speculations and prove the real involvement of the PC in these effects.

Confocal microscopy confirmed uptake of digested NPs and it was generally higher for PC NPs than for pristine Fe_3O_4 NPs. This effect of NP uptake enhancement induced by the PC is in agreement with other data in literature. Indeed cationic USPIONs,[40] polystyrene NPs,[52] polymeric NPs,[53] silver NPs[18] and pegylated core-shell NPs[54] were reported to show higher cellular uptake when bearing a PC but, in all these studies, the PC originated from plasma or serum. While paracellular transport can be excluded given the size of the NPs, transcytosis was confirmed especially in D2-NPs incubated cells displaying vesicles in close proximity to the basal membrane. Multiple endocytic energy-dependent routes (e.g. clathrin, calveolin mediated endocytosis) can be speculated[48,13] given the differences in size, density and corona composition of the PC complexes.

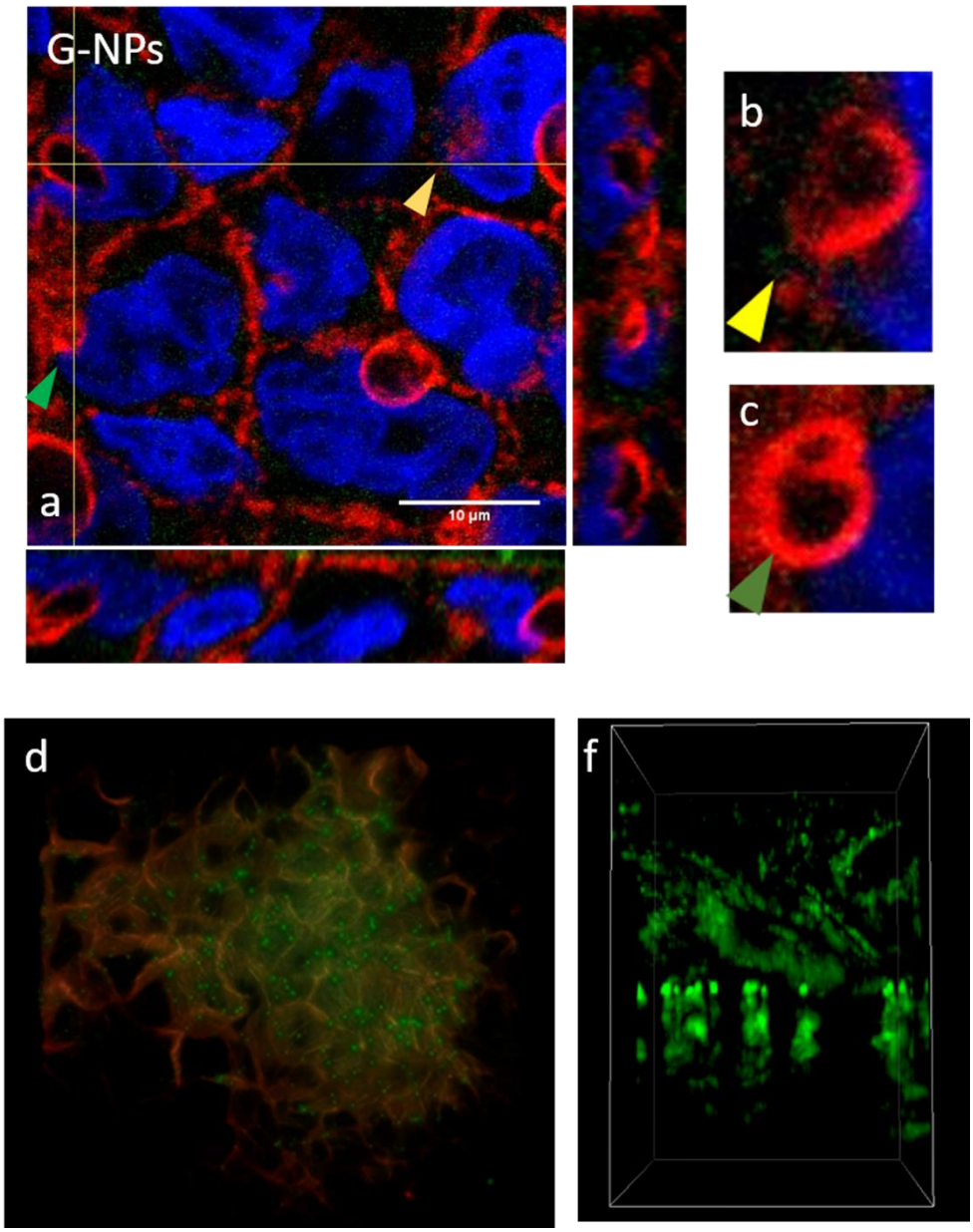

Figure 6.13 Confocal stacks of G-NPs incubated Caco-2 monolayer. A) Orthogonal stacks and some zoomed details (b-c) highlighted by arrows. D) View from the bottom of the monolayer; f) stack in the zeta direction in which is visible the cell skeleton auto- fluorescing in green and porous channels containing green labelled NPs. Actin filaments were stained by Phalloidin- Texas Red (591/608 nm) and nuclei by Hoechst 33342 (350/461 nm). Fe_3O_4 NPs were labelled by BODIPY FL-EDA (500/510 nm).

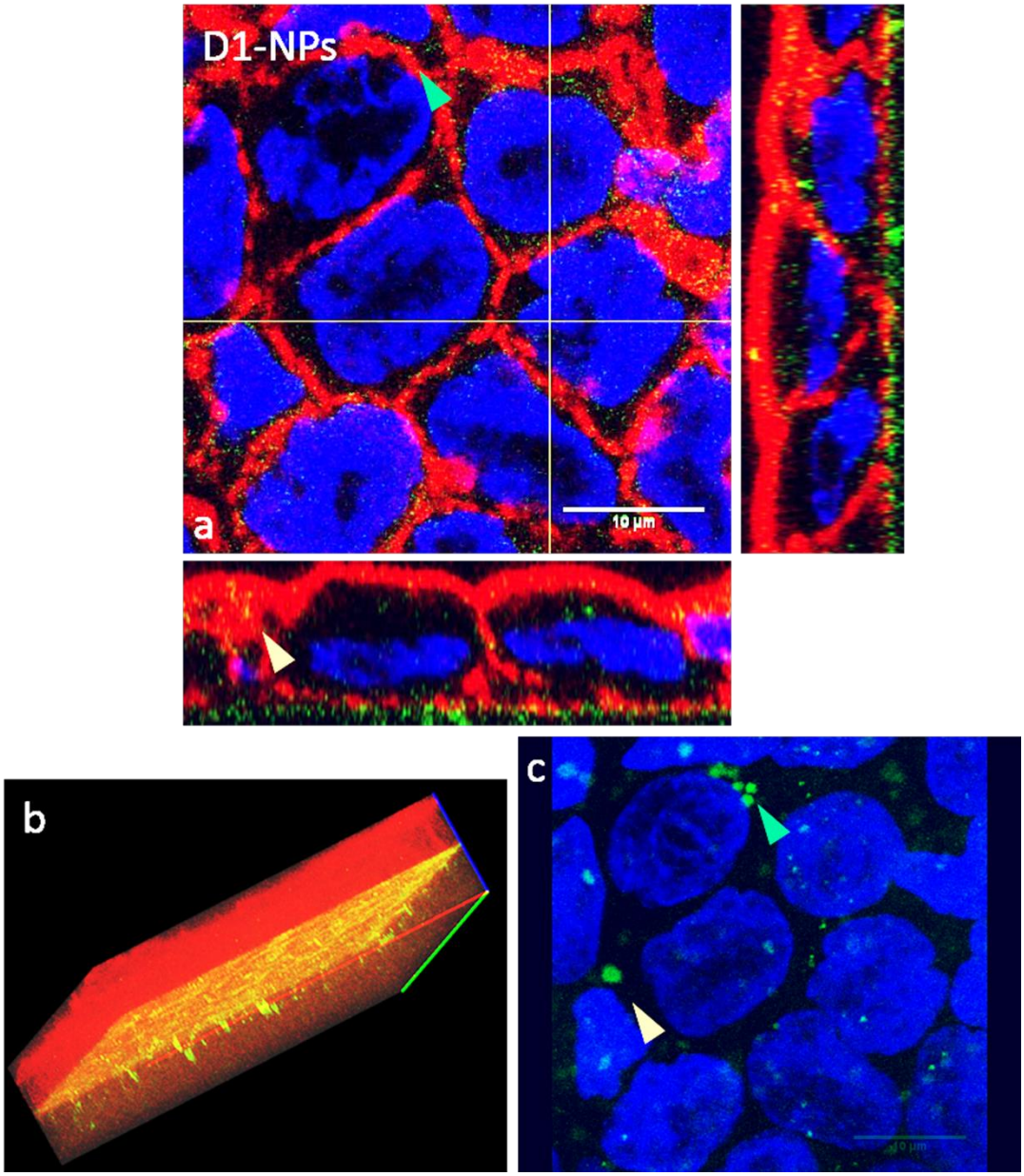

Figure 6.14 Confocal stacks of D1-NPs incubated monolayer. A) Orthogonal stacks of Caco-2 cells and some highlighted details. B) 3D reconstruction of cells skeleton, NPs and support membrane. C) Nuclei and NPs clusters viewed from the top. Arrows show same details in a different prospective. Actin filaments were stained by Phalloidin- Texas Red (591/608 nm) and nuclei by Hoechst 33342 (350/461 nm). Fe_3O_4 NPs were labelled by BODIPY FL-EDA (500/510 nm). Rendering was done by ImageJ.

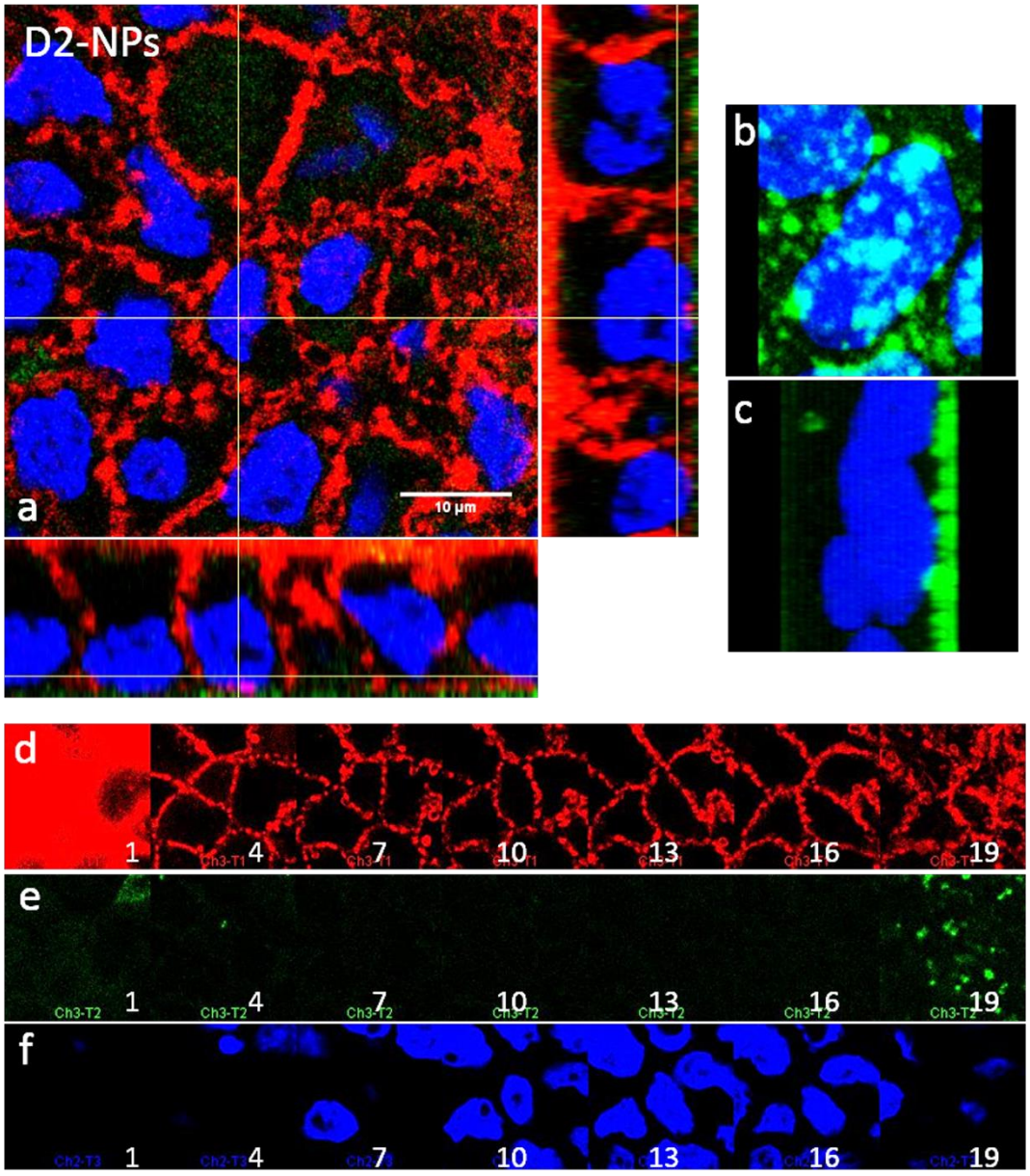

Figure 6.15 Confocal stacks of D2-NPs incubated monolayer. A) Orthogonal stacks of Caco-2 cells in the XY, YZ, XZ planes. B-C) view from the bottom and the side of the monolayer showing nuclei and NPs. D-E-F) sequence of layers from 1 to 19 divided in the three channels, red (actin), green (NPs) and blue (nuclei) respectively. Actin filaments were stained by Phalloidin- Texas Red (591/608 nm) and nuclei by Hoechst 33342 (350/461 nm). Fe_3O_4 NPs were labelled by BODIPY FL-EDA (500/510 nm). Rendering was done by ImageJ.

6.5 Conclusions

In this chapter, PC complexes from complex food matrixes were investigated. First of all, NP stability was tested in fluids simulating digestion phases (oral, gastric and duodenal) and combination of high ionic strength with pH conditions were found to affect NPs colloidal stability.

When NPs were incubated with digested skimmed milk powder proteins, a PC was formed. The possibility to recover proteins-NP complexes by sucrose gradient UC was explored, given the rich nature of the protein mixture. PC NPs recovered from gastric fluid seemed to be only slightly affected by the isolation procedure, UC versus conventional centrifugation, in terms of size (similar hydrodynamic sizes and size distributions), while PC composition was quite different. For duodenal mixture, differences were more pronounced. Protein agglomerates of high density in standard centrifugation co-precipitated with NPs modifying PC composition and promoting the formation of aggregates. Exploiting differences in density and size among proteins aggregates and PC complexes, UC allowed the recovery of monodispersed PC NPs.

The versatility of UC technique allowed the recovery of NPs when they were co-digested with bread matrix. Adjusting the gradient density, the speed and duration of the centrifugation, effective separation of PC complexes from bread particulate was possible. The PC NPs formed during the different phases of the digestion were dissimilar in size and corona composition. Some corona proteins were shown to resist the digestion extending their transition time in the gut. This finding can be relevant for the study of peptides that cause immunological response like in celiac disease or in toxicological evaluations.

In the last part of the chapter, corona effects on NP uptake and translocation across a Caco-2 cell monolayer were evaluated. Although NP uptake in Caco-2 cells was not quantified, it was confirmed that the corona enhanced the uptake of magnetite NPs in agreement with previous results reported in the literature for other NPs bearing plasma or serum derived coronas. Different coronas induced different alterations in the cell morphology. UC-based isolation of PC-NP complexes was useful to recover several PC NPs population and to remove the excess of GI fluids that were shown to induce a certain level of cytotoxicity in previous results. [18] It is likely that differences in size, density and corona composition for the various PC-NP complexes may lead to different routes of uptake and translocation that need to be further investigated.

To the best of our knowledge there are no works in which NPs subjected to simulated digestion in the presence of food matrix were isolated from the digestive chyme and characterized in terms of corona composition and structure to evaluate their effect on cell morphology and uptake.

6.6 Bibliography

(1) Clift, M. J. D.; Bhattacharjee, S.; Brown, D. M.; Stone, V. *Toxicology Letters* **2010**, *198*, 358.

(2) Lefebvre, D. E.; Venema, K.; Gombau, L.; Valerio, L. G.; Raju, J.; Bondy, G. S.; Bouwmeester, H.; Singh, R. P.; Clippinger, A. J.; Collnot, E.-M.; Mehta, R.; Stone, V. *Nanotoxicology* **2014**, 1.

(3) Setyawati, M. I.; Tay, C. Y.; Leong, D. T. *Small* **2015**, *11*, 3458.

(4) Borel, T.; Sabliov, C. M. *Annual Review of Food Science and Technology* **2014**, *5*, 197.

(5) Maiorano, G.; Sabella, S.; Sorce, B.; Brunetti, V.; Malvindi, M. A.; Cingolani, R.; Pompa, P. P. *ACS Nano* **2010**, *4*, 7481.

(6) Peng, Q.; Zhang, S.; Yang, Q.; Zhang, T.; Wei, X.-Q.; Jiang, L.; Zhang, C.-L.; Chen, Q.-M.; Zhang, Z.-R.; Lin, Y.-F. *Biomaterials* **2013**, *34*, 8521.

(7) Yang, S.-C.; Paik, S.-Y.-R.; Ryu, J.; Choi, K.-O.; Kang, T. S.; Lee, J. K.; Song, C. W.; Ko, S. *Food Chemistry* **2014**, *161*, 185.

(8) Zimmermann, E.; Müller, R. H. *European Journal of Pharmaceutics and Biopharmaceutics* **2001**, *52*, 203.

(9) Böhmert, L.; Girod, M.; Hansen, U.; Maul, R.; Knappe, P.; Niemann, B.; Weidner, S. M.; Thünemann, A. F.; Lampen, A. *Nanotoxicology* **2013**, *8*, 631.

(10) Hadjidemetriou, M.; Al-Ahmady, Z.; Mazza, M.; Collins, R. F.; Dawson, K.; Kostarelos, K. *ACS Nano* **2015**.

(11) Kreyling, W. G.; Fertsch-Gapp, S.; Schäffler, M.; Johnston, B. D.; Haberl, N.; Pfeiffer, C.; Diendorf, J.; Schleh, C.; Hirn, S.; Semmler-Behnke, M.; Epple, M.; Parak, W. J. *Beilstein Journal of Nanotechnology* **2014**, *5*, 1699.

(12) Docter, D.; Westmeier, D.; Markiewicz, M.; Stolte, S.; Knauer, S. K.; Stauber, R. H. *Chemical Society Reviews* **2015**, *44*, 6094.

(13) Jahn, M. R.; Shukoor, I.; Tremel, W.; Wolfrum, U.; Kolb, U.; Nawroth, T.; Langguth, P. *Journal of Pharmacy and Pharmacology* **2011**, *63*, 1522.

(14) Pereira, D. I. A.; Mergler, B. I.; Faria, N.; Bruggraber, S. F. A.; Aslam, M. F.; Poots, L. K.; Prassmayer, L.; Lönnerdal, B.; Brown, A. P.; Powell, J. J. *PLoS ONE* **2013**, *8*, e81250.

(15) Ensign, L. M.; Cone, R.; Hanes, J. *Advanced Drug Delivery Reviews* **2012**, *64*, 557.

(16) Walczak, A. P.; Kramer, E.; Hendriksen, P. J. M.; Tromp, P.; Helsper, J. P. F. G.; van der Zande, M.; Rietjens, I. M. C. M.; Bouwmeester, H. *Nanotoxicology* **2015**, *9*, 453.

(17) Walczak, A. P.; Kramer, E.; Hendriksen, P. J. M.; Helsdingen, R.; van der Zande, M.; Rietjens, I. M. C. M.; Bouwmeester, H. *Nanotoxicology* **2015**, *9*, 886. (18)

Lichtenstein, D.; Ebmeyer, J.; Knappe, P.; Juling, S.; Böhmert, L.; Selve, S.; Niemann, B.; Braeuning, A.; Thünemann A. F.; Lampen, A. *Biological Chemistry* **2015**, *396*, 1255.

(19) Minekus, M.; Alminger, M.; Alvito, P.; Ballance, S.; Bohn, T.; Bourlieu, C.; Carriere, F.; Boutrou, R.; Corredig, M.; Dupont, D.; Dufour, C.; Egger, L.; Golding, M.; Karakaya, S.; Kirkhus, B.; Le Feunteun, S.; Lesmes, U.; Macierzanka, A.; Mackie, A.; Marze, S.; McClements, D. J.; Menard, O.; Recio, I.; Santos, C. N.; Singh, R. P.; Vegarud, G. E.; Wickham, M. S. J.; Weitschies, W.; Brodkorb, A. *Food & Function* **2014**, *5*, 1113.

(20) Di Silvio, D.; Rigby, N.; Bajka, B.; Mayes, A.; Mackie, A.; Baldelli Bombelli, F. *Nanoscale* **2015**, *7*, 11980

(21) Woolnough, J. W.; Bird, A. R.; Monro, J. A.; Brennan, C. S. *International Journal of Molecular Sciences* **2010**, *11*, 2780.

(22) Hummel, B. C. *Canadian Journal of Biochemistry and Physiology* **1959**, *37*, 1393.

(23) Frenkel, Y. V.; Clark, A. D.; Das, K.; Wang, Y.-H.; Lewi, P. J.; Janssen, P. A. J.; Arnold, E. *Journal of Medicinal Chemistry* **2005**, *48*, 1974.

(24) Peters, R.; Kramer, E.; Oomen, A. G.; Herrera Rivera, Z. E.; Oegema, G.; Tromp, P. C.; Fokkink, R.; Rietveld, A.; Marvin, H. J. P.; Weigel, S.; Peijnenburg, A. A. C. M.; Bouwmeester, H. *ACS Nano* **2012**, *6*, 2441.

(25) Bergin, I. L.; Witzmann, F. A. *International journal of biomedical nanoscience and nanotechnology* **2013**, *3*, 10.1504/IJBNN.2013.054515.

(26) Picariello, G.; Miralles, B.; Mamone, G.; Sánchez-Rivera, L.; Recio, I.; Addeo, F.; Ferranti, P. *Molecular Nutrition & Food Research* **2015**, *59*, 948.

(27) Macierzanka, A.; Sancho, A. I.; Mills, E. N. C.; Rigby, N. M.; Mackie, A. R. *Soft Matter* **2009**, *5*, 538.

(28) Defernez, M.; Mandalari, G.; Mills, E. N. C. *ELECTROPHORESIS* **2010**, *31*, 2838.

(29) Kitabatake, N.; Kinekawa, Y.-I. *Journal of Agricultural and Food Chemistry* **1998**, *46*, 4917.

(30) Docter, D.; Distler, U.; Storck, W.; Kuharev, J.; Wünsch, D.; Hahlbrock, A.; Knauer, S. K.; Tenzer, S.; Stauber, R. H. *Nat. Protocols* **2014**, *9*, 2030.

(31) Monopoli, M. P.; Aberg, C.; Salvati, A.; Dawson, K. A. *Nat Nano* **2012**, *7*, 779.

(32) Monogioudi, E.; Faccio, G.; Lille, M.; Poutanen, K.; Buchert, J.; Mattinen, M.-L. *Food Hydrocolloids* **2011**, *25*, 71.

(33) Liu, C.; Sawaya, M. R.; Eisenberg, D. *Nat Struct Mol Biol* **2011**, *18*, 49.

(34) Winuprasith, T.; Chantarak, S.; Suphantharika, M.; He, L.; McClements, D. J. *Journal of Colloid and Interface Science* **2014**, *426*, 333.

(35) Maldonado-Valderrama, J.; Woodward, N. C.; Gunning, A. P.; Ridout, M. J.; Husband, F. A.; Mackie, A. R.; Morris, V. J.; Wilde, P. J. *Langmuir* **2008**, *24*, 6759.

(36) Hoebler, C.; Lecannu, G.; Belleville, C.; Devaux, M.-F.; Popineau, Y.; Barry, J.-L. *International Journal of Food Sciences and Nutrition* **2002**, *53*, 389.

(37) Calabretta, M.; Jamison, J. A.; Falkner, J. C.; Liu, Y.; Yuhas, B. D.; Matthews, K. S.; Colvin, V. L. *Nano Letters* **2005**, *5*, 963.

(38) Akagawa, M.; Handoyo, T.; Ishii, T.; Kumazawa, S.; Morita, N.; Suyama, K. *Journal of Agricultural and Food Chemistry* **2007**, *55*, 6863.

(39) Zariwala, M. G.; Elsaid, N.; Jackson, T. L.; Corral López, F.; Farnaud, S.; Somavarapu, S.; Renshaw, D. *International Journal of Pharmaceutics* **2013**, *456*, 400.

(40) Kenzaoui, B. H.; Vilà, M. R.; Miquel, J. M.; Cengelli, F.; Juillerat-Jeanneret, L. *International Journal of Nanomedicine* **2012**, *7*, 1275.

(41) Brun, E.; Barreau, F.; Veronesi, G.; Fayard, B.; Sorieul, S.; Chaneac, C.; Carapito, C.; Rabilloud, T.; Mabondzo, A.; Herlin-Boime, N.; Carriere, M. *Particle and Fibre Toxicology* **2014**, *11*, 13.

(42) Hallez, Y. *Colloids and Surfaces A: Physicochemical and Engineering Aspects* **2012**, *414*, 466.

(43) Roth, C. M.; Neal, B. L.; Lenhoff, A. M. *Biophysical Journal* **1996**, *70*, 977.

(44) Ye, D.; Raghnaill, M. N.; Bramini, M.; Mahon, E.; Aberg, C.; Salvati, A.; Dawson, K. A. *Nanoscale* **2013**, *5*, 11153.

(45) Ye, D.; Dawson, K. A.; Lynch, I. *Analyst* **2015**, *140*, 83.

(46) Surribas, A.; Resina, D.; Ferrer, P.; Valero, F. *Microbial Cell Factories* **2007**, *6*, 15.

(47) Verano-Braga, T.; Miethling-Graff, R.; Wojdyla, K.; Rogowska-Wrzesinska, A.; Brewer, J. R.; Erdmann, H.; Kjeldsen, F. *ACS Nano* **2014**, *8*, 2161.

(48) Bannunah, A. M.; Vllasaliu, D.; Lord, J.; Stolnik, S. *Molecular Pharmaceutics* **2014**, *11*, 4363.

(49) Stern, S. T.; Adiseshaiah, P. P.; Crist, R. M. *Particle and Fibre Toxicology* **2012**, *9*, 20.

(50) Rivabene, R.; Mancini, E.; De Vincenzi, M. *Biochimica et Biophysica Acta (BBA) - Molecular Basis of Disease* **1999**, *1453*, 152.

(51) Giovannini, C.; Sanchez, M.; Straface, E.; Scazzocchio, B.; Silano, M.; De Vincenzi, M. *Toxicology* **2000**, *145*, 63.

(52) Tenzer, S.; Docter, D.; Kuharev, J.; Musyanovych, A.; Fetz, V.; Hecht, R.; Schlenk, F.; Fischer, D.; Kiouptsi, K.; Reinhardt, C.; Landfester, K.; Schild, H.; Maskos, M.; Knauer, S. K.; Stauber, R. H. *Nat Nano* **2013**, *8*, 772.

(53) Leroux, J.-C.; Gravel, P.; Balant, L.; Volet, B.; Anner, B. M.; Allémann, E.; Doelker, E.; Gurny, R. *Journal of Biomedical Materials Research* **1994**, *28*, 471.

(54) Pelaz, B.; del Pino, P.; Maffre, P.; Hartmann, R.; Gallego, M.; Rivera-Fernández, S.; de la Fuente, J. M.; Nienhaus, G. U.; Parak, W. J. *ACS Nano* **2015**, *9*, 6996.

Chapter 7. Conclusions and Future work

The aim of this thesis was to investigate the effect of the protein corona (PC) formation on NPs-membrane interactions. PC derived from different biologically relevant fluids (i.e. blood and gastrointestinal fluids) were studied and NPs developed for drug delivery purposes were chosen for the project. In particular, core-shell magnetite NPs with carboxylate and pegylated surfaces were employed.

In Chapter 3, the synthetic procedure followed to produce these core-shell NPs was presented. The process is based on the coating of inorganic NPs by an amphiphilic polymer. The functions of the polymer are multiple: first of all, it was used to make the NPs water-soluble; secondly, it was exploited to allow an easier surface functionalization; third, it was used to offer a hydrophobic pocket for encapsulating hydrophobic drugs. The procedure showed to be versatile and reproducible as it was applicable to two metallic NPs stabilized in organic solvent by different ligands: Au and Fe_3O_4 NPs. Functionalization with PEG chains and fluorescent molecules was also successfully performed as well as a model drug, Leflunomide, was loaded into the hydrophobic shell without altering NPs structure and stability. Several characterization techniques were used to fully describe and purify these NPs in order to have monodispersed well-characterized NPs to apply to the biological environment. Among the used techniques DLS, TEM and NTA gave complementary information about the size of the NPs in dried and solvated state revealing small and monodispersed core-shell NPs (diameters < 15 nm), which presented an hydrodynamic diameter of about 50 nm. Two procedures were compared to purify the NPs from excess of reagents, namely sucrose gradient UC and SEC. UC was more effective than SEC in removing the complete excess of polymer.

In Chapter 4, PC of several NPs was investigated. The common strategy to achieve PC NPs isolation is performing various steps of centrifugation and buffer washings to separate the loosely bound proteins from the HC. However, this approach was not always effective, especially when working with NPs characterized by low tendency to sediment and adsorb proteins, or high tendency to aggregate. Moreover, the isolation of PC NPs should be as less invasive as possible in altering the structure of the PC NPs *in situ*. A procedure based on sucrose gradient UC was developed and adapted to isolated PC NPs deriving from the NPs incubation in serum. In Table 7.1, the panel of NPs used in this work is presented and their key-properties are highlighted. Core-shell Fe_3O_4 NPs developed in this work as well as other

commercially available NPs were studied. As largely discussed in Chapter 4, FBS concentration, NPs surface functional groups and size contribute to determine the nature of the corona proteins composition. Core material and NPs density seem to be less determinant in this regard but can guide the choice of the methodology used to recover PC NPs in the way to preserve, as much as possible, the *in situ* complexes nature.

Table 7.1 Panel of NPs employed throughout the work for which PC NPs where recovered using both sucrose-gradient ultracentrifugation and standard washing/centrifugation cycles as reported in Chapters 2 and 4.

NP	Diameter [nm]	Functional group	Core material	Core density [g/cm^3]
PS-COOH20*	20	COOH	Polystyrene	1.05
PS-COOH100*	100	COOH	Polystyrene	1.05
PS-PEG*	100	PEG	Polystyrene	1.05
SiO_2*	50	OH	Silica	2
Fe_3O_4**	~10	COOH	magnetite	5.2
Fe_3O_4-PEG**	~10	COOH/PEG	magnetite	5.2

* Provided by the manufacturers; **obtained by TEM.

UC was superior to conventional centrifugation procedure in most of the cases:

- PS-COOH20: they are defined as "light" NPs, for which standard centrifugation was not effective in guaranteeing a complete precipitation and hence recovery due to NPs core size and density;
- PS-PEG: pegylation determine a poor corona and a complete NPs recovery is necessary for further analysis. As in the previous case the recovery by centrifugation is limited by the core density;
- SiO_2: they were shown to present simultaneously as two PC NPs populations (d_{H1} ~100 nm and d_{H2} ~150 nm) in 10% FBS were and they could not be selectively recovered by centrifugation;
- Fe_3O_4/Fe_3O_4-PEG: core, size and density and surface functionalizations of such NPs would favour aggregation by standard centrifugation. PC Fe_3O_4 NPs were separated by UC from excess of proteins without inducing aggregation and disclosing two populations (d_{H1}~90 nm and d_{H2}~140 nm) which had higher cellular uptake in M2O2 compared to HC NPs obtained by standard centrifugation.

In Chapter 5 the interaction between NPs and membranes was also investigated in the presence of the PC, in particular HC and *in situ* NPs from/in serum were studied. The SLB structure was characterized coupling QCM-D and NR techniques. QCM-D sensitivity showed to be inadequate to detect the adsorption of small NPs such as 20 nm carboxylated polystyrene NPs, carboxylated and pegylated Fe_3O_4 NPs. Moreover, subtle rearrangements on the SLB molecular structure induced by NP application were not detectable. NR was more suitable to highlight these subtle changes induced by NP application on the lipid bilayer organization. Although SLB disruption and NP adsorption were not confirmed, conformational effects caused by the application of the two carboxylated NPs were observed by NR analysis. PC effect was found to be different between HC and *in situ* NPs. In particular, HC NPs caused little perturbation on the SLB, while *in situ* NPs induced a reorganization of the lipids compatible with a lipid exchange between the PC and SLB. This was instead not observed when pure FBS was applied highlighting a possible effect of the soft corona proteins in the interaction with the bilayer.

Finally, Chapter 6 aim was to apply the techniques developed in the previous chapters to characterize PC NPs in gastrointestinal fluid. The relevance of this part of the thesis is evident when considering the toxicological implication of voluntary or involuntary oral ingestion of NPs. Sucrose gradient UC allowed to recover PC NPs from simulated gastric and intestinal fluids when *in vitro* digestion was performed in presence of food. The physical-chemical characterization of the isolated complex revealed structures whose corona evolved during digestion retaining some key-peptides during the simulated digestion. The biological response was studied on Caco-2 monolayers for some of PC NPs isolated. The effects on cells were different and alterations at level of the membrane were mainly highlighted for one population of PC NPs isolated from the intestinal fluid.

The results reported in this thesis can be continued at different levels:

NP synthesis: the developed NPs in this thesis were characterized in a parallel project (data not shown) for their toxicity and they resulted to be no toxic and/or low toxic in a broad range of concentration. Thus, we foresee their use as drug delivery systems. However, the design of these NPs can be improved functionalizing their surface with targeting moieties towards biological targets (i.e. peptides, antibodies, proteins, sugars, etc.). Moreover, the work on the drug loading needs to be refined in terms of quantitative evaluation of the encapsulated drug to optimize the procedure and extend the range of possible drugs to embed. The loaded NPs

should also be applied to different cell lines to evaluate the drug release. Finally, the developed NPs should be superparamagnetic, thus they could be used upon application of an alternating magnetic field either for hyperthermia or for responsive drug release.

Characterization of PC NPs: deeper structural characterization of the PC complexes could be done using sophisticated techniques as Small Angle Neutron Scattering (SANS) and Small Angle X-rays Scattering (SAXS) to resolve the structure at sub-nanometer scale and evidence differences between PC NPs coexisting *in situ*. In fact, sucrose gradient UC offers a procedure able to separate and recover different PC NP populations. Proteomic studies could also be performed to describe the PC composition both qualitatively and quantitatively.

Interactions with models of biological membrane: NR and QCM-D showed to be powerful techniques to study NP-SLB interactions, some limitations were pointed out and need to be addressed although. SLB might be a too stable film to properly indicate the effect of the NPs on its structure, thus floating bilayers might be a more sensitive option. Moreover, the composition of the bilayer can be varied using charged lipids, modifying the film fluidity and embedding proteins. The vertical geometry of the NR cell might have been a limiting factor for the NPs adsorption on the SLB. Concentration, size and surface effects need to be studied deeper. Side-projects are being developed following these indications.

Biological response: More systematic studies with different cell lines to quantify NP uptake needs to be done. Correlations between membrane models and endothelial cells would be useful to evidence which effect caused by NPs on the lipid bilayer have biological relevance. Toxicological implication other than cell viability have to be considered as testified by Caco-2 cells, also when a PC is present. Furthermore, it would be interesting the characterization of the uptake route in particular for digested NPs. The use of more biological relevant digestive models can also be considered for a deeper investigation of the impact of NPs on the GI tract.

Chapter 8. Appendix

8.1 Sucrose-gradient ultracentrifugation optimization for recovering PC NPs: Silica NPs

Table 2.3 in Chapter 2 summarizes the optimized conditions for separating NPs employing sucrose-gradient ultracentrifugation (UC). As example of the optimization process, we described the isolation process of PC NPs for silica NPs incubated in 10% FBS.

Silica NPs employed in the work had a diameter of 50 nm (provided by the manufacturer, Kisker) and a density of 2 g/cm^3. NPs at final concentration of 0.25 mg/ml were incubated in 10% FBS for one hour at 37°C to promote the formation of a stable hard corona. The formation of two PC NPs populations was expected.[1]

An initial gradient was prepared taking into account the work done by Franks *et al.*[2]: they separated by size silica NPs using analytical ultracentrifugation (UC) with a sucrose density between 2-15 w/w.

Ten solutions were prepared in the range 1.5-15% w/w of sucrose and they were layered in 1ml aliquots in a 13 ml centrifugal tube starting from the densest that was layered twice. To promote the formation of a linear gradient, it was left to diffuse at room temperature for 1 hour. *In situ* NPs were deposited on top of the tube gradient and it was run for 15 minutes at 12k rcf. At the end of the run, twelve 1ml fractions were collected from the top to the bottom of the tube by pipette. Aliquots were analysed by size by Nanoparticles Tracking Analysis (NTA): the technique allowed the immediate analysis of NPs diluting them from 10 to 50 times reducing the influence of sucrose solution refractive index. Samples were diluted in water to reach the ideal concentration of 1-3x10^{-8} particles/ml. Results are presented in Fig. 8.1.

The most concentrated aliquot was the second fraction, it superimposed well with the *in situ* NPs and with most of the remaining fractions that contained less NPs. Fraction 1 was yellowish and contained a small amount of NPs, highlighting the presence of serum proteins. The separation of the PC complexes was non complete. In fact, two populations, of average hydrodynamic diameters of 100 nm and 200 nm, are distinguished in fraction 3 and fractions 4-5, but they are wide in distribution and less concentrated than fraction 2 that included both populations. Fractions 10-12 could not been analysed due to the low particles concentration.

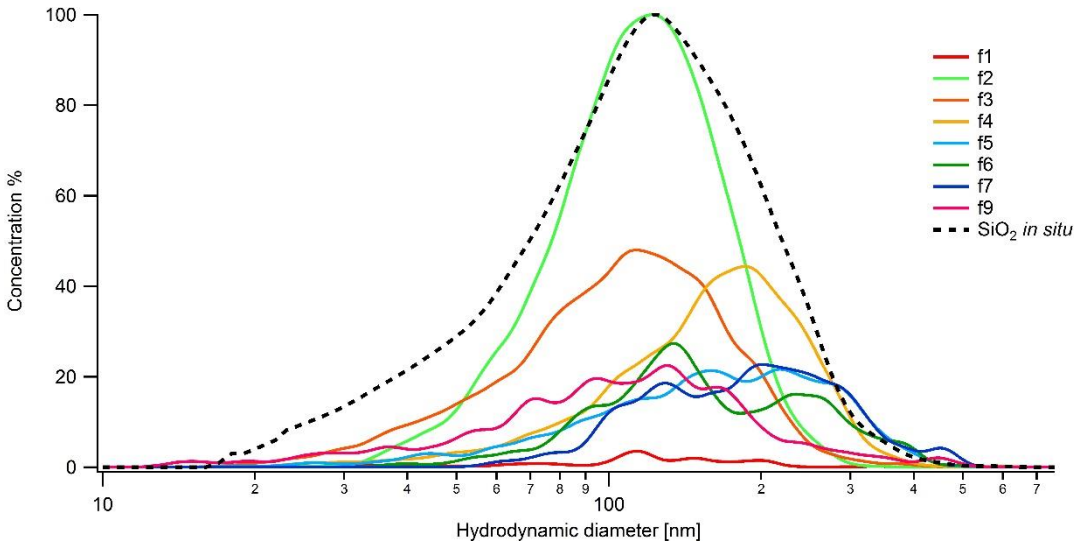

Figure 8.1 Hydrodynamic diameter distributions measured by NTA on SiO_2 NPs incubated in 10% FBS. The black dashed line represents the *in situ* NPs before UC. The aliquots concentration is reported to the most concentrated aliquot to facilitate the comparison among fractions isolated by UC. Curves are the average of three measurements of 60 seconds.

Considering the wide distribution of the NPs and the limited diffusion of the NPs through the gradient, we decided to increase the sucrose-gradient range (3-30% w/w). Moreover a longer centrifugation time was applied (30 minutes) keeping the velocity constant (12k rcf).

In Fig. 8.2, the results of the new UC attempt are presented through the analysis by NTA of the 12 collected aliquots. Aliquots f1- 4 and f10- 11 were poor in NPs as shown by the scheme (Fig. 8.2a) and by the almost-flat distributions (Fig. 8.2b) indicating that NPs diffused nicely through the gradient and the separation of the NPs from the excess of proteins was successful. F12 was not suitable for the analysis. PC NPs concentrated in fractions from 5 to 9. The five fractions overlapped with the *in situ* complexes highlighting the recovery of complexes representative of the *in situ* PC NPs. Aliquots f5-7 were composed of a first PC NPs population whose average hydrodynamic diameter was about 100 nm. The second population, located in aliquots f8-9, was described by and average size of about 150 nm.

Aliquots 5-7 and 8-9 were joint and dialysed overnight at 4°C against PBS to remove sucrose. The two samples were characterized by DLS and NTA and PC composition was described finally by SDS-PAGE. Results are presented in Chapter 4.

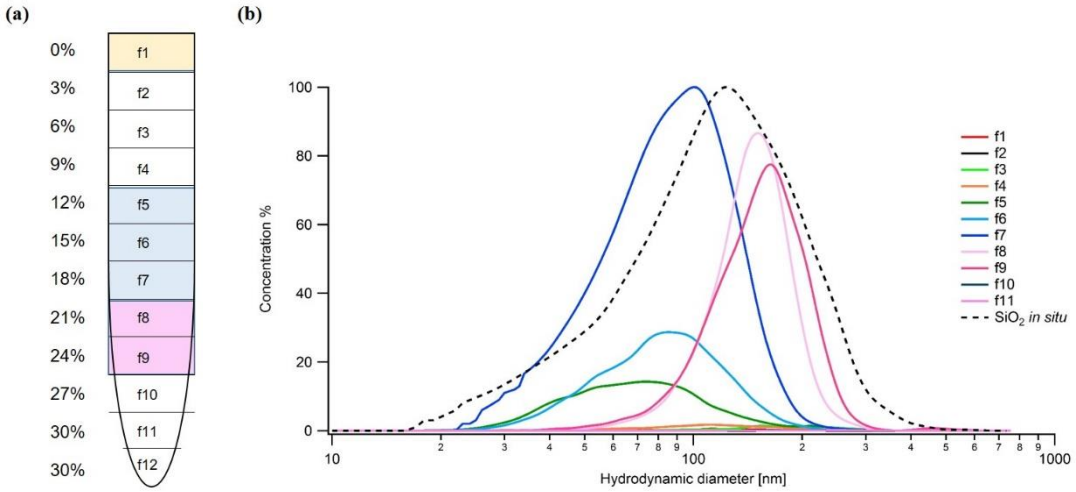

Figure 8.2 A) Scheme of the sucrose layers arrangement after UC of SiO_2 NPs incubated in 10% FBS. The yellow area at the top of the gradient represented weakly bound proteins; blue and pink areas represented the two PC complexes. B) Hydrodynamic diameter distributions measured by NTA. The black dashed line represents the *in situ* NPs before UC. The aliquots concentration is reported to the most concentrated aliquot to facilitate the comparison among fractions isolated by UC. Curves are the average of three measurements of 60 seconds.

Overall, the separation process was suitable for isolating PC NPs populations and get rid of the unbound and weakly attached proteins. The protocol was optimized starting from studies present in literature and a first screening of the sample that underwent UC evidenced the poor resolution in separating PC complexes obtained by the first set of parameters (sucrose gradient 1.5-15% w/w, 15 minutes, 12k rcf, 20°C). The adjustment of the sucrose-gradient width and the ultracentrifugation time (sucrose gradient 3-30% w/w, 30 minutes, 12k rcf, 20°C) allowed to separate efficiently the unbound proteins from the NPs and distinguish two populations of PC NPs in two different regions of the sucrose gradient.

8.2 Technical tip: high-resolution isolation of nanoparticle–protein corona complexes from physiological fluids

The research paper mentioned below is from *Di Silvio D. et al*. and the results are presented in Chapter 4 and Chapter 6. The full paper and the supporting info are reported in the following pages.

Di Silvio, D.; Rigby, N.; Bajka, B; Mayes, A.; Mackie, A; Baldelli Bombelli F.; *Nanoscale* **2015**, *7*, 11980.

Nanoscale

PAPER

View Article Online
View Journal | View Issue

CrossMark

Cite this: *Nanoscale*, 2015, **7**, 11980

Technical tip: high-resolution isolation of nanoparticle–protein corona complexes from physiological fluids†

Desirè Di Silvio,[a,b] Neil Rigby,[b] Balazs Bajka,[b] Andrew Mayes,[c] Alan Mackie[b] and Francesca Baldelli Bombelli*[a,d]

Nanoparticles (NPs) in contact with biological fluids are generally coated with environmental proteins, forming a stronger layer of proteins around the NP surface called the hard corona. Protein corona complexes provide the biological identity of the NPs and their isolation and characterization are essential to understand their *in vitro* and *in vivo* behaviour. Here we present a one-step methodology to recover NPs from complex biological media in a stable non-aggregated form without affecting the structure or composition of the corona. This method allows NPs to be separated from complex fluids containing biological particulates and in a form suitable for use in further experiments. The study has been performed systematically comparing the new proposed methodology to standard approaches for a wide panel of NPs. NPs were first incubated in the biological fluid and successively recovered by sucrose gradient ultracentrifugation in order to separate the NPs and their protein corona from the loosely bound proteins. The isolated NP–protein complexes were characterized by size and protein composition through Dynamic Light Scattering, Nanoparticle Tracking Analysis, SDS-PAGE and LC-MS. The protocol described is versatile and can be applied to diverse nanomaterials and complex fluids. It is shown to have higher resolution in separating the multiple protein corona complexes from a biological environment with a much lower impact on their *in situ* structure compared to conventional centrifugal approaches.

Received 22nd April 2015,
Accepted 2nd June 2015

DOI: 10.1039/c5nr02618k

www.rsc.org/nanoscale

Introduction

In the last decades, nanoparticles (NPs) have found several applications in a wide range of fields, such as medicine,[1,2] cosmetics,[3] paints,[4] high-tech,[5–7] and food industries[8] and by 2020 nanotechnology is forecast to produce about 60 000 tons of NPs per year.[9] The wide use of NPs in several areas has exponentially increased their exposure to humans, both intentionally and unintentionally. In order to understand the potential impact of engineered nanomaterials (ENMs) on human health, it is fundamental to fully characterize them in relevant biological fluids.[10] In fact, when in contact with biological fluids, NPs spontaneously interact and adsorb proteins on their surface forming what is known as a protein corona (PC).[11,12] This corona provides the biological identity of the NP and determines its interactions with the surrounding biological matter.[13,14]

The PC has a dynamic structure formed by external layers of proteins that quickly exchange with the surrounding environment (soft corona) and an inner layer of proteins strongly bound to the NP surface (hard corona).[15–18] The PC composition depends on the NP's physical–chemical properties and size, but also the media composition and incubation time have been found to have strong effects.[19–21] Generally, the hard corona is very stable and almost irreversibly bound to the NP surface when the experimental conditions are kept constant,[12] although it has recently been shown that small alterations in the composition of the biological media can strongly modify the hard corona.[22] Moreover, preliminary studies on the evolution of the PC, where NPs were sequentially incubated in different biological fluids, have shown that even if changes occur in the PC upon incubation in the second biological fluid, a sort of fingerprint of the "history" of the NP is kept.[23] Thus, isolating HC complexes is crucial to independently study their composition and to be able to relate possible biological responses to it.

One of the biggest concerns in this scenario is to isolate HC complexes that preserve the features of those *in situ* in the bio-

[a]*School of Pharmacy, University of East Anglia, Norwich Research Park, NR4 7TJ Norwich, UK*
[b]*Institute of Food Research, Norwich Research Park, Colney Ln, NR4 7UA Norwich, UK*
[c]*School of Chemistry, University of East Anglia, Norwich Research Park, NR4 7TJ Norwich, UK*
[d]*Fondazione Centro Europeo Nanomedicina c/o Laboratory of Nanostructured Fluorinated Materials (NFMLab), Department of Chemistry, Materials, and Chemical Engineering "Giulio Natta", Politecnico di Milano, Milan, Italy.*
E-mail: francesca.baldelli@polimi.it

†Electronic supplementary information (ESI) available. See DOI: 10.1039/c5nr02618k

logical fluid. Commonly, an *ex situ* approach is used to separate protein–NP complexes from the excess of fluid and isolate hard corona (HC) complexes: sequential cycles of centrifugation/washing are carefully optimized according to the NP and media properties.[24,25] In many cases this approach is suitable and gives reliable results, but multiple purification steps can alter the equilibrium of the system and lead to corona modifications due to the time scales that characterize the dynamic nature[26] of the complexes. Application of this approach to NPs characterized by small diameters (about 5–20 nm) and/or low densities (close to 1 g cm^{-3}) may not achieve a good separation between unbound proteins and PC complexes. High speeds and long times are often necessary with promotion of extensive aggregation with respect to what occurs *in situ*. These effects are even more accentuated in the isolation of HC complexes for NPs that do not form rich coronas (for example pegylated NPs). For this reason it becomes important to develop methodologies that minimize the number of steps of the *ex situ* purification of HC complexes to affect as little as possible their properties from *in situ*.

Furthermore, PC complexes are often very heterogeneous presenting simultaneously monomers, dimers, trimers, *etc.* for which the actual composition is unknown. In this regard, the biological impact of these co-existing complexes formed by the same NPs might be different as they have different sizes and are likely to carry different proteins. Thus, it is important to be able to separate those different complexes and independently study their effect on the biological matter. Recently, the use of differential sedimentation centrifugation (DCS) permitted the analytical separation of different populations of HC complexes for different NPs and demonstrated that they were representative of those *in situ*. However, this technique does not allow the recovery of the different populations for further studies.[12,27] In particular, their recovery becomes important to determine the physical and biological properties of these complexes. Conventional procedures allow the isolation and recovery of mixed PC populations, which are also aggregated with respect to their *in situ* cognate PC complexes.

Many techniques have been applied to separate and study PC complexes such as size-exclusion chromatography (SEC), magnetic separation through the use of magnetic columns (MACS) able to separate PC complexes of magnetic NPs,[28] and field-flow-field fractionation.[29,30] However, none of these methodologies are preparative and permit full recovery of the HC complexes for further studies. Preparative and analytical ultracentrifugation (UC) are widely exploited in biology to isolate cell components and explore protein thermodynamics.[31] Density gradient UC has been extended to purify NPs from the excess of coating agents,[32] and obtain narrow size distributions.[33,34] Recently, Docter, Tenzer and co-workers[35,36] and Werwie and co-workers[37] used a sucrose cushion as the first step to separate unbound proteins from corona complexes followed by centrifugal washing to obtain HC complexes.

Here we propose the use of sucrose gradient UC as a one-step methodology to gently separate HC complexes from *in situ* complex physiological fluids such as bovine serum and digestive fluids. We have shown that this procedure has a much lower impact on the structure of the complexes and a much higher resolution in separating different complexes with respect to conventional protocols. In fact, this methodology permitted full recovery of HC complexes *ex situ* minimizing modifications with respect to those *in situ* and allowing separation of the different populations co-existing *in situ* (see Scheme 1).

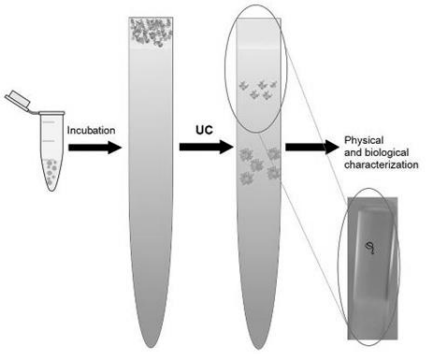

Scheme 1 Scheme of the methodology to isolate and study HC NPs. NPs are incubated in a biological fluid and then subjected to ultracentrifugation (UC). In the image of the vial on the far left, the pink dots are the NPs and the yellow background is the biological medium. In the images of the UC vials (middle images), the green dots represent some proteins that form diverse coronas around the NPs and are separated by UC exploiting density differences.

NPs of different size, material and surface coating were tested in serum and in simulated digestive fluids. The PC complexes isolated by conventional centrifugation methods and UC were analysed by size through Nanoparticle Tracking Analysis (NTA) and Dynamic Light Scattering (DLS). The PC composition was investigated by SDS-PAGE and for the PC complexes obtained from digestive fluids, Mass Spectrometry analysis was also performed to confirm the identities of the recovered proteins. Moreover, to prove how the isolation procedure influenced the interaction of the PC complexes with biological matter, the PC complexes of magnetite NPs recovered from serum by both UC and conventional centrifugation methods were incubated on cells in serum-free conditions to compare their NP cellular uptake.

Experimental section

Materials

Yellow-green carboxylate-modified polystyrene NPs of 100 nm and 20 nm nominal diameter were purchased from Invitrogen (PS-COOH100 and PS-COOH20). PS-COOH100 NPs were pegylated through EDAC chemistry using Jeffamine M1000 (Hunts-

man) and purified by centrifugal washings (3 × 30 minutes at 17 000 rcf, 20 °C) (PS-PEG). Bare 50 nm silica NPs were purchased from Kisker (SiO_2). Carboxylated Fe_3O_4 NPs were synthesized following the protocol of Sun *et al.*[38] and coated by poly(maleic)-*alt*-1-octadecene (Sigma) according to Lin *et al.*[39] obtaining NPs of about 50 nm in hydrodynamic diameter. For cell uptake studies, Fe_3O_4 NPs were fluorescently labelled with BODIPY FLEDA (Lifetechnologies) which was attached to the NP surface by EDAC chemistry. Foetal bovine serum (FBS) was purchased from Fisher. Sucrose, sodium phosphate dibasic, potassium phosphate monobasic, sodium chloride and potassium chloride are from Sigma.

Preparation of the protein corona samples

NPs in PBS were incubated in 10%, 55% and 90% v/v FBS for one hour at 37 °C. NPs dispersed in FBS solution are called *in situ*, HC NPs isolated through ultracentrifugation are labelled as UC; HC NPs isolated by a conventional methodology (three centrifugations at 15 500 rcf at 4 °C and re-suspensions in 500 μl PBS pH 7.4) are labelled as HC. The samples were characterized by NTA and DLS before and after incubation.

Simulated salivary, gastric and duodenal digestions

An AT-700 pH Stat Kyoto Electronic Manufacturing Company was used to run simulated digestions. Digestion mixture compositions, time points at which samples were taken and timescales for digestions varied. Buffer solutions were used in all digestions but whilst the desirable pH was set at the beginning of each phase of digestion, it was not actively controlled throughout (but instead monitored and recorded during the sample taking). The chosen food material was skimmed milk powder (SMP, 34 mg ml^{-1}) and individual enzymes in the different digestion phases were used. Pepsin (from porcine gastric mucosa, Sigma-Aldrich, Lot. 091M7020 V) was used in the gastric phase, and trypsin (from porcine pancreas, Sigma-Aldrich, Lot. 045K7775) and chymotrypsin (from bovine pancreas, Sigma-Aldrich, Lot. 060M7007 V) were used for the duodenal phase, as well as bile. Fe_3O_4 NPs at a final concentration of 1.5×10^{13} NPs per ml were incubated with 1 ml of fluid collected at time points corresponding to the oral phase (2 min, pH 7, amylase), before the start of the gastric phase (60 min), after the gastric phase was finished (120 min, pH 3) and after duodenal digestion (240 min, pH 7.0). The NPs were incubated at 37 °C for one hour in a Brunswick Scientific Excella E24 Incubator Shaker. Equal volumes of purified water were incubated with the fluids to act as controls.

Ultracentrifugation

Solutions of sucrose were prepared at increasing concentrations and 11 ml of the linear sucrose gradient solutions were layered in 13 ml tubes and left to equilibrate overnight before being subjected to ultracentrifugation using a SW41 Ti rotor (Beckman Coulter) at 20 °C. 0.7 ml of the samples was loaded and different protocols were used according to the physical properties of the NP and the biological media (details of the gradient are given in Table 1). After the run, aliquots of 1 ml were collected by sucking up sucrose from the top of the tubes to the bottom and analysed to identify protein corona NPs either by screening by dimension or UV absorption at 260 nm.

Table 1 Ultracentrifugation experimental conditions used to separate the NPs from the biological fluids. Particles were in PBS, pH 7.4

Type of NP	Nominal size [nm]	NPs per ml [a]	Sucrose density Δ [% w/w]	Speed [rcf]	Time [min]
PS-COOH100	100	3.6×10^{11}	5–30	77k	60
PS-COOH20	20	4.5×10^{13}	4–40	110k	120
PS-PEG	100	3.6×10^{11}	3–30	60k	60
SiO_2	50	1.9×10^{13}	3–30	12k	20
Fe_3O_4	50	1.5×10^{13}	35–60/70	187k	120

[a] Concentration of the NPs in the *in situ* samples before being loaded in the ultracentrifuge.

Dynamic light scattering (DLS)

Hydrodynamic diameters were measured by Zetasizer SZ (Malvern). 50 μl of the samples were diluted in 400 μl of PBS in 1 ml cuvettes to obtain attenuation values in the 7–9 range and measured at 25 °C, equilibrating samples for 120 seconds prior to measurement. Data were presented as an average of three measurements. UC samples were dialysed against PBS (2000 MWCO, Spectrum labs) for at least 24 hours at 4 °C before analysis. The Z-averaged sizes (Z-ave) and the polydispersity index (PdI) were obtained by cumulant analysis of the autocorrelation function.

Nanoparticle tracking analysis (NTA)

Samples were analysed by NTA by diluting them with MQ water to reach an ideal concentration of $1–3 \times 10^8$ NPs per ml. For fluorescently-labelled particles a fluorescence filter (λ of 488 nm) was used. Three videos of sixty seconds were collected for each sample and analysed by NTA software. The software is able to track NPs individually and calculates the diffusion coefficient for each one. In this way, a mean value for the hydrodynamic diameter (Mean) is obtained with the relative standard deviation (SD) in respect to all tracks. Results are presented as an average of three independent measurements.

SDS-PAGE electrophoresis

Dialysed samples were concentrated by Amicon centrifugal filters (MWCO 100 kDa, Millipore) at 405 rcf to a final volume of 200 μl. 30 μl were added to 15 μl of SDS-PAGE loading buffer 3× (10% DTT, Thermo Scientific) and kept at 98 °C for 5 minutes. Digested samples that did not contain NPs were mixed in the loading buffer without any previous treatment and denatured as above. HC samples were prepared by re-suspending the pellet in 60 μl of PBS to which 30 μl of the loading buffer was added before denaturation. 20 μl of the samples and 5 μl of a molecular ladder (Pageruler Broad Range, Biolabs) were loaded in the wells of 12% Precast Gel NuPAGE (Life Technology). Samples from the simulated digestion were loaded on 10% Precast Gel NuPAGE (Life Technology) and the

molecular ladder used was Mark12 Unstained standard from Invitrogen (5 μl). The running buffer used was MES buffer (NuPAGE 20×, Invitrogen). Gels were run at 200 V for 35 minutes. Gels were developed by Sypro Ruby Protein Stain (Biorad) and imaged by Biorad Pharos FX+, the software used to elaborate the images was Image Lab (Biorad).

LC-MS

A ProPick instrument was used to locate and cut bands from the gel. The bands were digested at 37 °C for three hours by 10 mM ammonium bicarbonate 10 ng μl^{-1} Trypsin Gold (Promega, V528A in 50 mM acetic acid) (prepared 01-May-14). 1% formic acid (Sigma) was added prior to freezing the samples and storing at −80 °C. Samples were washed in 50% acetonitrile (Fisher), vortexed and dried out at the Low Drying setting (no heat) on a Speed Vac SC110 (Savant) fitted with a Refrigerated Condensation Trap and a Vac V-500 (Buchi). Samples were again stored at −80 °C until ready for Orbitrap analysis. Protein identification was achieved by combining spectrum quality scoring obtained from a conventional database search program MASCOT (Matrix Science, London, England). Search parameters were: peptide mass and fragment mass tolerances of 5 ppm and 0.5 Da respectively, the variable modification was oxidation (M), the fixed modification was carbamidomethyl (C), the enzyme specificity was trypsin, and two missed cleavages were allowed. All of the taxonomy database was searched.

Cell uptake experiments

M202 cell lines were incubated at 37 °C, 5% CO2/95% air and were cultured in RPMI-1640 (Life Technologies, Carlsbad, CA) supplemented with 10% heat-inactivated foetal bovine serum (FBS), 2 mM L-glutamine, 100 μg ml^{-1} penicillin and 100 μg ml^{-1} streptomycin all purchased from Life Technologies, Carlsbad, CA. P12 cells were seeded at a density of 4×10^4 cells per ml on glass coverslips and left to adhere overnight. The cells were incubated with Fe_3O_4 NPs (10^{12} NPs per ml) for 2, 4 and 24 hours. In particular cells were treated with fluorescently-labelled bare Fe_3O_4 NPs, HC, UC1 and UC2. The cells were washed with PBS (×3) and fixed (5% formaldehyde, 2% sucrose, 0.02% w/v sodium azide in PBS) then permeabilized (5 min with 0.1% Triton X-100 in PBS). Texas Red®-X Phalloidin (Life Technologies) (6.6 μM) was employed to stain actin filaments and Hoechst 33342 dye to stain nuclei (2 μg ml^{-1}, Sigma). The coverslip was mounted face down on a slide for a microscope with 12 μl of mounting media (Vectashield, Vector), left to dry overnight and then sealed with nail varnish. A Zeiss LSM510-META confocal microscope (UEA) was used to image cells in multi-track mode. ImagePro software was used to elaborate the z-stack recorded. ImagePro software was used to process images.

Results and discussion

Isolation of hard corona (HC) complexes from FBS

NPs of different size, material and surface coating (see Table 1) were incubated at 37 °C in FBS and separated by the excess of proteins by UC on a sucrose gradient. The recovered HC complexes were further characterized and compared with those *in situ* and those isolated by conventional centrifugation protocols. We chose five different types of NPs that spanned a variety of materials and presented different PC complexes to prove the suitability of this protocol to successfully separate HC complexes of diverse properties. In particular, PS-COOH100 NPs were chosen as the control sample for comparing PC complexes obtained with our novel procedure with those obtained using the conventional approach,[12] and PS-COOH20 NPs were chosen as an example of NP–protein complexes that cannot be isolated by normal centrifugation, which promoted extensive aggregation and loss of material in the recovery of HC complexes.[19] PS-PEG NPs were chosen as an example of NPs with a reduced tendency to form a PC in biological environments and thus are very difficult to isolate and recover from the biological fluid,[40–42] while SiO_2 NPs are NPs able to form two populations of HC complexes that could be successfully separated and recovered by UC.[27] Lastly, Fe_3O_4 NPs are an example of engineered NPs designed for biomedical applications, for which the conventional approaches promoted extensive aggregation.[43] For all the samples the excess of proteins from the media were enriched in the lower density sucrose layer at the top of the tube as shown in Scheme 1.

The validation of the UC procedure for isolating HC complexes was first performed by studying 100 nm PS-COOH NPs dispersed in 90% FBS, whose PC complexes have already been extensively characterized in the literature.[19,44] PS-COOH100 *in situ* was shown to form rather monodisperse PC complexes with a hydrodynamic diameter of about 130 nm (see Table 2). The isolation of such complexes by normal centrifugation promoted limited aggregation leading to the formation of HC NPs with hydrodynamic diameters of about 170 nm and characterized by a higher PdI. The same sample subjected to UC produced three separated bands at different concentrations in the sucrose gradient, two of which contained similar complexes and were pooled together. This indicated that with this pro-

Table 2 DLS and NTA characterization of PS-COOH100 NPs in PBS, 90% FBS, and of HC complexes isolated by centrifugation (HC) and ultracentrifugation (UC 1–2)

	DLS		NTA		
	D_H[b] [nm]	PdI[b]	Mean[c] [nm]	SD[c] [nm]	NPs/ml
PS-COOH[a]	100.8 ± 0.7	0.01	78 ± 3	29 ± 2	7×10^{12}
PS-COOH *in situ*	128.1 ± 0.9	0.03	130 ± 1	31 ± 1	3×10^{12}
PS-COOH HC	168.0 ± 0.9	0.26	154 ± 3	52 ± 7	7×10^{12}
PS-COOH UC1	122.2 ± 1.7	0.01	117 ± 1	34 ± 1	5×10^{12}
PS-COOH UC2	131.4 ± 1.6	0.01	126 ± 2	35 ± 1	1×10^{12}

[a] In PBS pH 7.4. [b] Hydrodynamic diameter (D_H) and polydispersity index (PdI) obtained by cumulant analysis of the autocorrelation functions. [c] Mean is the averaged size of all tracked particles and SD is the related Standard Deviation. All the data are presented as the average of three independent measurements.

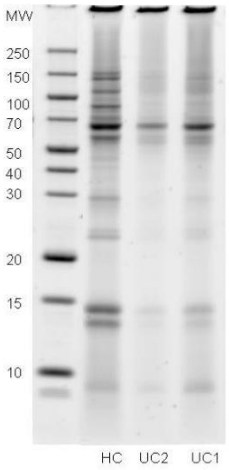

Fig. 1 HC complexes of PS-COOH100. SDS-PAGE gel of the HC complexes of PS-COOH100 NPs in 90% FBS isolated by conventional centrifugation methods (hard corona, HC) and sucrose ultracentrifugation (UC) respectively, as indicated by the label below the tracks of the gel.

cedure it was possible to separate in one-step process HC complexes with a structure similar to those *in situ* and a high resolution in separation by size. In fact, complexes differing by only 7% in size (122 nm and 131 nm) were isolated in two well-separated sucrose bands (see Fig. 1 UC1 and UC2). The strength of this methodology resides also in the full recovery of the material that could be further analysed to determine the composition of the PC by SDS-PAGE (see Fig. 1) and size (Table 2).

A more challenging task was to recover HC complexes of 20 nm PS-COOH NPs, for which the conventional centrifugation methodology did not work effectively as it promoted extensive aggregation and loss of material as indicated by the hydrodynamic diameter of about 250 nm with a PdI of over 0.5 (see Table 3 and Fig. S1 in the ESI†). In fact, the incubation in 90% FBS caused the formation of aggregates with an averaged hydrodynamic diameter of 65 nm compared with 30 nm of the bare NPs in PBS, and the long times and high speed necessary to sediment the HC complexes clearly amplified this effect. The use of UC allowed us not only to avoid this aggregation, but also to separate the different populations of complexes. In particular, the presence of a small population of large aggregates of about 240 nm was highlighted. This population was mainly formed by proteins, as indicated by the low density of the sucrose layer (UC1) where they accumulated compared to that of UC2 and UC3, containing most of the complexes. This was also confirmed by the concentrations revealed by NTA for NPs in the UC2 and UC3 sucrose layers, which were comparable to that of the NPs *in situ*. Moreover, the hydrodynamic

Table 3 DLS and NTA characterization of PS-COOH20 NPs in PBS and 90% FBS

	DLS		NTA		
	D_H[b] [nm]	PdI[b]	Mean[c] [nm]	SD[c] [nm]	NPs/ml
PS-COOH[a]	32.5 ± 0.1	0.10	64 ± 21	28 ± 5	3×10^{12}
PS-COOH *in situ*	67.6 ± 0.7	0.31	81 ± 3	38 ± 6	8×10^{12}
PS-COOH HC	247.3 ± 7.6	0.65	186 ± 18	66 ± 6	6×10^{11}
PS-COOH UC1	259.5 ± 4.6	0.43	86 ± 5	59 ± 4	7×10^{11}
PS-COOH UC2	68.2 ± 0.1.9	0.16	58 ± 1	26 ± 1	1×10^{13}
PS-COOH UC3	91.1 ± 1.9	0.18	73 ± 3	35 ± 3	9×10^{12}

[a] In PBS pH 7.4. [b] Hydrodynamic diameter (D_H) and polydispersity index (PdI) obtained by cumulant analysis of the autocorrelation functions. [c] Mean is the averaged size of all tracked particles and SD is the related Standard Deviation. All the data are presented as the average of three independent measurements.

sizes of the complexes recovered from the UC2 and UC3 layers were comparable to those of the *in situ* samples and also characterised by a lower PdI related to the separation from the larger protein aggregates as shown in Fig. 2a. The lower sizes detected by NTA for the HC and UC1 samples confirmed the presence of big protein aggregates in these samples, whose lower sizes were likely due to a partial disaggregation by dilution (required for measuring NTA). SDS-PAGE analysis, reported in Fig. 2b, showed that fractions UC2 and UC3 were very similar in protein composition, while UC1 was enriched with proteins of M_w = 60–70 kDa and 150 kDa (probably BSA and IgG).

Another case where conventional centrifugation methods have not been very effective in isolating HC complexes is for NPs that do not show a high tendency to adsorb proteins, *e.g.* pegylated NPs. The difficulty isolating hard corona becomes even greater when these NPs have a low density such as polymeric NPs and liposomes. Ultracentrifugation was used to separate liposomes by size[45] and recently Pozzi and coworkers[46] showed that liposome pegylation could be exploited both to reduce protein adsorption to limit macrophage uptake and to enrich the residual corona with apolipoproteins that bind specifically to some receptors of prostate cancer cells. Pegylated polystyrene NPs (100 nm size) were incubated in 90% FBS and characterized by DLS and NTA (Table 4). Their dynamic properties did not change significantly with respect to those in PBS indicating a weak interaction with the environmental proteins and no significant changes in the structure of the bare NPs, although protein adsorption could not be completely ruled out. HC complexes isolated by centrifugation were extensively aggregated with respect to those *in situ* and some loss of material occurred (see Fig. S1 in the ESI†). The same sample was separated by UC and a well-defined single band enriched in NPs was isolated. The recovered NPs were analysed by DLS and NTA and the results were very similar to those *in situ*. DLS, unlike NTA, showed an increase in the diameter and PdI with respect to *in situ* samples (Fig. 3a) and a slight loss of NPs, likely due to the very similar density to the

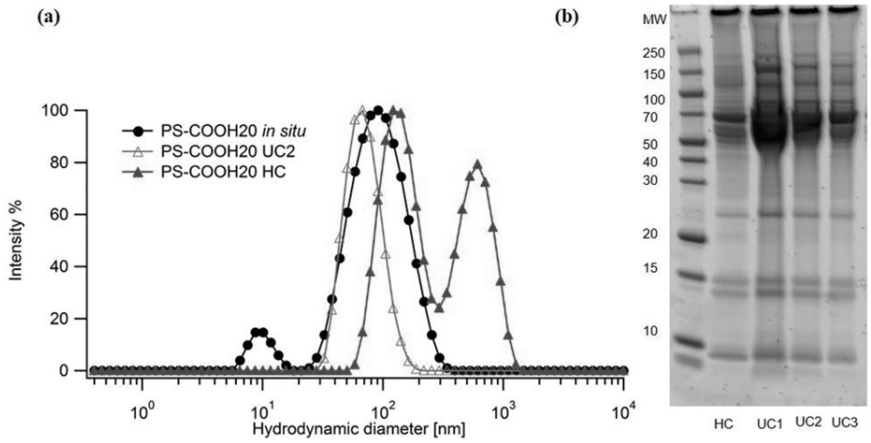

Fig. 2 HC complexes of PS-COOH20 in 90% FBS. (a) Size distribution by intensity percentage of NPs *in situ* (black dots), HC complexes isolated by centrifugation (HC, red triangles) and ultracentrifugation (UC2, green empty triangles). (b) SDS-PAGE gel of the complexes in 90% FBS isolated by conventional centrifugation methods (hard corona, HC) and ultracentrifuge (UC1–2), respectively, as indicated by the labels below the tracks of the gel.

Table 4 DLS and NTA characterization of PS-PEG NPs in different media

	DLS		NTA		
	D_H[b] [nm]	PdI[b]	Mean[c] [nm]	SD[c] [nm]	NPs/ml
PS-PEG[a]	106.3 ± 0.7	0.04	125 ± 1	38 ± 1	3×10^{12}
PS-PEG *in situ*	105.9 ± 0.5	0.10	136 ± 1	42 ± 2	4×10^{11}
PES-PEG HC	155.7 ± 2.5	0.22	123 ± 10	36 ± 8	1×10^{11}
PS-PEG UC	137.1 ± 0.1	0.22	118 ± 6	34 ± 1	7×10^{10}

[a] In PBS pH 7.4. [b] Hydrodynamic diameter (D_H) and polydispersity index (PdI) obtained by cumulant analysis of the autocorrelation functions. [c] Mean is the averaged size of all tracked particles and SD is the related Standard Deviation. All the data are presented as the average of three independent measurements.

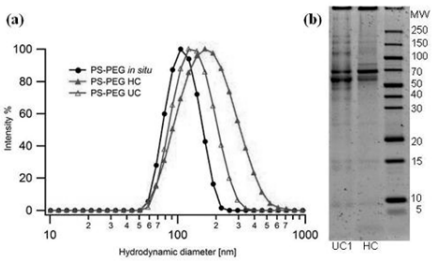

Fig. 3 HC complexes of PS-PEG. (a) Size distribution by intensity percentage of PS-PEG NPs *in situ* in 90% FBS (black dots), HC complexes isolated by centrifugation (HC, red triangles) and ultracentrifugation (UC, green empty triangles). (b) SDS-PAGE gel of the HC complexes of PS-PEG NPs in 90% FBS isolated by ultracentrifugation (UC) and conventional centrifugation methods (HC), respectively, as indicated by the labels below the tracks of the gel.

proteins. The corona composition of the complexes isolated by the two methods was compared by SDS-PAGE (see Fig. 3b) and differences could be seen especially for high molecular weight proteins indicating that aggregation and loss of material can ultimately affect the properties of the hard corona of the *in situ* samples. Thus, UC was shown to be a promising method for recovering HC complexes of pegylated nanomaterials and allows their further characterization and biological response.

Protein coronas of 50 nm SiO_2 NPs have been shown to be very different depending on the protein concentration in the biological fluids,[27] in particular they form larger aggregates at lower protein concentrations (dimer, trimer, *etc.*), while smaller and more monodispersed protein–NP complexes form at higher protein concentrations. Here we tried to separate the NP–protein complexes in 10% FBS (protein concentration 0.0036 g ml^{-1}) in more resolved fractions containing the different species present *in situ* and compare them with the analogue complexes in 90% FBS (protein concentration 0.032 g ml^{-1}). Also in this case the formation of protein–NP agglomerates of different size and composition in 10% FBS made their isolation impractical by conventional centrifugation as extensive aggregation occurred as shown in Table 5. UC resulted in successful separation and recovery of two equivalent (in number of NPs) fractions of NP–protein complexes

Table 5 DLS and NTA characterization of silica NPs in 10% and 90% FBS

	DLS		NTA		
	D_H [b] [nm]	PdI [b]	Mean [c] [nm]	SD [c] [nm]	NPs/ml
SiO_2 [a]	46.7 ± 0.5	0.02	37 ± 4	18 ± 4	6×10^{12}
SiO_2 10% *in situ*	141.5 ± 0.2	0.19	211 ± 13	65 ± 8	1×10^{13}
SiO_2 10% HC	291.0 ± 3.9	0.36	157 ± 2	73 ± 1	1×10^{11}
SiO_2 10% UC1	123.5 ± 1.7	0.23	98 ± 3	43 ± 8	3×10^{10}
SiO_2 10% UC2	179.1 ± 0.9	0.30	153 ± 21	41 ± 9	4×10^{10}
SiO_2 90% *in situ*	81.1 ± 0.3	0.20	108 ± 5	36 ± 4	1×10^{13}
SiO_2 90% HC	129.7 ± 4.4	0.27	174 ± 13	75 ± 15	1×10^{12}
SiO_2 90% UC	80.2 ± 1.1	0.22	101 ± 4	38 ± 1	9×10^{10}

[a] In PBS pH 7.4. [b] Hydrodynamic diameter (D_H) and polydispersity index (PdI) obtained by cumulant analysis of the autocorrelation functions. [c] Mean is the averaged size of all tracked particles and SD is the related Standard Deviation. All the data are presented as the average of three independent measurements.

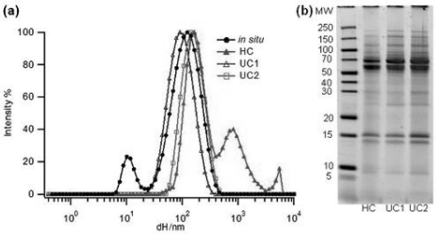

Fig. 5 Fe_3O_4 in 55% FBS. (a) Size distributions from DLS measurements of Fe_3O_4 NPs *in situ* and HC complexes recovered by ultracentrifugation (UC1–2) and by centrifugal washings (HC). (b) SDS-PAGE of hard corona complexes isolated by conventional centrifugation (HC) and by density gradient ultracentrifugation (UC1–2).

characterized by hydrodynamic diameters of 110 and 180 nm, respectively. SDS-PAGE showed a different pattern of proteins for the two fractions highlighting the different nature of these complexes that are likely to interact differently with biological matter (Fig. 4a). For the samples incubated in 90% FBS, HC and UC samples showed a very similar protein pattern but DLS and NTA results clearly showed that the NP–protein complexes isolated by UC had a structure more representative of that *in situ*.

The possibility of isolating those complexes without altering their physical properties is clearly important for studying their biological response in more detail. Fluorescently-labelled water soluble oleic acid coated Fe_3O_4 NPs (see Fig. S2–S4 and Table S1 in the ESI†) coated by PMAO polymer were incubated in 55% FBS. Larger NP–protein complexes were observed *in situ* by DLS together with the protein background (peak at 10–15 nm) as shown by the size distribution reported in Fig. 5a. HC samples also showed extensive aggregation and the pellet obtained by centrifugation could not be completely resuspended. In contrast, UC samples were successfully isolated and recovered in two NP–protein fractions containing structures of about 77 nm and 140 nm in size, respectively, and that seem to correspond to the species present in the *in situ* sample. The protein patterns were analysed by SDS-PAGE and qualitatively they seemed to be very similar indicating that in this case, NP–protein complexes of different diameters (monomer and dimers) were enriched with similar proteins (Table 6).

HC complexes recovered by centrifugation and UC were then incubated at a comparable concentration, determined by NTA and fluorescence, in serum-free conditions with M202 cells.

Fe_3O_4 NPs were covalently labelled with a fluorescent dye and cells were stained for actin filaments and nuclei. In Fig. 6 representative images of cells incubated for two hours with PC samples in serum-free conditions are reported. A different fluorescent pattern between PC NPs isolated by conventional centrifugation methods (Fig. 6a) and those obtained by UC (Fig. 6b and 6c) can be observed. In fact, the images show that samples treated with HC NPs are characterized by large fluo-

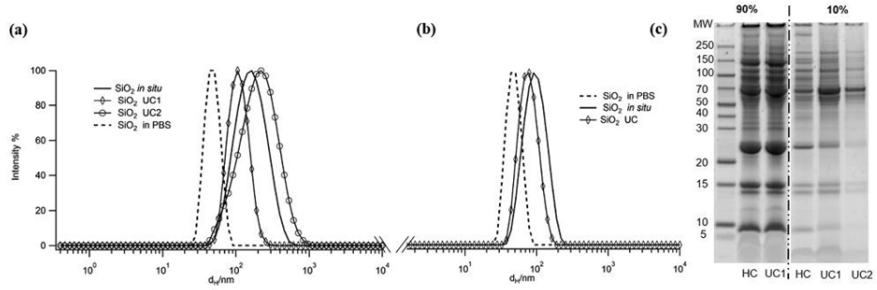

Fig. 4 Characterization of SiO_2 NPs. In graphs (a) and (b) size distributions by intensity percentage of SiO_2 NPs in 10% and 90% FBS, respectively, are reported, compared to NPs in PBS (dashed line). (c) SDS-PAGE gel of the hard corona complexes of SiO_2 NPs in 10% and 90% FBS isolated by ultracentrifugation (UC) and conventional centrifugation methods (HC), respectively, as indicated by the labels below the tracks of the gel.

Table 6 DLS and NTA characterization of Fe_3O_4 NPs in 55% FBS

	DLS		NTA	
	D_H [b] [nm]	PdI [b]	Mean [c] [nm]	SD [c] [nm]
Fe_3O_4 [a]	51.4 ± 0.3	0.17	93 ± 7	42 ± 12
Fe_3O_4 *in situ*	63.1 ± 1.8	0.50	157 ± 3	51 ± 4
Fe_3O_4 HC [d]	251.8 ± 9.5	0.55	n.d.	n.d.
Fe_3O_4 UC1	77.4 ± 0.2	0.26	90 ± 1	33 ± 1
Fe_3O_4 UC2	147.1 ± 4.3	0.20	139 ± 3	47 ± 2

[a] in PBS pH 7.4. [b] Hydrodynamic diameter (D_H) and polydispersity index (PdI) obtained by cumulant analysis of the autocorrelation functions. [c] Mean is the averaged size of all tracked particles and SD is the related Standard Deviation. All the data are presented as the average of three independent measurements. [d] Sample too polydispersed to be measured.

rescent aggregates hardly taken up by the cells, while those treated with the PC complexes from UC fractions are more monodispersed in size and showed a much higher cell uptake. No significant differences are instead observed in NP cell uptake from the two UC fractions indicating that, in this case, differently structured PC complexes are "seen" similarly by the cells. This is also in agreement with the protein corona pattern observed in the SDS-PAGE (see Fig. 5). Uptake experiments done at different times of incubation, 4 h and 24 h, did not show major changes (data not shown).

Recovery of HC complexes from gastrointestinal fluids

The importance of this methodology has also been demonstrated in the recovery of NP–protein complexes from different non-serum biological fluids such as simulated gastrointestinal fluids. The digestion of NPs in these fluids required a very long and complex protocol (see Materials and methods sections) for which the isolation with conventional methods was ineffective, due to the NP concentration and agglomeration problems. Investigation of the protein coronas of NPs in gastrointestinal fluids is important in relation to the application of NPs in food,[8] food packaging, toxicology[47–49] and medicine. It has been shown that NPs such as iron oxide and Ag NPs tend to aggregate in the gastrointestinal tract[50,51] because of the extreme conditions of ionic strength and pH. In a recent paper, Seung-Chul Yang and co-workers[52] proposed a procedure to stabilize iron oxide NPs in aqueous solution and highlighted that in digestive fluids aggregation occurred, but primary particle size measurements are still possible if factors affecting colloidal stability such as enzymes, pH and electrolytes were removed from samples.

In this scenario, density gradient UC is the appropriate technique to extract PC complexes from these fluids without over-manipulating the samples. In particular, we incubated Fe_3O_4 NPs in simulated salivary, gastric and intestinal fluids prepared as described in the Materials and methods sections. NPs appeared to be stable in salivary and gastric fluids forming small clusters of about 100 nm (see Fig. 5 and 6 in the ESI†), while extensive aggregation occurred in the intestinal conditions. In saliva and gastric fluids the recovery and analysis of PC complexes was also possible with conventional methods, although their protein composition was likely affected with respect to that *in situ*. In fact, although NTA showed very similar distributions for corona complexes isolated by UC compared to those by the normal protocol (Fig. 7a), the protein patterns, shown in the SDS-PAGE, were different (Fig. 7b) indicating a strong enrichment of proteins in the HC samples probably due to contamination from protein agglomerates that sediment together with the PC complexes. These aggregates are instead removed in the first sucrose gradient layers by UC with the recovery of pure fractions with PC complexes. Subsequent LC-MS analysis of the PC complexes isolated by UC showed that they were mainly composed of pepsin (34 kDa), some selected peptides from β-casein hydrolysis at a very low molecular weight (6 kDa),[53,54] α-lactalbumin (14.4 kDa) and β-lactoglobulin (18.4 kDa), while HC fractions were characterized by some stronger bands at a high molecular weight and consisted of a number of hydrolysed fragments not easily identifiable[55] probably due to an

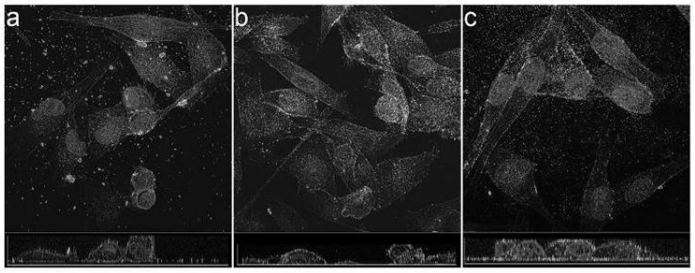

Fig. 6 Fe_3O_4 PC uptake. Confocal images of M202 cells after 2 hours of incubation with Fe_3O_4 PC complexes (10^{12} NPs per ml) isolated a) by centrifugation (HC), and (b) and (c) by ultracentrifugation. Actin filaments were stained by Texas Red®-X Phalloidin (red channel), nuclei by Hoechst 33342 (blue channel) and NPs by BODIPY FL EDA (green channel).

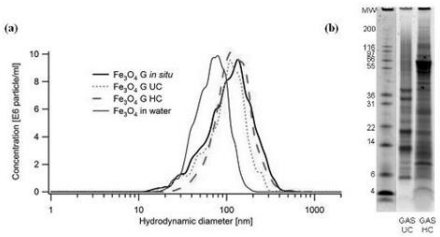

Fig. 7 Fe_3O_4 NPs in simulated gastric fluid. (a) Size distributions obtained from NTA for Fe_3O_4 NPs incubated with gastric fluids and the relative hard coronas isolated by ultracentrifugation (UC) and centrifugation (HC). (b) SDS-PAGE of the hard corona samples isolated by ultracentrifugation (UC) and conventional centrifugation (HC) methods, respectively, as indicated by the labels below the tracks of the gel.

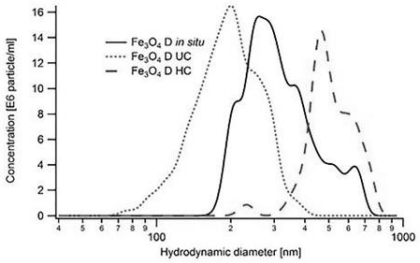

Fig. 8 Fe_3O_4 NPs in simulated intestinal fluid. Size distributions obtained from NTA for Fe_3O_4 NPs incubated with intestinal fluids for one hour and the relative hard coronas isolated by ultracentrifugation (UC) and centrifugation (HC).

extended exposure time with the biological fluid during the pellet procedure in the centrifuge (see the ESI† for LC-MS data).[35,56,57]

In contrast, the extensive aggregation combined with the complex composition of the intestinal media made it impossible to extract the PC complexes from this environment by conventional methods. Mainly composed of enzymes (trypsin, 23 kDa, and chymotrypsin, 25 kDa) and some persistent peptides, the intestinal environment led to strong NP aggregation but the PC complexes could be isolated through UC. NTA on the starting sample (*in situ*) showed a wide range of particulates ranging from 200 nm to micron size. NTA on UC fractions containing PC complexes recovered from this environment showed a small and relatively narrow population without contamination of the larger complexes that were instead found in the HC complexes isolated by centrifugal washings (see Fig. 8).

To rule out the possibility of proteins running through the sucrose gradient, control gels were performed with fluids in the absence of NPs as can be seen in Fig. 9. The first two sucrose fractions of all samples (with and without NPs) contained the unbound proteins, showing a similar composition in both samples (lanes 1–2, Fig. 9a and lanes 1*–2*, Fig. 9b). In the sample with the NPs the sucrose layer labelled as 8 showed the presence of a rich protein pattern with respect to the control that did not show the presence of any protein (lane 8*, Fig. 9c). In fact, sucrose fraction 8 was also brown coloured indicating the presence of Fe_3O_4 NPs. The hard and soft coronas obtained by centrifugation are very similar (lane HC and SC of Fig. 9a) while the corona isolated by UC (lane 8, Fig. 9a) presented some notable bands at 21 kDa persistent from the gastric phase and chymotrypsin at 25 kDa. Bile salts caused desorption of proteins according to their concentration and exposure time,[35,58,59] therefore also in this case the ability of UC to limit the contact time between the PC complexes and biological medium may affect the corona composition. Some bands at a higher molecular weight could not be found anywhere else and showed quite regular spacing among them.

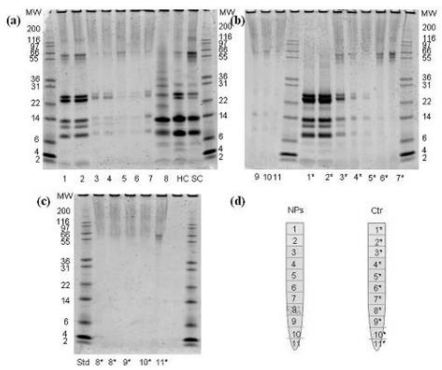

Fig. 9 SDS-PAGE of Fe_3O_4 NPs in simulated intestinal fluid. (a) SDS-gel containing UC fractions of the sample of intestinal fluid containing the NPs. Lane 8 contains the PC complexes, and the lanes called HC and SC contain soft corona and hard corona complexes, respectively, isolated by conventional methods. (b) and (c) Control samples without NPs to show no contamination from free proteins in the lanes with the PC complexes. (d) Schematic drawing of the sucrose layer arrangement in the UC tube showing where the NPs and proteins were found in the samples with NPs (NPs) and without NPs (Ctr).

From molecular weight estimation, we assume these to be oligomers of a very small fragment (4.9 kDa) although lower weight oligomers seem to be missing.

Conclusions

In this study we demonstrated that sucrose gradient ultracentrifugation is an effective tool in the isolation of protein corona complexes from complex biological media without

affecting their structure and composition with respect to those *in situ*. This approach can be applied to a wide range of nanoparticles by simply tuning the experimental conditions (centrifugation rate, time, temperature). Moreover, it proved to be a less invasive method keeping the structure and composition of the PC complexes intact as well as having a much higher resolution compared to conventional approaches in terms of separation by size. In fact, not only could the NPs be fully recovered from the environment, but also the structure of the resulting NP–protein complexes was more representative of that of the complexes *in situ*. Isolated PC complexes were also incubated with cells and those recovered by the UC methodology showed much less aggregation and a higher uptake with respect to those recovered by conventional methods. Moreover, it also allowed a fine separation of the different protein–NP aggregates to be present simultaneously in the biological environment even from very complex matrices such as simulated digestive fluids. In fact, to the best of our knowledge, this is the first example of the recovery of PC complexes from digestive fluids, in which NPs are known to aggregate extensively (mostly in intestinal conditions).

The ability to isolate and recover different NP–protein complexes in a stable form with such a high size resolution from diverse biological media may have a significant impact on the interpretation of the role of the protein corona in the interaction with cellular mechanisms. However, the biological relevance of these different complexes remains to be investigated.

Acknowledgements

This work was supported by funds from the British Skin Foundation and the Royal Society. FBB thanks the financial support from Regione Lombardia (Fondo per lo Sviluppo e la Coesione – FAS 2007–2013). Dr Davide Carta and Procarta are acknowledged for their help with NTA measurements. We thank Francesco Rossi for the preparation of digestive fluids.

Notes and references

1 D. Mishra, J. R. Hubenak and A. B. Mathur, *J. Biomed. Mater. Res., Part A*, 2013, **101**, 3646–3660.
2 M. L. Etheridge, S. A. Campbell, A. G. Erdman, C. L. Haynes, S. M. Wolf and J. McCullough, *Nanomedicine*, 2013, **9**, 1–14.
3 E. W. Group, Nano-materials: prevalence in personal care products, http://www.ewg.org/skindeep/2007/08/25/hundreds-of-personal-care-products-contain-poorly-studied-nano-materials/.
4 J. P. Kaiser, S. Zuin and P. Wick, *Sci. Total Environ.*, 2013, **442**, 282–289.
5 W. Zheng, P. Huang, D. Tu, E. Ma, H. Zhu and X. Chen, *Chem. Soc. Rev.*, 2015, **44**(6), 1379–1415.
6 Z. Valerio, A. Gabriele De, V. Luigi, C. Valentina, M. Claudia, G. Jacek, R. Andrea, C. Aldo Di and M. B. Thomas, *Nanotechnology*, 2013, **24**, 255401.
7 A. N. Shipway, E. Katz and I. Willner, *ChemPhysChem*, 2000, **1**, 18–52.
8 T. Borel and C. M. Sabliov, *Annu. Rev. Food Sci. Technol.*, 2014, **5**, 197–213.
9 N. Lewinski, V. Colvin and R. Drezek, *Small*, 2008, **4**, 26–49.
10 A. E. Nel, L. Madler, D. Velegol, T. Xia, E. M. V. Hoek, P. Somasundaran, F. Klaessig, V. Castranova and M. Thompson, *Nat. Mater.*, 2009, **8**, 543–557.
11 T. Cedervall, I. Lynch, S. Lindman, T. Berggård, E. Thulin, H. Nilsson, K. A. Dawson and S. Linse, *Proc. Natl. Acad. Sci. U. S. A.*, 2007, **104**, 2050–2055.
12 D. Walczyk, F. Baldelli Bombelli, M. P. Monopoli, I. Lynch and K. A. Dawson, *J. Am. Chem. Soc.*, 2010, **132**, 5761–5768.
13 M. Mahmoudi, J. Meng, X. Xue, X. J. Liang, M. Rahman, C. Pfeiffer, R. Hartmann, P. R. Gil, B. Pelaz, W. J. Parak, P. del Pino, S. Carregal-Romero, A. G. Kanaras and S. Tamil Selvan, *Biotechnol. Adv.*, 2014, **32**, 679–692.
14 C. D. Walkey and W. C. W. Chan, *Chem. Soc. Rev.*, 2012, **41**, 2780–2799.
15 I. Lynch and K. A. Dawson, *Nano Today*, 2008, **3**, 40–47.
16 S. Milani, F. Baldelli Bombelli, A. S. Pitek, K. A. Dawson and J. Rädler, *ACS Nano*, 2012, **6**, 2532–2541.
17 J. Wang, U. B. Jensen, G. V. Jensen, S. Shipovskov, V. S. Balakrishnan, D. Otzen, J. S. Pedersen, F. Besenbacher and D. S. Sutherland, *Nano Lett.*, 2011, **11**, 4985–4991.
18 E. A. Vogler, *Biomaterials*, 2012, **33**, 1201–1237.
19 M. Lundqvist, J. Stigler, G. Elia, I. Lynch, T. Cedervall and K. A. Dawson, *Proc. Natl. Acad. Sci. U. S. A.*, 2008, **105**, 14265–14270.
20 E. Casals, T. Pfaller, A. Duschl, G. J. Oostingh and V. Puntes, *ACS Nano*, 2010, **4**, 3623–3632.
21 W. G. Kreyling, S. Fertsch-Gapp, M. Schäffler, B. D. Johnston, N. Haberl, C. Pfeiffer, J. Diendorf, C. Schleh, S. Hirn, M. Semmler-Behnke, M. Epple and W. J. Parak, *Beilstein J. Nanotechnol.*, 2014, **5**, 1699–1711.
22 A. Albanese, C. D. Walkey, J. B. Olsen, H. Guo, A. Emili and W. C. W. Chan, *ACS Nano*, 2014, **8**, 5515–5526.
23 M. Lundqvist, J. Stigler, T. Cedervall, T. Berggård, M. B. Flanagan, I. Lynch, G. Elia and K. Dawson, *ACS Nano*, 2011, **5**, 7503–7509.
24 V. Sherwood, D. Di Silvio and F. Baldelli Bombelli, *Nanoscopic Agents in a Physiological Environment: The Importance of Understanding Their Characteristics*, Springer, Berlin Heidelberg, 2014, ch. 36, pp. 1–26.
25 S. R. Saptarshi, A. L. Duschl A Fau - Lopata and A. L. Lopata, *J. Nanobiotechnol.*, 2013, **11**, 26.
26 P. d. Pino, B. Pelaz, Q. Zhang, P. Maffre, G. U. Nienhaus and W. J. Parak, *Mater. Horiz.*, 2014, **1**, 301–313.
27 M. P. Monopoli, D. Walczyk, A. Campbell, G. Elia, I. Lynch, F. Baldelli Bombelli and K. A. Dawson, *J. Am. Chem. Soc.*, 2011, **133**, 2525–2534.
28 U. Sakulkhu, M. Mahmoudi, L. Maurizi, J. Salaklang and H. Hofmann, *Sci. Rep.*, 2014, 4.

29 L. Böhmert, M. Girod, U. Hansen, R. Maul, P. Knappe, B. Niemann, S. M. Weidner, A. F. Thünemann and A. Lampen, *Nanotoxicology*, 2013, **8**, 631–642.
30 J. Ashby, S. Schachermeyer, S. Pan and W. Zhong, *Anal. Chem.*, 2013, **85**, 7494–7501.
31 G. J. Howlett, A. P. Minton and G. Rivas, *Curr. Opin. Chem. Biol.*, 2006, **10**, 430–436.
32 K. L. Planken and H. Colfen, *Nanoscale*, 2010, **2**, 1849–1869.
33 N. Kanokwan, R. Vinayak, A. F. Jeffrey and R. Vytas, *Nanotechnology*, 2013, **24**, 155701.
34 K. E. Moore, M. Pfohl, F. Hennrich, V. S. K. Chakradhanula, C. Kuebel, M. M. Kappes, J. G. Shapter, R. Krupke and B. S. Flavel, *ACS Nano*, 2014, **8**, 6756–6764.
35 D. Docter, U. Distler, W. Storck, J. Kuharev, D. Wünsch, A. Hahlbrock, S. K. Knauer, S. Tenzer and R. H. Stauber, *Nat. Protocols*, 2014, **9**, 2030–2044.
36 S. Tenzer, D. Docter, J. Kuharev, A. Musyanovych, V. Fetz, R. Hecht, F. Schlenk, D. Fischer, K. Kiouptsi, C. Reinhardt, K. Landfester, H. Schild, M. Maskos, S. K. Knauer and R. H. Stauber, *Nat. Nanotechnol.*, 2013, **8**, 772–781.
37 M. Werwie, N. Fehr, X. Xu, T. Basché and H. Paulsen, *Biochim. Biophys. Acta*, 2014, **1840**, 1651–1656.
38 S. Sun, H. Zeng, D. B. Robinson, S. Raoux, P. M. Rice, S. X. Wang and G. Li, *J. Am. Chem. Soc.*, 2003, **126**, 273–279.
39 C.-A. J. Lin, R. A. Sperling, J. K. Li, T.-Y. Yang, P.-Y. Li, M. Zanella, W. H. Chang and W. J. Parak, *Small*, 2008, **4**, 334–341.
40 S. Stolnik, S. Dunn, M. Garnett, M. Davies, A. A. Coombes, D. C. Taylor, M. P. Irving, S. C. Purkiss, T. F. Tadros, S. Davis and L. Illum, *Pharm. Res.*, 1994, **11**, 1800–1808.
41 J.-C. Leroux, P. Gravel, L. Balant, B. Volet, B. M. Anner, E. Allémann, E. Doelker and R. Gurny, *J. Biomed. Mater. Res.*, 1994, **28**, 471–481.
42 V. Torrisi, A. Graillot, L. Vitorazi, Q. Crouzet, G. Marletta, C. Loubat and J. F. Berret, *Biomacromolecules*, 2014, **15**, 3171–3179.
43 M. Mahmoudi, M. A. Shokrgozar, S. Sardari, M. K. Moghadam, H. Vali, S. Laurent and P. Stroeve, *Nanoscale*, 2011, **3**, 1127–1138.
44 M. Jansch, P. Stumpf, C. Graf, E. Rühl and R. H. Müller, *Int. J. Pharm.*, 2012, **428**, 125–133.
45 V. Sánchez-López, J. M. Fernández-Romero and A. Gómez-Hens, *Anal. Chim. Acta*, 2009, **645**, 79–85.
46 D. Pozzi, V. Colapicchioni, G. Caracciolo, S. Piovesana, A. L. Capriotti, S. Palchetti, S. De Grossi, A. Riccioli, H. Amenitsch and A. Lagana, *Nanoscale*, 2014, **6**, 2782–2792.
47 G. Maiorano, S. Sabella, B. Sorce, V. Brunetti, M. A. Malvindi, R. Cingolani and P. P. Pompa, *ACS Nano*, 2010, **4**, 7481–7491.
48 M. J. D. Clift, S. Bhattacharjee, D. M. Brown and V. Stone, *Toxicol. Lett.*, 2010, **198**, 358–365.
49 Q. Peng, S. Zhang, Q. Yang, T. Zhang, X.-Q. Wei, L. Jiang, C.-L. Zhang, Q.-M. Chen, Z.-R. Zhang and Y.-F. Lin, *Biomaterials*, 2013, **34**, 8521–8530.
50 E. Zimmermann and R. H. Müller, *Eur. J. Pharm. Biopharm.*, 2001, **52**, 203–210.
51 Y. V. Frenkel, A. D. Clark, K. Das, Y.-H. Wang, P. J. Lewi, P. A. J. Janssen and E. Arnold, *J. Med. Chem.*, 2005, **48**, 1974–1983.
52 S.-C. Yang, S.-Y.-R. Paik, J. Ryu, K.-O. Choi, T. S. Kang, J. K. Lee, C. W. Song and S. Ko, *Food Chem.*, 2014, **161**, 185–191.
53 A. Macierzanka, A. I. Sancho, E. N. C. Mills, N. M. Rigby and A. R. Mackie, *Soft Matter*, 2009, **5**, 538–550.
54 M. Defernez, G. Mandalari and E. N. C. Mills, *Electrophoresis*, 2010, **31**, 2838–2848.
55 N. Kitabatake and Y.-I. Kinekawa, *J. Agric. Food Chem.*, 1998, **46**, 4917–4923.
56 M. P. Monopoli, C. Aberg, A. Salvati and K. A. Dawson, *Nat. Nanotechnol.*, 2012, **7**, 779–786.
57 E. Monogioudi, G. Faccio, M. Lille, K. Poutanen, J. Buchert and M.-L. Mattinen, *Food Hydrocolloids*, 2011, **25**, 71–81.
58 T. Winuprasith, S. Chantarak, M. Suphantharika, L. He and D. J. McClements, *J. Colloid Interface Sci.*, 2014, **426**, 333–340.
59 J. Maldonado-Valderrama, N. C. Woodward, A. P. Gunning, M. J. Ridout, F. A. Husband, A. R. Mackie, V. J. Morris and P. J. Wilde, *Langmuir*, 2008, **24**, 6759–6767.

Electronic Supplementary Material (ESI) for Nanoscale.

Supplementary Information

High-resolution isolation of protein corona nanoparticles from complex physiological fluids

Desirè Di Silvio,[a,b] Neil Rigby,[b] Balazs Bajka[b], Andrew Mayes,[c] Alan Mackie [b] and Francesca Baldelli Bombelli*[a]

Figure S1

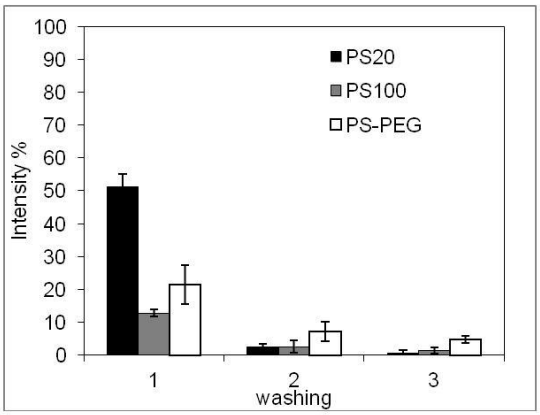

Figure S1. Fluorescence intensity emission of the surnatant solutions compared to that of the initial stock solutions when centrifugal washings are performed on *in situ* samples of polystyrene NPs prepared as described in the Material and Method section. The excitation and emission wavelengths weres 490 nm and 515 nm, respectively.

Figure S2

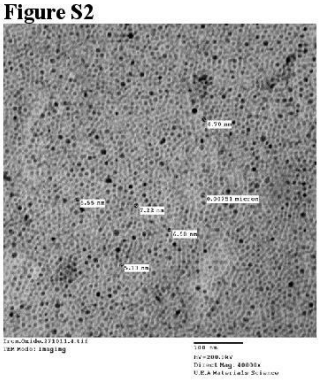

Figure S2. TEM image of Fe_3O_4 NPs stabilized by oleic acid and dispersed in toluene. 1 drop of the dispersionsi was placed on the carbon film 300 mesh Cu(50)(Agar Scientific). The instrument was Joel 200EX with tungsten filament and acceleration voltage of 180kV to 200kV.

Figure S3

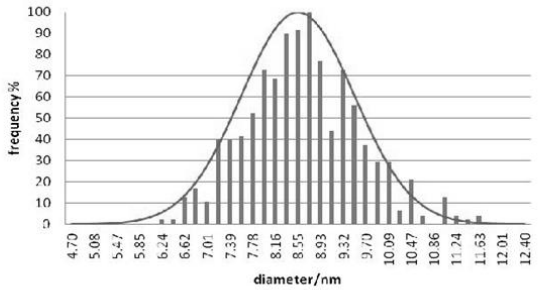

Figure S3. Statistical size distributions on 500 NPs imaged by TEM and analysed by ImageJ software.

Figure S4

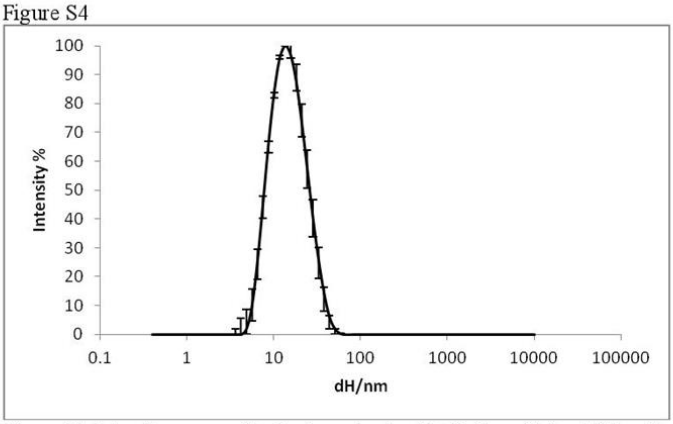

Figure S4. Intensity averaged hydrodynamic size distribution obtained fitting the DLS auto-correlation functions by cumulant analysis of Fe_3O_4 NPs stabilized by oleic acid in toluene.

Table S1. Physical parameters used to derive the concentration of the sample in NPs/ml from ICP- AES measures that give the total iron concentration in mg/l. The diameter value was extracted from the TEM images statistic.

NPs	Density [g/cm³]	Diameter NP [nm]	Volume [cm³]	Weight NP [g]
Fe_3O_4	5.2	8.5±1.0	$3.2*10^{-19}$	$1.7*10^{-12}$

Figure S5

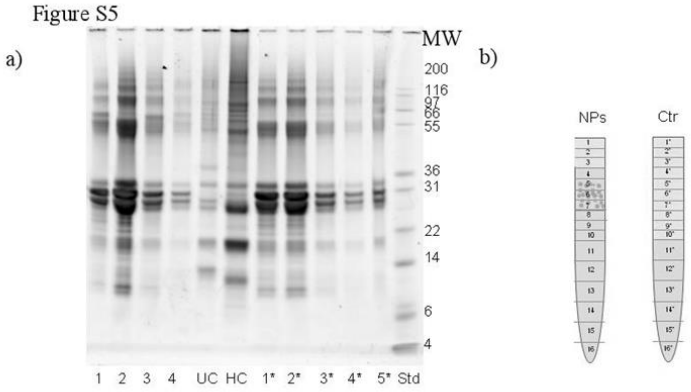

Figure S5. a) SDS-PAGE of Fe_3O_4 NPs in oral fluids. b) Scheme of the sucrose layer arrangement in the UC tube showing where NPs and proteins were located. A control sample was run on the fluid without NPs in the same experimental conditions. The first 5 ml of sucrose were collected in fractions of 0.5 ml, while from number 6th in 1ml aliquots. NPs were found in fractions 5 to 7 that were pooled together in one fraction (UC). HC was isolated centrifuging the same sample after incubation (HC). Samples decorated with * are the fractions from the control.

Figure S6

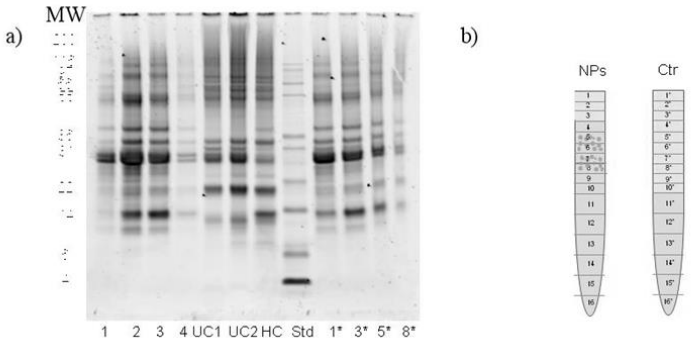

Figure S6. a) SDS-PAGE of Fe_3O_4 NPs in fluid before gastric phase. B) Scheme of the sucrose layer arrangement in the ultracentrifuge tubes showing where NPs and proteins were located. A control was performed on fluid in the same condition of NPs replacing them with water. The first 5 ml of sucrose were collected in fractions of 0.5 ml, while from number 6th in 1ml aliquots. NPs were found in fractions 5 to 7 that were pooled together in one fraction (UC1) and in 8 (UC2). HC was isolated centrifuging the same sample after incubation (HC). Samples decorated with * are the fractions from the control.

Figure S7

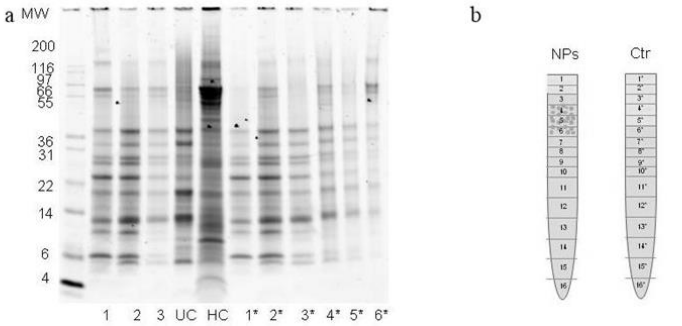

Figure S7 a) SDS-PAGE of Fe_3O_4 NPs in gastric fluid after 120 min. b) Scheme of the sucrose layer arrangement in the ultracentrifuge tubes showing where NPs and proteins were located. A control was performed on fluid in the same condition of NPs replacing them with water. The first 5 ml of sucrose were collected in fractions of 0.5 ml, while from number 6 in 1ml aliquots. NPs were found in fractions 4 to 6 that were pooled together in one fraction (UC). HC was isolated centrifuging the same sample after incubation (HC). Samples decorated with * are the fractions from the control.

Figure S8

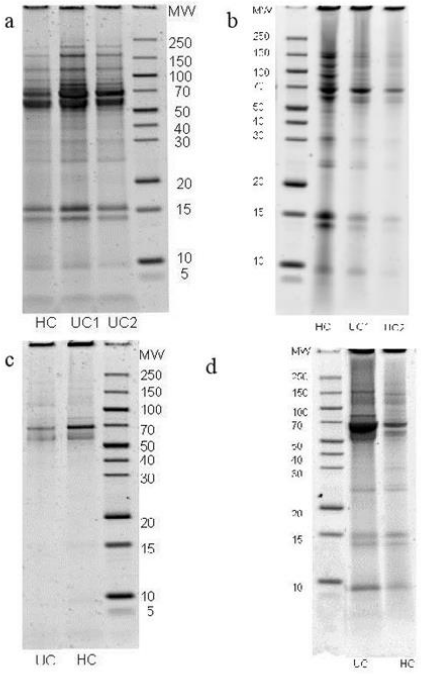

Figure S8. SDS PAGE of a) Fe_3O_4 NPs in 90% FBS, b) PS-COOH100 in 55% FBS, c) PS-PEG in 55% FBS, d) PS-COOH20 in 55% FBS. Lanes labeled as UCs and HCs represent samples isolated through ultracentrifugation and standard centrifugal washings, respectively.

Figure S9. LC-MS

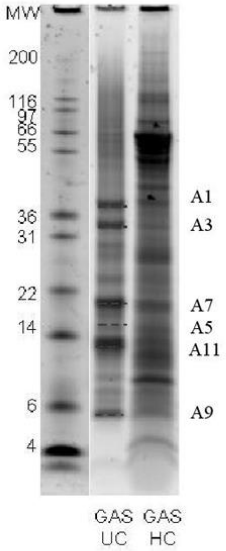

Figure S9 Gastric digestion gel in which are highlighted with a red dashed line all bands analysed by LC-MS. The band code is reported on the side of the gel in the correspondent order. Below tables listing major peptides found in bands analyzed.

Table S1. Mass Spectrometry results (from gel reported in Figure 7b)

Lane A1

Name	alpha-s2-casein	Major allergen beta-lactoglobulin	Butyrophilin	Vicilin 47k
coverage %	20	28	6	35
score	46	36	45	166
nominal mass	26173	20355	59912	49542
signal sequence length	15	16	26	24
total peptide length	222	178	562	437

Lane A3

name	Vicilin 47k	Major allergen beta-lactoglobulin	Butyrophilin	alpha-s1-casein	alpha-s2-casein	Convicilin	pepsine a
coverage %	39	34	26	32	31	5	4
score	299	178	134	99	69	62	48
nominal mass	49542	20355	59912	24498	26173	60139	41635
signal sequence length	24	16	26	15	15	-	15
total peptide length	437	178	562	214	222	511	385

Lane A5

name	alpha-s2-casein	Beta-lactoglobulin	Butyrophilin	Vicilin 47k	Galectin	Lactoferrin	alpha-s1-casein
coverage %	52	44	11	25	8	7	32
score	166	153	98	81	81	72	69
nominal mass	26173	20176	59912	49542	15095	79998	24498
signal sequence length	15	16	26	24	-	-	15
total peptide length	222	178	526	437	136	708	214

Lane A7

name	Major allergen beta-lactoglobulin	alpha-s2-casein	alpha-s1-casein	Alpha-lactalbumin	Vicilin 47k
coverage %	64	40	26	16	18
score	178	173	75	48	46
nominal mass	20355	26173	24498	16750	49542
signal sequence length	16	15	15	19	24
total peptide length	178	222	214	142	437

Lane A9

name	ALB protein	Alpha-lactalbumin	Beta-lactoglobulin;	Lactoferrin	Vicilin 47k	Beta casein	Butyrophilin	Albumin-1 A OS= Pisum sativum	Alpha-S2-casein
coverage %	16	38	17	6	8	37	4	6	29
score	140	115	68	67	42	49	46	34	23
nominal mass	71244	16750	20176	79998	49542	5164	59912	14473	26173
signal sequence length	25	19	16	19	24		26	26	22
total peptide length	607	142	178	708	437	45	526	130	222

Lane A11

name	Serum albumin	alpha-s2-casein	Butyrophilin
coverage %	19	38	4
score	169	128	47
nominal mass	55487	26173	59912
signal sequence length	-	15	26
total peptide length	476	222	526

8.3 Effect of protein corona magnetite nanoparticles derived from bread in vitro digestion on Caco-2 cells morphology and uptake

The research paper mentioned below is from *Di Silvio D. et al*. and the results are presented in Chapter 6. The full paper and the supporting info are reported in the following pages.

Di Silvio, D.; Rigby, N.; Bajka, B; Mackie, A; Baldelli Bombelli F.; *The International Journal of Biochemistry and Cell Biology* **In Press, Corrected Proof, Available online 11 November 2015**

G Model
BC-4721; No. of Pages 11
ARTICLE IN PRESS
The International Journal of Biochemistry & Cell Biology xxx (2015) xxx–xxx
Contents lists available at ScienceDirect
The International Journal of Biochemistry & Cell Biology
journal homepage: www.elsevier.com/locate/biocel

Effect of protein corona magnetite nanoparticles derived from bread *in vitro* digestion on Caco-2 cells morphology and uptake

Desirè Di Silvio[a,b,**], Neil Rigby[b], Balazs Bajka[b], Alan Mackie[b], Francesca Baldelli Bombelli[c,*]

[a] School of Pharmacy, University of East Anglia, Norwich Research Park, Norwich, United Kingdom
[b] Institute of Food Research, Norwich Research Park, Norwich, United Kingdom
[c] Department of Chemistry, Materials and Chemical Engineering Giulio Natta, Politecnico di Milano, Milan, Italy

ARTICLE INFO

Article history:
Received 8 September 2015
Received in revised form 16 October 2015
Accepted 17 October 2015
Available online xxx

Keywords:
Protein corona
Nanoparticle
Gastrointestinal digestion
Bread
Caco-2
Cell uptake

ABSTRACT

Nanoparticles (NPs) in biological fluids immediately interact with proteins forming a biomolecular corona (PC) that imparts their biological identity. While several studies on the formation of the PC in human plasma have been reported, the PC of orally administrated NPs has been less investigated, mostly in the presence of a food matrix. In fact, food matrixes when digested are subject of several dynamic changes that will certainly affect the PC formed on the NPs. The lack of studies on this topic is clearly related to the difficulty in isolating representative PC NPs from such a complex environment. In this work magnetite NPs were added to *in vitro* simulated digestion simultaneously with bread and PC NPs were isolated after gastric and duodenal phases by sucrose gradient ultracentrifugation (UC). The PC NPs were characterized in terms of size and protein composition. Translocation studies were then performed on Caco-2 monolayers in a serum free environment and cell morphology was characterized by confocal microscopy. PC NPs isolated from gastric and duodenal phases were different in size, surface charge and protein corona composition. NP cellular uptake was enhanced by the *digestive* PC inducing morphology changes in the cell monolayer. Overall, in this work we were able to isolate PC NPs from digested fluids in the presence of a food matrix and study their biological response on Caco-2 cells.

1. Introduction

When NPs are in a biological environment they readily interact with the surrounding proteins that adsorb to the surface forming a PC (Walczyk et al., 2010). The PC composition confers a biological identity to the NP (Cedervall et al., 2007; Lynch et al., 2007; Walczyk et al., 2010) that determines NP-cell interactions (Lundqvist et al., 2008; Lynch et al., 2007; Monopoli et al., 2012; Soenen et al., 2015; Walkey et al., 2014).

PCs from blood have been extensively studied for many NPs (Cai et al., 2013; Foroozandeh and Aziz, 2015; Ghavami et al., 2013; Jansch et al., 2012; Sherwood et al., 2014; Treuel et al., 2015) and only recently PCs obtained from *in vitro* models have been compared to those isolated from blood *in vivo* (Hadjidemetriou et al., 2015) and the dynamic nature of the blood circulation seemed to modify corona composition and morphology. In contrast, PCs formed in fluids other than blood, such as gastrointestinal (GI) fluids have been less extensively investigated, even though they are important for pharmacological and toxicological reasons (Clift et al., 2010; Lefebvre et al., 2014; Setyawati et al., 2015). In fact, the oral delivery route is one of the most commonly used for drug delivery and ingestion of NPs represents a probable way for NPs to enter the human body, being extensively used in food industry as additives (flavour, texture, stability improvements) (Borel and Sabliov, 2014) and in packaging (Clift et al., 2010; Maiorano et al., 2010; Peng et al., 2013).

The GI tract is a complex environment characterized by pH ranging from two to eight, high electrolyte concentrations, enzymes and food matrix that change dynamically. All these elements can affect NPs colloidal stability (Böhmert et al., 2013; Yang et al., 2014; Zimmermann and Müller, 2001) and PC composition with consequences for bioavailability and toxicity. For example, recently, core–shell gold NPs were shown to be subject to proteolytic

Abbreviations: NP, nanoparticle; UC, ultracentrifugation; PC, protein corona; GI, gastrointestinal; SSF, simulated salivary fluid; SGF, simulated gastric fluid; SIF, simulated intestinal fluid; PMAO, poly (maleic)-alt-1-octadecene; CF, carboxyfluorescien; FA, fluoresceinamine; SFM, serum free medium.

* Corresponding author.
** Corresponding author at: School of Pharmacy, University of East Anglia, Norwich Research Park, Norwich, United Kingdom.
E-mail address: francesca.baldelli@polimi.it (F. Baldelli Bombelli).

http://dx.doi.org/10.1016/j.biocel.2015.10.019
1357-2725/

Please cite this article in press as: Di Silvio, D., et al., Effect of protein corona magnetite nanoparticles derived from bread *in vitro* digestion on Caco-2 cells morphology and uptake. Int J Biochem Cell Biol (2015), http://dx.doi.org/10.1016/j.biocel.2015.10.019

Table 1
Final concentrations of the salts used in SSF, SGF, SIF according to INFOGEST recommendations (Minekus et al., 2014).

	SSF [mmol/l]	SGF [mmol/l]	SIF [mmol/l]
KCl	15.1	6.9	6.8
KH_2PO_4	3.7	0.9	0.8
$NaHCO_3$	13.6	25	85
NaCl	–	47.2	38.4
$MgCl_2(H_2O)_6$	0.15	0.1	0.33
$(NH_4)_2CO_3$	0.06	0.5	–
$CaCl_2(H_2O)_2$[a]	1.5	0.15	0.6
KCl	15.1	6.9	6.8

[a] It was added to the final mixture to avoid precipitation.

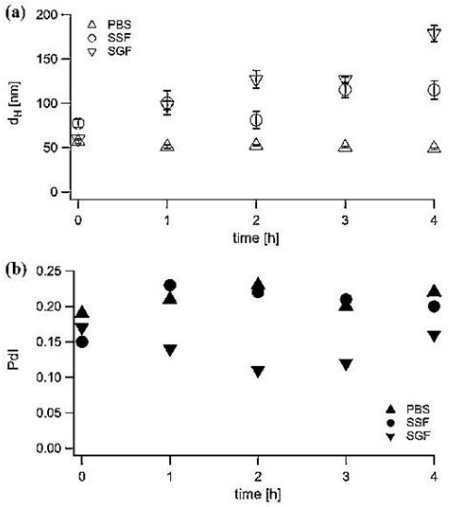

Fig. 1. Fe_3O_4 NPs colloidal stability. (a) Hydrodynamic diameters variation by time for Fe_3O_4 NPs incubated in PBS (triangle), in SSF (circle) and in SGF (upside-down triangle) at 37 °C. (b) PdI variation for the same samples. Hydrodynamic diameters and PdI were obtained by DLS from cumulant analysis of the auto-correlation data.

Table 2
Characterization of Fe_3O_4 NPs in PBS by DLS and NTA and cognate PC complexes isolated from simulated gastric fluid by UC (G-NPs).

	Fe_3O_4-NPs	G-NPs
d_H [nm][a]	73 ± 8	245 ± 13
SD [nm][b]	32 ± 18	60 ± 17
d_H [nm][c]	46.9 ± 0.9	199.2 ± 0.2
PdI[d]	0.20 ± 0.01	0.26 ± 0.01
Zp [mV]	−21.6 ± 1.5	−4.3 ± 0.2

All data were presented as the average of three indipendent measurements with relative standard deviation.

[a] Hydrodynamic diameter (d_H) was calculated avaraging the hydrodynamic diameters of all NPs tracked in a particle-by-particle modality by NTA.

[b] SD is the standard deviation on all the hydrodynamyc diameters measured in a particle-by-particle modality by NTA.

[c] Hydrodynamic diameter (d_H) obtained by DLS from the cumulant analysis of the auto-correlation data.

[d] Polydispertity indexes (PdI) were obtained by DLS from the cumulant analisys of the auto-correlation data.

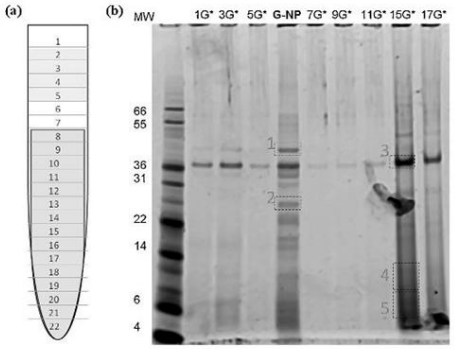

Fig. 2. Isolation of PC–NPs complexes from simulated gastric fluid. (a) Schematic drawing of the sucrose layers of the UC of the simulated gastric fluid enriched with bread and NPs. Upper fractions (2–5) contained NPs, while lower fractions contained floating starch residues. A control experiment only on digested bread without NPs was also performed in the same conditions. (b) SDS–PAGE of fractions 2–5 (G-NP lane) and fractions isolated from the digestion without NPs (lanes marked with * symbol). Bands labelled with dashed lines and numbers were characterized by LC–MS.

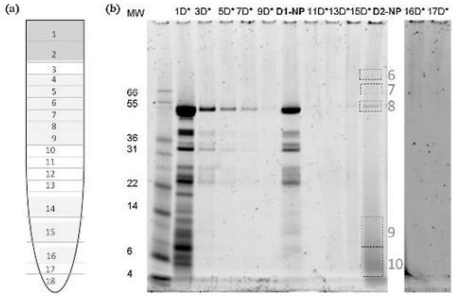

Fig. 3. Isolation of PC–NPs complexes from simulated intestinal fluid. (a) Schematic drawing of the sucrose layers of the UC of the simulated duodenal fluid enriched with bread and NPs. Highlighted fractions at the top of the gradient contained bile salts and low density peptides. Pink fractions (4–9 and 14–16) contained NPs. A control experiment only on digested bread without NPs was also performed in the same conditions. (b) SDS–PAGE of fractions 4–9 and 14–16 (D1-NP and D2-NPs lanes respectively). Lanes labelled with * were loaded with fractions from the control without NPs. Bands labelled with dashed lines and numbers were characterized by LC–MS.

enzymes and pH conditions in lysosomes when they were internalized by macrophages and endothelial cells. The shell was partially removed and PC affected by the altered coating (Kreyling et al., 2014). Moreover, Docter et al. (2015) in a recent review highlighted the lack of reports about the influence of PC complexes on the GI tract albeit some studies revealed that upon NPs exposure gut homeostasis was altered.

Several models have been proposed to simulate the ingestion process. *In vivo* mammalian models have been used, but *in vitro* models are generally preferred because they are more versatile, less expensive and do not require ethical approval. *In vitro* models can be dynamic when physical processing of the food and temporal changes of the gastrointestinal conditions (pH changes, enzymes and electrolytes concentrations) mimic

Please cite this article in press as: Di Silvio, D., et al., Effect of protein corona magnetite nanoparticles derived from bread *in vitro* digestion on Caco-2 cells morphology and uptake. Int J Biochem Cell Biol (2015), http://dx.doi.org/10.1016/j.biocel.2015.10.019

Table 3
Characterization by DLS and NTA of Fe_3O_4 NPs in PBS and PC complexes isolated from intestinal fluids by UC after dialysis (D1- and D2-NPs).

	Fe_3O_4-NPs	D1-NPs	D2-NPs
d_H [nm][a]	73 ± 8	116 ± 14	143 ± 17
SD [nm][b]	32 ± 18	55 ± 9	48 ± 9
d_H [nm][c]	46.9 ± 0.9	85.7 ± 2.9	116.6 ± 5.2
PdI [nm][d]	0.20 ± 0.01	0.21 ± 0.02	0.23 ± 0.01
Zp [mV]	−21.6 ± 1.5	−24.2 ± 0.4	−16.1 ± 1.2

All data were presented as the average of three indipendent measurements with relative standard deviation.
[a] Hydrodynamic diameter (d_H) was calculated averaging the hydrodynamic diameters of all NPs tracked in a particle-by-particle modality by NTA.
[b] SD is the standard deviation on all the hydrodynamyc diameters measured in a particle-by-particle modality by NTA.
[c] Hydrodynamic diameter (d_H) obtained by DLS from the cumulant analysis of the auto-correlation data.
[d] Polydispertity indexes (PdI) were obtained by DLS from the cumulant analisys of the auto-correlation data.

the *in vivo* digestive process. They can also be static when there are synthetic fluids that reproduce chemically and enzymatically the environmental conditions encountered in the distinct areas of the GI tract and the meal/enzyme ratio is kept constant. The INFOGEST COST action network aimed to give some recommendations to achieve standard conditions for static *in vitro* digestion to allow comparison of results among research groups (Minekus et al., 2014). In this work we adopted a static *in vitro* model following INFOGEST recommendations as described in detail in Section 2.2.

The lack of absorption in most *in vitro* models can be partially covered by cell culture models. Cell monolayers are often used to assess epithelial permeability of compounds. Immortalized Caco-2 cell lines are commonly used because they are able to form an adherent monolayer that shows some characteristics of the gut epithelium. Thus, translocation studies can be performed when they are grown on semi-permeable membranes mimicking the transport of substances from the apical to the basolateral side (Lefebvre et al., 2014). Other models are based on Caco-2 co-culture with other cells that are able to express mucus (Ensign et al., 2012).

There are many studies on translocation of NPs across Caco-2 monolayers (Lefebvre et al., 2014), but most of them deal with *in situ* NPs. Walczak et al. (2015b) investigated polymeric NPs translocation in different *in vitro* models taking into account the formation of a corona upon exposure to complete cell medium. Afterwards, the same group showed that NPs, if subject of *in vitro* digestion, express a different corona upon contact with cell culture medium compared to pristine NPs (Walczak et al., 2015a). On the other hand, Lichtenstein et al. (2015) studied the impact of food on silver NPs digestion. They modified the *in vitro* digestion model of Böhmert et al. (2013) by adding food components to the digestive fluid. They found that the corona originating from food digestion was able to stabilize NPs in full cell medium, while NPs digested without food extensively aggregated. They showed also that the NPs digested with food had similar uptake to nondigested NPs, while those digested without food showed less uptake.

To the best of our knowledge there is no previous work in which NPs subjected to simulated digestion in the presence of food matrix were isolated from the digestive chime and characterized in terms of corona composition and structure. In our previous work we showed the suitability of sucrose gradient ultracentrifugation (UC) to recover PC complexes representative of those *in situ* incubating magnetite NPs with gastric and duodenal digestion of skimmed milk powder (Di Silvio et al., 2015). The NPs were coated with a polymer shell functionalized with a fluorescent molecule, which was shown to be stable during the digestion. Here we describe the simultaneous simulated *in vitro* digestion of NPs and bread as a more representative model of the *in vivo* digestive process. PC complexes were isolated by sucrose gradient UC after gastric and duodenal phases. The recovered PC complexes were characterized by size, surface charge and corona composition by dynamic light scattering (DLS), nanoparticles tracking analysis (NTA), SDS–PAGE and LC–MS. The effect of the corona on uptake and translocation through a Caco-2 monolayer was investigated in serum free environment to stress on the role of the corona formed during digestion. Laser scanning confocal microscopy (LSCM) was used to assess morphological alteration in the monolayer.

2. Materials and methods

2.1. Fluorescent magnetite NPs synthesis

Carboxylated Fe_3O_4 NPs were synthesized following the protocol of Sun et al. (2003) and coated by poly (maleic)-alt-1-octadecene (PMAO, Sigma) according to Lin et al. (2008) for water transfer. Sucrose density gradient ultracentrifugation (6.6–66 w/w%, 187k rcf, 4 h, 20 °C) was performed to purify them from excess polymer. Purified NPs were fluorescently labelled by BODIPY® FLEDA (LifeTechnologies) through N-(3-dimethylaminopropyl)-N′-ethylcarbodiimide hydrochloride chemistry (Sigma). This dye was chosen because, according to the supplier, its quantum yield is minimally affected by the pH and polarity of the solvent (Karolin et al., 1994). Unbound free dye was removed by Amicon centrifugal filters (50 kDa MWCO, 360 rcf). Sucrose, sodium phosphate dibasic, potassium phosphate monobasic, sodium chloride and potassium chloride are from SIGMA.

2.2. In vitro *static digestion*

The *in vitro* model adopted in this work to simulate digestion is based on INFOGEST recommendations (Minekus et al., 2014). The protocol aims to mimic the *in vivo* conditions that describe the oral, gastric and small intestinal phases. Specific pH, electrolyte concentrations and enzymes characterize each phase. In Table 1, a summary of the electrolytes final concentrations in the simulated salivary fluid (SSF), simulated gastric fluid (SGF) and simulated intestinal fluid (SIF) is reported. The pH was adjusted by concentrated solutions of HCl and NaOH during the digestion at pH 3 and 7 for SGF and SIF, respectively. Calcium salt solutions were added to the final mixture of each phase to avoid precipitation in the electrolyte solutions.

The digestive simulation was performed at 37 °C under magnetic stirring. The oral phase lasted for 2 min and α-amylase was not added to the mixture (Woolnough et al., 2010). The gastric phase lasted for 2 h: SGF and Porcine Pepsin (final activity 2000 U/ml, Sigma Pepsin, P7012) were added. In the duodenal phase SIF, bile salts (160 mM) and pancreatin from porcine pancreas (final trypsin activity 100 U/ml, Sigma, P7545) were added to the mixture. Pancreatin in SIF formed a fibrous precipitate that was centrifuged at 4 °C for 1 min. Negligible loss of activity was assessed using the p-toluene-sulfonyl-L-arginine methyl ester (TAME) assay for trypsin activity (Hummel, 1959).

2.3. Sucrose gradient ultracentrifugation

Solutions of sucrose (Sigma) were prepared at increasing concentration from 6.6 w/w% to 66 w/w% in water and 11 ml of linear sucrose gradient were layered in 13 ml tubes and left to equilibrate overnight before being subjected to ultracentrifugation (UC) using a SW41 Ti rotor (Beckman Coulter) at 20 °C. 0.5 ml of sample was loaded in two tubes. UC was run for 1 h at 20 °C at 48k rcf and 195k rcf for gastric and duodenal samples, respectively. Collected fractions were analyzed and those fractions containing PC NPs were

Please cite this article in press as: Di Silvio, D., et al., Effect of protein corona magnetite nanoparticles derived from bread *in vitro* digestion on Caco-2 cells morphology and uptake. Int J Biochem Cell Biol (2015), http://dx.doi.org/10.1016/j.biocel.2015.10.019

Table 4
Selected peptides common to G-NPs and D2-NPs complexes. Bands were highlighted in Figs. 2b and 3b.

Name	Taxonomy	Nominal mass	Band	Coverage[a]	Score[b]
Vicilin 47k	*Pisum sativum*	49542	B1	37	188
			B2	34	172
			B5	47	264
			B6	18	109
Legumin	*Pisum sativum*	59633	B9	26	268
			B1*	23	115
			B2	26	265
0.19 dimeric alpha-amylase inhibitor	*Aegilops tauschii*	13881	B4	77	792
			B5	70	343
Dimeric alpha-amylase inhibitor	*Triticum dicoccoides*	15666	B9	29	213
			B10	49	215
Lectin	*Cicer arietinum*	26363	B2	48	265
			B6	37	102
Adh1p	*S. cerevisiae*	37296	B3	51	322
			B6	19	94
			B7	20	98
			B8	38	156
			B9	54	361
			B10	56	676

[a] Sequence coverage is calculated by dividing the number of amino acids observed by the protein amino acid length.
[b] The score is a probability based score. The total score is the probability (P) that the observed match is a random event. Score = $-10 \times \mathrm{Log}_{10}(P)$.

dialysed against PBS (3–5k MWCO, SpectrumLabs) overnight at 4 °C. Before analysis, the sample volume was reduced to 300 μl by 50 kDa MWCO Amicon centrifugal concentrator at 405 rcf.

2.4. Dynamic Light Scattering and Z-potential

Hydrodynamic diameters of dialysed dispersions were measured by Zetasizer SZ (Malvern). 50 μl of the samples were diluted in 400 μl of PBS in 1 ml cuvette to obtain attenuation values in the 7–9 range and measured at 25 °C equilibrating samples for 120 s prior to measurement. Data were presented as an average of three measurements. The Z-averaged sizes (Z-ave) and the polydispersity index (PdI) were obtained by cumulant analysis of the auto-correlation functions. Zeta potential (Zp) was measured using disposable capillary cells (Malvern). Data are the average of three measurements of 10 runs each.

2.5. Nanoparticles tracking analysis

Samples in sucrose were analyzed by NTA diluting them with MQ water to reach an ideal concentration of $1–3 \times 10^8$ NPs/ml. Three videos of 60 s were collected for each sample and analyzed by NTA software. The software is able to track NPs individually and calculate their diffusion coefficients. In this way, a mean value of the hydrodynamic diameter (Mean) is obtained with the relative standard deviation (SD) with respect to all tracks. Results are presented as an average of three independent measurements.

2.6. SDS–PAGE

30 μl of sample were added to 15 μl of SDS–PAGE loading buffer 3x (10% DTT, Thermo Scientific) and kept at 98 °C for 5 min. Digested samples that did not contain NPs were mixed to the loading buffer without any previous treatment and denatured as above. 20 μl of samples and 5 μl of molecular ladder (Mark12 Unstained standard, Invitrogen) were loaded on 10% Precast Gel NuPAGE (Life Technology). The running buffer used was MES buffer (NuPAGE 20×, Invitrogen). Gels were run at 200 V for 35 min. Gels were developed by Sypro Ruby Protein Stain (Biorad) and imaged by Biorad Pharos FX+, the software used to elaborate images was Image Lab (Biorad).

2.7. LC–MS

ProPick instrument was used to locate and cut bands from the gel. Bands were digested at 37 °C for 3 h by 10 mM ammonium bicarbonate 10 ng/μl trypsin gold (Promega, V528A in 50 mM Acetic Acid) (prepared 01-May-14). 1% formic acid (Sigma) was added prior freezing samples and storing at −80 °C. Samples were washed in 50% acetonitrile (Fisher), vortexed and dried out at the Low Drying setting (no heat) on a Speed Vac SC110 (Savant) fitted with a refrigerated condensation trap and a Vac V-500 (Buchi). Samples were again stored at −80 °C until ready for Orbitrap analysis. Protein identification was achieved by combining spectrum quality scoring obtained from a conventional database search program MASCOT (Matrix Science, London, England). Search parameters were peptide mass and fragment mass tolerances of 5 ppm and 0.5 Da respectively, variable modification was oxidation (M), fixed modification carbamidomethyl (C), enzyme specificity was trypsin, two missed cleavages were allowed. All taxonomy database was searched. Peptides with high scores were listed. The score represents the probability that the match found is a random event, so the higher it is the more likely is the match.

2.8. Translocation experiment and laser scanning confocal microscopy (LSCM)

Caco-2 monolayer was used as model to study the effect of the digested corona on NPs cellular uptake and transport across the membrane in the gastro-intestinal tract. Cells at the 12th passage were seeded at a concentration of 2.5×10^5 cells/ml on an HTS transwell 24 well plate, 0.4 μm pore size (Costar, 3524, Corning). Cells were incubated in 37 °C, 5% CO_2/95% air. Cells were cultured in RPMI-1640 supplemented with 10% heat-inactivated foetal bovine serum (FBS), 2 mM L-glutamine, 100 μg/ml penicillin and 100 μg/ml streptomycin all purchased Life Technologies, Carlsbad, CA. Media was changed every two days and Transepithelial Electric Resistance (TEER) was measured by MilliCell (Millipore) just before changing the media to assess the integrity of the cell barrier. TEER was expressed in $\Omega\,cm^{-1}$ as the product $(R - R_b) \times A$, where R and R_b are the resistance (Ω) of the cells and the blank, respectively, and A is the surface area of the insert (cm). When the TEER values were >300 $\Omega\,cm^{-1}$, transport experiment was performed. The

Please cite this article in press as: Di Silvio, D., et al., Effect of protein corona magnetite nanoparticles derived from bread *in vitro* digestion on Caco-2 cells morphology and uptake. Int J Biochem Cell Biol (2015), http://dx.doi.org/10.1016/j.biocel.2015.10.019

G Model
BC-4721; No. of Pages 11
ARTICLE IN PRESS
D. Di Silvio et al. / The International Journal of Biochemistry & Cell Biology xxx (2015) xxx–xxx 5

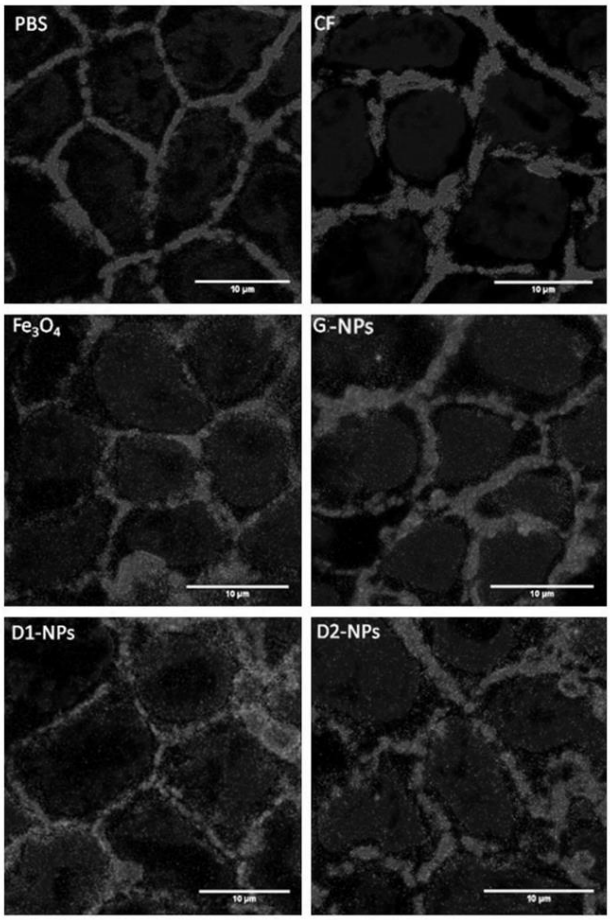

Fig. 4. Caco-2 monolayers incubated with NPs. Confocal snapshots of Caco-2 monolayer after 4 h of incubation with SFM:PBS 1:1 (PBS), carboxyfluorescein (CF), bare Fe_3O_4 (Fe_3O_4), PC complexes isolated from gastric (G1-NPs) and duodenal digestion (D1-NPs and D2-NPs). F-Actin filaments were stained by Phalloidin-Texas Red (591/608 nm) and nuclei by Hoechst 33342 (350/461 nm). Fe_3O_4 NPs were labelled by BODIPY FL-EDA (500/510 nm). Images were rendered using ImageJ.

apical and basolateral chambers were filled with serum free medium (SFM) after PBS (3×) rinsing to remove phenol red and FBS proteins from the chambers and cells were allowed equilibrating for 1 h. 100 µl of the apical medium were replaced with PC NPs from the gastric digestion (G-NPs) and the duodenal digestion (D-NPs) to get a final concentration of 2×10^{12} NPs/ml. Control wells with pristine Fe_3O_4 NPs at the same concentration as the PC complexes, PBS (100 µl) and carboxyfluorescein (CF, Sigma) were prepared in parallel and incubation at 37 °C was performed for 4 h. 100 µl of basolateral medium were sampled at 60, 120, 180 and 240 min and replaced with the same volume of fresh medium. TEER after 4 h was measured to assess the effect of the NPs on the transepithelial electric resistance. The presence of NPs in the collected medium from the basolateral chamber was revealed by fluorescence using a plate reader exciting at 492 nm and collecting emission at 520 nm. Cells were three times washed with PBS and fixed with 5% formaldehyde for 10 min, then they were treated with Triton-x 0.5% for 3 min and again washed for three times with PBS. F-Actin staining was performed by Texas-Red Phalloidin (6.6 µM, Invitrogen) and nuclei by Hoechst 33258 (2 µg/ml, Sigma). After staining, the membranes were cut from the insert, placed on a glass slide and covered by a coverslip with mounting medium in between (Vectashield, Vector). Zeiss LSM510-META confocal microscope (UEA) was used to image cell monolayer and NPs using a multi-channel

Please cite this article in press as: Di Silvio, D., et al., Effect of protein corona magnetite nanoparticles derived from bread *in vitro* digestion on Caco-2 cells morphology and uptake. Int J Biochem Cell Biol (2015), http://dx.doi.org/10.1016/j.biocel.2015.10.019

G Model
BC-4721; No. of Pages 11
ARTICLE IN PRESS

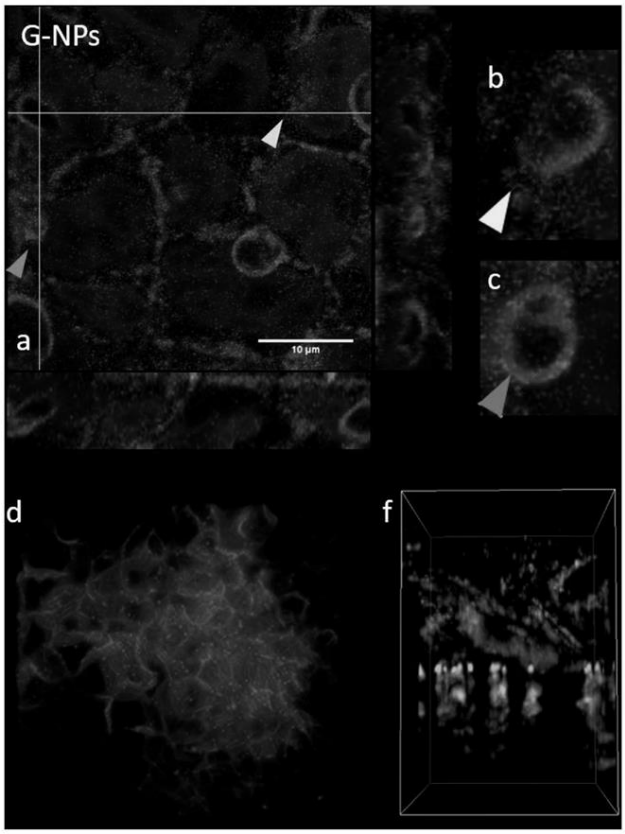

Fig. 5. Confocal stacks of G-NPs incubated Caco-2 monolayer. (a) Orthogonal stacks and some zoomed details (b, c) highlighted by arrows. (d) View from the bottom of the monolayer; (f) stack in the zeta direction in which is visible the cell skeleton auto-fluorescing in green and porous channels containing green labelled NPs. Actin filaments were stained by Phalloidin-Texas Red (591/608 nm) and nuclei by Hoechst 33342 (350/461 nm). Fe_3O_4 NPs were labelled by BODIPY FL-EDA (500/510 nm).

mode with three different excitation wavelengths for nuclei, actin and NPs. Image rendering was done using ImageJ software.

A control experiment was performed with digested NPs, CF, Fluoresceinmamine (FA, Sigma) and SFM in a transwell dish without cell monolayer and their translocation across the membrane was monitored using the same method followed when cells were present. Fluorescence at 520 nm was measured for media from the apical and basolateral chambers.

3. Results and discussion

3.1. Stability of NPs in simulated gastrointestinal fluids

NPs have been largely characterized in plasma for their possible applications in clinics as diagnostic and drug delivery systems (Jansch et al., 2012; Mahmoudi et al., 2011; Sakulkhu et al., 2014; Simberg et al., 2009). The intravenous administration of drugs is very common, but ingestion is the main route for oral nanoformulations and for NPs used as additives in food and food packaging. Thus, characterization of NPs in the GI environment is of primary interest.

As for NPs in blood, NPs in the GI tract will certainly interact with biomolecules present in this complex and dynamic environment forming a PC. However, not many studies reporting on the characterization of the PC associated with NPs subjected to digestion are reported in the literature. This is mainly due to the experimental difficulty in isolating PC NPs from such a dynamic environment without modifying their properties. For example, Jahn et al. (2011) studied the uptake of hemin-coupled iron hydroxide NPs on Caco-2 cells and they speculated a strong effect due to the colloidal stability of such NPs in the medium, but they did not perform any stability study. Pereira et al. (2013) found that Fe(III)-oxo hydroxide NPs forms ferrihydrite-like complexes after a simulated *in vitro* digestion. PC NPs could not be isolated from GI fluids without

Please cite this article in press as: Di Silvio, D., et al., Effect of protein corona magnetite nanoparticles derived from bread *in vitro* digestion on Caco-2 cells morphology and uptake. Int J Biochem Cell Biol (2015), http://dx.doi.org/10.1016/j.biocel.2015.10.019

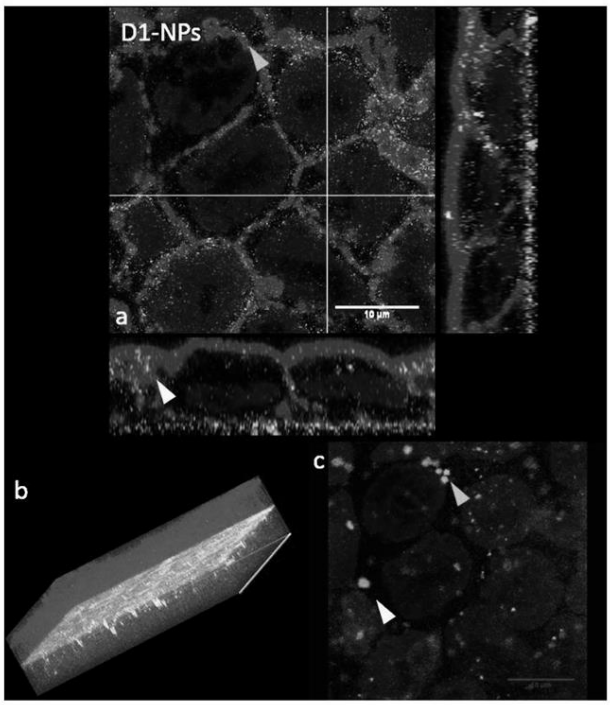

Fig. 6. Confocal stacks of D1-NPs incubated Caco-2 monolayer. (a) Orthogonal stacks of Caco-2 cells and some highlighted details. (b) 3D reconstruction of cells skeleton, NPs and support membrane. (c) Nuclei and NPs clusters viewed from the top. Arrows showed same details in different prospective. Actin filaments were stained by Phalloidin-Texas Red (591/608 nm) and nuclei by Hoechst 33342 (350/461 nm). Fe_3O_4 NPs were labelled by BODIPY FL-EDA (500/510 nm). Images were rendered using ImageJ.

aggregation, but they used the approach to synthesize ferrihydrite complexes *ex novo* for studying their biological response on Caco-2 cells, bypassing the isolation of such NPs from digestive fluids. Finally Yang et al. (2014) studied the behaviour of iron oxide NPs in GI fluids observing their tendency to aggregate if specific surface coating (citrate ions) were not performed.

In this study, we used fluorescently labelled carboxylated magnetite NPs. They were composed of a magnetite core, Fe_3O_4 of 10 nm and an amphiphilic polymer coating (poly (maleic)-alt-1-octadecene) that makes them water-soluble and easily surface modifiable thanks to the carboxylic groups available to form amide bonds with primary amines (see Fig. SI1 in the SI) (Sun et al., 2003). In physiological buffer at pH 7.4 they exhibited a hydrodynamic diameter of about 50 nm, a quite narrow size distribution (PdI of 0.20) and a negative Zp (−21 mV). We tested their stability over 4 h at 37 °C in simulated digestive fluids to assess the effect of pH and ionic strength before the addition of enzymes and food, thus before being coated by a PC. In Fig. 1 size distribution trends are reported for these Fe_3O_4 NPs in PBS, simulated salivary fluid (SSF) and simulated gastric fluid (SGF). NPs in simulated intestinal fluid (SIF) immediately precipitated likely due to the high electrolytes concentration that shields NPs surface negative charge (Bergin and Witzmann, 2013; Frenkel et al., 2005; Peters et al., 2012; Yang et al., 2014; Zimmermann and Müller, 2001). In SSF, the averaged hydrodynamic sizes of the NPs mostly increased with respect to those in PBS during the first hour of incubation, reaching a plateau with an average size almost double that of the starting one in PBS. PdI values were in contrast comparable to those in PBS. In SGF NP hydrodynamic sizes appeared to slowly increase over time to reach an average value almost three time larger than the starting one. On the other hand, PdI values appeared invariant with time. Overall, these results showed that when the NPs reach the gastric environment they form agglomerates of uniform dimensions.

3.2. Simulated gastric and duodenal digestion of bread in the presence of NPs

The isolation of PC–NPs complexes originating from NPs co-digested with bread is very interesting but extremely challenging. In fact, bread is a common food in the daily diet but as all cereal based food it is a very complex matrix (Hoebler et al., 2002).

During the simulated digestion of bread, insoluble protein aggregates were formed particularly in the gastric phase. Hydrolysis occurred over time, proteins were converted into low molecular weight peptides, and food particulates decreased in size. Recently, Lichtenstein et al. (2015) performed simultaneous digestion of NPs, bread and other food. They studied the size and aggregation of *in situ* complexes by SAXS at the end of the duodenal phase, but

Please cite this article in press as: Di Silvio, D., et al., Effect of protein corona magnetite nanoparticles derived from bread *in vitro* digestion on Caco-2 cells morphology and uptake. Int J Biochem Cell Biol (2015), http://dx.doi.org/10.1016/j.biocel.2015.10.019

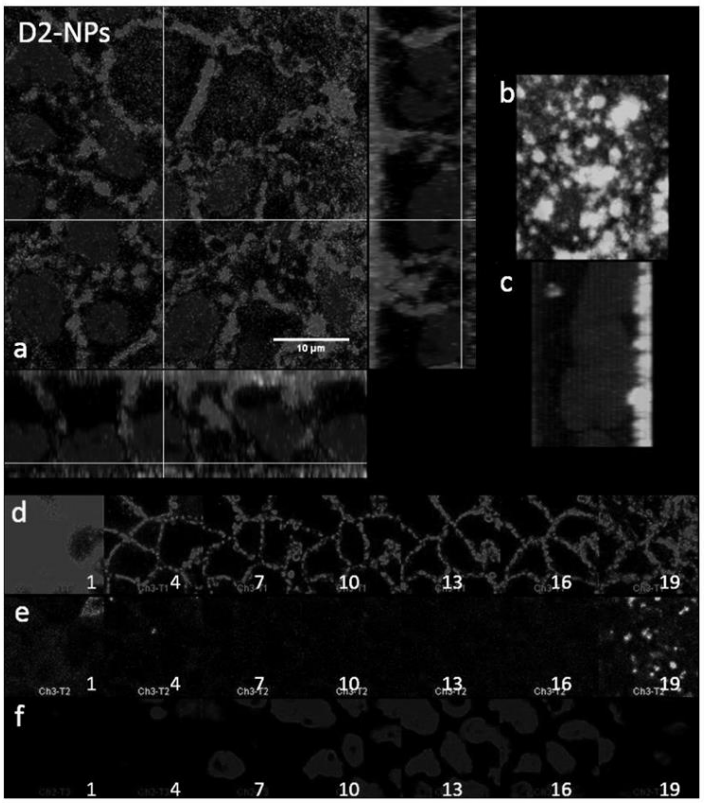

Fig. 7. Confocal stacks of D2-NPs incubated Caco-2 monolayer. (a) Orthogonal stacks of Caco-2 cells in the XY, YZ, XZ planes. (b, c) View from the bottom and the side of the monolayer showing nuclei and NPs. (d–f) Sequence of layers from 1 to 19 divided in the three channels, red (actin), green (NPs) and blue (nuclei) respectively. Actin filaments were stained by Phalloidin-Texas Red (591/608 nm) and nuclei by Hoechst 33342 (350/461 nm). Fe_3O_4 NPs were labelled by BODIPY FL-EDA (500/510 nm). Images were rendered using ImageJ. (For interpretation of the references to color in figure legend, the reader is referred to the web version of the article.)

HC NPs were not isolated and characterized in terms of composition and evolution over time. In this work, we have focused on the evolution of the NPs during the different phases of the digestion with particular attention to the characterization of the structure and composition of protein corona NPs. In fact we exploited the methodology described in our previous work based on sucrose gradient ultracentrifugation (UC) for successfully recovering PC–NP complexes from both gastric and duodenal phases.

The recovery of PC–NP complexes from the gastric phase required the optimization of UC parameters (sucrose concentration, speed and time). We used a wide concentration gradient with a short and slow centrifugation (6.6–66% at 48k rcf) to avoid co-localization of PC complexes and starch particulate. We achieved separation of NPs and unbound peptides. The NPs were located at the top of the gradient corresponding to a sucrose concentration between 10% and 20 w/w% (upper zone in Fig. 2a), while starch residues were spread on the gradient at higher densities (lower zone in Fig. 2a). The application of standard centrifugation protocols, even trying different experimental conditions, did not allow the separation of PC NPs from starch residues, but lead to the formation of strong irreversible aggregates. PC NPs recovered by UC were characterized by DLS and showed a hydrodynamic size about three/four time larger compared to the size of the equivalent NPs in PBS, as reported in Table 2. During digestion, NPs density decreased as it can be inferred from NPs location in the sucrose gradient. Indeed, while pristine NPs moved to about 40 w/w% sucrose concentration, the PC NPs only reached the area between 10% and 20%. This is likely due to the formation of multi-particle protein agglomerates stabilized by the PC, which are characterized by a lower overall density depending on the partial specific volume and the frictional coefficient variations of the complexes. PC composition of the isolated NPs was determined by SDS–PAGE. In Fig. 2b, the lane labelled as G-NPs corresponds to the UC fractions where NPs subjected to gastric digestion were found (fractions 2–5). This sample was clearly enriched with proteins when compared to the same fractions of the control without NPs (3G*, 5G*). Some bands of

Please cite this article in press as: Di Silvio, D., et al., Effect of protein corona magnetite nanoparticles derived from bread *in vitro* digestion on Caco-2 cells morphology and uptake. Int J Biochem Cell Biol (2015), http://dx.doi.org/10.1016/j.biocel.2015.10.019

the PC around 36–40 kDa (probably a mixture of polypeptides from albumins and globulins) were also found in the analogous lanes of the control sample (1G*–5G*), thus they might be contaminants from the environment and not associated with the corona. While a characteristic protein pattern, not observable in the equivalent lanes of the control, is observed at M_W lower than 36 kDa. A similar protein pattern, but much more diffuse, appeared in the control sample in the higher density fractions where starch residues were clearly visible.

The texture of the mixture after 2 h of duodenal digestion became liquid without solid residues. The agglomerates formed by NPs and peptides in the gastric phase partially disaggregated in duodenal conditions. UC on aliquots isolated from such a mixture was performed for 1 h at 195 krcf. After the run, a brown band (D2-NPs) was visible at high sucrose concentration (fractions 14–16 at about 55 w/w% sucrose concentration) as shown in Fig. 3a. A screening of all the fractions by size disclosed another population of PC complexes (D1-NPs) located from fraction 4 to fraction 9. Bile and unbound low-density peptides were located in the top of the sucrose gradient. Overall, two different populations of PC NPs were formed and characterized by hydrodynamic diameters smaller than 150 nm. D1-NPs were about 20% smaller in hydrodynamic size compared to D2-NPs, but they had a sensibly different density. Both complexes were characterized by negative Zp, possibly because of the absorption of bile salts on their surface (Table 3). In Fig. 3b protein corona profiles by SDS–PAGE are shown. As expected many peptides were found in the first fraction and their concentration decreased increasing the sucrose density and no peptides were detected in high-density sucrose bands (11D*–17D*). The PCs associated to the complexes extracted by the two different fractions were completely different. The D1 PC was mainly composed of pancreatic enzymes (lipase and amylase at 55 kDa, trypsin and chymotrypsin at 24 kDa) as it can be expected based on the composition of the duodenal environment. D2 PC was instead enriched with peculiar proteins such as the band at 55 kDa and some other bands at higher molecular weights. Moreover, the diffuse band observed in the gastric sample seemed to be protected from digestion, while in the control sample without NPs the same bands in the high-density fractions (15*-16*-17*D) were not detected.

LC–MS analysis on selected bands from gel in Figs. 2b and 3b highlighted that G-NPs corona was enriched in albumins and globulins such as Serpin, GSP-1 Grain Softness Protein (17 kDa), albumin-2 (26 kDa) and Avenin-like A1 (19 kDa). Those proteins were mostly found in high molecular weight bands suggesting the presence of peptides aggregates. The diffuse band at low molecular weight contained mainly peptides from beta-amylase, 0.19 dimeric alpha-amylase inhibitor and albumin-2 indicating that they were preserved during digestion. Such proteins were also identified in the D2-NPs corona as listed in Table 4 (full proteomic characterization can be found in SI Tables SI1 and SI2). To the best of our knowledge, this is the first time that proteomic analysis of PC from food containing digestive juices has been described. Moreover, the reported incomplete digestion of some proteins can have important biological implications considering that some of those peptides were recognized to be allergens (Akagawa et al., 2007) and could induce prolonged adverse reactions in the gut.

3.3. Translocation and uptake of PC complexes

There are many articles about uptake and translocation of NPs through monolayers of Caco-2 cells (Jahn et al., 2011; Zariwala et al., 2013) or co-culture that produce mucus (Kenzaoui et al., 2012). Brun et al. (2014) described titanium oxide NPs uptake in Caco-2 mono and co-cultures and in mice, studying the PC composition of NPs incubated in 10% serum proteins and subjected to simulated digestion. However, none of these studies reported detailed descriptions of isolated PC NPs from digestive juices. Also Walczak et al. (2015a,b) highlighted the role of the PC, formed upon exposure to complete cell medium, on Caco-2 uptake. Lichtenstein et al. (2015), on the other hand, pointed out the importance of a food matrix during NPs *in vitro* digestion showing that the formation of the PC imparted colloidal stability to the NPs in the GI fluids.

Here, we focused on the characterization of PC–NP complexes formed during food-NP digestion, which were successfully isolated from the biological environment by a UC protocol developed in our lab. PC–NP complexes separated from the digestive chyme were applied to Caco-2 monolayers in a serum free environment. Fluorescence measurements did not detect NPs translocation to the basolateral chamber for any of the samples, so for ruling out the possibility that NPs transmembrane diffusion was hindered by the pore size (Hallez, 2012; Roth et al., 1996), a translocation experiment was performed without a cell monolayer, which demonstrated the ability of the NPs to translocate (see Fig. SI2 in SI). Nevertheless, NPs could agglomerate inside the cells and be transcytosed as larger aggregates that would not pass through membrane pores (Ye et al., 2013, 2015). Thus, confocal microscopy was used to elucidate NPs cellular localization as well as their passage through the pores of the insert membrane (Bannunah et al., 2014; Verano-Braga et al., 2014).

In Fig. 4, an overview of Caco-2 monolayers is displayed. Control samples incubated with PBS and carboxyfluorescein (CF) were characterized by normal cell architecture with intact actin skeleton and tight junctions. Slight alterations of the actin network were observed in the sample treated with pristine NPs (Fe_3O_4), while alterations in membrane morphology are evident for all the samples treated with PC NPs. The treatment of cells with PC NPs increased the number of vesicles in the apical membrane, as it can be seen in G-NPs and D1-NPs treated cells (Figs. 5a, b and 6a, b), while such vesicles were observed associated with the basal membrane in the cells incubated with D2-NPs highlighting transcytosis. For this sample, the orthogonal view shown in Fig. 7a displays the status of the cell walls very close to the insert membrane and in Fig. 7d clusters that co-localize with those vesicles associated with the basal membrane are shown (Fig. 7d, layer 19d–f). Those kinds of alterations could not be picked up by TEER as the values did not change significantly (Lichtenstein et al., 2015) (see Fig. SI3 in SI). Brun et al. (2014) showed that also titanium oxide NPs did not affect TEER values for monolayers indicating membrane integrity and unaffected paracellular transport of cells, but they also showed for the same samples metabolic abnormalities, oxidative stress and DNA damage (Bergin and Witzmann, 2013; Böhmert et al., 2013; Stern et al., 2012). PC composition might have a role in the morphological alterations encountered: some peptides found in the corona of G-NPs such as serpin, alpha-amylase inhibitor, and lectin were digestion-protected and were found in the PC of D2-NPs. Those proteins were shown to be allergens (Akagawa et al., 2007) and the presence of gliadin-derived peptides cannot be excluded. Gliadins are the gluten water-soluble component and the derived peptides were proved to induce cytotoxicity and apoptosis in Caco-2 cells with particular effect on membrane proteins and redox activities (Giovannini et al., 2000; Rivabene et al., 1999). However, more studies are necessary to investigate these speculations and prove the real involvement of the PC in these effects.

Confocal microscopy confirmed uptake of digested NPs and it was generally higher for PC NPs than for pristine Fe_3O_4 NPs. In particular, PC NPs seemed to induce the formation of invaginations in the intersections among cells (see Fig. SI4 in the SI). This effect of NP uptake enhancement induced by the PC is in agreement with other data in literature. Indeed cationic USPIONs (Kenzaoui et al., 2012), polystyrene NPs (Tenzer et al., 2013), polymeric NPs (Leroux et al., 1994), silver NPs (Lichtenstein et al., 2015) and pegylated core–shell NPs (Pelaz et al., 2015) were reported to show higher

Please cite this article in press as: Di Silvio, D., et al., Effect of protein corona magnetite nanoparticles derived from bread *in vitro* digestion on Caco-2 cells morphology and uptake. Int J Biochem Cell Biol (2015), http://dx.doi.org/10.1016/j.biocel.2015.10.019

cellular uptake when bearing a PC but, in all these studies, the PC originated from plasma or serum.

Among digested samples, it is difficult to determine those that showed the highest NP uptake. For example, NPs from gastric digestion were quite monodispersed (see Table 2) and big clusters inside the cytoplasm were not detected, while NPs accumulated between the basal membrane of the cells and the polyester membrane support. In Fig. 5c, a high density of NP clusters is observed with a view from the bottom of the basal membrane and in Fig. 5d the passage of NPs through the porous channels is confirmed by a 3D rendering of a stack in the orthogonal direction from the top of the cells going through the support membrane.

After duodenal digestion, D1-NPs appeared in the cells mainly as big clusters enclosed in vesicles as shown in Fig. 6a and c with an orthogonal stack and a top view of the monolayer, respectively. Clusters seemed to be similar in size although the optical resolution does not allow an accurate determination. Moreover, the quantum yield of the fluorescent molecules might be affected by the environmental pH, although it has been reported that the dye used is very little affected by solvent polarity and pH (Karolin et al., 1994). However, most of the NPs are located between the basal and the support membranes and at the top of the porous channels (Fig. 6b). It is likely, in this case, that channels were blocked by the clusters being larger than the nominal pore size, and indeed fluorescent spots were mainly located in the upper part of the support rather than in the lower part.

D2-NPs were both attached to the apical membrane (layer 1 of Fig. 7d–f) and spread throughout the cytoplasm surrounding nuclei (Fig. 7a and e, layers 7-10-13). The NPs inside the cells appeared as clusters. Large clusters were also located between adjacent cells (layer 4 in Fig. 7d–f) and on the bottom of the cells entrapped in vesicles (Fig. 7b and c). For all digested samples, accumulation between the basal membrane and the support seemed to take place. While paracellular transport can be excluded given the size of the NPs, transcytosis was confirmed especially in D2-NPs incubated cells displaying vesicles in close proximity to the basal membrane. Multiple endocytic energy-dependent routes (*e.g.* clathrin, calveolin mediated endocytosis) can be speculated, given the differences in size, density and corona composition of the PC complexes (Bannunah et al., 2014; Jahn et al., 2011). More images for digested NPs interacting with the cell are provided in the SI, Figs. S5–7.

4. Conclusions

In this paper, we have described for the first time PC NPs originating from the simultaneous digestion of NPs with food matrix. The PC NPs formed during the different phases of the digestive process were different in size and corona composition. Moreover, we observed that some corona proteins were shown to resist the duodenal digestion extending their persistance in the gut. This finding could be of interest in the study of peptides that cause immunological response like in celiac disease. Although we did not precisely quantify NP uptake in Caco-2 cells, we confirmed that the corona enhanced the uptake of magnetite NPs in agreement with previous results reported in the literature for other NPs bearing plasma or serum derived coronas. Furthermore, we managed to demonstrate that different coronas induced different alterations in the cell morphology. In addition, UC-based isolation of PC–NP complexes was highly successful in removing the excess GI fluids that have been shown to induce a certain level of cytotoxicity in previous results (Lichtenstein et al., 2015). Moreover, it is likely that differences in size, density and corona composition for the various PC–NP complexes may lead to different routes of uptake and translocation but this needs to be further investigated.

Conflict of interest

The authors declare no conflict of interest.

Acknowledgements

This work was supported by funds from University of East Anglia (UEA, UK) and the BBSRC through the ISP grant BB/J004545/1 to IFR. FBB thanks the financial support from Regione Lombardia (Fondo per lo Sviluppo e la Coesione–FAS 2007–2013). The authors thank Dr Francis Mulholland for LC–MS analysis.

Appendix A. Supplementary data

Supplementary data associated with this article can be found, in the online version, at http://dx.doi.org/10.1016/j.biocel.2015.10.019.

References

Akagawa, M., Handoyo, T., Ishii, T., Kumazawa, S., Morita, N., Suyama, K., 2007. Proteomic analysis of wheat flour allergens. J. Agric. Food Chem. 55, 6863–6870.
Bannunah, A.M., Vllasaliu, D., Lord, J., Stolnik, S., 2014. Mechanisms of nanoparticle internalization and transport across an intestinal epithelial cell model: effect of size and surface charge. Mol. Pharm. 11, 4363–4373.
Bergin, I.L., Witzmann, F.A., 2013. Nanoparticle toxicity by the gastrointestinal route: evidence and knowledge gaps. Int. J. Biomed. Nanosci. Nanotechnol., 3, http://dx.doi.org/10.1504/IJBNN.2013.054515.
Böhmert, L., Girod, M., Hansen, U., Maul, R., Knappe, P., Niemann, B., Weidner, S.M., Thünemann, A.F., Lampen, A., 2013. Analytically monitored digestion of silver nanoparticles and their toxicity on human intestinal cells. Nanotoxicology 8, 631–642.
Borel, T., Sabliov, C.M., 2014. Nanodelivery of bioactive components for food applications: types of delivery systems, properties, and their effect on ADME profiles and toxicity of nanoparticles. Annu. Rev. Food Sci. Technol. 5, 197–213.
Brun, E., Barreau, F., Veronesi, G., Fayard, B., Sorieul, S., Chaneac, C., Carapito, C., Rabilloud, T., Mabondzo, A., Herlin-Boime, N., Carriere, M., 2014. Titanium dioxide nanoparticle impact and translocation through ex vivo, in vivo and in vitro gut epithelia. Part. Fibre Toxicol. 11, 13.
Cai, X., Ramalingam, R., Wong, H.S., Cheng, J., Ajuh, P., Cheng, S.H., Lam, Y.W., 2013. Characterization of carbon nanotube protein corona by using quantitative proteomics. Nanomedicine 9, 583–593.
Cedervall, T., Lynch, I., Lindman, S., Berggård, T., Thulin, E., Nilsson, H., Dawson, K.A., Linse, S., 2007. Understanding the nanoparticle–protein corona using methods to quantify exchange rates and affinities of proteins for nanoparticles. Proc. Natl. Acad. Sci. USA 104, 2050–2055.
Clift, M.J.D., Bhattacharjee, S., Brown, D.M., Stone, V., 2010. The effects of serum on the toxicity of manufactured nanoparticles. Toxicol. Lett. 198, 358–365.
Di Silvio, D., Rigby, N., Bajka, B., Mayes, A., Mackie, A., Baldelli Bombelli, F., 2015. Technical tip: high-resolution isolation of nanoparticle–protein corona complexes from physiological fluids. Nanoscale, 7.
Docter, D., Westmeier, D., Markiewicz, M., Stolte, S., Knauer, S.K., Stauber, R.H., 2015. The nanoparticle biomolecule corona: lessons learned – challenge accepted? Chem. Soc. Rev. 44, 6094–6121.
Ensign, L.M., Cone, R., Hanes, J., 2012. Oral drug delivery with polymeric nanoparticles: the gastrointestinal mucus barriers. Adv. Drug Deliv. Rev. 64, 557–570.
Foroozandeh, P., Aziz, A.A., 2015. Merging worlds of nanomaterials and biological environment: factors governing protein corona formation on nanoparticles and its biological consequences. Nanoscale Res. Lett. 10, 221.
Frenkel, Y.V., Clark, A.D., Das, K., Wang, Y.-H., Lewi, P.J., Janssen, P.A.J., Arnold, E., 2005. Concentration and pH dependent aggregation of hydrophobic drug molecules and relevance to oral bioavailability. J. Med. Chem. 48, 1974–1983.
Ghavami, M., Saffar, S., Abd Emamy, B., Peirovi, A., Shokrgozar, M.A., Serpooshan, V., Mahmoudi, M., 2013. Plasma concentration gradient influences the protein corona decoration on nanoparticles. RSC Adv. 3, 1119–1126.
Giovannini, C., Sanchez, M., Straface, E., Scazzocchio, B., Silano, M., De Vincenzi, M., 2000. Induction of apoptosis in Caco-2 cells by wheat gliadin peptides. Toxicology 145, 63–71.
Hadjidemetriou, M., Al-Ahmady, Z., Mazza, M., Collins, R.F., Dawson, K., Kostarelos, K., 2015. In vivo biomolecule corona around blood-circulating clinically used and antibody-targeted lipid bilayer nanoscale vesicles. ACS Nano 9, 8142–8156.
Hallez, Y., 2012. Analytical and numerical computations of the van der Waals force in complex geometries: application to the filtration of colloidal particles. Colloids Surf. A: Physicochem. Eng. Asp. 414, 466–476.
Hoebler, C., Lecannu, G., Belleville, C., Devaux, M.-F., Popineau, Y., Barry, J.-L., 2002. Development of an in vitro system simulating bucco-gastric digestion to assess the physical and chemical changes of food. Int. J. Food Sci. Nutr. 53, 389–402.

Please cite this article in press as: Di Silvio, D., et al., Effect of protein corona magnetite nanoparticles derived from bread *in vitro* digestion on Caco-2 cells morphology and uptake. Int J Biochem Cell Biol (2015), http://dx.doi.org/10.1016/j.biocel.2015.10.019

Hummel, B.C., 1959. A modified spectrophotometric determination of chymotrypsin, trypsin, and thrombin. Can. J. Biochem. Physiol. 37, 1393–1399.
Jahn, M.R., Shukoor, I., Tremel, W., Wolfrum, U., Kolb, U., Nawroth, T., Langguth, P., 2011. Hemin-coupled iron(III)-hydroxide nanoparticles show increased uptake in Caco-2 cells. J. Pharm. Pharmacol. 63, 1522–1530.
Jansch, M., Stumpf, P., Graf, C., Rühl, E., Müller, R.H., 2012. Adsorption kinetics of plasma proteins on ultrasmall superparamagnetic iron oxide (USPIO) nanoparticles. Int. J. Pharm. 428, 125–133.
Karolin, J., Johansson, L.B.A., Strandberg, L., Ny, T., 1994. Fluorescence and absorption spectroscopic properties of dipyrrometheneboron difluoride (BODIPY) derivatives in liquids lipid membranes, and proteins. J. Am. Chem. Soc. 116, 7801–7806.
Kenzaoui, B.H., Vilà, M.R., Miquel, J.M., Cengelli, F., Juillerat-Jeanneret, L., 2012. Evaluation of uptake and transport of cationic and anionic ultrasmall iron oxide nanoparticles by human colon cells. Int. J. Nanomed. 7, 1275–1286.
Kreyling, W.G., Fertsch-Gapp, S., Schäffler, M., Johnston, B.D., Haberl, N., Pfeiffer, C., Diendorf, J., Schleh, C., Hirn, S., Semmler-Behnke, M., Epple, M., Parak, W.J., 2014. In vitro and in vivo interactions of selected nanoparticles with rodent serum proteins and their consequences in biokinetics. Beilstein J. Nanotechnol. 5, 1699–1711.
Lefebvre, D.E., Venema, K., Gombau, L., Valerio, L.G., Raju, J., Bondy, G.S., Bouwmeester, H., Singh, R.P., Clippinger, A.J., Collnot, E.-M., Mehta, R., Stone, V., 2014. Utility of models of the gastrointestinal tract for assessment of the digestion and absorption of engineered nanomaterials released from food matrices. Nanotoxicology, 1–20.
Leroux, J.-C., Gravel, P., Balant, L., Volet, B., Anner, B.M., Allémann, E., Doelker, E., Gurny, R., 1994. Internalization of poly(D,L-lactic acid) nanoparticles by isolated human leukocytes and analysis of plasma proteins adsorbed onto the particles. J. Biomed. Mater. Res. 28, 471–481.
Lichtenstein, D., Ebmeyer, J., Knappe, P., Juling, S., Böhmert, L., Selve, S., Niemann, B., Braeuning, A., Thünemann Andreas, F., Lampen, A., 2015. Impact of food components during in vitro digestion of silver nanoparticles on cellular uptake and cytotoxicity in intestinal cells. Biol. Chem. 396, 1255–1264.
Lin, C.-A.J., Sperling, R.A., Li, J.K., Yang, T.-Y., Li, P.-Y., Zanella, M., Chang, W.H., Parak, W.J., 2008. Design of an amphiphilic polymer for nanoparticle coating and functionalization. Small 4, 334–341.
Lundqvist, M., Stigler, J., Elia, G., Lynch, I., Cedervall, T., Dawson, K.A., 2008. Nanoparticle size and surface properties determine the protein corona with possible implications for biological impacts. Proc. Natl. Acad. Sci. U.S.A. 105, 14265–14270.
Lynch, I., Cedervall, T., Lundqvist, M., Cabaleiro-Lago, C., Linse, S., Dawson, K.A., 2007. The nanoparticle–protein complex as a biological entity; a complex fluids and surface science challenge for the 21st century. Adv. Colloid Interface Sci. 134–135, 167–174.
Mahmoudi, M., Shokrgozar, M.A., Sardari, S., Moghadam, M.K., Vali, H., Laurent, S., Stroeve, P., 2011. Irreversible changes in protein conformation due to interaction with superparamagnetic iron oxide nanoparticles. Nanoscale 3, 1127–1138.
Maiorano, G., Sabella, S., Sorce, B., Brunetti, V., Malvindi, M.A., Cingolani, R., Pompa, P.P., 2010. Effects of cell culture media on the dynamic formation of protein–nanoparticle complexes and influence on the cellular response. ACS Nano 4, 7481–7491.
Minekus, M., Alminger, M., Alvito, P., Ballance, S., Bohn, T., Bourlieu, C., Carriere, F., et al., 2014. A standardised static in vitro digestion method suitable for food – an international consensus. Food Funct. 5, 1113–1124.
Monopoli, M.P., Aberg, C., Salvati, A., Dawson, K.A., 2012. Biomolecular coronas provide the biological identity of nanosized materials. Nat. Nano 7, 779–786.
Pelaz, B., del Pino, P., Maffre, P., Hartmann, R., Gallego, M., Rivera-Fernández, S., de la Fuente, J.M., Nienhaus, G.U., Parak, W.J., 2015. Surface functionalization of nanoparticles with polyethylene glycol: effects on protein adsorption and cellular uptake. ACS Nano 9, 6996–7008.
Peng, Q., Zhang, S., Yang, Q., Zhang, T., Wei, X.-Q., Jiang, L., Zhang, C.-L., Chen, Q.-M., Zhang, Z.-R., Lin, Y.-F., 2013. Preformed albumin corona, a protective coating for nanoparticles based drug delivery system. Biomaterials 34, 8521–8530.
Pereira, D.I.A., Mergler, B.I., Faria, N., Bruggraber, S.F.A., Aslam, M.F., Poots, L.K., Prassmayer, L., Lönnerdal, B., Brown, A.P., Powell, J.J., 2013. Caco-2 cell acquisition of dietary iron(III) invokes a nanoparticulate endocytic pathway. PLOS ONE 8, e81250.
Peters, R., Kramer, E., Oomen, A.G., Herrera Rivera, Z.E., Oegema, G., Tromp, P.C., Fokkink, R., Rietveld, A., Marvin, H.J.P., Weigel, S., Peijnenburg, A.A.C.M., Bouwmeester, H., 2012. Presence of nano-sized silica during in vitro digestion of foods containing silica as a food additive. ACS Nano 6, 2441–2451.
Rivabene, R., Mancini, E., De Vincenzi, M., 1999. In vitro cytotoxic effect of wheat gliadin-derived peptides on the Caco-2 intestinal cell line is associated with intracellular oxidative imbalance: implications for coeliac disease. Biochim. Biophys. Acta 1453, 152–160.
Roth, C.M., Neal, B.L., Lenhoff, A.M., 1996. Van der Waals interactions involving proteins. Biophys. J. 70, 977–987.
Sakulkhu, U., Mahmoudi, M., Maurizi, L., Salaklang, J., Hofmann, H., 2014. Protein corona composition of superparamagnetic iron oxide nanoparticles with various physico-chemical properties and coatings. Sci. Rep. 4, 5020.
Setyawati, M.I., Tay, C.Y., Leong, D.T., 2015. Mechanistic investigation of the biological effects of SiO_2, TiO_2, and ZnO nanoparticles on intestinal cells. Small 11, 3458–3468.
Sherwood, V., Di Silvio, D., Baldelli Bombelli, F., 2014. Nanoscopic agents in a physiological environment: the importance of understanding their characteristics. Top. Med. Chem., 1–26.
Simberg, D., Park, J.-H., Karmali, P.P., Zhang, W.-M., Merkulov, S., McCrae, K., Bhatia, S.N., Sailor, M., Ruoslahti, E., 2009. Differential proteomics analysis of the surface heterogeneity of dextran iron oxide nanoparticles and the implications for their in vivo clearance. Biomaterials 30, 3926–3933.
Soenen, S.J., Parak, W.J., Rejman, J., Manshian, B., 2015. (Intra)cellular stability of inorganic nanoparticles: effects on cytotoxicity particle functionality, and biomedical applications. Chem. Rev. 115, 2109–2135.
Stern, S.T., Adiseshaiah, P.P., Crist, R.M., 2012. Autophagy and lysosomal dysfunction as emerging mechanisms of nanomaterial toxicity. Part. Fibre Toxicol. 9, 20.
Sun, S., Zeng, H., Robinson, D.B., Raoux, S., Rice, P.M., Wang, S.X., Li, G., 2003. Monodisperse MFe_2O_4 (M = Fe, Co Mn) nanoparticles. J. Am. Chem. Soc. 126, 273–279.
Tenzer, S., Docter, D., Kuharev, J., Musyanovych, A., Fetz, V., Hecht, R., Schlenk, F., Fischer, D., Kiouptsi, K., Reinhardt, C., Landfester, K., Schild, H., Maskos, M., Knauer, S.K., Stauber, R.H., 2013. Rapid formation of plasma protein corona critically affects nanoparticle pathophysiology. Nat. Nano 8, 772–781.
Treuel, L., Docter, D., Maskos, M., Stauber, R.H., 2015. Protein corona – from molecular adsorption to physiological complexity. Beilstein J. Nanotechnol. 6, 857–873.
Verano-Braga, T., Miethling-Graff, R., Wojdyla, K., Rogowska-Wrzesinska, A., Brewer, J.R., Erdmann, H., Kjeldsen, F., 2014. Insights into the cellular response triggered by silver nanoparticles using quantitative proteomics. ACS Nano 8, 2161–2175.
Walczak, A.P., Kramer, E., Hendriksen, P.J.M., Helsdingen, R., van der Zande, M., Rietjens, I.M.C.M., Bouwmeester, H., 2015a. In vitro gastrointestinal digestion increases the translocation of polystyrene nanoparticles in an in vitro intestinal co-culture model. Nanotoxicology, 1–9.
Walczak, A.P., Kramer, E., Hendriksen, P.J.M., Tromp, P., Helsper, J.P.F.G., van der Zande, M., Rietjens, I.M.C.M., Bouwmeester, H., 2015b. Translocation of differently sized and charged polystyrene nanoparticles in in vitro intestinal cell models of increasing complexity. Nanotoxicology 9, 453–461.
Walczyk, D., Bombelli, F.B., Monopoli, M.P., Lynch, I., Dawson, K.A., 2010. What the cell "Sees" in bionanoscience. J. Am. Chem. Soc. 132, 5761–5768.
Walkey, C.D., Olsen, J.B., Song, F., Liu, R., Guo, H., Olsen, D.W.H., Cohen, Y., Emili, A., Chan, W.C.W., 2014. Protein corona fingerprinting predicts the cellular interaction of gold and silver nanoparticles. ACS Nano 8, 2439–2455.
Woolnough, J.W., Bird, A.R., Monro, J.A., Brennan, C.S., 2010. The effect of a brief salivary α-amylase exposure during chewing on subsequent in vitro starch digestion curve profiles. Int. J. Mol. Sci. 11, 2780–2790.
Yang, S.-C., Paik, S.-Y.-R., Ryu, J., Choi, K.-O., Kang, T.S., Lee, J.K., Song, C.W., Ko, S., 2014. Dynamic light scattering-based method to determine primary particle size of iron oxide nanoparticles in simulated gastrointestinal fluid. Food Chem. 161, 185–191.
Ye, D., Dawson, K.A., Lynch, I., 2015. A TEM protocol for quality assurance of in vitro cellular barrier models and its application to the assessment of nanoparticle transport mechanisms across barriers. Analyst 140, 83–97.
Ye, D., Raghnaill, M.N., Bramini, M., Mahon, E., Aberg, C., Salvati, A., Dawson, K.A., 2013. Nanoparticle accumulation and transcytosis in brain endothelial cell layers. Nanoscale 5, 11153–11165.
Zariwala, M.G., Elsaid, N., Jackson, T.L., Corral López, F., Farnaud, S., Somavarapu, S., Renshaw, D., 2013. A novel approach to oral iron delivery using ferrous sulphate loaded solid lipid nanoparticles. Int. J. Pharm. 456, 400–407.
Zimmermann, E., Müller, R.H., 2001. Electrolyte- and pH-stabilities of aqueous solid lipid nanoparticle (SLN™) dispersions in artificial gastrointestinal media. Eur. J. Pharm. Biopharm. 52, 203–210.

Please cite this article in press as: Di Silvio, D., et al., Effect of protein corona magnetite nanoparticles derived from bread *in vitro* digestion on Caco-2 cells morphology and uptake. Int J Biochem Cell Biol (2015), http://dx.doi.org/10.1016/j.biocel.2015.10.019

Supplementary Material

Effect of protein corona magnetite nanoparticles derived from bread in vitro digestion on Caco-2 cells morphology and uptake

Desirè Di Silvio[a, b], Neil Rigby[b], Balazs Bajka[b], Alan Mackie[b] and Francesca Baldelli Bombelli[c]

[a] School of Pharmacy, University of East Anglia, Norwich Research Park, NR4 7TJ, Norwich, United Kingdom

[b] Institute of Food Research, Norwich Research Park, NR4 7UA, Norwich, United Kingdom

[c] Department of Chemistry, Materials and Chemical Engineering Giulio Natta, via Mancinelli 7, 20131Politecnico di Milano, Milan, Italy

Summary

Fig. S1 Characterization of fluorescently labelled carboxylated Fe_3O_4 NPs.

Fig. S2 Translocation of pristine NPs, PC-NPs complexes from gastric and duodenal digestion and control molecules across cells-free transwell dish.

Fig. S3 Change of TEER values.

Fig. S4 Confocal stacks of pristine NPs incubated Caco-2 monolayer.

Fig. S*5* Confocal stacks of G-NPs incubated Caco-2 monolayer.

Fig. S6 Confocal micrograph of D1- NPs incubated Caco-2 monolayer.

Fig. S*7* Confocal stacks of D2-NPs incubated Caco-2 monolayer.

Table S1 Identification of protein bands extracted from gel shown in Fig. 2b.

Table S2 Identification of protein bands extracted from gel shown in Fig. 3b.

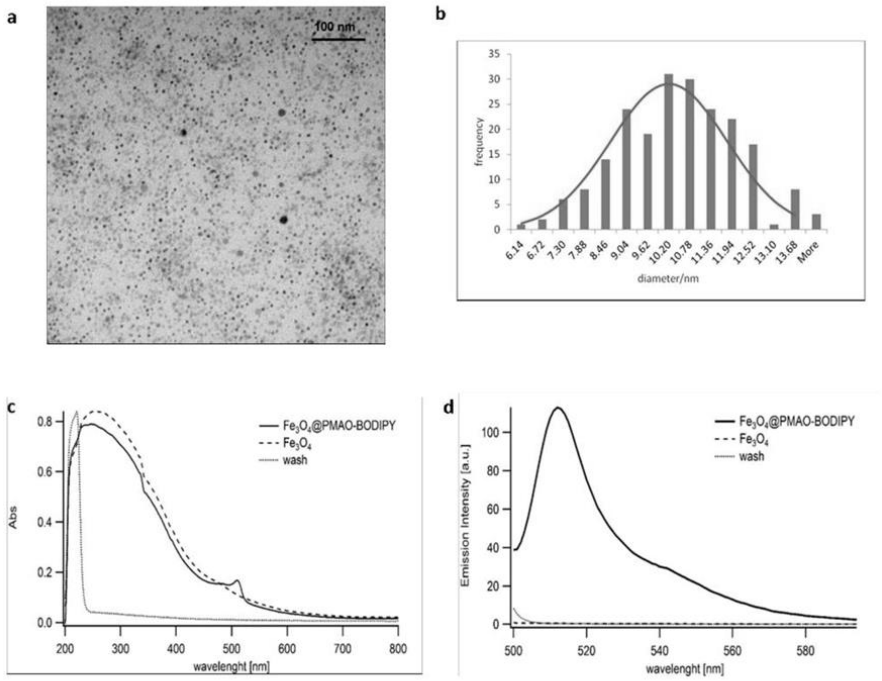

Fig. S5 Characterization of fluorescently labelled carboxylated Fe_3O_4 NPs. A) TEM image of carboxylated Fe_3O_4 NPs stabilized by oleic acid and dispersed in PBS. 1 drop of the dispersions was placed on the carbon film 300 mesh Cu (50) (Agar Scientific). The instrument was Joel 200EX with tungsten filament and acceleration voltage of 180kV to 200kV. B) Statistical size distributions on 250 NPs imaged by TEM and analysed by ImageJ software. C-D) Uv-vis and fluorescence emission (λ_{ecc}= 500 nm) spectra, respectively, of BODIPY labelled NPs (full line), unlabelled NPs (dashed line) and the washing water after unbound dye purification (dotted line).

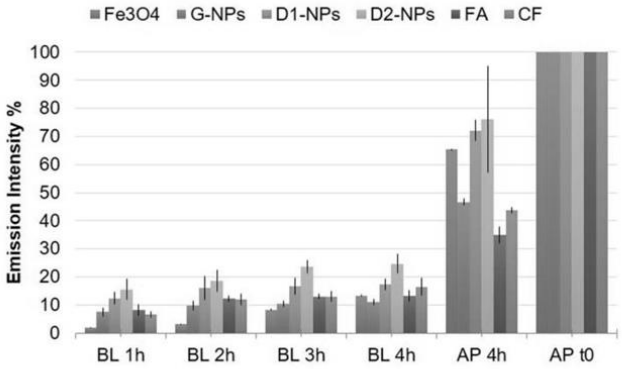

Fig. S 6 Translocation of pristine NPs, PC-NPs complexes from gastric and duodenal digestion and control molecules across cells-free transwell dish. Fluorescence emission intensities for samples from the basolateral chambers after 1, 2, 3, and 4 hours of incubation (BL 1h, 2h, 3h, 4h) and for the apical chambers at the beginning of the experiment (AP t0) and after 4 hours (AP 4h). Fluorescence emission was measured with a plate reader with excitation wavelength at 492 nm and emission at 520 nm. Data are the average of three different replicates.

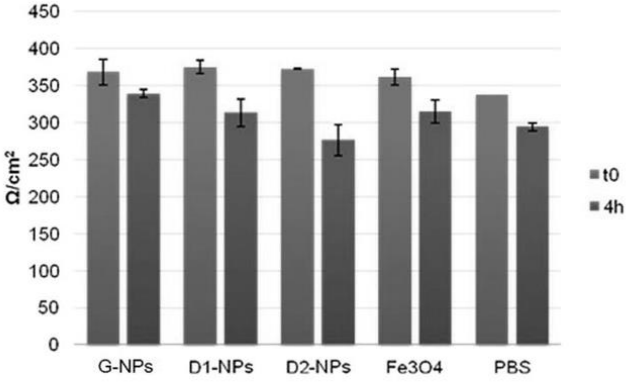

Fig. S7 Change of TEER values. Measures were done before and after 4 hours incubation with pristine NPs, PC-NPs complexes and buffer.

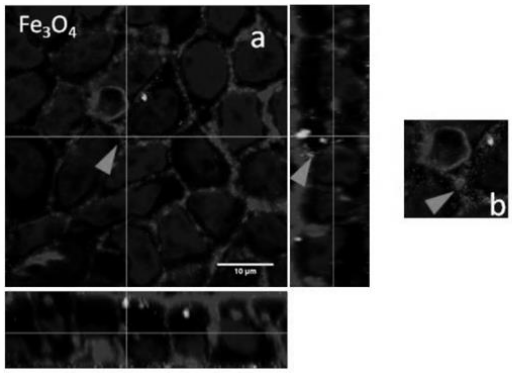

Fig. S8 Confocal stacks of pristine NPs incubated Caco-2 monolayer. A) Orthogonal stacks of the cells. B) Zoomed detail highlighted by green arrow. Actin filaments were stained by Phalloidin- Texas Red (591/608 nm) and nuclei by Hoechst 33342 (350/461 nm). Fe_3O_4 NPs were labelled by BODIPY FL-EDA (500/510 nm).Images were rendered by ImageJ.

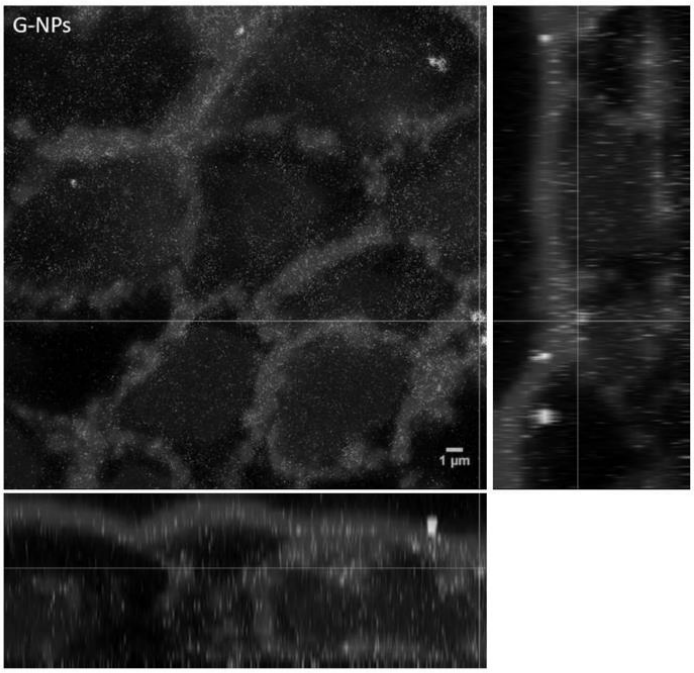

Figure S5 Confocal stacks of G- NPs incubated Caco-2 monolayer. Orthogonal stacks of the cells. Actin filaments were stained by Phalloidin- Texas Red (591/608 nm) and nuclei by Hoechst 33342 (350/461 nm). Fe_3O_4 NPs were labelled by BODIPY FL-EDA (500/510 nm).Images were rendered by ImageJ.

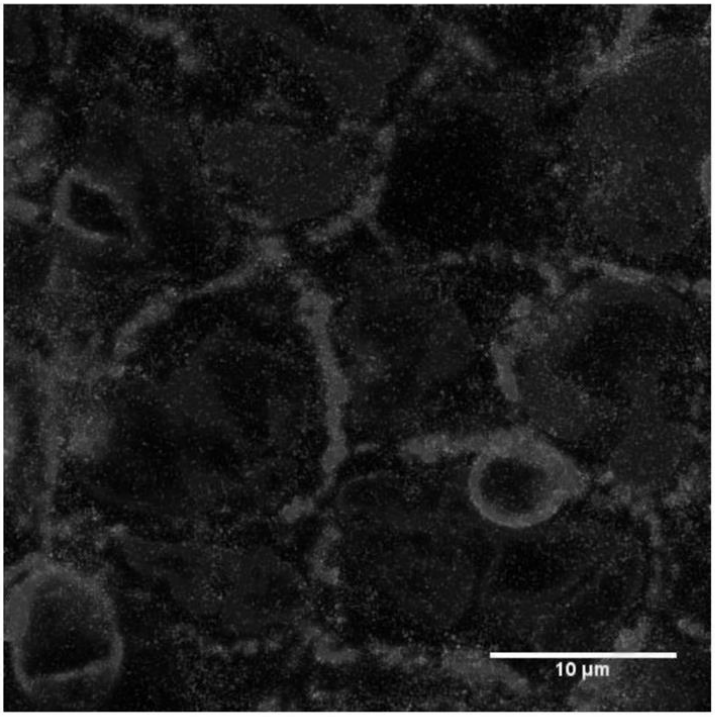

Figure S6 Confocal micrograph of D1- NPs incubated Caco-2 monolayer. Actin filaments were stained by Phalloidin- Texas Red (591/608 nm) and nuclei by Hoechst 33342 (350/461 nm). Fe_3O_4 NPs were labelled by BODIPY FL-EDA (500/510 nm).Images were rendered by ImageJ.

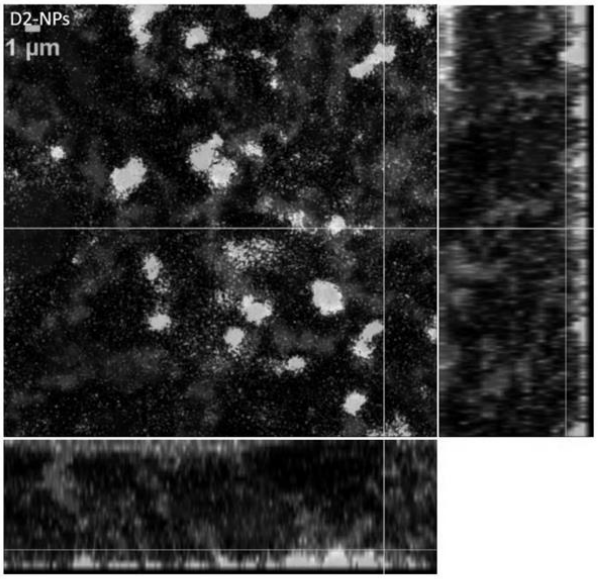

Figure S7 Confocal stacks of D2- NPs incubated Caco-2 monolayer. Orthogonal stacks of the cells close to the basal membrane. Actin filaments were stained by Phalloidin- Texas Red (591/608 nm) and nuclei by Hoechst 33342 (350/461 nm). Fe_3O_4 NPs were labelled by BODIPY FL-EDA (500/510 nm). Images were rendered by ImageJ.

Supplementary Table S 1 *Identification of protein bands extracted from gel shown in Fig.2b*

Name	Taxonomy	Coverage[1]	Score[2]	Nominal mass
		B1		
serpin-Z1a	triticum aestivum	35	404	43262
albumin-2	pisum sativum	58	276	26393
GSP-1 Grain Softness Protein	triticum aestivum	35	223	17494
vicilin 47k	pisum sativum	37	188	49542
LegA class - Q9T0P5	pisum sativum	23	115	59153

Avenin-like a1	triticum aestivum	35	91	19513
	B2			
serpin-Z1a	triticum aestivum	23	284	43262
Lectin	cicer arietinum	48	265	26363
Legumin	pisum sativum	26	265	59633
Vicilin 47k	pisum sativum	34	172	49542
GSP-1 Grain Softness Protein	Triticum turgidum	20	115	18701
	B3			
12S seed storage globulin 1	Triticum urartu	33	363	64230
YDL124W-like protein	S. cerevisiae	48	330	35653
serpin-Z1a	triticum aestivum	27	313	43262
Adh1p	S. cerevisiae	51	322	37296
Malate dehydrogenase	triticum aestivum	37	315	35805
Transaldolase	S. cerevisiae	53	299	37127
Ade1p	S. cerevisiae	69	255	34639
Phosphoglycerate kinase	S. cerevisiae	49	293	44768
Pepsine	Sus Scrofa	4	136	41635
	B4			
beta amylase	Triticum urartu	49	1216	58995
0.19 dimeric alpha-amylase inhibitor	Aegilops tauschii	77	792	13881
serpin-Z1a	Triticum aestivum	37	482	43262
Sucrose synthase 1	Aegilops tauschii	31	366	44300
Glucose-1-phosphate adenylyltransferase	Triticum aestivum	47	403	52400
Alpha amylase inhibitor CM3	Triticum durum	57	363	18893

Thioredoxin	S. cerevisiae	66	286	11311
		B5		
beta amylase	Triticum urartu	52	772	58995
Albumin-2	pisum sativum	74	759	26393
0.19 dimeric alpha-amylase inhibitor	Aegilops tauschii	70	343	13881
Seed biotin-containing protein SBP65	pisum sativum	27	315	59632
serpin-Z1a	Triticum aestivum	25	303	43262
vicilin 47k	pisum sativum	47	264	49542

[1]Sequence coverage is calculated by dividing the number of amino acids observed by the protein amino acid length
[2]The score is a probability based score. The total score is the probability (P) that the observed match is a random event. Score = -10 x LOG_{10} (P)

Supplementary Table S 2 *Identification of protein bands extracted from gel shown in Fig.3b*

Name	**Taxonomy**	**Coverage[1]**	**Score[2]**	**Nominal mass**
		B6		
Enolase	S. cerevisiae	22	129	46830
Phosphoglycerate kinase	S. cerevisiae	27	126	44783
vicilin 47k	pisum sativum	18	109	49922
Lectin	Cicer arietinum	37	102	26363
Adh1p	S. cerevisiae	19	94	37296
		B7		
Adh1p	S. cerevisiae	20	98	37296
		B8		
Amylase	Sus Scrofa	45	824	20733
ATP synthase alpha chain	S. cerevisiae	43	434	55530
Pancreatic lipase	Sus Scrofa	52	328	52446

Adh1p	S. cerevisiae	38	156	37296
Phosphoglycerate kinase	S. cerevisiae	34	141	44768
Por1p	S. cerevisiae	20	116	30524
	B9			
Phosphoglycerate kinase	S. cerevisiae	63	829	44768
Enolase	S. cerevisiae	44	707	46830
Tdh3p	S. cerevisiae	52	610	35825
pyruvate kinase	S. cerevisiae	51	531	54909
Adh1p	S. cerevisiae	54	361	37296
Dimeric alpha-amylase inhibitor	triticum dicoccoides	29	213	15904
legumin a2	pisum sativum	26	268	59633
thioredoxin	S. cerevisiae	53	260	11311
	B10			
Phosphoglycerate kinase	S. cerevisiae	57	1008	44768
Eno 2	S. cerevisiae	51	957	46993
pyruvate kinase	S. cerevisiae	61	86	54909
Tdh3p	S. cerevisiae	59	743	358825
Adh1p	S. cerevisiae	56	676	37296
Dimeric alpha-amylase inhibitor	triticum dicoccoides	49	215	15666
Pancreatic colipase	Sus Scrofa	45	287	12702
Thioredoxin	S. cerevisiae	66	277	11311

[1]Sequence coverage is calculated by dividing the number of amino acids observed by the protein amino acid length
[2]The score is a probability based score. The total score is the probability (P) that the observed match is a random event. Score = -10 x LOG_{10} (P)

8.4 Nanoscopic Agents in a Physiological Environment: The Importance of Understanding Their Characteristics

The book chapter detailed below contain a discussion on protein corona NPs characterization and issues about effective NPs *in vivo* targeting. It has been cited throughout the all thesis.

Sherwood, V.; Di Silvio, D.; Baldelli Bombelli, F. *Topics in Medicinal Chemistry* **2014,** Springer Berlin Heidelberg, 1.

Top Med Chem
DOI: 10.1007/7355_2013_36

Nanoscopic Agents in a Physiological Environment: The Importance of Understanding Their Characteristics

Victoria Sherwood, Desirè Di Silvio, and Francesca Baldelli Bombelli

Abstract The application of nanotechnology in medicine signifies one of the most exciting developments in science over the last decade. Even though advancement has been made in nanoparticle engineering in terms of size, shape and surface functionalisation, the behaviour in vivo remains poorly characterised and understood. The potential impact of engineered nanomaterials on human health is strictly related to their behaviour in the biological environment. When in contact with biological fluids, nanoparticles spontaneously interact and adsorb proteins to dramatically change their surface properties. Thus, the nanoparticle surface acquires a new biological identity that will influence its stability and interaction with the cellular machinery, thereby affecting the nanoparticle biodistribution in vivo. This protein coating 'expressed' at the nanoparticle surface is what is 'read' by the cells. Consequently, methods to effectively study the structure and composition of this bio-nano interface have been emerging as key objectives in nanoscience. In this chapter, we discuss the state-of-the-art techniques for the physico-chemical characterisation of nanoparticle-protein complexes in the biological environment with particular emphasis on their impact on the efficiency and safety of a new generation of nanomedicines. We also highlight the barriers faced by nanomedicines for effective targeting and delivery in vivo.

Keywords Engineered nanomaterials, Nanomedicine, Nanoparticles, Nanotoxicology, Protein corona

V. Sherwood and D. Di Silvio
School of Pharmacy, University of East Anglia, Norwich Research Park, Norwich, UK

F. Baldelli Bombelli (✉)
School of Pharmacy, University of East Anglia, Norwich Research Park, Norwich, UK

CEN-European Centre for Nanomedicine c/o Dipartimento di Chimica, Materiali ed Ingegneria Chimica "Giulio Natta", Politecnico di Milano, Milan, Italy
e-mail: f.baldelli-bombelli@uea.ac.uk

8.5 Fe_3O_4-COOH NPs calibration curve

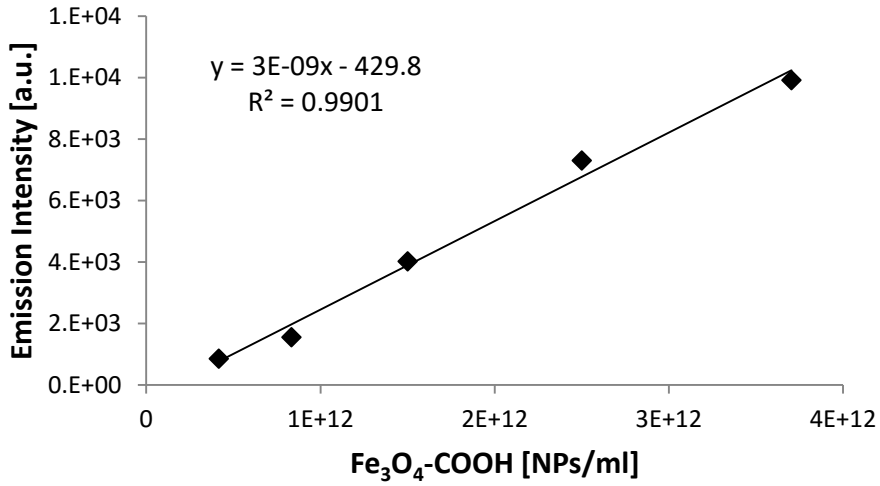

Figure 8.3 Concentration of Fe_3O_4-COOH NPs (NPs/ml) versus emission intensity. The solid line is the best linear fit of the emissions collected. The measurements were done by plate reader with excitation wavelength at 492 nm and emission at 520 nm. NPs were dispersed in serum free media without phenol red.

8.6 Bibliography

(1) Monopoli, M. P.; Walczyk, D.; Campbell, A.; Elia, G.; Lynch, I.; Baldelli Bombelli, F.; Dawson, K. A. *Journal of the American Chemical Society* **2011**, *133*, 2525.

(2) Franks, K.; Braun, A.; Charoud-Got, J.; Couteau, O.; Kestens, V.; Lamberty, A.; Linsinger, T. P. J.; Roebben, G.; Materials, I. f. R.; Measurements *Certification of the Equivalent Spherical Diameters of Silica Nanoparticles in Aqueous Solution: Certified Reference Material ERM-FD304*; Publications Office, 2012.